The Photodynamic Therapeutic Activities and Optical Limiting Properties of Metalated Asymmetric Porphyrins and Corroles

by

Kristen Paige Burgess

A thesis submitted in fulfilment of the requirements for the degree of

MASTER OF SCIENCE

AT

RHODES UNIVERSITY

May 2023

“Equipped with his five senses, man explores the universe around him and calls the adventure Science.”

– Edward Hubble.

Acknowledgements

First and foremost, I would like to extend my sincerest gratitude to Professor Mack. Your guidance over the last three years has been unwavering, and I would not be the young academic I am today without your support and encouragement. You have been an excellent teacher and leader in my academic journey thus far.

To Professor Nyokong, thank you for all the wisdom you offer. You are a phenomenal leader, and I aspire to be even half the scientist and woman you are today. The opportunities I have been fortunate enough to embrace would not have been possible without being a part of your lab, and I will be grateful forever.

To Dr Britton and Gail Cobus, thank you for your continued help. This lab is lucky to have you around to run things so smoothly. You have been a huge help in my journey thus far, and I am very grateful.

Azole, thank you for the support you offered me while applying my compounds in photodynamic antimicrobial chemotherapy (PACT). You were so helpful and engaged me in intellectually stimulating conversations, yet you taught me how to be independent and to take the initiative with my work.

To Nnamdi, thank you for your help during training and conducting PDT, especially on this challenging timeline. You allowed us to be independent and problem-solve alone but were always a call away for help.

To the rest of S22, you have all been an integral part of my research experience. I am absolutely delighted that I have had the opportunity to work with all of you and grateful for everything I have learnt from each of you, as well as all the laughs along the way. I will miss you all and wish you all the best in your future academic endeavours.

Thank you to my friends and family for believing in me more than I sometimes do. A task this daunting is seemingly impossible without a warm hug or a shoulder to cry on every now and then. You have all been so much more than just that for me. I am eternally grateful for all of you, and I would not be the woman I am today without you.

Abstract

Cancer is a devastating disease that is a leading cause of death worldwide. Despite the available cancer treatments, there is a significant need to improve the therapeutic approach towards this disease. Photodynamic therapy (PDT) is an alternative approach for treating cancer, which requires a photosensitiser, molecular oxygen and light. Although some porphyrin-based derivatives have been approved by the United States Food and Drug Administration (FDA) and other similar agencies elsewhere for photodynamic therapy, their relatively poor photophysicochemical properties mean that there is an ongoing need for new photosensitiser dyes. Singlet oxygen photosensitiser dyes can also be used to treat bacteria that develop antimicrobial resistance in the context of photodynamic antimicrobial chemotherapy (PACT).

The main aim of this study was to synthesise and characterise a series of porphyrin dyes with 4-quinolinyl, thien-2-yl and 4-bromo-thien-2-yl *meso*-aryl groups and their Sn(IV) and In(III) complexes, as well as their corrole analogues. Corroles are contracted macrocycles that have interesting optical properties. The corroles selected for study were found to be difficult to synthesise and purify and had unfavourable photophysicochemical properties and were thus omitted from the PDT and PACT biological applications within this thesis. High- and low-symmetry A_4 and ABAB type *meso*-tetraarylporphyrins porphyrins were synthesised to improve the photophysicochemical properties of the photosensitisers; the utility of these dyes as photosensitisers was studied against the MCF-7 breast cancer cell line for PDT and against *Staphylococcus aureus* and *Escherichia coli* for PACT.

The thienyl-2-yl rings were introduced to red shift the lowest energy Q band towards the phototherapeutic window, while quaternisation of the nitrogen and sulfur atoms of the 4-quinolinyl and thien-2-yl rings to introduce a cationic nature was explored to improve the bioavailability of the drugs and uptake into the target cell walls for improved efficacy. Heavy Sn(IV) and In(III) central metal ions were introduced to enhance the singlet oxygen quantum

yields and limit aggregation through axial ligation. The bromine atoms of the 4-bromo-thien-2-yl *meso*-aryl rings were also introduced to enhance the singlet oxygen quantum yields of the dyes.

Furthermore, the utility of the porphyrin and corrole molecules for optical limiting properties to limit laser radiation to protect optical devices, including eyes, was explored by the z-scan technique. One of the dyes studied, Sn(IV) tetrathien-2-ylporphyrin, that exhibited the most favourable reverse saturable absorbance (RSA) response was embedded into a poly(bisphenol carbonate A) polymer thin film to further explore its suitability for practical applications.

Table of Contents

List of Figures

List of Tables

List of Schemes

List of Abbreviations

^{1}H NMR	Proton nuclear magnetic resonance
B3LYP	Becke, 3-parameter, Lee-Yang-Parr
CFU	Colony forming units
CAM	Coulomb-attenuating method functional
$CDCl_3$	Deuterated chloroform
ΔHOMO	Separation of MOs derived from the HOMO of the parent perimeter
ΔLUMO	Separation of MOs derived from the LUMO of the parent perimeter
DCM	Dichloromethane
DDQ	2,3-Dichloro-5,6-dicyano-1,4-benzoquinone
DLS	Dynamic Light Scattering
DMA	9,10-Dimethylanthracene
DMEM	Dulbecco's Modified Eagle's Medium
DMF	N,N-Dimethylformaldehyde
DMSO	Dimethyl sulfoxide
HOMO	Highest occupied molecular orbital
IC_{50}	Half maximal inhibitory concentration
IUPAC	International Union of Pure and Applied Chemistry
IC	Internal conversion
INI	Institute for Nanotechnology Innovation
ISC	Intersystem crossing
LUMO	Lowest unoccupied molecular orbital
MCF-7	Michigan Cancer Foundation-7
MO	Molecular orbital
MALDI	Matrix-assisted laser desorption ionisation
MS	Mass Spectroscopy
MSA	Methanesulfonic acid
MeOH	Methanol
OD	Optical density
PACT	Photodynamic antimicrobial therapy
PDT	Photodynamic therapy
PS	Photosensitiser
ROS	Reactive oxygen species
RT	Room temperature
TLC	Thin layer chromatography
TOF	Time of flight

TPP	Free-base tetraphenylporphyrin
TPC	Triphenylcorrole
NCTPP	N-confused tetraphenylporphyrin
UV-vis	Ultraviolet-visible spectroscopy
XRD	X-ray diffraction spectroscopy
ZnTPP	Zinc tetraphenylporphyrin

List of Symbols

β	Nonlinear absorption coefficient
γ	Second-order hyperpolarizability
I_{lim}	Optical limiting threshold
$Im[\chi^{(3)}]$	Third-order nonlinear susceptibility
η	Refractive index
Φ_{Δ}	Singlet oxygen quantum yield
Φ_{F}	Fluorescence quantum yield
S_0	Singlet ground state
S_1	Singlet excited state
SDD	Gaussian09 default basis set
t	Time
T_n	Triplet excited state
ε	Molar extinction coefficient
m/z	Mass to charge ratio
λ	Wavelength
T_F	Fluorescence lifetime
T_T	Triplet lifetime
e^-	Electron

CHAPTER ONE

INTRODUCTION

1.1 Problem statement

Currently, there is a global drive toward the design of more selective and efficacious therapies to combat the increasingly problematic disease of cancer. Photodynamic therapy is an alternative, less invasive cancer therapy that uses light to activate molecular dyes, stimulating the formation of cytotoxic singlet oxygen ($^1O_2$), the therapeutic agent. Despite the fact that there are existing clinically-approved photosensitiser drugs, there is scope to improve their properties through rationally selected structural modifications. Porphyrin derivatives are known for their inherent photosensitising abilities, but they absorb weakly in the near-infrared of the visible region, and, thus, present issues with deeply rooted tumours and, particularly within the African context, cause negative side effects due to the interaction of endogenous biomolecules with the incident photons.

This thesis reports the photophysicochemical properties of a series of porphyrin derivatives with 4-quinolinyl, thien-2-yl and 4-bromo-thien-2-yl *meso*-aryl groups and their Sn(IV) and In(III) complexes and the activity of these molecular dyes during *in vitro* anticancer and antimicrobial therapy studies. Additionally, the optical limiting properties of the synthesised dyes were also assessed.

1.2 Target disease: cancer

Cancer is a problematic disease that is characterised by rapid and uncontrollable cellular growth in particular regions of the body; the cancerous cells are capable of invading and destroying healthy surrounding tissue, which is not limited to organs themselves.[1]

Cancer broadly refers to more than 277 different cancer diseases and currently is the second leading cause of death worldwide.[2] The variety within cancer poses a major challenge in terms of diagnostics, as well as the efficacy of treatments, because each cancer behaves differently.[2] Since different stages of cancer have been identified, it can be concluded that several gene mutations are involved in cancer pathogenesis and the development of the disease.[2] The uncontrollable cell growth can be attributed to these genetic mutations that are either stimulated by environmental or inherited genetic factors.[2]

In 2020, nearly ten million deaths were caused by cancer, which accounted for one in six deaths documented in that year.[3] The most common cancers globally are breast, lung, prostate, colon, and rectal cancer.[3]

Metastasis is a process that occurs whereby cancer spreads beyond the usual boundaries of the cell and invades other parts of the body and other organs: the primary cause of death in cancer is caused by widespread metastases. Cancer exploits the circulatory and lymphatic systems of the body to spread to surrounding tissues. However, upon early detection and treatment, the disease is usually manageable.[2,3]

Generally, cancer disrupts cellular signalling pathways, which leads to the uncontrollable growth and reduction of apoptosis (a genetically regulated form of cell death that is an essential biological process, especially in the immune system).[2,4] In addition, genetic mutations also lead to the dysfunction of vital genes.[2] The interaction between genetic predispositions and three major external factors leads to the pathogenesis of cancer:

1) Physical carcinogens: high energy radiation (e.g. ultraviolet) and ionising radiation are known to induce cancer cell formation.[3]
2) Chemical carcinogens: these are agents that interact at a molecular level and induce genetic mutations that are not repaired before replication of the cell. Common chemical carcinogens include asbestos, components of tobacco smoke and alcohol.[3,5]
3) Biological carcinogens: these are infections from parasites, bacteria, and viruses (such as the human papillomavirus) that lead to genetic mutations.[3]

Although Africa is experiencing significant improvements in population health (attributed to declining mortality rates, decreased fatality from HIV/AIDS and increased lifespans in general), the morbidity and mortality rates due to non-infectious diseases, such as cancer, are rising.[6] Cancer is an emerging problem in Africa: 57% of all new cancer cases in the world occur in low-income areas, and this is exacerbated by increased life expectancies and a lack of awareness and preventative strategies.[7] For this reason, this thesis details the synthesis, characterisation and subsequent application of molecular photosensitising agents within an African context; this will be elaborated on further.

1.3 Porphyrin derivatives and their nomenclature

Porphyrins are macrocyclic structures that have been researched extensively due to their potential application within various fields, including but not limited to the biomedical field.[8] They consist of four pyrrole moieties that are linked *via* methene bridges in a planar manner.[9,10] They are widely distributed throughout nature, mostly in their metalated forms, as iron or magnesium complexes.[11] Porphyrins are well known for their function as prosthetic groups in various essential metabolites in biological systems, including but not limited to haemoglobin, cytochromes, enzymes, and chlorophylls.[11] Their ubiquity in Nature stems from their ability to store and transport oxygen, mediate photosynthetic energy production, and their significance as enzymes and vitamins.[10] Porphyrins are heteroaromatic due to their extended conjugated 18 π-electron systems. This leads to their intense colours.[10] Their electronic structures contain 26 π-electrons in total, with 18 delocalised on the inner ligand perimeter according to Hückel's law of aromaticity.[12]

Porphyrin molecules and their derivatives have been explored as contrast agents for magnetic resonance imaging (MRI), as photocatalytic and non-linear optic agents and in molecular electronic devices. This investigation will focus on their potential utility in the biomedical field, since they have been reported to possess potential as drugs in the photodynamic therapeutic approach to cancer.[8,10] The central cavity of porphyrin molecules is suitable for coordinating various metal ions and other compounds, leading to the formation of metalloporphyrins.[10] The significance of this will be discussed below in **Section 1.7**. The photophysical properties of porphyrins and metalloporphyrins govern their biological significance, and this is a direct result of the physicochemical properties of the compounds, which can be tuned *via* structural modifications.[8,10] They are attractive within the sphere of biomedical research due to their interesting photophysical properties, such as long wavelengths of light absorption and emission, low *in vivo* toxicity, and high singlet oxygen quantum yields.[10]

Since these compounds play a significant role in many disciplines, it is essential to have a uniform nomenclature system.[13] The first nomenclature to be applied to the porphyrin system was Hanz Fischer's method, outlined in **Figure 1.3.1**. The bridging *meso*- or methene carbons are labelled **α**, **β**, **γ**, and **δ**, whereas the linking **α**-carbons are left unassigned. The **β**-carbons are numbered from 1-8.

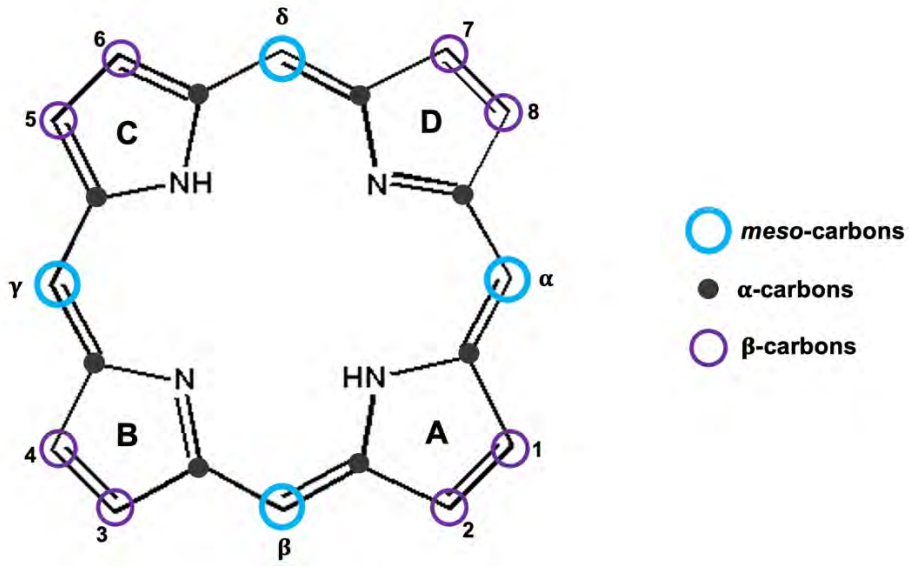

Figure 1.3.1. Fischer's nomenclature for porphine (the parent compound of porphyrin systems).[13]

The IUPAC subsequently provided a more comprehensive numbering scheme for the porphyrin that has proven more useful for interdisciplinary communication.[13] The numbering in this nomenclature is from 1-24, with every atom in the parent structure included, as outlined in **Figure 1.3.2**.

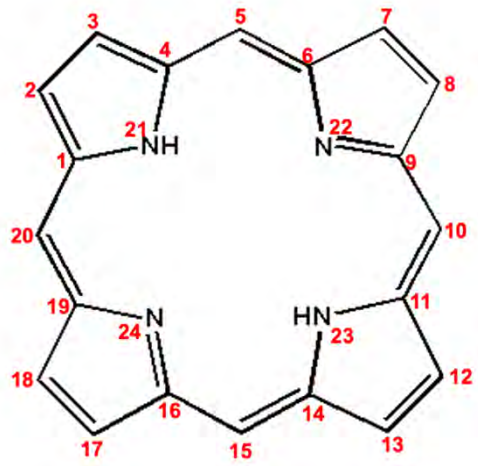

Figure 1.3.2. IUPAC nomenclature for porphine, where every atom is assigned a number.[13]

1.4 Corroles

Corrole compounds are derivatives of porphyrins that are heteroaromatic and tetrapyrrolic, but contain a direct pyrrole-pyrrole bond and, consequently, only three methene bridges.[14,15] In a similar manner to porphyrins, they have 18 π-electrons on the inner ligand perimeter, as there is an additional protonated pyrrole nitrogen upon loss of the bridging *meso*-carbon.[16] The structure of a corrole is depicted in **Figure 1.4.1**. Corroles have been explored extensively in the past two decades, due to their increased metabolic rate in the body and favourable potential as cancer therapeutic agents. Corroles have a contracted ring structure, which affords a lower C_{2v} symmetry, more intense absorption of light at the lower energy end of the visible spectrum and lower oxidation potentials.[17,18] They have only been explored extensively in the last two decades due to a breakthrough made by Gryko *et al*. in their previously challenging synthesis.[17]

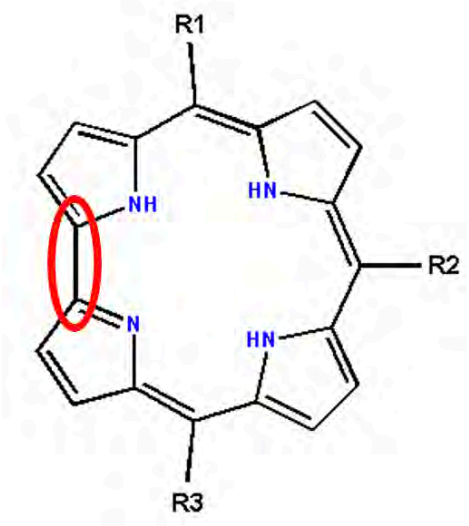

Figure 1.4.1. The structure of a corrole with the pyrrole-pyrrole bond highlighted.[17]

Corroles can be exploited for photodynamic therapy applications due to their increased absorption at the lower energy range of the visible region. Ultimately this means that they will absorb light of longer wavelength more efficiently. This affords a more efficacious therapy, since the aim is to exploit the phototherapeutic window, which is highlighted in **Figure 1.4.2**. This helps avoid the development of negative side effects that occur when endogenous

biological molecules interact with the incident radiation, as well as achieving deeper penetration into the tissue.[19]

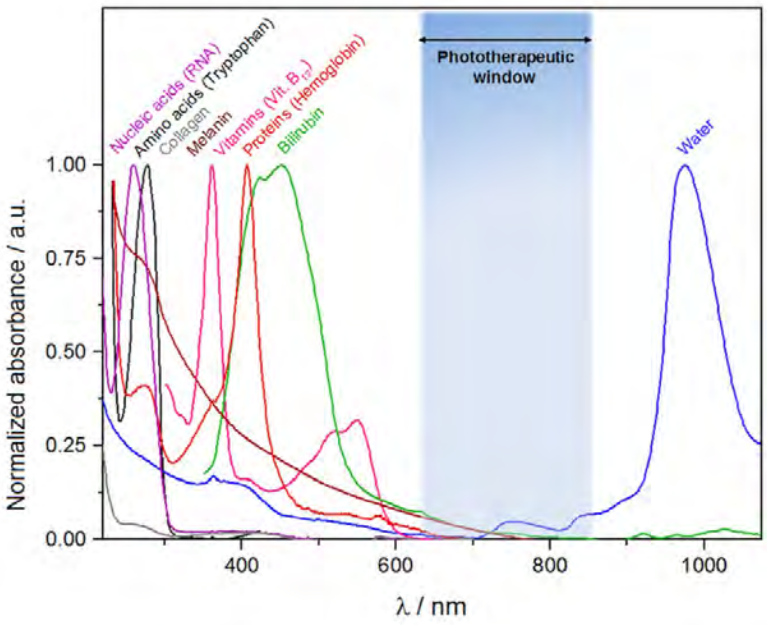

Figure 1.4.2. The phototherapeutic window (highlighted in blue) normally should be used within this therapy. This results from the absorption of light by endogenous biological molecules in the visible range and by water in the infrared. Reproduced with permission from Reference **20**, © Elsevier 2016.

Corroles can be metalated; their free-base and metalated counterparts have been studied for various applications due to their potential as drug candidates for cancer, diabetes, and neurodegenerative diseases, antibacterial agents in photodynamic antimicrobial therapy, and as bio-imaging agents.[17] Their potential as imaging agents within the biomedical sphere stems from their apparent increased fluorescence upon contraction of the macrocyclic cavity.[17] In addition, corroles can form stable conjugates with proteins, which expands their utility for application in biological systems.[18]

Corroles are more acidic than their porphyrin counterparts since they contain three pyrrole- and imine-like nitrogen donors.[21] Corroles can coordinate metal ions in high oxidation states, due to the formation of a tetradentate trianion (i.e. a tribasic ligand) upon metalation.[18,21] There has been growing interest in these contracted ring structures for applications since their

optical, redox, and coordination properties are significantly modified.[16] Corroles are near planar due to their heteroaromaticity.[18]

In nomenclature terms, the missing *meso*-carbon is omitted in the numbering process. This results in the inner nitrogens in porphyrins and corroles being assigned identically.[22] Porphyrins and corroles that contain differing *meso*-groups are named similarly: if they contain two different functionalities at the *meso*-positions, a porphyrin would be referred to as either a *trans*- or *cis*-A_2B_2 depending on whether these groups are opposite or next to each other, respectively.[22] Corroles are named in the same manner.

This investigation will focus primarily on a comparison of corrole compounds with their porphyrin counterparts. Symmetric and asymmetric corroles and porphyrins will be studied to explore the effect of a loss of symmetry on the photophysicochemical and redox properties of the photosensitising agents.

1.5 The synthetic history of the macrocycles in this investigation

1.5.1 The history of porphyrins

Porphyrins are readily available *via* biosynthetic routes with relatively simple precursors and in biological systems[23]; a great deal of interest and research over the past century has led to the development of synthetic pathways to exploit the rich chemistry of these compounds.[11]

The history of porphyrin synthesis began with Hans Fischer: in 1929, he started developing methodologies for porphyrin synthesis using dipyrromethene salts and organic acid solvents that, ultimately, afforded multiple naturally occurring porphyrins at low synthetic yield.[24] He was honoured as a Nobel Laureate in 1930 for his discovery of essential biological pigments, such as hemin (a component of haemoglobin) and chlorophylls, and particularly, for his synthesis of the former.[25]

In 1935, Paul Rothemund reported the first synthesis of porphyrins from a reaction between aldehydes, pyrrole and methanol; he conducted this reaction under three different conditions: 1) at room temperature for several weeks, 2) heated under reflux for 15–25 h, or 3) in a sealed tube place in a water bath at 85–90°C for 10–20 h, detailed by **Scheme 1.5.1.1**.[26,27]

In Rothemund's early work, acetaldehyde was primarily used to yield tetramethylporphin, which lacks aromatic groups at the *meso*-positions of the porphyrin; he also attempted to use formaldehyde, which yields the tetracyclic parent compound of porphyrins, porphin, which has a slightly atypical UV-visible absorption spectrum.[27] He applied this approach to determine the utility of using a series of different aldehydes in a porphyrin synthesis, which led to very important developments in this field.[26] Rothmund also coordinated the porphyrins to copper and achieved increased yields when performing the reactions in pyridine.

Rothemund and Menotti reported the first synthesis of *meso*-tetraphenylporphyrin (TPP) in 1941: this was achieved under anaerobic conditions in a sealed tube in pyridine at 200°C and resulted in a 5% yield of the target compound.[28,29]

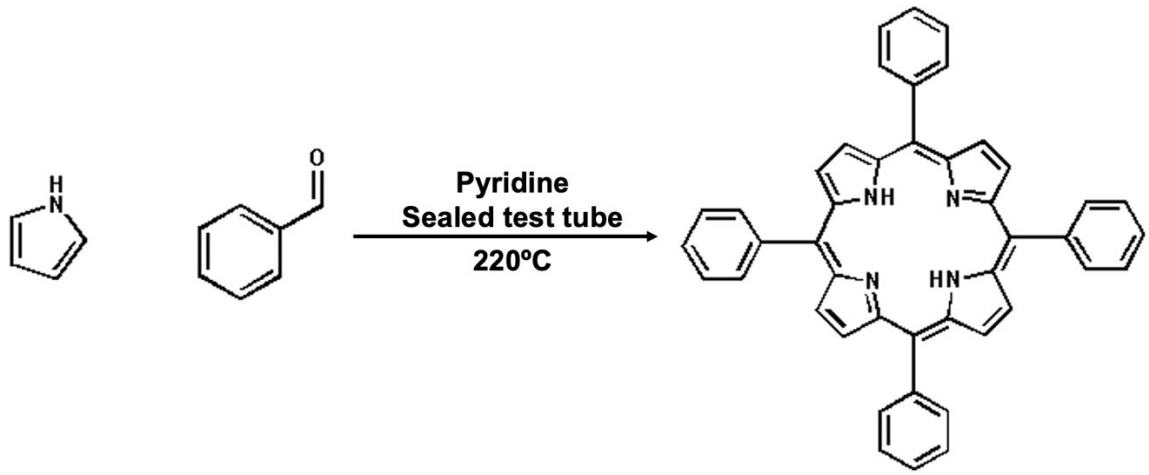

Scheme 1.5.1.1. The synthetic scheme that Rothemund used to yield tetraphenylporphyrin in the 1930s.[25,26]

Further synthetic developments were achieved to improve the yields of the target porphyrins, as well as the versatility of the reaction. Adler and Longo and their co-workers developed a refined method for the synthesis of *meso*-substituted symmetrical porphyrins: this involved reacting equimolar amounts of pyrrole and benzaldehyde in propionic acid or acetic acid as solvents that usually yields the porphyrin in one step and can achieve yields of up to 30% (**Scheme 1.5.1.2**).[28] The reaction is carried out in aerobic conditions, and the increased yields afford large-scale synthesis of porphyrins, which had been problematic previously.

The Adler-Longo method can be slightly problematic when dealing with aldehydes that are sensitive to the harsh acidic environment. For example, alkyl and aromatic derivatives with ionisable functional groups tend to form porphyrin acid salts. This limits the applicability of this particular synthesis when designing porphyrins that bear these functionalities. The main reason for this is the increased solubility experienced upon forming the porphyrin acid salts, which hinders the precipitation event carried out with methanol and water to yield crystals that

can be subjected to chromatographic purification.[30] The harsh reaction conditions used in the Adler-Longo synthesis of porphyrins also limit the yields, in addition to the versatility of the reaction.[31] As a result, it lacked rational and reproducible access to different *meso*-substituents.[31]

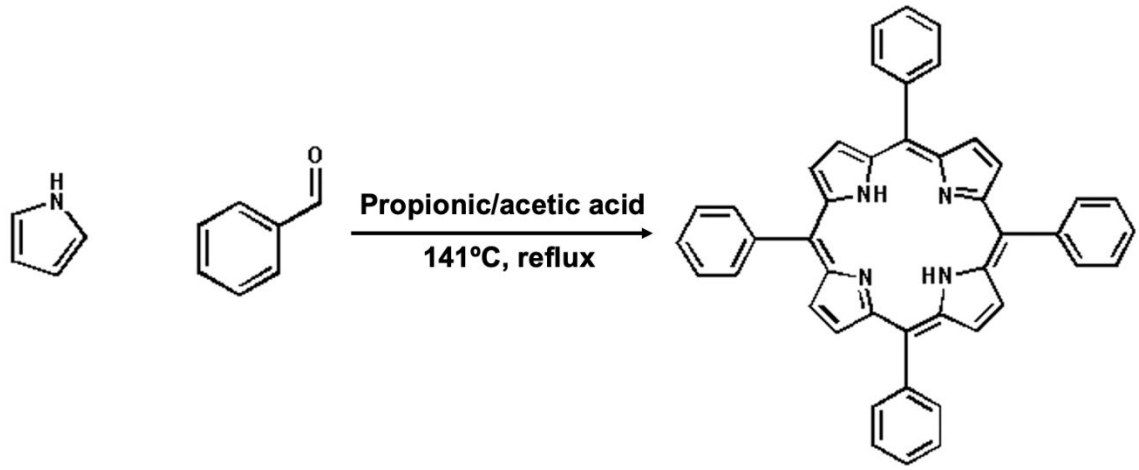

Scheme 1.5.1.2. The optimised synthetic strategy developed in the 1960s by Adler and Longo *et al.* to yield tetraphenylporphyrin.[28]

Despite its drawbacks, the Adler-Longo synthesis of porphyrins is the most routinely used approach for preparing porphyrins. It has been adapted to yield asymmetric porphyrins in what is known as statistical condensation reactions.[32] This usually involves the reaction between two different aldehydes in the desired ratio of the substitution at the *meso*-positions of the porphyrin with pyrrole added in equimolar quantities to the aldehydes: for an A_3B porphyrin, one would use 3 eq of the aldehyde A, 1 eq of aldehyde B and 4 eq of pyrrole (**Scheme 1.5.1.3**). This proves incredibly problematic at the purification stage and is not a feasible option for large-scale syntheses.[32]

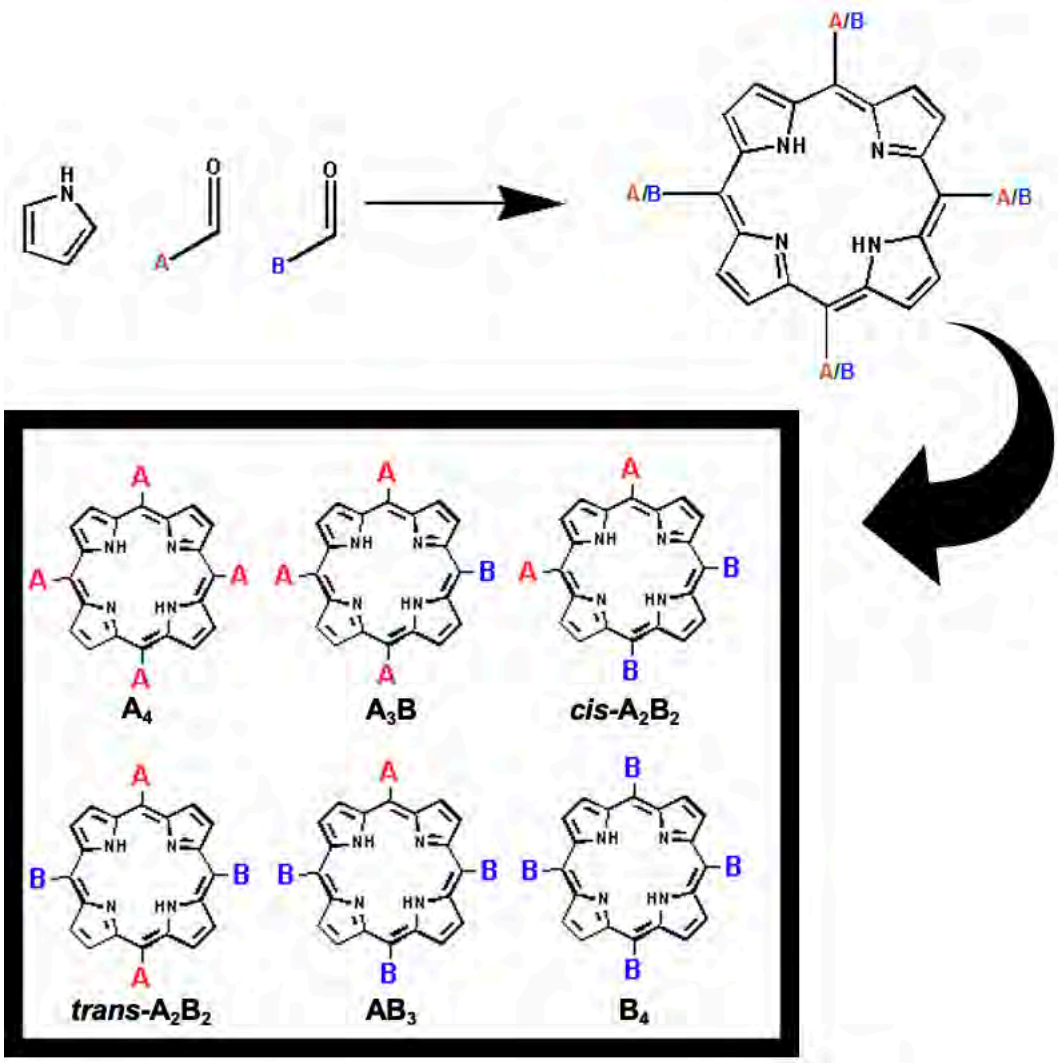

Scheme 1.5.1.3. The general synthetic scheme for a statistical condensation reaction.[32]

Having encountered the disadvantages associated with the Rothemund and the Adler-Longo methods, Jonathan Lindsey opted to design a more efficient reaction that was more generally applicable for asymmetric syntheses by utilising a two-step mechanism.[31] The conditions used are less harsh and, in some ways, attempted to adopt a biomimetic approach: 1) an acid-catalyzed condensation of an aldehyde and pyrrole to yield a porphyrinogen as a precursor, and 2) an oxidation reaction achieving $6e^-/6H^+$oxidative dehydrogenation, ultimately yielding the target porphyrin (**Scheme 1.5.1.4**).[31] Relatively mild conditions are achieved in this synthesis: a chlorinated solvent that contains an acid (usually TFA or $BF_3{\cdot}O(Et)_2$, an oxidant that is soluble in organic solvent systems, such as tetrachloro-1,4-benzoquinone (*p*-chloranil) or 2,3-dichloro-5,6-dicyano-1,4-benzoquinone (DDQ), and dilute concentrations of the pyrrole and aldehydes (0.01 M). These reaction conditions help to limit the formation of

oligopyrromethanes and enhance the formation of porphyrinogens, which are subsequently oxidised to yield the porphyrin macrocycle. The reaction conditions were optimised by systematically varying the reactant concentrations, the type and concentration of the acid catalyst, determining the suitable aldehydes, and general conditions for the reaction.[31]

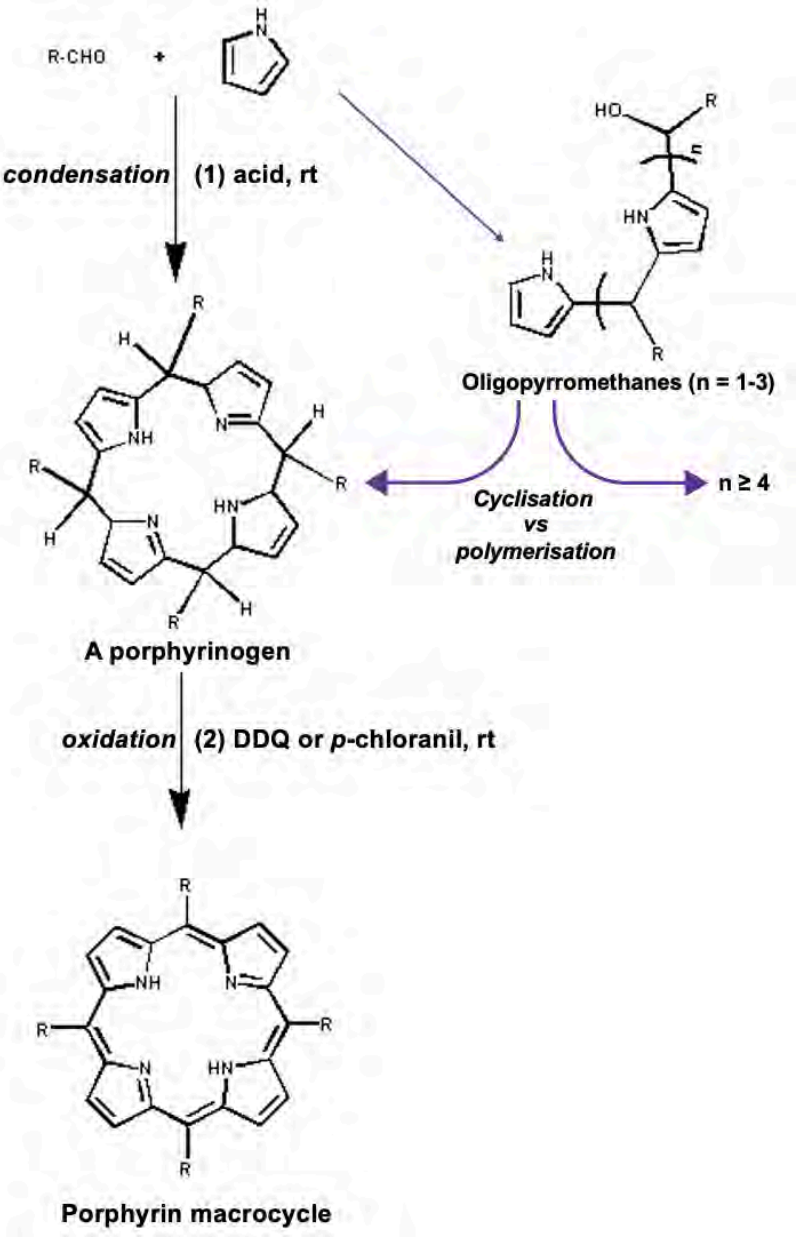

Scheme 1.5.1.4. The synthetic scheme for Lindsey's route to yield a porphyrin, which relies on a biomimetic approach.[31]

Although a statistical condensation reaction can yield a desired asymmetric porphyrin, it is inappropriate for large-scale syntheses. Lindsey *et al.* attempted to find better approaches to yield a particular asymmetric porphyrin more selectively to limit the amount of chromatography required.[31] The major strategy adopted to increase the selectivity of an asymmetric porphyrin

synthesis was to employ dipyrromethane (DPM) precursors (**Scheme 1.5.1.5**). There are multiple methods to achieve the synthesis, but a considerable challenge presents itself in preventing the DPM from oligomerising and halting the reaction at the DPM required for further use in the porphyrin synthesis. In Lindsey's one-flask DPM synthesis, pyrrole is used as both the reactant and the solvent with an acid (TFA, $BF_3 \cdot O(Et)_2$, or $InCl_3$) added at room temperature. Since pyrrole is used as the solvent, particularly high ratios of pyrrole:aldehyde (25:1 to 100:1) are used to limit the oligomerisation event. The DPM can be purified *via* column chromatography. This synthesis has proven useful in yielding hundreds of different stable DPMs in a reaction that can be scaled up to produce over 100 g.

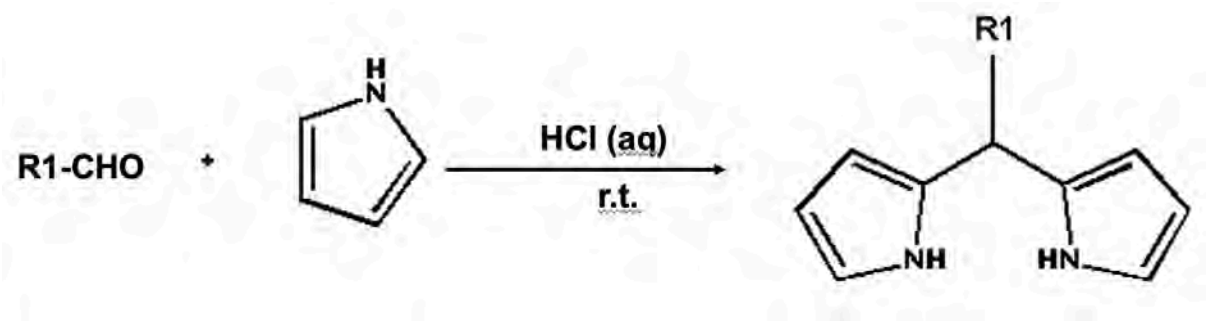

Scheme 1.5.1.5. A synthetic approach used by Rohand *et al.* to yield dipyrromethanes.[33]

Although ABCD porphyrins can be yielded from a series of reactions with DPMs, in this investigation, it was *trans*-A_2B_2 porphyrins that were synthesised.

1.5.2 The history of corroles

Kay and Johnson discovered corroles *via* serendipity in 1964. The Johnson research group aimed to synthesise a corrin ligand, but instead achieved the synthesis of a corrole *via* the cyclisation of *a,c*-biladienes .[34] Since then, corroles have become an extensively researched molecule rather than an academic curiosity.[34] In 1999, there was an important advance in their synthesis: two research groups independently published research on the synthesis of A_3-corroles in a one-pot manner; this was achieved with pyrrole and aromatic aldehydes as the reagents.[34] Despite the very low yields, the fact that these molecules could be prepared in essentially one step was a great advance in the field. Since corroles provide properties that differ markedly from porphyrins, this advance was necessary to facilitate important research that was subsequently conducted.[34]

Kay and Johnson, as previously mentioned, were the first to prepare corrole macrocycles.[22] The synthesis involved the irradiation of a basic solution of 1,19-dideoxybiladiene-ac in methanol under a 200 W tungsten bulb; complete cyclisation was observed after only 10 min, as outlined in **Scheme 1.5.2.1**.[22]

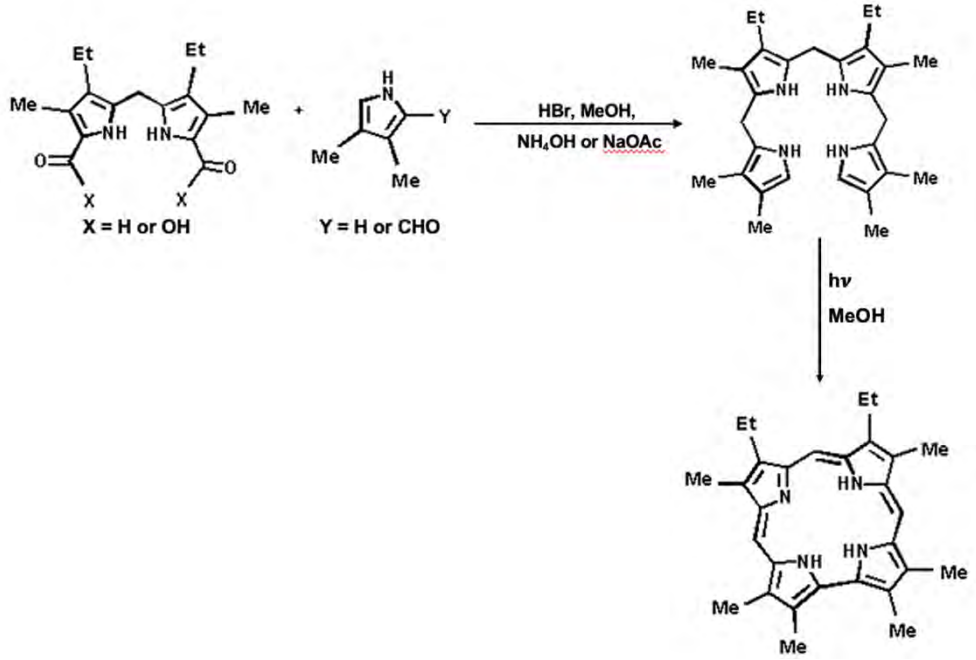

Scheme 1.5.2.1. The synthetic scheme that Kay and Johnson used to achieve the first corrole macrocycle.[22]

The Kay and Johnson group was able to form the first metalated corrole complexes with Zn(II) and Ni(II) as the coordinated ions, and they also reported the basic nature of the NH bond in corroles *via* deuterium exchange studies.[22] "Templated macrocyclisation" was achieved by the same research group: $Co(OAc)_2$ was used in the cyclisation step to yield cobalt corroles, and this has remained the synthetic approach of choice for most research groups (**Scheme 1.5.2.2**).[22]

Chan and co-workers reported a method to obtain a rhenium-oxo complex of 5,10,15-*tris*-trifluoromethylcorrole in 1998: 5,10,15,20-*tetrakis*(trifluoromethyl)porphyrin was converted into this corrole *via* a metal-assisted ring-contraction mechanism.[22,35]

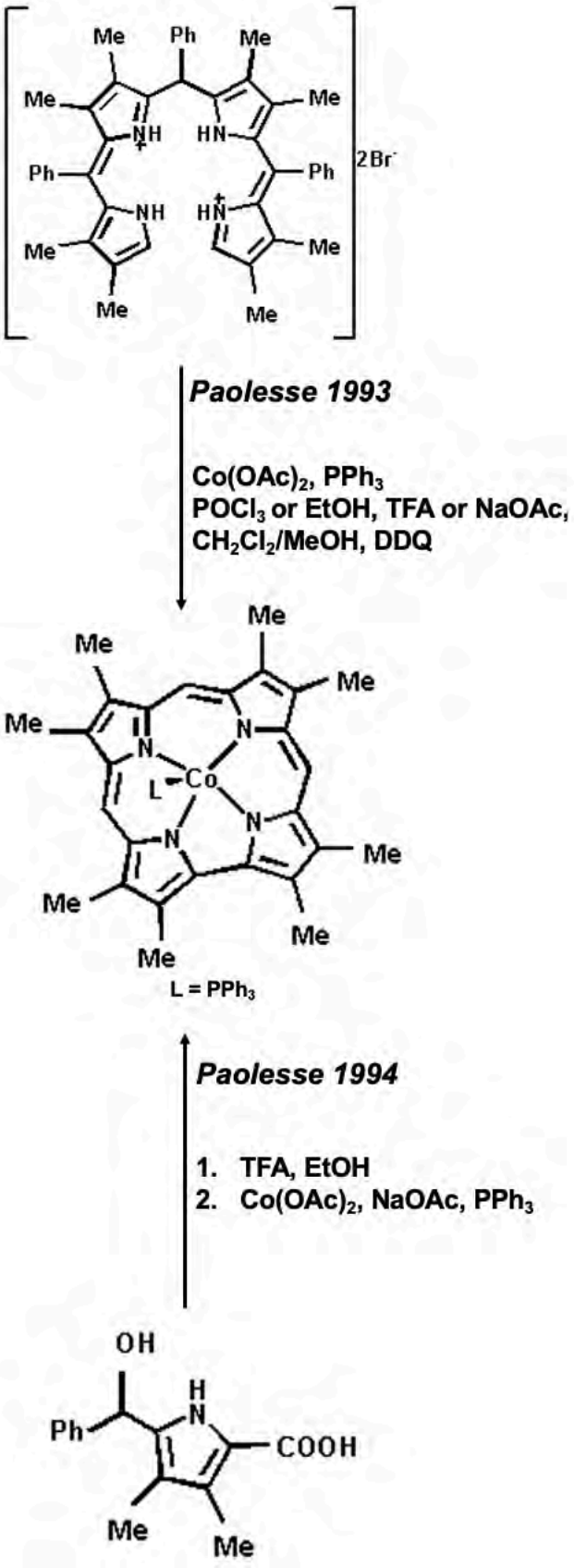

Scheme 1.5.2.2. Paolesse's approach reported in the 1990s for preparing metalated corroles *via* two different synthetic strategies.[22]

It was not until 1999 that the breakthrough for corrole synthesis was achieved when two independent research groups published papers describing the direct synthesis of *meso*-substituted corroles with aromatic aldehydes and pyrrole as the starting reagents.[18,22,34] The first method, reported by the Paolesse group and detailed by **Scheme 1.5.2.3**, was a slight modification of the Rothemund reaction, an already widely established approach to yield porphyrins; nonetheless, the reaction used the same mechanism required to yield the porphyrin counterparts.[22] The reaction conditions (including but not limited to the acid type and concentration, the concentrations and molar ratio of the reactants) that were used affected the products that were yielded: the polypyrrolic products were either closed-chained like porphyrins or open-chained like bilanes, which are important precursors for preparing corroles.[22]

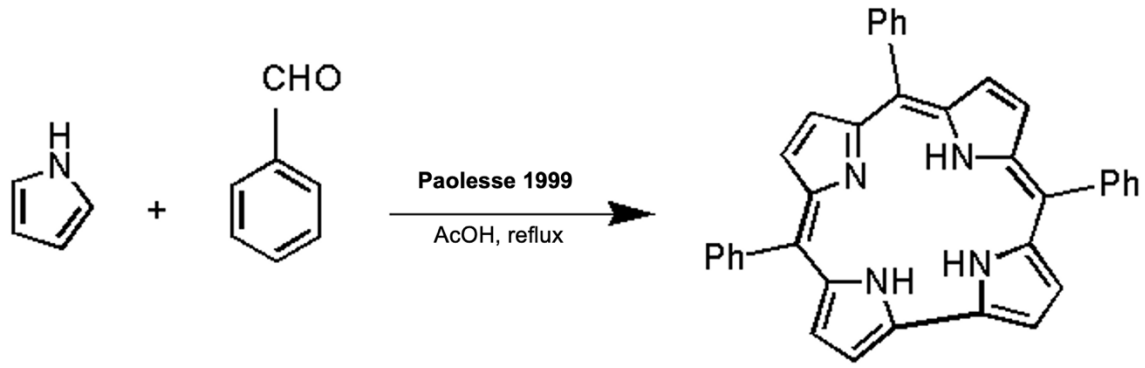

Scheme 1.5.2.3. The 1999 approach for synthesising free base corroles reported by the Paolesse research group.[22]

While triphenylcorrole was synthesised in a reaction that closely resembles the Rothemund reaction (3:1 ratio between pyrrole and benzaldehyde, respectively), the first *tris*-pentafluorophenyl-corrole was reported by Gross and coworkers in a reaction that more closely resembles the Lindsey reaction. This was achieved with equimolar quantities of the relevant aromatic aldehyde and pyrrole mixed on a solid support, such as alumina; after the condensation step, the reaction was diluted with dichloromethane and oxidised with the use of DDQ.[22] It was initially assumed that an acid catalyst was not necessary for this reaction, but it was later discovered that small amounts of acid present in the aldehydes were catalysing the reaction.[22] Although the yields of corrole products were between 5 and 15% initially, it was

a turning point in their synthesis and provided scope for further optimisation, which was later achieved.[22]

The revolution of corrole synthesis was not achieved until Gross *et al.* developed a one-pot synthetic approach to yield corroles that many researchers continue to use.[18,36] This synthesis was a direct approach that uses pyrrole and an aromatic aldehyde and facilitates the synthesis of the corrole target product in a single day; the synthesis can be performed in three different ways, including with a solid-support, with an acid-catalyst, or neat.

Furthermore, in 2006 Gryko *et al.* made a breakthrough in the synthesis of *trans*-A_2B corroles: the synthetic approach involved using a dipyrromethane and a secondary aromatic aldehyde in a water/methanol solvent mixture. They achieved yields of approximately 50% when the reactants were relatively small and/or hydrophilic. Sterically hindered dipyrromethanes require an increased MeOH/H_2O ratio (2:1), and they were still able to achieve yields of approximately 30%. Gryko *et al.*'s synthetic approach could achieve gram quantities and afforded a relatively simplified chromatography and/or crystallisation process. Additionally, they found that *p*-chloranil generally gives higher yields of corroles (except in the case of aldehydes with strong electron-withdrawing groups).[34] To date, this synthetic approach developed by Gryko *et al.* remains the most efficient procedure for preparing high- and low-symmetry corroles, as outlined by **Scheme 1.5.2.4**.

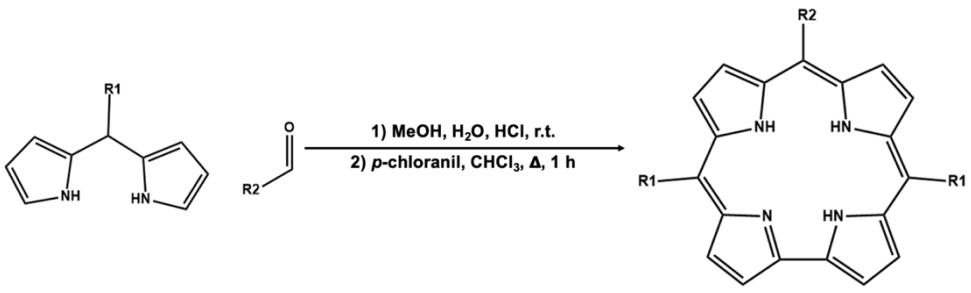

Scheme 1.5.2.4. Gryko *et al*.'s synthetic approach to yield a *trans*–A_2B corrole.[34]

1.6 Electronic and optical properties of porphyrin-type molecules

The characteristic colours observed in porphyrinoid compounds can be attributed to their electronic properties: $\pi \rightarrow \pi^*$ transitions occur after absorption of incident photos in the visible region, unlike what would be the case for most transition metal complexes. Porphyrins display well-known spectroscopic trends in their absorption spectra: an intense B (or Soret) band around 400 nm and a weaker absorption band envelope in the 500–750 nm range termed the Q bands (**Figure 1.6.1**).[37]

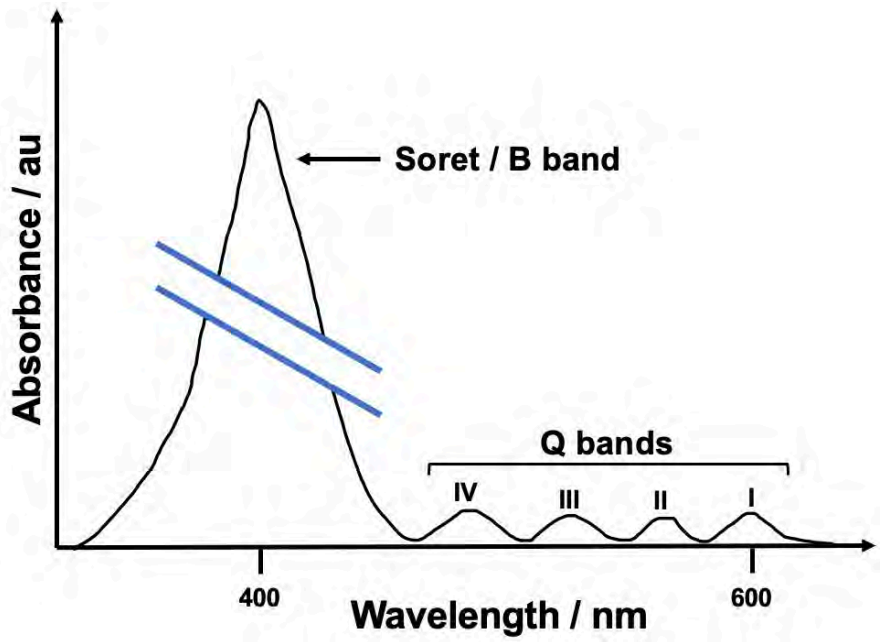

Figure 1.6.1. A schematic representation of a typical UV-visible absorption spectrum of a free-base porphyrin, depicting the characteristic Soret (or B band) and the Q band envelope.[38]

The nodal patterns of the HOMO and LUMO orbitals of porphyrin macrocycles and their derivatives provide the starting point in conceptual frameworks such as Gouterman's 4-orbital model and Michl's perimeter model for analysing how transitions between the orbitals give rise to the typical spectral bands that are observed (**Figure 1.6.2**).

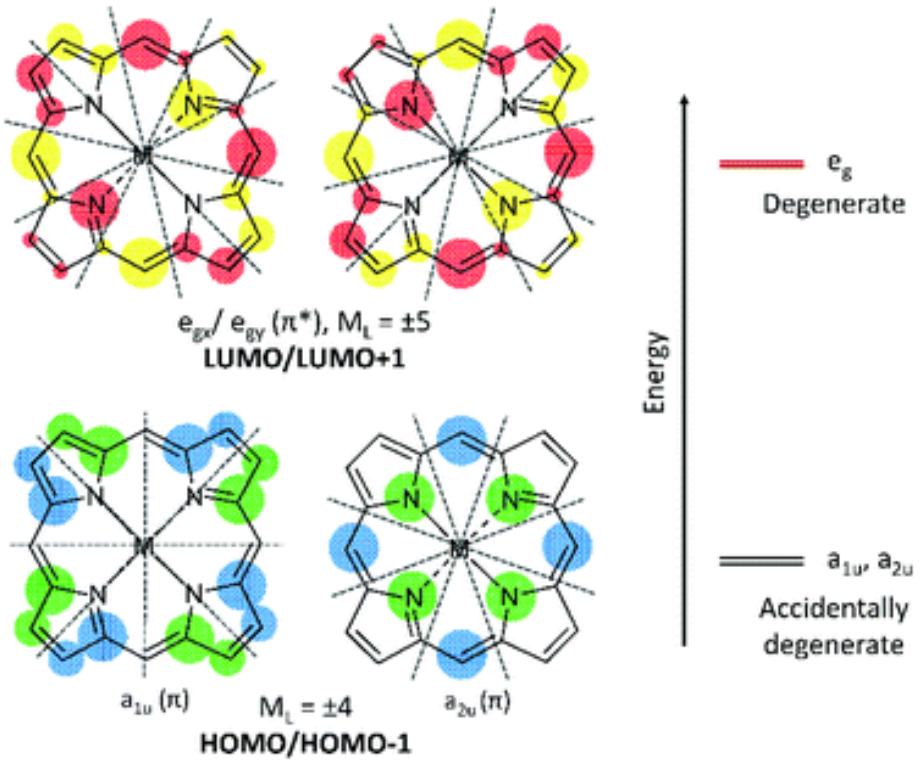

Figure 1.6.2. The nodes for the HOMOs (4 nodal planes; M_L = ±4) and LUMOs (5 nodal planes; M_L = ±4) are depicted by the dotted grey lines; these represent metallated porphyrins with an 18 π electron ring. The blue and green represent the electron density of occupied π molecular orbitals, and the red and yellow represent that of unoccupied π* molecular orbitals. Reproduced with permission from Reference 39, © Royal Society of Chemistry 2017.

Although density functional theory (DFT) and time-dependent density functional theory (TD-DFT) are routinely used to calculate the MO energies and predict the absorption spectra, older conceptual frameworks, such as Gouterman's 4-orbitals model and Michl's perimeter model, still prove useful in identifying and analysing the trends associated with the electronic and optical properties across series of related macrocyclic structures.[16]

In the 1960s, Martin Gouterman provided a theoretical evaluation of the absorption spectra of porphyrins.[16] A comparison was made between porphyrins and a D_{16h} symmetry 16-atom 18 π-electron $C_{16}H_{16}^{2-}$ model species: cyclic polyenes (the [16]annulene dianion mentioned or [18]annulene) are used because they are considered a parent ligand of porphyrins and their analogues.[16] It was termed the four-orbital model, and it affords a ready explanation of the absorption spectra of tetrapyrrolic macrocycles, like porphyrins and their analogues, as well as phthalocyanines.[16] Michl's perimeter *4N + 2* and *4N* models, as well as Gouterman's 4

orbital model, will be used as the conceptual framework to understand the effect that the contraction of the macrocycle (in the case of the corrole) and the isomerisation (in the case of the N-confused porphyrin) have on the electronic structures and optical properties of the series of compounds.

In the 1940s, molecular orbital theory was used by Platt to assign the major spectral bands in optical spectrum of benzene: the M_L = 0, ±1, ±2, 3 angular nodal properties of the π system MOs were taken into consideration, where M_L (magnetic quantum number) describes the orbital angular momentum within the π system.[40] Two transitions exist between the orbitally degenerate highest occupied molecular orbital (HOMO) and the lowest unoccupied molecular orbital (LUMO), namely, the allowed (ΔM_L = ±1) transition and the forbidden (ΔM_L = ±3) transition.[16] The allowed and forbidden considerations come about since magnetic vector of the incident photon can only rotate once per wavelength, at most. In the 1960s, Gouterman applied this theoretical evaluation to porphyrinoid systems: here, there is an M_L = 0, ±1, ±2, ±3, ±4, ±5, ±6, ±7, 8 sequence in the MOs of the inner ligand perimeter of a $C_{16}H_{16}^{2-}$ parent species (**Figure 1.6.3**). Once pyrrole rings are introduced into the parent ligand perimeter, a loss of symmetry is observed from D_{16h} (as seen in the parent 16 atom sp^2-hybridized carbon atom ring) to D_{4h}. A degenerate LUMO ($1e_g^*$ or **-a** and **-s**) and a nondegenerate HOMO ($1a_{1u}$ and $1a_{2u}$ or **a** and **s**). with M_L = ±5 and M_L = ±4 angular nodal patterns respectively exist. Gouterman's four orbital model accounts for the B and Q bands observed in porphyrinoid spectra with the consideration of allowed ΔM_L = ±1 and forbidden ΔM_L = ±9 transitions, respectively, which is outlined in **Figure 1.6.4**.[41,42]

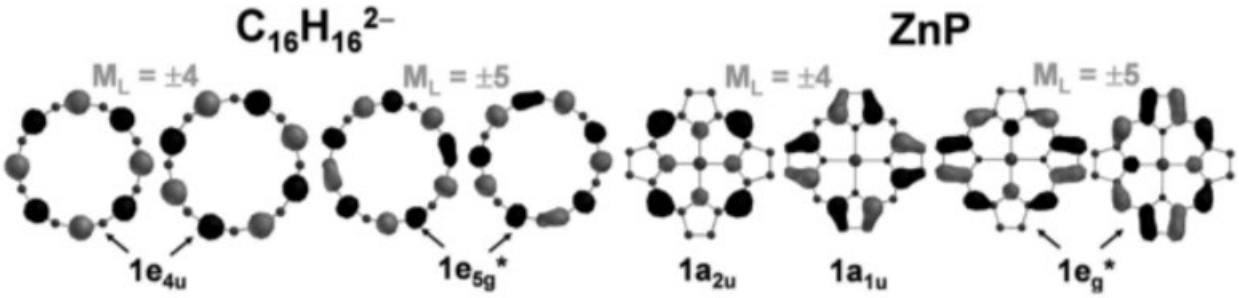

Figure 1.6.3. The four frontier π-MOs of the parent ($C_{16}H_{16}^{2-}$) perimeter and a zinc porphyrin. Reproduced with permission from Reference 16, © American Chemical Society.

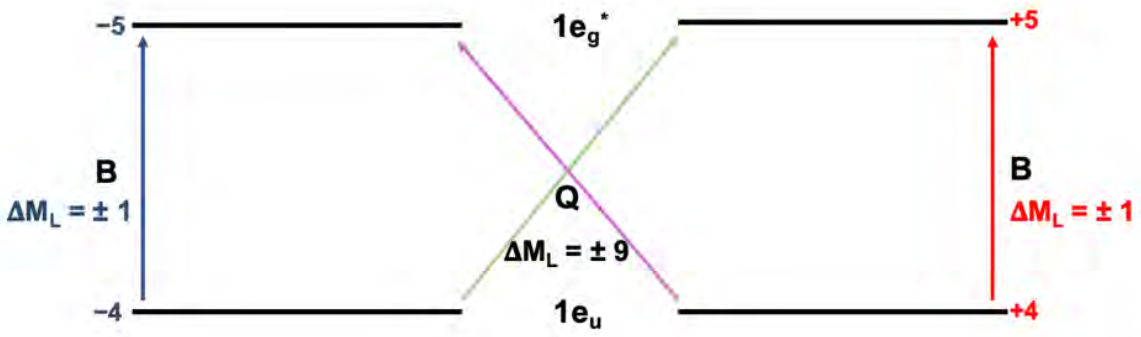

Figure 1.6.4. Gouterman's four-orbital model explains the electronic transitions that give rise to the B and Q bands in porphyrinoid systems.[16]

The Q bands of porphyrins are almost fully forbidden due to the accidental degeneracy of the $1a_{1u}$ and $1a_{2u}$ MOs: this results in a close to perfect cancellation of the electric dipole transition moments that arise from the near equal contributions of the $1a_{1u} \rightarrow e_g^*$ and $1a_{2u} \rightarrow e_g^*$ transitions.[16,41,42] When the structure of a porphyrin ligand is modified, the energies of the frontier π-MOs can be significantly altered so that there is a significant lifting of the near degeneracy of the $1a_{1u}$ and $1a_{2u}$ MOs; this leads to a mixing of the allowed and forbidden properties of the B and Q bands, respectively, Since the electric dipole transition moments that arise from the $1a_{1u} \rightarrow e_g^*$ and $1a_{2u} \rightarrow e_g^*$ transitions are no longer equal, they can no longer cancel, so there is an intensification of the Q bands.

Michl introduced an **a**, **s**, **-a** and **-s** terminology for the MOs derived from the HOMO and LUMO of the parent hydrocarbon perimeter.[16] When nodal planes are aligned with the *yz*

plane, the MOs are labelled **a** or **-a** depending on whether it is a HOMO or LUMO orbital, respectively, and if there are large MO coefficients on this plane, the MO is **s** or **-s** (**Figure 1.6.5**).[43,44] This convention will be used within this thesis to facilitate comparisons between structures of differing symmetry.

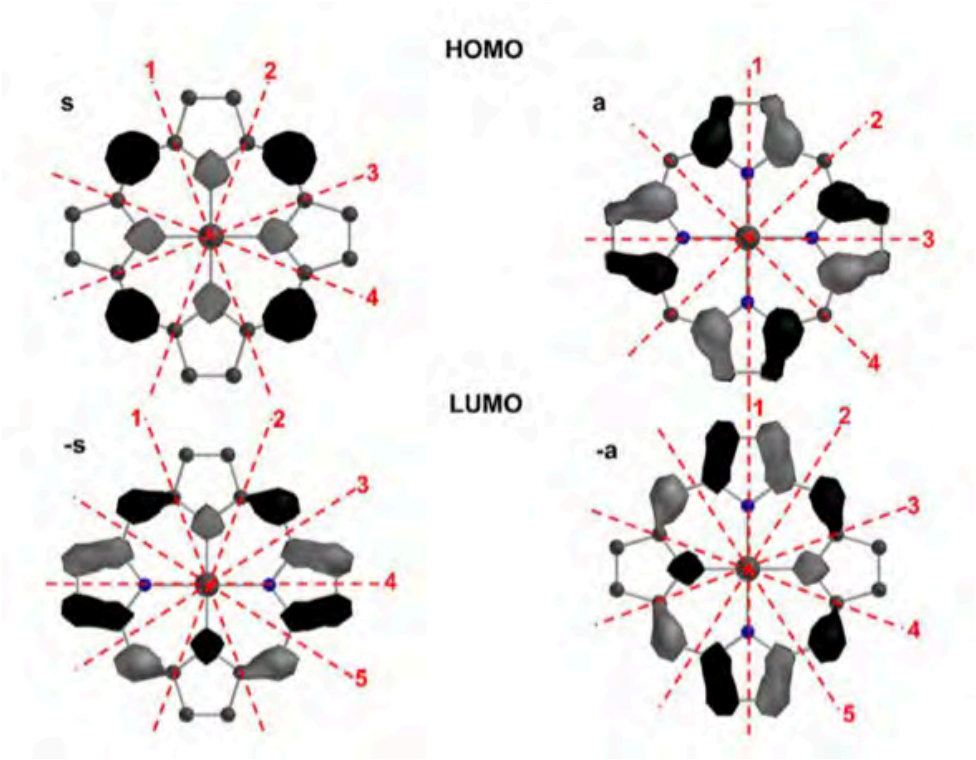

Figure 1.6.5. Angular nodal patterns for **a**, **s**, **-a** and **-s** MOs of a ZnTPP. This model can be used to qualitatively assess how structural modifications modify the MOs energies and hence the optical and redox properties. Reproduced with permission from Reference **45**, © American Chemical Society 2005.

The mixing of the Q and B band forbidden and allowed properties are controlled by the relative energy separations of the MOs derived from the HOMO and LUMO of the parent hydrocarbon perimeter; there will be referred to as ΔHOMO and ΔLUMO values, as they are referred to in Michl's terminology.[16] When ΔHOMO ≈ ΔLUMO, the Q band remains largely forbidden, and most of the intensity observed in the Q band region of a spectrum is obtained by vibrational borrowing from the allowed B transition.[41] In contrast, if structural modifications cause a splitting of the MOs derived from the HOMO and LUMO of the parent hydrocarbon perimeter so that ΔHOMO > ΔLUMO or ΔLUMO > ΔHOMO, the Q bands become more intense $|\Delta HOMO - \Delta LUMO|^2$ increases.[16,46-49]

In the case of corroles, specifically, the contraction in the macrocycle results in a further loss of symmetry of the ligand: this, ultimately, results in a loss of degeneracy of the MOs derived from the the HOMO and the LUMO of the parent perimeter.[16] The *x*- and *y*-polarised components of the Q and B bands split because they no longer lie at the same wavelength.[16] In addition, since the *x*- and *y*-polarised components of the Q bands cannot cancel each other, the forbidden and allowed properties of the B and Q bands mix, which results in relatively intense Q bands in the spectra of corrole macrocycles, which is advantageous in the context of PDT.[16]

In the case of N-confused porphyrins, a structural isomer of porphyrin, one of the pyrrole rings is inverted to the outer perimeter of the macrocyclic structure. The structure of the N-confused porphyrin isomer is given in **Figure 1.6.6**.

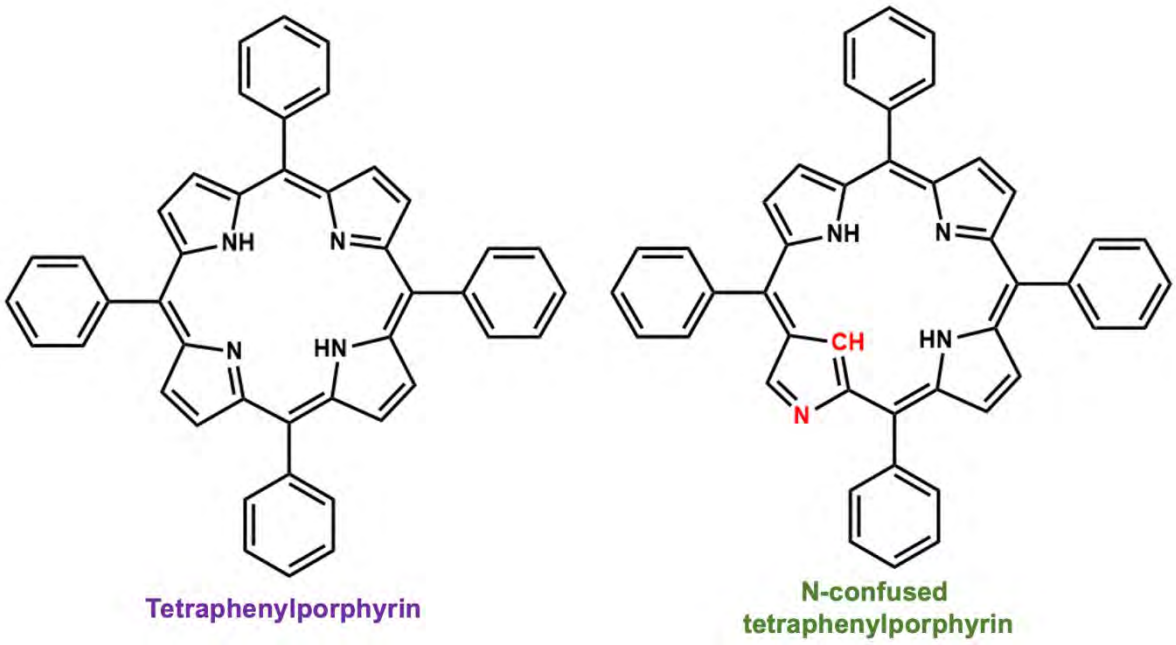

Figure 1.6.6. The structures of tetraphenylporphyrin and N-confused tetraphenylporphyrin (an isomer of the former).

Upon inverting the nitrogen to the exterior position within the macrocyclic structure, the **a** MO is stabilized by placing the electronegative nitrogen into a position with a large MO coefficient. The **-a** orbital is stabilized for the same reason. The **s** orbital is destabilized due to the

replacement of an electronegative nitrogen with a relatively electropositive carbon atom. The **-s** orbital is also destabilized for this reason. We, thus, expect to see an intensification of the Q bands within the porphyrinoid system and a red shift upon narrowing the HOMO-LUMO gap and allowing for transitions at higher wavelengths (lower energy), which is advantageous within the context of PDT. As previously mentioned, when $\Delta HOMO \approx \Delta LUMO$, the Q band still remains largely forbidden, and this phenomenon will be explored *via* molecular modelling within this investigation.

N-confused porphyrins were initially investigated in this thesis, but upon a failed synthesis of the molecule (see **Section 2.10.5**), the focus was reverted primarily to porphyrins and corroles.

1.7 Photophysicochemical properties of porphyrin/corrole systems

The resultant toxicity from the interactions of the photosensitiser with light needs to be carefully controlled and exploited.[50] This implies the need to understand the mechanism of these reactions and the efficiency of the processes that occur to generate the toxic response.

An efficient photosensitiser will have sufficient absorption of photons within the phototherapeutic window and produce high singlet oxygen quantum yields and long-lived triplet states.[51]

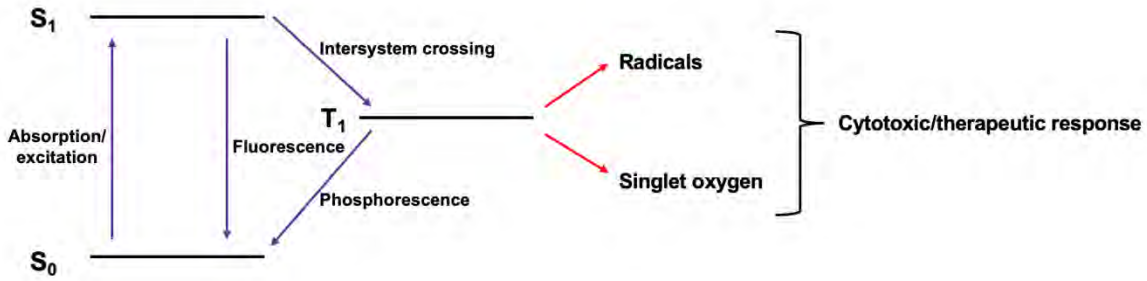

Figure 1.7.1. A simplified Jablonski diagram that shows the possible events after a photosensitising agent has been photoexcited. The vibrational energy levels of the photosensitiser have not been shown.[52]

The porphyrin photosensitiser initially is in its singlet ground state (i.e. S_0 in **Figure 1.7.1.**), and this state is characterised by a fully paired set of electrons with a total spin of 0 and a multiplicity of 1.[53] When the photosensitiser is exposed to an appropriate wavelength of incident radiation, one of these electrons is excited to a previously unoccupied orbital of higher energy upon the absorption of a photon. Since this state of excitation is unfavourable in energetic terms, the molecule will eventually return to the ground state; this deactivation of the excited state can happen *via* several mechanisms.[53]

Although the vibrational energies have not been shown in the above figure, if, upon excitation, the photosensitiser occupies a high vibrational level of a state, it will quickly relax to the lowest energetic level of that state in a process known as vibrational relaxation (VR) or internal conversion and the energy is dissipated in the form of heat.[53]

Molecular relaxation is the process that occurs when the dye returns to the S_0 state from an excited state. This usually results in the emission of a secondary photon *via* fluorescence. Relaxation to the S_0 state can also occur by heat dissipation.[53] Fluorescence occurs from the lowest vibrational level of an excited state, and the emitted photon will always have lower energies than those that excited the electrons; this is known as a Stokes shift.[54]

If the dye does not emit a photon *via* a fluorescence event, it may undergo a transition to occupy an isoenergetic level of the triplet state (denoted as T_1 in **Figure 1.7.1.**). The state is characterised by two unpaired electrons having the same spin.[53] The transition to the triplet state is non-radiative and is referred to as intersystem crossing. Although this is known as a spin-forbidden transition (since it violates the rule of no spin changes during a transition between electronic states), most photosensitising agents have high quantum efficiencies for this particular process, which is ideal for their envisaged applications.[53] Spin-orbit coupling, the interaction between the magnetic and spin-motion magnetic momenta of an electron, is prevalent in the context of heavy atoms and increases the probability of such an event.[53,55]

Once the triplet state is occupied, it can interact with surrounding molecular oxygen to produce the cytotoxic species (*via* one of two mechanisms) to achieve the therapeutic effect. Radiative relaxation back to S_0 can be achieved *via* phosphorescence.

1.7.1 Fluorescence Quantum Yields

The efficiency of the fluorescence process can be assessed *via* fluorescence quantum yields, which are the ratio between the number of photons emitted and the number of photons absorbed.

A comparative method was used to determine the fluorescence quantum yields using zinc tetraphenyl porphyrin (ZnTPP) in DMSO as a standard (Φ_F = 0.039) .[43]

$$\Phi_F = \Phi_F^{std} \times \frac{F \times A_{std} \times n^2}{F_{std} \times A \times n_{std}^2} \qquad \textbf{(1.1)}$$

In the above equation, F and F_{std} are the areas under the curves of the sample and standard, respectively; A_{std} and A are the absorbances of the standard and the sample at the excitation wavelength, respectively. Lastly, n refers to the refractive indices of the solvents used for the sample and the standard solutions.

For PDT to be effective, the rate of the fluorescence process needs to be limited to allow for an efficient population of the triplet state *via* maximal ISC. The heavy atom effect can be exploited in this case to increase the efficiency of the ISC and the resultant population of the triplet manifold.[56,57] This investigation will exploit this effect *via* co-ordination to high valent ions, such as Sn(IV) and P(V) to exploit this effect, particularly in the case of the former, as well as the introduction of heavy atoms such as bromine to the *meso*-aryl rings.

1.7.2 Singlet Oxygen Quantum Yields

PDT is reliant on the production of highly reactive and cytotoxic singlet oxygen ($^1O_2$) from the interaction with the triplet state of the photosensitising agent (reached by the absorption of light and an ISC event) and molecular oxygen ($^3O_2$).[58] In theory, the greater the singlet oxygen quantum yields, the more effective the therapeutic approach will be, in theory. This is a primary objective in the design of efficient photosensitising agents. The triplet state of the photosensitiser, shown as T_1 in **Figure 1.7.1**, needs to be reached *via* ISC to afford the production of singlet oxygen for the therapy to be effective.

This quantum yield is quantitatively determined by using a spectroscopic approach: a chemical trap is used to quench the singlet oxygen produced by the photosensitiser upon irradiation at predetermined intervals. The chemical traps utilised in organic solvents are typically either 9,10-dimethylanthracene (DMA) or 1,3-diphenylisobenzofuran (DPBF); this study used the former. The idea behind the spectroscopic approach is that the chemical trap (DMA) reacts with the singlet oxygen produced by the dye when exposed to laser radiation and reduces the ability of DMA to absorb within the visible region, due to the loss of aromaticity upon the incorporation of the highly reactive $^1O_2$ to form an endoperoxide (**Figure 1.7.2.1**).[59,60]

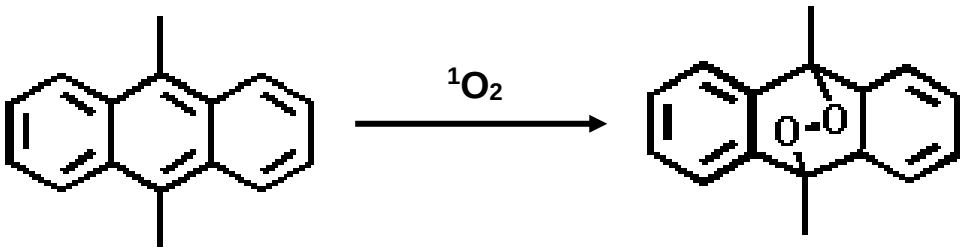

Figure 1.7.2.1. A scheme showing the formation of an endoperoxide from 9,10-dimethylanthracene *via* singlet oxygen produced by the photosensitising agents.[60]

The efficiency of the singlet oxygen production is, thus, also measured with a comparative method: ZnTPP is used as the reference compound (Φ_Δ = 0.55 in DMSO). The singlet oxygen quantum yield (Φ_Δ) value for each compound is then determined with the following equation:

$$\Phi_\Delta = \Phi_\Delta^{std} \times \frac{R \times I_{Abs}^{std}}{R^{std} \times I_{Abs}} \quad \textbf{(1.2)}$$

Φ_Δ^{std} is the singlet oxygen quantum yield of the standard, ZnTPP. *R* and R^{std} are the photodegradation rates of DMA by the sample and standard, respectively; these values are derived from the gradients of the linear plots between the photoirradiation time intervals and the change in maximum absorbance of DMA at 318 nm in the sample and the standard solutions. I_{Abs} and I_{Abs}^{Std} are the rates of light absorption by the sample and standard, respectively. The concentration of the chemical trap was kept constant in the sample and the standard solutions.

1.7.3 Triplet lifetimes

Since the existence of the triplet manifold is required for the generation of cytotoxic species in PDT *via* either of the two mechanisms, it is essential to have long-lived triplet states, as this is an indicator of the efficiency of the photosensitiser as a PDT therapeutic agent. The rationale behind this is that with longer-lived triplet states, there is an increased probability of interactions between this state and molecular oxygen within the biological environment, ultimately leading to higher singlet oxygen quantum yields and a more efficacious therapeutic approach.[61,62] Longer triplet lifetimes enhance the intermolecular processes, and it is a pivotal feature of photosensitiser agents in applications, such as PDT, that require electron or energy transfer.[63]

The triplet lifetimes of porphyrinoids vary based on molecular differences: heavy metals tend to reduce the triplet lifetimes of the organic macrocycles because the increased spin-orbit coupling promotes not only ISC, but also phosphorescence.[64]

This thesis will detail the method used to determine the triplet lifetimes and the effect this parameter has on the photodynamic activity of the dyes.

1.7.4 Molar Extinction Coefficients

The molar extinction coefficient of a sample is a value that is assigned to describe how efficiently a compound absorbs light at a particular wavelength. The Beer-Lambert Law can be used to quantify the coefficients by relating the attenuation of light to the properties of the material that the light interacts with.[65] Two essential proportionalities exist: firstly, the absorbance of the material at a particular wavelength is proportional to the concentration of the sample (A α C) and, secondly, the absorbance of the sample is proportional to the length of the light path through the cuvette (A α *l*). The Beer-Lambert Law arises from this:

$$A = log_{10}\left(\frac{I_0}{I}\right) = \varepsilon \times C \times l \qquad \textbf{(1.3)}$$

In this equation, A represents the absorbance of the sample at a particular wavelength. This is determined with a reference cell (I_o): where $I > I_0$, the sample has absorbed light. ε is the symbol that denotes the molar extinction coefficient of a compound; C is the concentration of the compound, and *l* is the pathlength of the light in cm (the width of the cuvette).[65]

Since the therapy is photo-dependent, the higher the molar extinction coefficient at the wavelength used to photoirradiate the photosensitiser dye, the more promising the compound is for PDT and PACT. This is because lower molecule concentrations of the molecule can achieve relatively efficient absorption at a particular wavelength, so lower concentrations are required to achieve the desired therapeutic effect. Ultimately, this would further reduce the development of negative side effects, decrease the scope for dye aggregation and improve bioavailability.[66]

1.8 Photodynamic Therapy (PDT)

Photodynamic therapy is a less invasive, clinically approved alternative therapeutic approach that exhibits a more selective cytotoxic effect on malignant/cancerous cells.[67,68] The process involves two fairly simple procedures detailed in **Figure 1.8.1**: administering a photosensitising agent and subsequent illumination of the tumour at a wavelength at which the photosensitiser primarily absorbs for activation and a resultant therapeutic effect.[67,68]

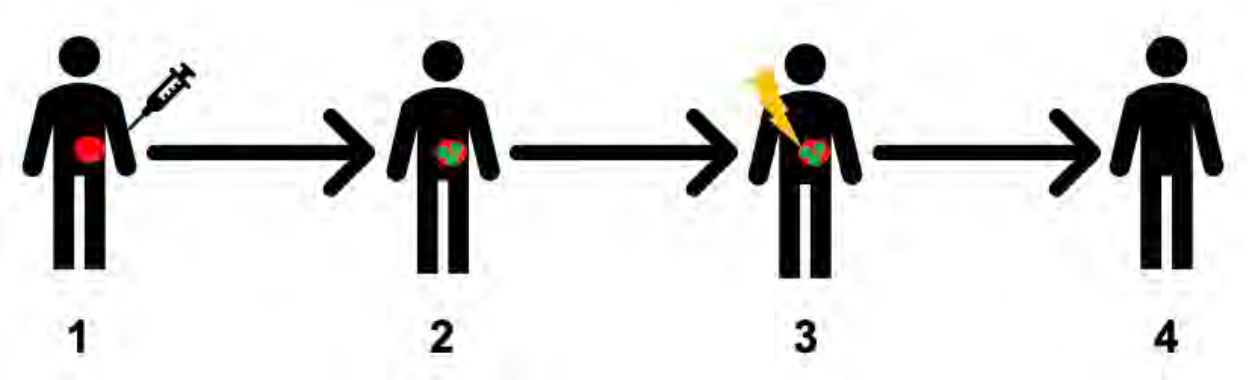

Figure 1.8.1. The scheme for photodynamic therapy. 1) The administration of the photosensitising drug, 2) the localisation of the drug (green) within cancerous tissues (red), 3) the activation of the drug with light, and 4) remission.[69]

This approach to cancer therapy is beneficial because it offers a high efficacy for small tumours that are superficially located and sometimes inoperable, minimal adverse side effects develop and leaves little to no scarring. In addition, subsequent treatments can be administered without the accumulation of toxicity within the body.[67,68] PDT has been acknowledged as a valuable treatment option for its effect on cancers and within the cosmetic realm as a primary therapy, as well as in combinatorial therapy.[67] Photosensitisers are activated by incident photons and, thus, present minimal normal tissue toxicity and there is a lack of resistance mechanisms developed by the body against these drugs, affording a promising alternative and selective therapeutic approach to cancer.[67]

This therapy requires the presence of molecular oxygen within the surrounding biological environment for the development of a photodynamic reaction.[70] This reaction has strict

requirements for an effective therapeutic effect. Firstly, the photosensitiser needs to localise within cancerous/diseased cells and tissues, only become toxic upon photoirradiation and have a suitable balance between hydrophobicity and hydrophilicity for effective drug transport, pharmacokinetics and bioavailability.[70] It should also clear rapidly from the body after achieving its therapeutic effect to avoid cumulative toxicity.[71]

In addition to the requirement of an effective photosensitiser with the above characteristics, it is also essential that they absorb light strongly within the phototherapeutic window: 650–850 nm.[72] This is the optimal wavelength range as it affords maximal penetration into human tissue and is the least harmful.[72] By using a wavelength of light within the phototherapeutic window, the scope for developing adverse side effects decreases because endogenous biomolecules within the human body do not absorb light within the region, as depicted in **Figure 1.4.2.**

Porphyrin derivatives have been chosen as the photosensitising agents of choice, as they absorb light within the phototherapeutic window and can be exploited for their photophysical properties in diagnoses or for their photochemical reactions in the context of therapy. In addition, these molecules have an affinity for neoplasms, tumour vessels, and proliferating endothelial tissues;[67,72] this affords increased selectivity, which is a primary reason for developing newer cancer therapies.

The mechanism of PDT includes the absorption of a photon by the photosensitiser resulting in the photoexcitation from the ground state to the excited singlet state.[68] Once the photosensitiser occupies this state, it can either relax and emit a photon *via* fluorescence or it can undergo a spin conversion (a quantum mechanics forbidden event) *via* intersystem crossing to populate the triplet manifold.[68] As previously mentioned, the therapy requires the presence of molecular oxygen: the excited triplet state of the photosensitiser can interact with diatomic oxygen to generate cytotoxic species. This happens in one of two ways: either there is a proton or electron transfer to facilitate the generation of radical species (Type I) or there

is a direct transfer of energy to the molecular oxygen, which results in the production of singlet oxygen (Type II).[68,73] The mechanisms are depicted in **Figure 1.8.2**.

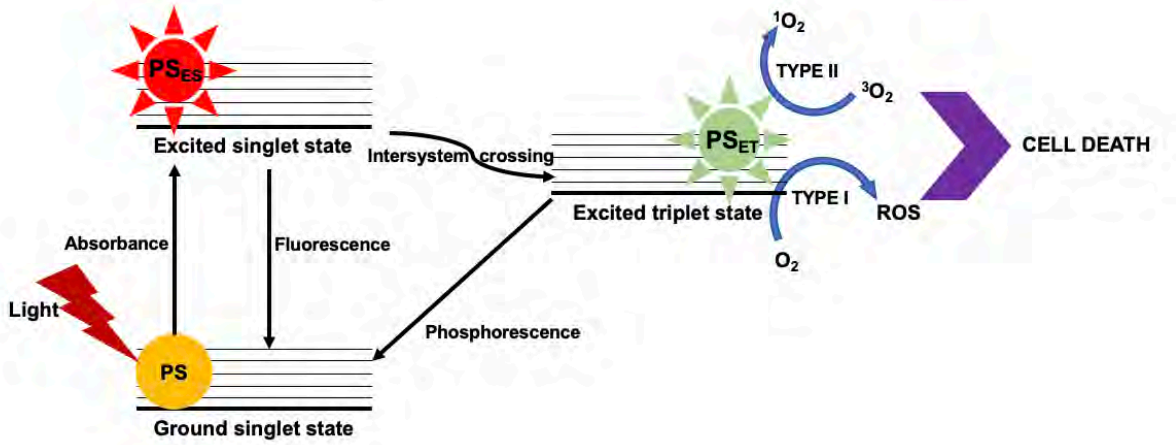

Figure 1.8.2. The mechanism of PDT. After absorption of a photon by the photosensitiser, the molecule converts to a singlet excited state. Either fluorescence or intersystem crossing occurs; the latter is required to generate cytotoxic species for the therapeutic effect.[74]

Singlet oxygen is the lowest electronic excited state of diatomic oxygen and is a reactive dienophile.[73] This is the therapeutic agent in PDT because it is responsible for the induction of apoptosis or necrosis, which leads to the subsequent generation of a cytotoxic response and the induction of immune signals.[73] Singlet oxygen is responsible for tumour ablation/destruction in photodynamic therapy. It causes oxidative stress on important biological macromolecules within the targeted tissue, such as proteins, nucleic acids, lipids and carbohydrates, within the targeted tissue.[72] This oxidative stress has at least three principal consequences within the biological system:

1. Direct cell death *via* apoptosis, necrosis, or autophagy,
2. Stimulation of an immune response, and
3. The occlusion of blood vessels within the vicinity of the tumour.[72]

All of these effects are responsible for the therapeutic response in attacking the diseased tissues.

In comparison to traditional therapies against cancer, PDT is often considered more cost-effective and efficacious. Traditional chemotherapies are infamous for their serious adverse effects and low therapeutic efficacy, due to a lack of selectivity.[75] They are also not sufficiently affordable.[75] Although the advantages of surgery to remove tumours may outweigh the

disadvantages in many cases, these procedures have long recovery periods and can cause damage to other organs in the body and blood loss, as well as the development of negative side effects related to the anaesthesia used.[76] Radiation is effective at slowing/stunting the growth of cancerous cells, but it is not selective in its approach; it damages the healthy cells in the vicinity, resulting in the development of side effects.[77] These side effects vary depending on the region of therapy, but they include fatigue, hair loss, memory and concentration issues, among many others.[77]

In addition to the previously mentioned advantages that PDT offers, the cell death that is induced by this therapy is also capable of stimulating an immune response: this happens *via* the triggering of maturation of dendritic cells upon the release of cell-death associated molecular patterns (CDAMPs) or damage-associated molecular patterns (DAMPs). The mature dendritic cells then migrate towards the lymph nodes and present antigens to $CD4^+$ or CD8 T^+ cells (T helper cells/cytotoxic T cells, respectively). Immunogenic cell death can be observed once the activated T cells have returned to the blood circulation and infiltration of the tumorous tissue takes place.[78]

It is apparent that there is a need for more effective cancer therapies. This thesis details the use of high- and low-symmetry porphyrins as photosensitising agents in photodynamic therapy.

1.9 Photodynamic Antimicrobial Chemotherapy (PACT)

PACT is a secondary application of the photosensitising dyes prepared in this investigation. This therapy makes use of the same mechanisms for generating cytotoxic species as PDT, only with different target cells for the cytotoxic singlet oxygen: bacteria (**Figure 1.9.1**). In recent years, PACT has been explored as a non-invasive therapeutic modality for bacterial, viral and fungal infections in recent years.[79] An enormous drive toward the development of effective strategies to combat infections caused by microbial pathogens has been underway over the last few decades and is still ongoing.[80] An antibiotic resistance crisis has emerged due to overuse and/or misuse of antibiotics, as well as the lack of design of newer and more effective drugs to combat microbial infections.[81] Currently, anti-microbial resistance (AMR) infections are responsible for 50000 deaths each year in Europe and the United States alone.[82,83] Projections for 2050 estimate that there will be 10 million deaths per year due to AMR infections if the crisis is not managed, which surpasses the estimated 8.2 million deaths related to cancer.[83] It is thus evident that there is a need to design novel therapies against microbial pathogens in order to continue saving millions of lives. PACT provides an opportunity to combat this ever-increasing concern.

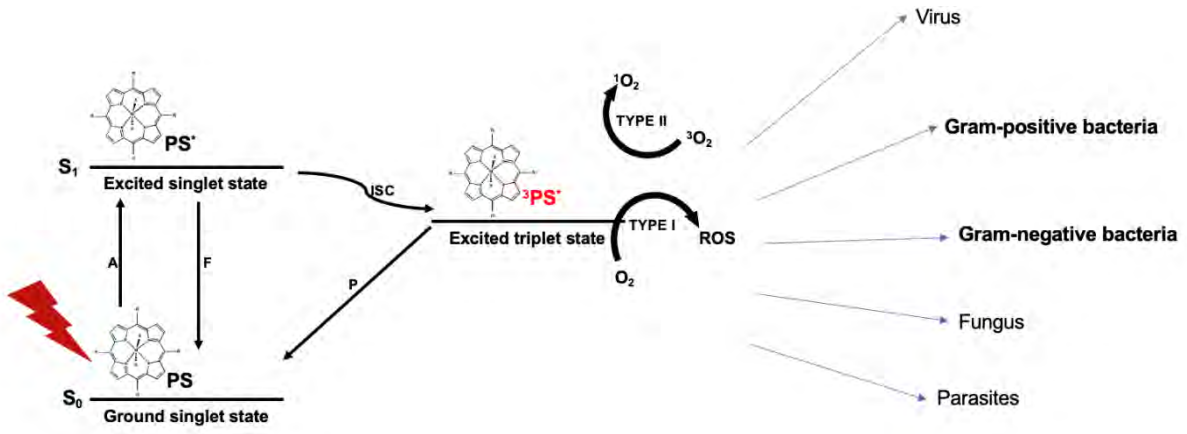

Figure 1.9.1. The mechanism of photodynamic antimicrobial therapy *via* the production of cytotoxic species by Type I and II photochemical reactions. This mechanism is responsible for the photoinactivation of bacteria: the photosensitiser (PS) absorbs light to reach the first singlet excited state (S_1) and then undergoes an intersystem crossing (ISC) event to the triplet manifold, which interacts with diatomic oxygen to produce reactive oxygen species (ROS). The rate of fluorescence (F) is minimised to achieve a high triplet state population.[84]

1.9.1. Target microorganisms

Bacteria fall into two major categories depending on the complex multi-layered structure that protects them from external hostile environments, which are outlined in **Figure 1.9.1.1**.[85] Gram-(+) bacteria do not have an outer membrane but have thick layers of peptidoglycan surrounding them that contain long anionic polymers known as teichoic acids.[85] Gram-(–) bacteria, on the other hand, have a thin peptidoglycan layer that is encapsulated in an outer membrane with lipopolysaccharides.

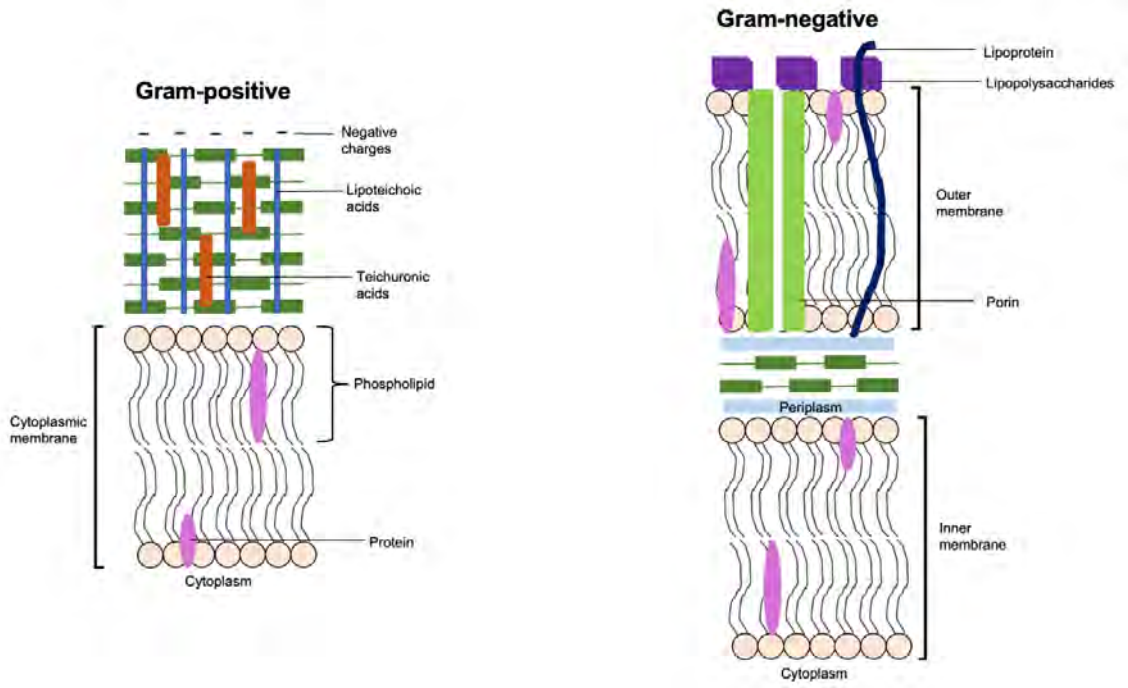

Figure 1.9.1.1 A graphic representation of the differences between the cell membrane structures of gram-(+) and –(–) bacteria.[84]

Although the structures of these organisms appear simple, their membranes are in reality relatively complex since they are adapted to protect them from adverse and hostile conditions.[85] This means that it takes extensive efforts to overcome the inherent protective mechanisms of the bacteria, and it will differ from one bacterium to the next. The bacteria involved in this investigation will be *Staphylococcus aureus* (*S. aureus*) to assess PACT activities of the dyes studied on a typical gram-(+) bacteria and *Escherichia coli* (*E. coli*) to assess the effect of PACT on a typical gram-(–) bacteria. Gram-(–) bacteria tend to be much

more resistant due to their distinctive structures and, thus, result in a higher percentage of morbidity and mortality globally.[86]

1.10 Optical limiting

As a tertiary application for this project, the optical limiting capabilities of the compounds were assessed. Optical limiting is both desirable and necessary for a range of applications that involve high-power light sources and sensitive photodetectors.[87] As higher-power lasers are constantly being developed, the demand for efficient optical limiters is required to limit the damage caused by the lasers; optical limiters should transmit low-intensity light (on-state) and block high-intensity light (off-state).[87] It is important for optical limiters to have a fast response time, high damage threshold, large turndown ratio, and high on-state transmission.[87] The most common designs for optical limiting agents employ the mechanism of two-photon absorption or absorption in nonlinear media, which is the limiting element.[87]

Optical limiting is an applied research area of non-linear optics, which, in general, is concerned with the interaction of intense coherent light with matter and how this interaction affects the optical properties of materials.[88] The use of organic and organometallic compounds for emerging photonic technologies is of interest to generate materials that can protect eyes and other optical sensors from laser beam pulses.[89] Optical limiting materials, due to their nonlinear absorbance of light, exhibit a decreasing transmittance as a function of intensity; they, thus, attenuate the intensity of high-intensity light from lasers and allow beams of light through that are safe for eyes and other optical sensors (**Figure 1.10.1**).[90]

When considering the design and mechanism of the protective devices needed within this context, it is important to consider why safety goggles/glasses are not appropriate. Safety glasses/goggles filter the light that passes through them and only allow certain wavelengths through that cannot cause damage to the retina, whereas optical limiting substances do not filter off any wavelength of light, but only allow a safe intensity of light to transmit through the substance and restrict high-intensity light.[90] An ideal optical limiter will allow the linear transmittance of light at low intensities, but once the limiting intensity (I_{lim}) threshold has been reached, the intensity will be attenuated *via* various different NLO mechanisms.

Ideally, there is a critical intensity threshold that these substances have at which the transmittance is rapidly reduced, thus reducing the intensity of light that is allowed to transmit through this material that is less than the intensity of light that would damage the eye or the sensor (**Figure 1.10.2**). In reality, however, the transmittance is more likely to decrease gradually with an increase in incident laser intensity rather than with a sharp decrease at this threshold.[91]

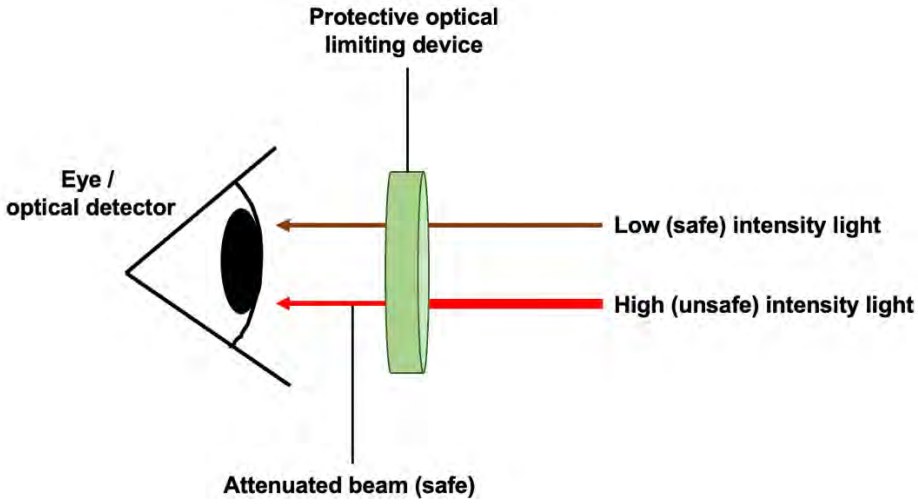

Figure 1.10.1. A representation of the function of an optical limiting device in the presence of normal/safe intensity light (linear transmittance) and high/unsafe intensity light (the attenuated beam of light transmission).[90]

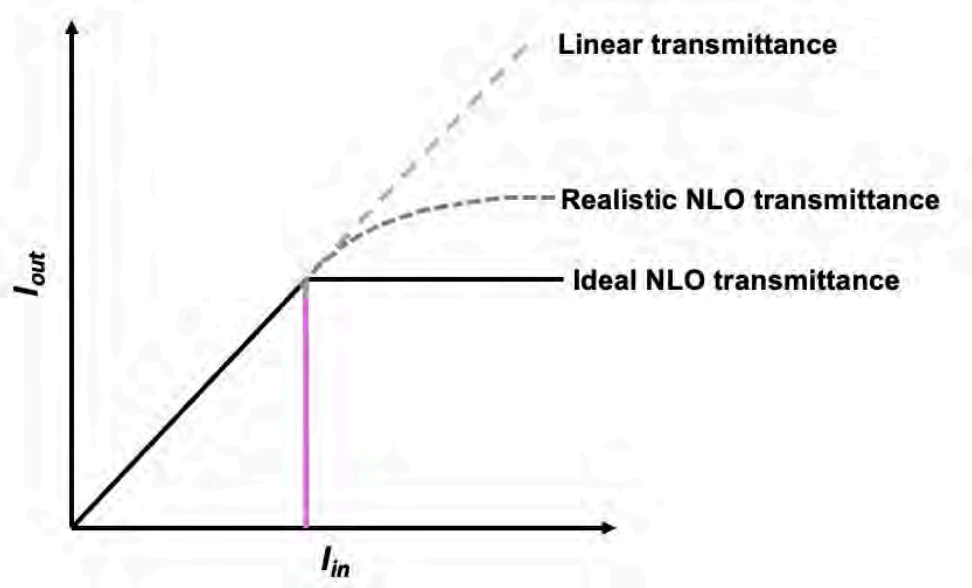

Figure 1.10.2. A graphical representation of the I_{in} and I_{out}, which are the incident and transmitted intensities of light, respectively. A comparison is drawn between normal substances that exhibit linear transmittance and optical limiting devices that deviate from linear transmittance at the limiting intensity (depicted by the purple line).[90,91]

This particular investigation will study the passive optical limiting potential of organic and organometallic macrocycles: it is passive optical limiting in that the inherent nonlinear transmittance of light is exploited, and it does not rely on any internal feedback mechanisms and mechanical structures to attenuate the incident radiation at high intensities.[90,92] This is advantageous, as it offers much faster response times, which is desirable in these applications.

Macrocycles, such as porphyrins and phthalocyanines, are promising materials for NLO applications. Their structural variability, strong intramolecular charge transfer (ICT), inherent nonlinear properties, and fast-response times make these π-conjugated organic chromophores promising within NLO applications.[93,94] Porphyrins and their analogues can be structurally modified *via* metalation, peripheral substitution, molecular symmetry, change of oxidation states, and conformational design to tailor them specifically for this application.[93] Asymmetric porphyrin analogues have increased polarizability, which is important for NLO applications. Metalated porphyrins, specifically, are excellent optical limiters due to their increased π-electron delocalisation and, hence, polarizability. In addition to metalation, the introduction of electron-withdrawing moieties at the porphyrin periphery is said to improve the NLO properties of the macrocycles. The introduction of electron-withdrawing groups (such as $-CH_3$, -Br, $-OCH_3$ or -Cl) at the acceptor part of the molecules, however, affords better tuning of the optical-electronic properties.[94] It has been found that the hyperpolarizability NLO parameter can be enhanced *via* structural modifications with electron-rich moieties, such as $-NO_2$ groups, and this can be rationalised due to the increased stabilisation of the charge transfer.[94] Overall, there are three main factors that play a significant role in determining the NLO response of a molecule:[95]

1) Extension of the π-conjugated system.
2) The strength of the electron-withdrawing or -donating groups present on the macrocycle.
3) The geometrical structure of the compound.

1.10.1 The Z scan technique

This particular investigation employs a single Gaussian laser beam in tight-focus geometry to study the nonlinear absorption (NLA); the transmittance of a nonlinear medium is measured in the absence of an aperture in front of a photodetector (D2, as depicted in **Figure 1.10.1.1**).[96,97] It measures the transmittance as a function of the sample position (z), which is measured with respect to the focal plane.[99] The sample is moved along the z direction of the focussed Gaussian beam, but the pulsed laser is held fixed.[90] Using a setup as depicted in **Figure 1.10.1.1**, information about the nonlinear refractive and nonlinear absorptive properties can be found. A dispersion-shaped curve is yielded from the plot of transmittance through the aperture in the far fields, and the nonlinear refractive index can be calculated from this data.[90]

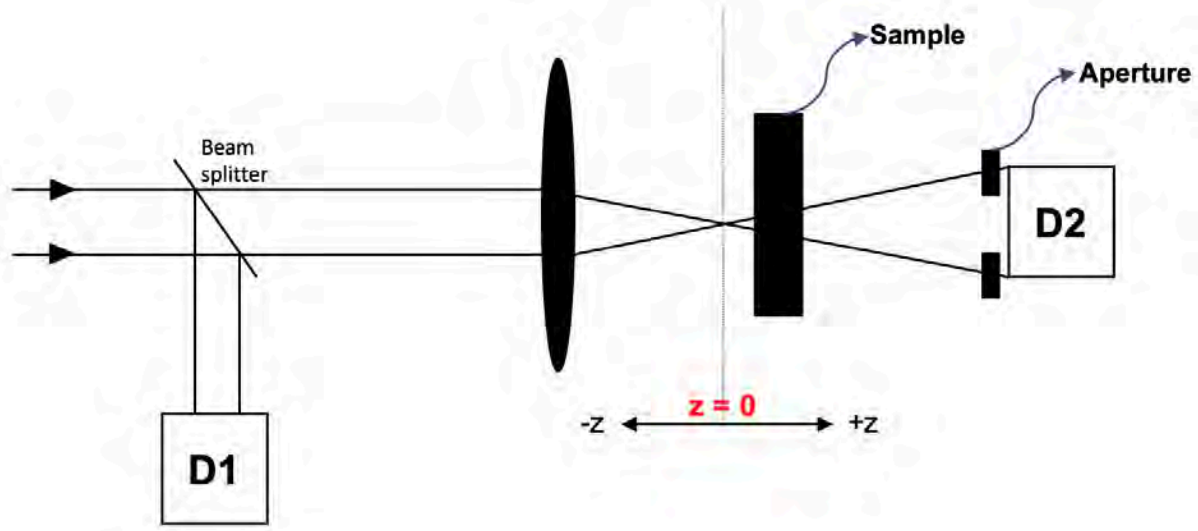

Figure 1.10.1.1. The Z-scan experimental apparatus, where the transmittance ratio D2/D1 is recorded as a function of the sample position z. The sample is translated from -z to +z through the focal point of a lens. D1 and D2 are detectors that are used to measure the intensity of the transmitted light.[97]

The results for the NLA are found by detecting the total energy transmitted from the sample, as well as a second detector that measures the intensity of the incident beam *via* a beam splitter. The experiment detailed within this thesis employed the second harmonic of an Nd:YAG laser at 532 nm as the source of the beam.[97]

The response of an optical limiter to high-intensity incident light is characterised by a reverse saturable absorption (RSA) response: at the negative and positive ends of the z position of the sample, the transmittance is high, and as the sample is moved towards the $z = 0$ position between $-z$ and z, the transmittance decreases.[97] RSA is characteristic of optical limiters, since they undergo a more intense excited state absorption (ESA) than the ground state absorption on the nanosecond timescale.[98]

There are two important mechanisms of optical limiting to consider (**Figure 1.10.1.2**): ESA, where there is an excitation of an electron from a lower excited state to a higher excited state, either in the singlet or triplet manifold of the photosensitiser and two-photon absorption (2-PA), which is a third-order nonlinear process that is characterised by a molecule simultaneously absorbing two photons when exposed to high-intensity incident light.[97]

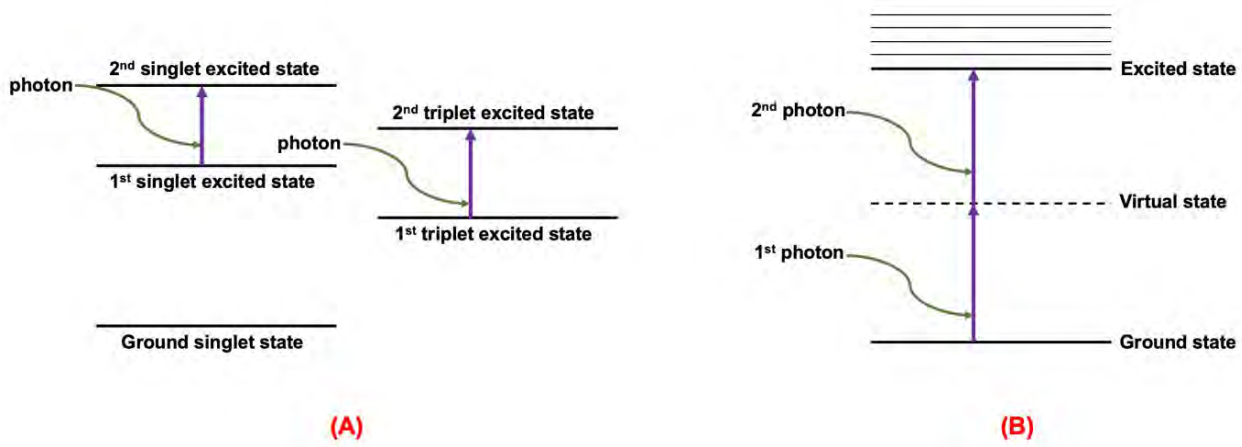

Figure 1.10.1.2. Jablonski diagrams for two mechanisms of nonlinearity: (a) Excited State Absorption, and (b) two-photon absorption.[97]

The work reported in this thesis focuses on the NLA properties of porphyrins (in their free-base and metalated forms, as well as symmetric and asymmetric molecules) and free-base corroles. Bromination of the thienyl moiety is also assessed using the open aperture z-scan technique.

The normalised energy transmittance is the measured quantity in an open-aperture z-scan experiment. It is given by **Equation 1.4** for a Gaussian pulse.[99]

$$T(z) = \frac{1}{\sqrt{\pi} q_0(z)} \int_{-\infty}^{\infty} \ln\left[1 + q_0(z) e^{\tau^2}\right] d\tau \quad \textbf{(1.4)}$$

In the above equation, q_0 is a parameter that characterises the extent of the nonlinear response and this parameter, upon employing a circular Gaussian beam, can be further described by:[100]

$$q_0(z) = \frac{2\beta P_0 L_{eff}}{\pi w^2(z)} \quad \textbf{(1.5)}$$

In the above equation, β is the nonlinear absorption coefficient of the material, P_0 is the peak power of the pulses, and, lastly, L_{eff} is the effective propagation/path length in a sample of length L and can be further described by **Equation 1.6**:[100]

$$L_{eff} = \frac{1 - e^{-aL}}{a} \quad \textbf{(1.6)}$$

Here, a is the linear absorption coefficient (cm^{-1}) of the molecule, which is to be measured at the intended wavelength employed in the application of the dyes.

In **Equation 1.7**, w_0, is the beam waist at the sample plane/focus (z = 0), which is defined as the distance from the beam centre to the point where the intensity decreases to $1/e^2$ of its axis value. This parameter is dependent on the sample position (z_s), and the following equation describes this dependence:[100]

$$w(z_s) = w_0 \times \sqrt{1 + \left(\frac{z_s - z_0}{z_R}\right)^2} \quad \textbf{(1.7)}$$

In **Equation 1.7**, z_0 is the location of the beam focus, while the parameter z_R is the Raleigh length, which is given by the following relationship.[100] In the following equation λ is the wavelength of the laser beam.

$$z_R = \frac{\pi w_0^2}{\lambda} \quad \textbf{(1.8)}$$

Equations 1.4-1.6 are valid for calculating third-order nonlinearities: the absorption coefficient of the photosensitiser has a linear dependence on the intensity of the incident beam. Essentially, these calculations can be used at moderate intensities where higher-order effects, such as excited state absorption, are absent and there is a two-photon absorption.[100] **Equations 1.4-1.9** can be used to determine the nonlinear absorption coefficient β from the experimental transmittance measurements. The parameter q_0 is determined by fitting **Equation 1.4** to the experimental data and, subsequently, β is calculated with **Equations 1.4-1.7**.[100]

Tsigaridas *et al.*[100] have produced an analytical formula that simplifies the calculation required to retrieve q_0 and it is given by **Equation 1.9:**

$$q_0 = \begin{cases} a_0 + a_1 T(z) + a_2 T^2(z) + a_3 T^3(z) \; for \; T(z) \leq 0.75 \\ c_0 + c_1 [T(z)]^{c_2} \; for \; T(z) \geq 0.75 \end{cases} \quad \textbf{(1.9)}$$

Where the coefficients a_0, a_1, a_2, a_3, c_0, c_1 and c_2 are given as 15.66, -7.45, 30.76, -8.97, -2.301, 2.156 and -1.563 for Gaussian pulses, respectively.[90,100] Upon substitution of **Equation 1.7** into **Equation 1.5** $q_0(z)$ can be determined via **Equation 1.10**:[90]

$$q_0(z) = \frac{Q_0}{1+(\frac{z}{z_0})^2} \quad \textbf{(1.10)}$$

where Q_0 is given by:[100]

$$Q_0 = \frac{2\beta P_0 L_{eff}}{\pi w_0^2} = \frac{2\beta P_0 L_{eff}}{\lambda z_R} \quad \textbf{(1.11)}$$

It can be noted from **Equation 1.10** that $q_0(z_s)$ that the curve has a maximum value (Q_0) at the beam waist, where $z_s = z_0$. The peak value and full width at half maximum (FWHM) can be used to yield the values of Q_0 and z_R, respectively, from the $q_0(z_s)$ curve. The nonlinear absorption coefficient is an important parameter for assessing the suitability of a particular material for optical limiting applications and can be calculated with **Equation 1.12**:

$$\beta = \frac{\lambda z_R Q_0}{2P_0 L_{eff}} \qquad \textbf{(1.12)}$$

The imaginary component of the third-order nonlinear susceptibility (Im[$\chi^{(3)}$]) measures the speed of the response of a particular optical limiting material to the perturbation induced by an incident laser pulse.[97] The imaginary component describes the nonlinear absorption, while the real component is descriptive of the nonlinear refraction of the material.[90] Im[$\chi^{(3)}$] has a directly proportional relationship with the effective nonlinear absorption coefficient, $\beta_{eff,}$ and this can be calculated with **Equation 1.13:**

$$Im[\chi^{(3)}] = \frac{\eta^2 \varepsilon_0 C \lambda \beta_{eff}}{2\pi} \qquad \textbf{(1.13)}$$

Where η, c, ε_0 and λ are the refractive index of the solvent, speed of light, the permittivity of free space, and the wavelength of the laser, respectively.[97] The optimal range reported for Im[$\chi^{(3)}$] is 10^{-9} – 10^{-15} esu for optical limiting applications.[97]

Upon interaction of the permanent dipole of the photosensitiser with the intense incident laser radiation, a resultant bias in the average orientation of the molecules occurs, leading to induced hyperpolarizability. It is, thus, useful to compare the suitability of different photosensitisers for this particular application by considering the second-order hyperpolarisability (γ), which describes the behaviour at the molecular level and the nonlinear absorption per mole of the OL compound.[90] The relationship between the imaginary

component of the third-order nonlinear susceptibility (Im[$\chi^{(3)}$]) and the hyperpolarizability (γ) is described by **Equation 1.14:**

$$\gamma = \frac{Im[\chi^{(3)}]}{f^4 C_{mol} N_A} \quad \textbf{(1.14)}$$

Where f is the Lorentz local field enhancement factor and f = (η^2 + 2)/3 (and η is the refractive index of the sample), C_{mol} is the molar concentration of the photosensitiser, and N_A is Avogadro's constant. The hyperpolarisability has an ideal range of 10^{-29} – 10^{-34} esu in the context of the OL materials.[97]

The limiting threshold intensity (I_{lim}) is defined as the input fluence at which the nonlinear transmittance is reduced to 50% of the linear transmittance value.[101] It can be rationalised that a good optical limiting material will have a lower I_{lim} value; this implies that the limiting would occur at a lower intensity. There are guidelines in place to determine the suitable exposure limits to different lasers that are provided by the International Commission on Non-Ionising Radiation Protection.[102] The following equation can then be used to determine the exposure limit as a function of time:

$$Exposure\ Limit = 2.7 C_A t^{0.75} J.cm^{-2} \quad \textbf{(1.15)}$$

Where C_A is a correction factor, which can be assumed to be 1 when dealing with a wavelength in the 400–700 nm range, and t is the exposure time. In the investigation, the exposure limit was determined to be 0.95 J/cm^2 assuming a 0.25 s exposure time (selected, as it is the average human blink reflex time upon exposure to a sudden light flux to the eye).[103]

The porphyrins and corroles applied in this application were selected as a means to assess the different responses of porphyrins, themselves, and their analogues to light and their suitability as optical limiting materials. In addition to this, the loss of symmetry is explored as

a means to improve the optical limiting potential of the materials. Lastly, the introduction of heavy atoms into the molecular structures is explored to determine whether this further enhances the optical limiting parameters of the organic molecules.

1.10.2. Thin films

Although it is important to investigate the optical limiting properties of dyes in solution, the dyes must be embedded in the solid state in the context of applications.[104] For applicability in real-world situations, these dyes would need to be incorporated into safety visors or windshields. In this work, the most promising optical limiting compound was embedded in a polymer thin film for NLO studies, and the polymer that was chosen was poly(bisphenol carbonate A), the structure of which is provided in **Figure 1.10.2.1**. Most protective eyewear and sports goggles are made from polycarbonate lenses. They are also used in the manufacturing of safety visors.[90,105]

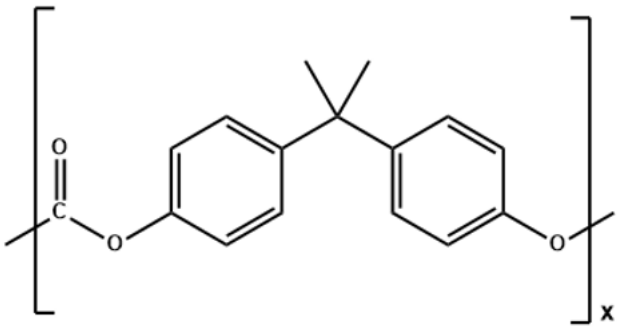

Figure 1.10.2.1. The structure of one unit of poly(bisphenol carbonate A).

1.11 Summary of aims

The aim of this investigation was to study the utility of A_4 and ABAB type tetraarylporphyrin macrocycles with 4-quinolinyl, thien-2-yl and 4-bromo-thien-2-yl meso-aryl groups and their Sn(IV) and In(III) complexes (**Figure 1.11.1**) and their A_3 and ABA type triarylcorroles derivatives (**Figure 1.11.2**) in the context of photodynamic therapy against cancer and bacteria (PDT and PACT). In a similar manner to what has been reported previously by Mack and coworkers,[18] the thien-2-yl rings were introduced to red shift the lowest energy Q band towards the therapeutic window, while quaternisation of the nitrogen and sulfur atoms of the 4-quinolinyl and the thien-2-yl rings to introduce a cationic nature was explored to improve the bioavailability of the drugs and uptake into the target cell walls for improved efficacy. Heavy Sn(IV) and In(III) central metal ions were introduced to enhance the singlet oxygen quantum yield and limit aggregation effects through axial ligation.[18] The bromine atoms of the 4-bromo-thien-2-yl meso-aryl rings were also introduced to enhance the singlet oxygen quantum yields of the dyes. As a tertiary application, the optical limiting properties of these molecules were also assessed. The lower symmetry of corroles due to the formation of a direct pyrrole-pyrrole bond makes these dyes potential strong candidates for this application by introducing a large groundstate dipole moment.

The initial aims involved the synthesis of high- and low-symmetry porphyrins and corroles that would be metalated with Sn(IV) and coordinated to P(V). Bromination of the moiety at the *meso*-position was also explored to improve the therapeutic efficacy of the photosensitisers. A later aim included the metalation of the porphyrins with In(III).

The aims of this thesis are summarised below:

1. The synthesis, purification and characterisation of the series of porphyrin and corrole photosensitisers with 4-quinolinyl, thien-2-yl and 4-bromo-thien-2-yl *meso*-aryl groups.

2. Quantifying the photophysicochemical properties of the photosensitisers, with a special focus on the ability to generate singlet oxygen after structural modifications.

3. Application of the molecules during *in vitro* analyses of the photodynamic chemotherapeutic activities (**Figure 1.11.1**): PDT (**Sn(IV)T4**, **In(III)T4**, **Sn(IV)T_{Br}4**, **Sn(IV)T2Q2**, **In(III)T2Q2**, and **Sn(IV)T2Q2^{+}**) and PACT (**Sn(IV)T4**, **In(III)T4**, **Sn(IV)T_{Br}4**, **Sn(IV)T2Q2**, **In(III)T2Q2**, **T_{Br}2Q2**, and **Sn(IV)T2Q2^{+}**).

4. A study of the nonlinear optical behaviour of the photosensitiser dyes (**Figure 1.11.1** and **Figure 1.11.2**) : (**T4**, **Sn(IV)T4**, **In(III)T4**, **T_{Br}4**, **Sn(IV)T_{Br}4**, **T2Q2**, **Sn(IV)T2Q2**, **In(III)T2Q2**, **T_{Br}2Q2**, **Sn(IV)T2Q2^{+}**, **T3**, and **T_{Br}3**).

5. Molecular modelling of the free base, Sn(IV), In(III) and P(V) porphyrins and corroles to better understand the structure-property relationship of these compounds.

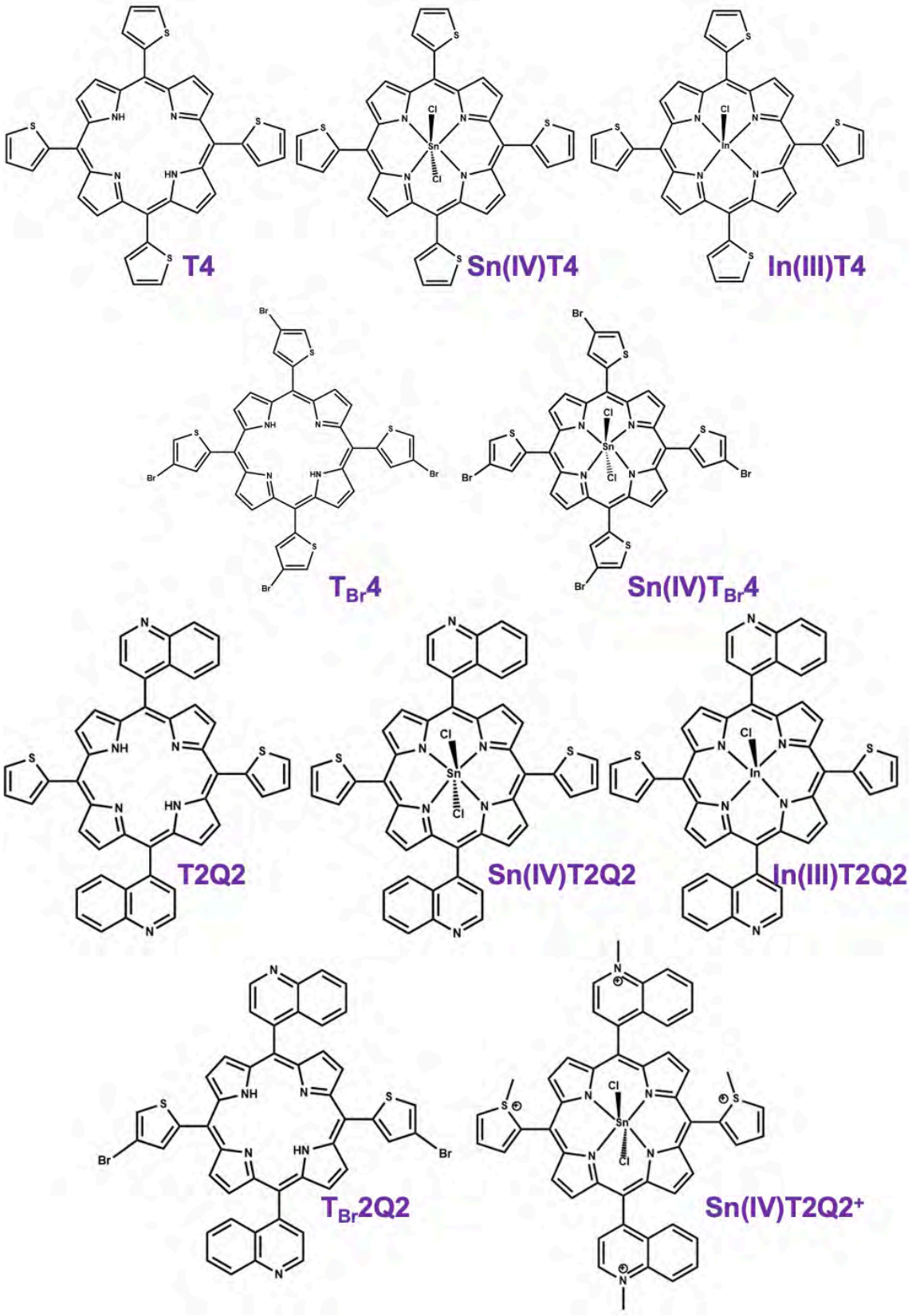

Figure 1.11.1. The porphyrin molecules that were synthesised in this thesis. PACT molecules (**Chapter 4**): **Sn(IV)T4**, **In(III)T4**, **Sn(IV)T_{Br}4**, **Sn(IV)T2Q2**, **In(III)T2Q2**, **T_{Br}2Q2**, and **Sn(IV)T2Q2^{+}**. PDT molecules (**Chapter 5**): **Sn(IV)T4**, **In(III)T4**, **Sn(IV)T_{Br}4**, **Sn(IV)T2Q2**, **In(III)T2Q2**, and **Sn(IV)T2Q2^{+}**. OL molecules (**Chapter 6**): **T4**, **Sn(IV)T4**, **In(III)T4**, **T_{Br}4**, **Sn(IV)T_{Br}4**, **T2Q2**, **Sn(IV)T2Q2**, **In(III)T2Q2**, **T_{Br}2Q2**, **Sn(IV)T2Q2^{+}**.

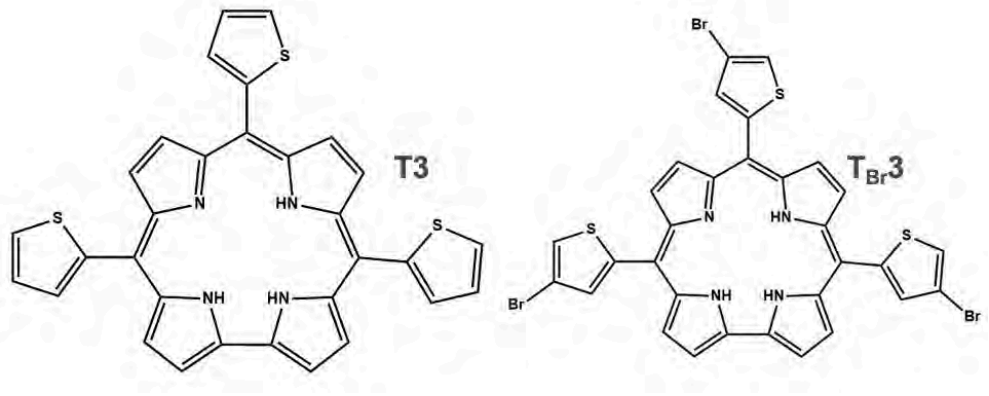

Figure 1.11.2. The corrole molecules that were synthesised in this thesis and studied for their optical limiting properties in **Chapter 6**.

Papers published: S. Dingiswayo, K. Burgess, B. Babu, J. Mack & T. Nyokong, “Photodynamic Antitumour and Antimicrobial Activities of Free-Base Tetra(4-methylthiolphenyl)chlorins and its Tin(IV) Complex”, *ChemPlusChem* **2022**, 87, e202200115.

CHAPTER TWO

EXPERIMENTAL

2.1 Materials

All reagents were obtained from commercial sources. Reagent grade 2-thiophenecarboxaldehyde, 4-bromo-2-thiophenecarboxaldehyde, pyridine and 5,10,15,20-tetraphenyl porphyrin (H_2TPP) were obtained from Sigma Aldrich. All solvents were of analytical grade and were purified and dried by routine procedures before use, where applicable. Similarly, *p*-chloranil (tetrachloro-1,4-benzoquinone), DDQ (2,3-dichloro-5,6-dicyano-1,4-benzoquinone) and deuterated chloroform ($CDCl_3$) for use in proton NMR was purchased from Sigma Aldrich. Hydrochloric acid (HCl, 32%), chloroform, dichloromethane, N,N-dimethylformamide, cyclohexane, petroleum ether, and methanol were obtained from local suppliers. Tin (II) chloride dihydrate ($SnCl_2{\cdot}2H_2O$) was purchased from Fluka Chemicals. Ultra-pure Type II water was obtained from an Elga Purelab Chorus 2 (RO/DI) system.

MCF-7 cell cultures were obtained from Cellonex®. Dulbecco's Modified Eagle Medium (DMEM) and Dulbecco's Phosphate Buffered Saline (DPBS) were purchased from Lonza®. 10% (v/v) heat-inactivated fetal bovine serum (FBS), as well as antibiotic mix (100 units/mL-penicillin-100µg/mL-streptomycin-amphotericin B), were obtained from Biowest®.

2.2 Equipment

- **Ground state absorption spectra** were obtained on an Evolution™ 350 UV-Vis spectrophotometer from Thermo Fischer Scientific™ and a Shimadzu UV-2550 spectrophotometer.
- **^{1}H NMR spectra** were recorded with a Bruker Fourier 80 MHz Benchtop or Bruker Avance II™ 600 MHz instrument. The spectra were obtained at ambient temperatures using deuterated solvents ($CDCl_3$ and DMSO-d_6).
- **Mass spectral data** were collected from a Bruker AutoFLEX III Smartbeam TOF/TOF mass spectrometer with either positive or negative ion mode used and a nitrogen laser as the ionizing source; α-cyano-4-hydroxycinnamic acid was the MALDI matrix employed.

- **Fluorescence yields** were obtained with a Varian Cary-Eclipse spectrofluorimeter. The fluorescence quantum yield (Φ_F) values were calculated *via* the comparative method by using emission and absorption spectra of ZnTPP (Φ_F = 0.039 in DMSO) as the standard.[106,107]
- **Singlet oxygen quantum yields** were quantified using a comparative method with DMSO as the solvent of choice. The Spectra-Physics® Primoscan OPO series (GWU Lasertechnik Vertriebsges, mbH) was pumped with a Spectra-Physics Quanta-Ray Lab Nd:YAG laser. The irradiation wavelength was the crossover between the absorbance of the standard (ZnTPP) and the sample.
- **Triplet state lifetimes** were recorded in DMSO at 470 nm using an Edinburgh Instruments LP980 spectrometer and an Ekspla NT-342B laser equipped with an OPO to provide an excitation wavelength (2.0 mJ excitation energy, 7 nm pulse duration and a 20 Hz repetition rate). The solutions were degassed with nitrogen for 30 min prior to the measurement, and the absorbances of the samples were maintained at approximately 1.5 for the Soret band. Exponential curve fitting of the decay curve was achieved using OriginPro 98 software, which was used to determine the triplet lifetimes of the photosensitisers.
- The Council for Scientific and Industrial Research's (CSIR) Centre for High Performance Computing (CHPC) in Cape Town was used as a platform to perform the theoretical calculations with the Gaussian software package.[108] **Geometry optimisations** were carried out at the B3LYP level of theory with SDD basis sets, while **TD-DFT calculations** used the Coulomb-attenuated B3LYP, i.e., CAM-B3LYP, functional with SDD basis sets. The simulated spectra were generated using Chemcraft software with a fixed bandwidth at 2000 cm^{-1}, and the molecular orbitals were visualised using Avogadro.
- **The MCF-7 cells** were cultured in Porvair 25 cm^2 flasks and during their log phase, the cells were passaged to 75 cm^2 Porvair flasks and incubated in a humidified atmosphere from Heal Force (37°C, 5% CO_2). A Zeiss AxioVert.A1 inverted microscope was used to examine the cells.

- **A Modulight® Medical Laser (ML) 7710-680 system**, fitted with a Thorlabs LED that emits light in the wavelength used within the particular application, was used for PDT and PACT.
- **An autoclave from China Medical Device (RAU-530D)** was used to sterilize the Luria broth, agar and all the equipment necessary for bacterial culturing.
- **The optical density (OD) of the bacterial culture** was measured using a Ledetect 96 microplate reader from Labxim products
- **The bacterial suspensions were mixed** with a Lasec® analogue vortex mixer.
- **The bacterial pellet** was obtained from the suspension by using a Hemle Z233M-2 centrifuge from Lasec®.
- **The colony-forming units (CFU/mL)** were determined by Scan® 500 series automatic colony counter from Interscience.
- **The open-aperture Z scan experiments** were performed with a frequency-doubled Nd:YAG laser (Quanta-Ray, 1.5 J with 7 ns HWHM pulse duration) as the excitation source. The laser was operated in a near-Gaussian transverse mode with a low pulse repetition rate of 10 Hz and an energy range of 0.1 μJ – 0.1 mJ at 532 nm. This low repetition rate of the laser prevents cumulative thermal nonlinearities. The beam was spatially filtered to remove the higher order modes and tightly focused with a 15 cm focal length lens. The z-scan data of the organic solutions were collected using a 2 mm quartz cuvette; UV visible absorption spectra were recorded before and after measurement to ensure that no aggregation effects were occurring, which could lead to significant nonlinear scattering (NLS) and, subsequently, interfere with the results being obtained within the nonlinear optics chapter of this thesis.

2.3 Synthesis of Porphyrins

2.3.1 5,10,15,20-tetrakis(thien-2-yl)porphyrin (T4)

A green synthetic approach was used to obtain T4 (**Scheme 2.3.1**).[109] 2-thiophenecarboxaldehyde (10 mmol, 1,12 g, 0.93 mL), and freshly distilled pyrrole (10 mmol, 0.67 g, 0.69 g, 0.69 mL) were dissolved in 500 mL of methanol. Subsequently, 250 mL of Millipore water (2:1) was added, followed by 20 mL of hydrochloric acid (32%). The reaction was stirred at room temperature for 2 h. The reaction mixture was then filtered over filter paper, and the precipitate was dissolved in 100 mL of DMF. This DMF solution was refluxed for a further 1.5 hours, and, subsequently, the solution was transferred to a beaker and stirred at room temperature overnight. Chromatographic separation (silica, $CHCl_3$) afforded 64 mg of **T4.** Yield: 1%. UV-vis ($CHCl_3$) λ / nm (log ε) 425 (5.57), 520 (4.23), 552 (3.82), 598 (3.81), 661 (3.47). ^{1}H NMR ($CDCl_3$, 80 MHz) δ_H / ppm 9.03 (s, 8H), 7.87 (d, 8H, J = 4.98 Hz), 7.49 (s, 4H), -2.67 (s, 2H, inner protons). MS (MALDI-TOF): *m/z* for $[M+H]^+$ 639.24 amu; calculated 638.86 amu.

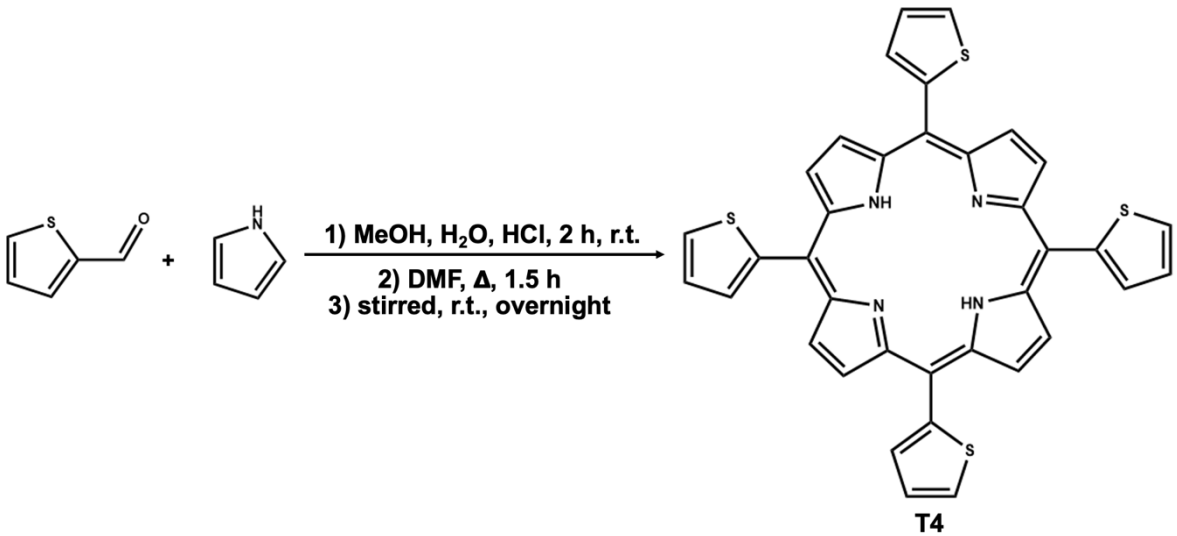

Scheme 2.3.1. The synthesis of **T4** using a green synthetic approach.[109]

2.3.2 5,10,15,20-tetrakis(thien-2-yl)porphyrinato tin(IV)-dichloride (Sn(IV)T4)

The free-base porphyrin (**T4**) (0.05 mmol, 30 mg) was dissolved in 15 mL of pyridine and excess tin (II) chloride dihydrate (at least 2 eq) was added.[110] The reaction mixture was refluxed for 3-4 h until a colour change in the solution was observed (**Scheme 2.3.2**). Millipore water was added to the round bottom flask to induce precipitation, followed by chloroform to extract the product from the solution. The organic layer was washed thoroughly with water and filtered to reduce the excess tin salt. Chromatographic separation (silica, $CHCl_3$) afforded 28 mg of **Sn(IV)T4.** Yield: 68%. UV-vis ($CHCl_3$) λ / nm (log ε) 437 (5.27), 567 (3.96), 613 (3.70). ^{1}H NMR ($CDCl_3$, 80 MHz) δ_H / ppm 9.40 (s, 8H, pyrrole protons), 8.08–7.93 (m, 8H, thienyl ring protons in positions 3&5), 7.62–7.51 (m, 4H, thienyl ring protons in position 4). MS (MALDI-TOF): *m/z* for $[M–Cl]^-$ 791.56 amu; calculated 826.46 amu.

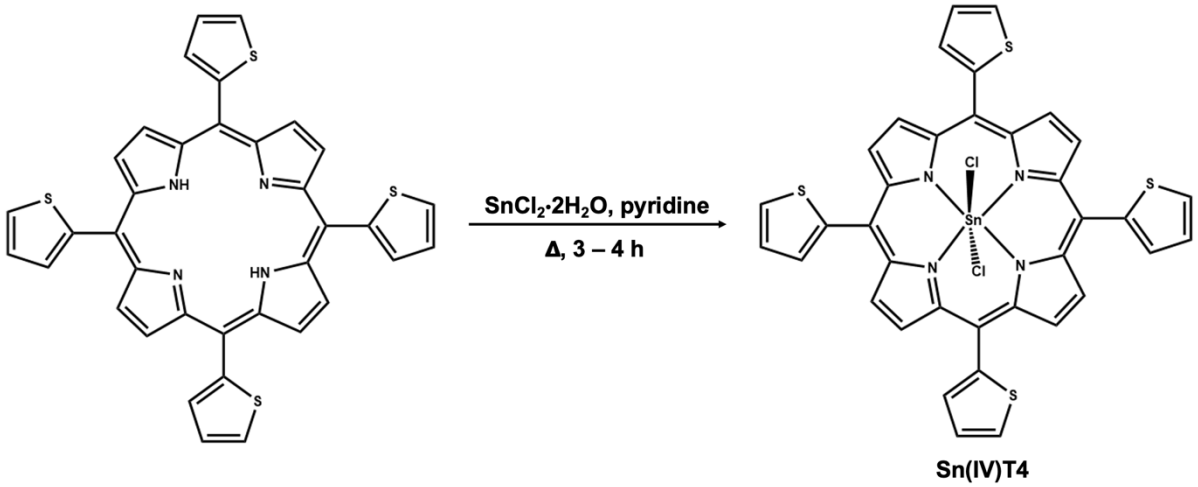

Scheme 2.3.2. The synthesis of **Sn(IV)T4** from **T4**.[110]

2.3.3 5,10,15,20-tetrakis(thien-2-yl)porphyrinato Indium(III)-chloride (In(III)T4)

The free-base porphyrin (15 μmol, 10 mg) was dissolved in acetic acid and sodium acetate (400 mg, 7 mL) was added. Thereafter, Indium (III) chloride tetrahydrate (17 μmol, 5 mg) was added. The reaction mixture was refluxed for 72 h (**Scheme 2.3.3**). The reaction mixture was washed with water after dissolving in $CHCl_3$, and lastly, washed with water that contained

$NaHCO_3$. Chromatographic separation (SiO_2, $CHCl_3$ (4): MeOH (1)) yielded 8 mg of **In(III)T4.** Yield: 80%. UV-vis ($CHCl_3$) λ / nm (log ε) 435 (4.80), 565 (3.48), 610 (3.06). ^{1}H NMR ($CDCl_3$, 80 MHz) δ_H / ppm 9.27 (s, 8H), 8.04–7.83 (m, 8H), 7.62–7.45 (m, 4H). MS (MALDI-TOF): *m/z* for $[M–Cl]^-$ 751.12 amu; calculated 787.12 amu.[111]

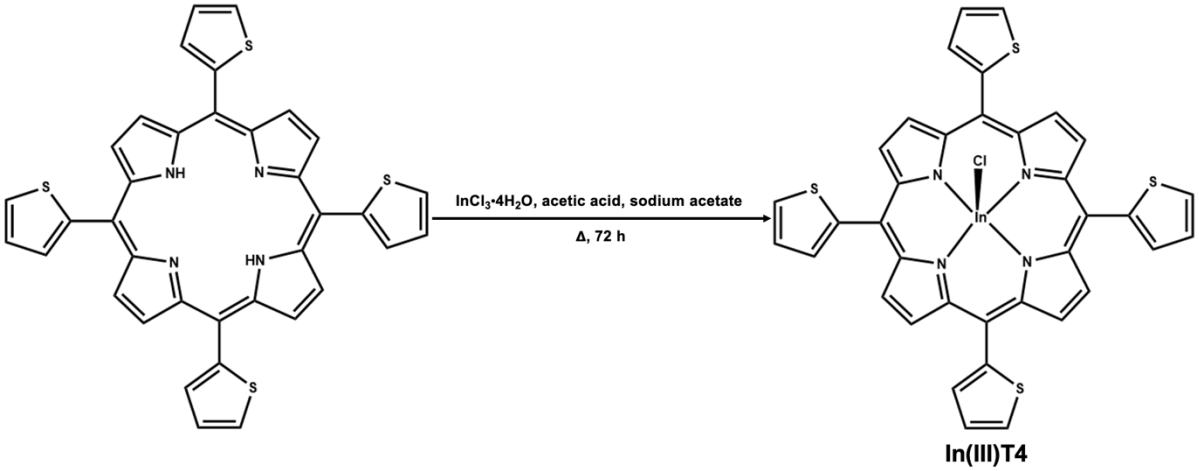

Scheme 2.3.3. The synthesis of **In(III)T4** from **T4**.[111]

2.3.4 5,10,15,20-tetrakis(4-bromo-thien-2-yl)porphyrin ($T_{Br}4$)

The Adler method of porphyrin synthesis was used to obtain $T_{Br}4$ (**Scheme 2.3.4**).[112] 4-bromo-2-thiophenecarboxaldehyde (50 mmol, 9.55 g) and freshly distilled pyrrole (50 mmol, 3,46 mL) were added to propionic acid (100 mL) and the mixture was refluxed for 3-4 h. The reaction was cooled on ice and methanol was added to induce precipitation. The reaction was filtered and washed with water. The solid was left overnight to dry to completion. Chromatographic separation (silica, $CHCl_3$) afforded 188 mg of **T_{Br}4.** Yield: 39%. UV-vis ($CHCl_3$) λ / nm (log ε) 425 (5.32), 521 (4.11), 554 (3.79), 599 (3.69), 663 (3.77). ^{1}H NMR ($CDCl_3$, 80 MHz) δ_H / ppm 9.08 (s, 4H), 8.65 (s, 4H), 8.23 (d, *J* = 6.70 Hz, 4H), 7.83 (d, *J* = 4.51 Hz, 4H), –0,66 (s, 2H, inner NH). MS (MALDI-TOF): *m/z* for $[M+H]^+$ 955.07 amu; calculated 954.45 amu.

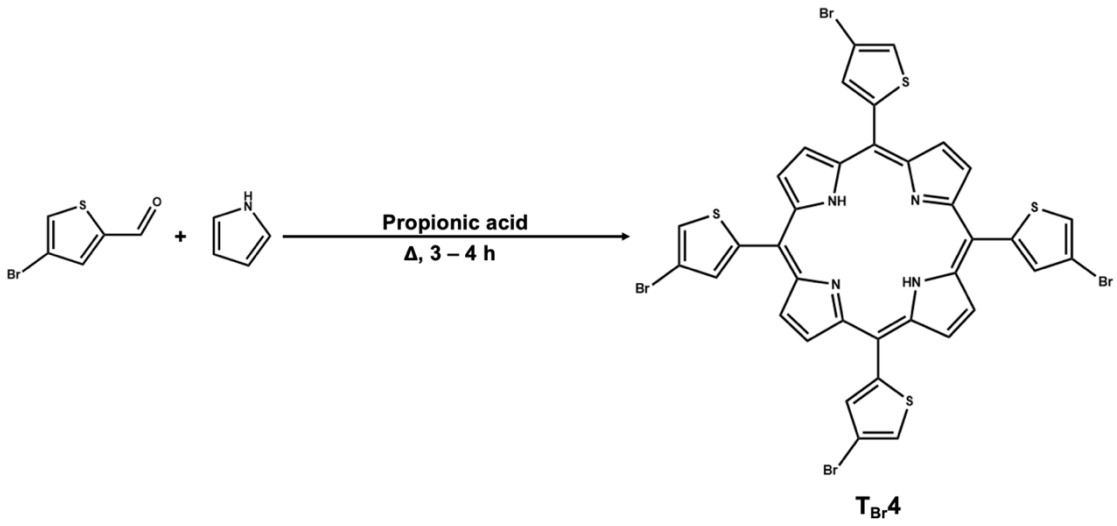

Scheme 2.3.4. The synthesis of $\mathbf{T_{Br}4}$ using the Adler method.[112]

2.3.5 5,10,15,20-tetrakis(4-bromo-thien-2-yl)porphyrinato tin(IV)-dichloride (Sn(IV)$T_{Br}4$)

The free-base porphyrin ($\mathbf{T_{Br}4}$) (0.05 mmol, 30 mg) was dissolved in 15 mL of pyridine and excess tin (II) chloride dihydrate (at least 2 equivalents) was added. The reaction mixture was refluxed for 3-4 h until a colour change in the solution was observed (**Scheme 2.3.5**). Millipore water was added to the round bottom flask to induce precipitation, and chloroform was used to extract the product out of the solution. The organic layer was washed thoroughly with water and filtered to reduce the excess tin salt. Chromatographic separation (silica, $CHCl_3$) afforded 27 mg of $\mathbf{Sn(IV)T_{Br}4}$ Yield: 47%. UV-vis ($CHCl_3$) λ / nm (log ε) 434 (4.68), 566 (3.38), 609 (3.07), 638 (3.19). ^{1}H NMR ($CDCl_3$, 80 MHz) δ_H / ppm 9.43 (s, 8H, thienyl ring), 7.93 (d, 8H, pyrrole protons). MS (MALDI-TOF): *m/z* for $[M–Cl]^-$ 1107.76 amu; calculated 1142.05 amu.[110]

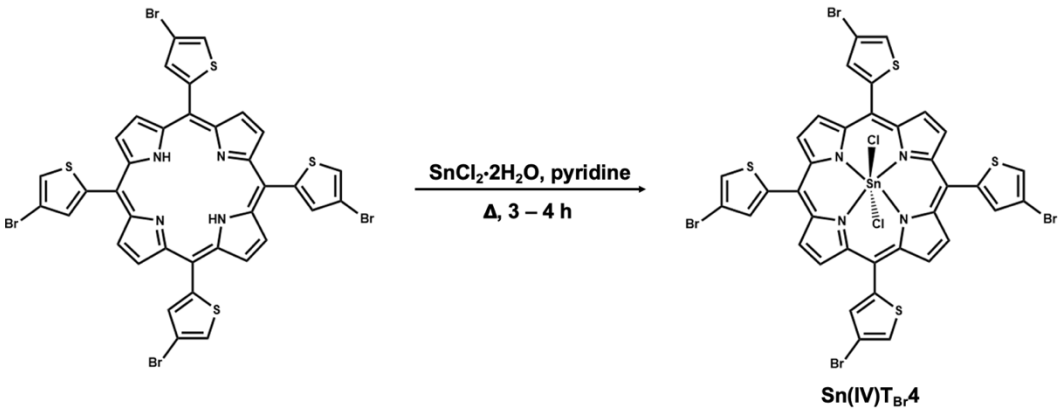

Scheme 2.3.5. The synthesis of $\mathbf{Sn(IV)T_{Br}4}$ from $\mathbf{T_{Br}4}$.[110]

2.3.6. 2,2'-(thien-2-ylmethylene)bis[1H-pyrrole]

To an aqueous mixture of HCl (a 100 mL 0.5% HCl solution), 1 eq of 2-thiophenecarboxaldehyde (15 mmol, 1.4 mL) was added and stirred at room temperature while purging the solution with N_2 (g). After 10 min, 3 eq of freshly distilled pyrrole (45 mmol, 3.12 mL) was added to the reaction, and the solution turned cloudy. The reaction was monitored *via* TLC: the reaction mixture was spotted on a silica TLC plate, and chloroform was used as a mobile phase. After TLC, the silica plate was dipped into an iodine chamber and upon the blue staining of the primary band, the synthesis of the DPM can be confirmed and the reaction was stopped after 5 min upon extracting the dipyrromethene with chloroform. The short reaction time was used to limit oligomerisation past the target DPM product. The DPM was not purified *via* column chromatography due to its highly reactive nature and was advanced immediately to the subsequent synthesis to yield the low-symmetry molecules.[333] **Scheme 2.3.6** details the synthesis of the DPM.

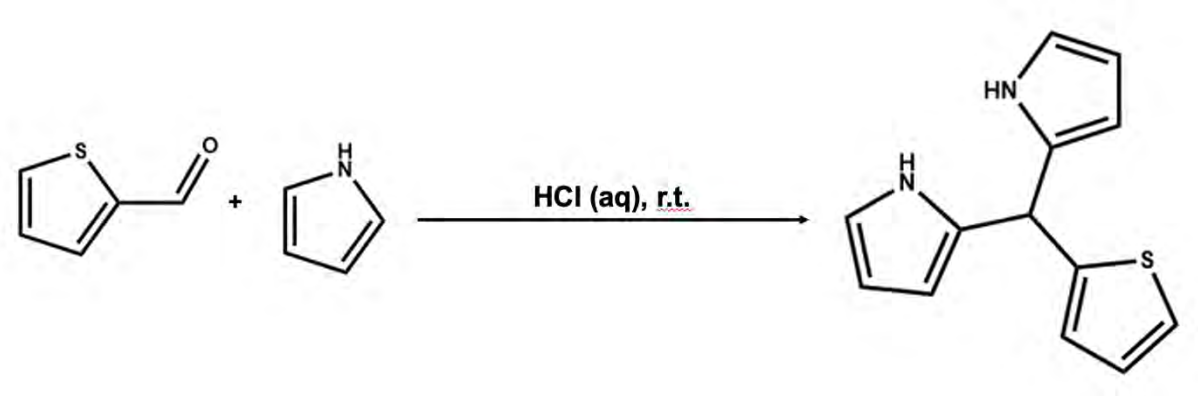

Scheme 2.3.6. The synthesis of the thien-2-yl-substituted dipyrromethane precursor for low-symmetry porphyrins.[33]

2.3.7 5,15-bis(thien-2-yl)-10,20-bis(4-quinolinyl)porphyrin (T2Q2)

Yielded from the low symmetry corrole synthesis of **T2Q** (**Scheme 2.3.7**):[14] 2,2′-(thien-2-ylmethylene)bis[1*H*-pyrrole] (dipyrromethane) (8.25 mmol) and 4-quinoline carboxaldehyde (4.24 mmol, 0.67 g) were added to a 250 mL solution of CH_2Cl_2 and trifluoracetic acid (65 μmol, 7.41 mg, 5 μL). The reaction was stirred at room temperature for 5 h. Afterwards, a solution of DDQ (4.5 mmol, 1.02 g) in 10 mL of toluene was added to the reaction mixture,

and the reaction was stirred for 5 min before allowing the solvent to dry. Chromatographic separation with a SiO_2 column and 1:3 hexane/$CHCl_3$ eluent and subsequently with an Al_2O_3 column and 7:3 hexane/ethyl acetate as eluent yielded 30 mg of **T2Q2**. Yield: 1%. UV-vis ($CHCl_3$) λ / nm (log ε) 423 (4.55), 518 (3.48), 554 (3.07), 593 (3.18), 648 (2.84). ^{1}H NMR ($CDCl_3$, 80 MHz) δ_H / ppm 9.37 (d, 2H, *J* = 4.47 Hz), 9.02 (d, 4H, *J* = 5.35 Hz), 8.53 ppm (d, 4H, *J* = 5.06 Hz, pyrrole protons), 8.27 (d, 2H, *J* = 4.64 Hz), 7.62–9.94 (m, 12H), 7.18 (s, 2H), –2.49 (s, 2H, inner protons). MS (MALDI-TOF): *m/z* for $[M+H]^+$ 729.41 amu; calculated 728.90 amu.

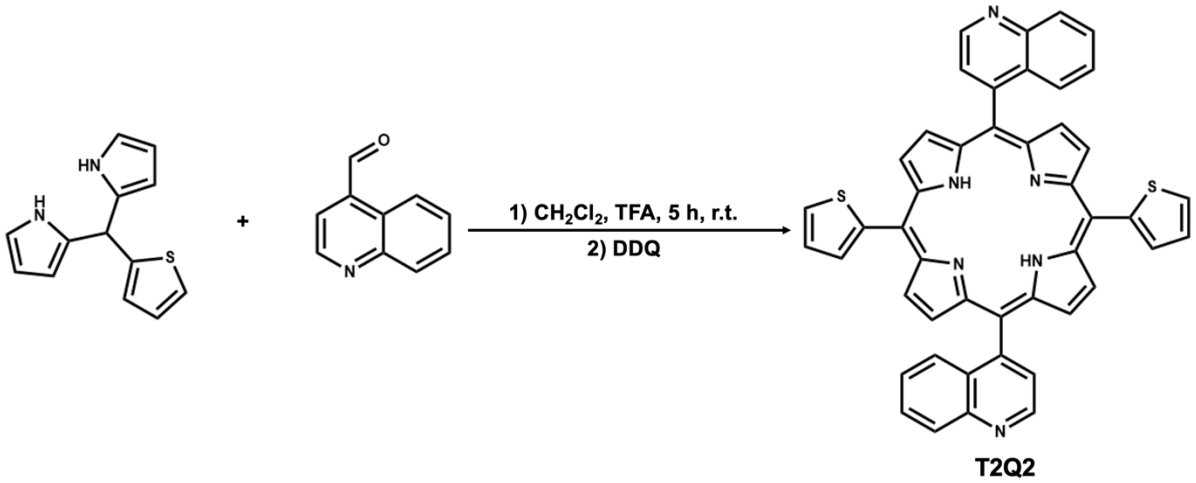

Scheme 2.3.7. The synthesis of the low-symmetry porphyrin **T2Q2** from a secondary aromatic aldehyde and the thien-2-yl-substituted dipyrromethane.[14]

2.3.8 5,15-bis(thien-2-yl)-10,20-bis(4-quinolinyl)porphyrinato tin(IV)-dichloride (Sn(IV)T2Q2)

The free-base porphyrin (**T2Q2**) (0.01 mmol, 10 mg) was dissolved in 10 mL of pyridine and excess tin (II) chloride dihydrate (at least 2 equivalents) was added. The reaction mixture was refluxed for 3-4 h until a colour change in the solution was observed (**Scheme 2.3.8**). Millipore water was added to the round bottom flask to induce precipitation, and chloroform was used to extract the product. The organic layer was washed thoroughly with water and filtered to reduce the excess tin salt. Chromatographic separation (silica, $CHCl_3$) afforded 8 mg of **Sn(IV)T2Q2** Yield: 64%. UV-vis ($CHCl_3$) λ / nm (log ε) 432 (4.53), 561 (3.24), 602 (2.78). ^{1}H

NMR ($CDCl_3$, 80 MHz) δ_H / ppm 9.31 (s, 4H), 8.91 (s, 1H), 8.40 (s, 1H), 7.71–8.04 (m, 18H), 7.05 (s, 2H). MS (MALDI-TOF): *m/z* for $[M-Cl]^-$ 882.05 amu; calculated 916.50 amu.

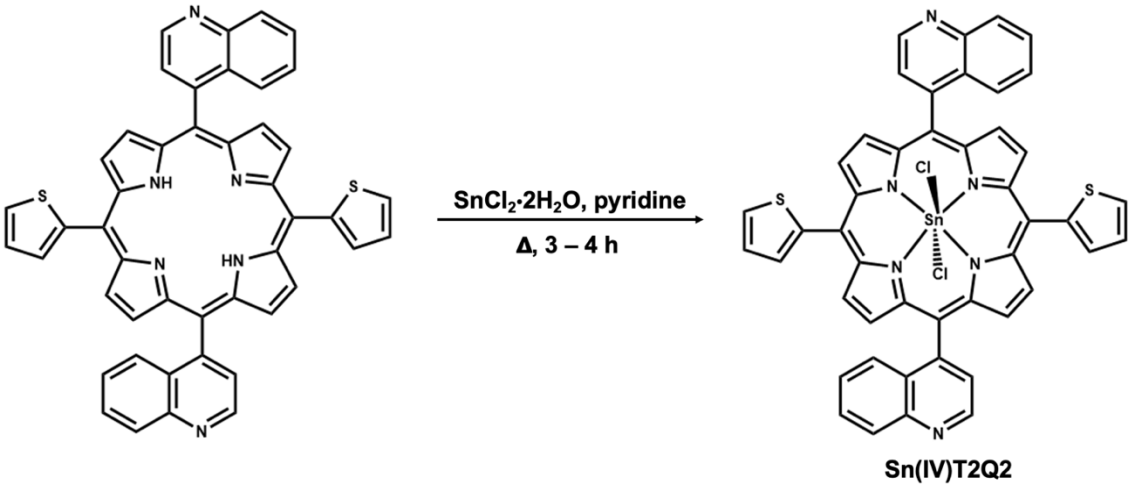

Scheme 2.3.8. The synthesis of **Sn(IV)T2Q2** from **T2Q2**.[110]

2.3.8 Quaternised 5,15-bis(thien-2-yl)-10,20-bis(4-quinolinyl)porphyrinato tin(IV)-dichloride (Sn(IV)T2Q2$^+$)

An excess of iodomethane (70 μmol, 4 μL) was added to a solution of **Sn(IV)T2Q2** (10 mg, 14 μmol) in anhydrous DMF (10 mL) under a nitrogen atmosphere and stirred at room temperature for 24 h. The solution was evaporated under vacuum, and the desired product was washed with diethyl ether (50 mL) and recrystallised in acetone to yield 8mg. Yield 75%. UV-vis ($CHCl_3$) λ / nm (log ε) 435 (3.32), 565 (2.54), 614 (2.35). ^{1}H NMR ($CDCl_3$, 80 MHz) δ_H / ppm no visible aromatic protons, 3.53 (s, methyl peak). MS (MALDI-TOF): *m/z* for $[M-Cl]^{4+}$ 235.90 amu; calculated 976.64 amu. **Scheme 2.3.9** details the synthesis of the quaternised molecule.

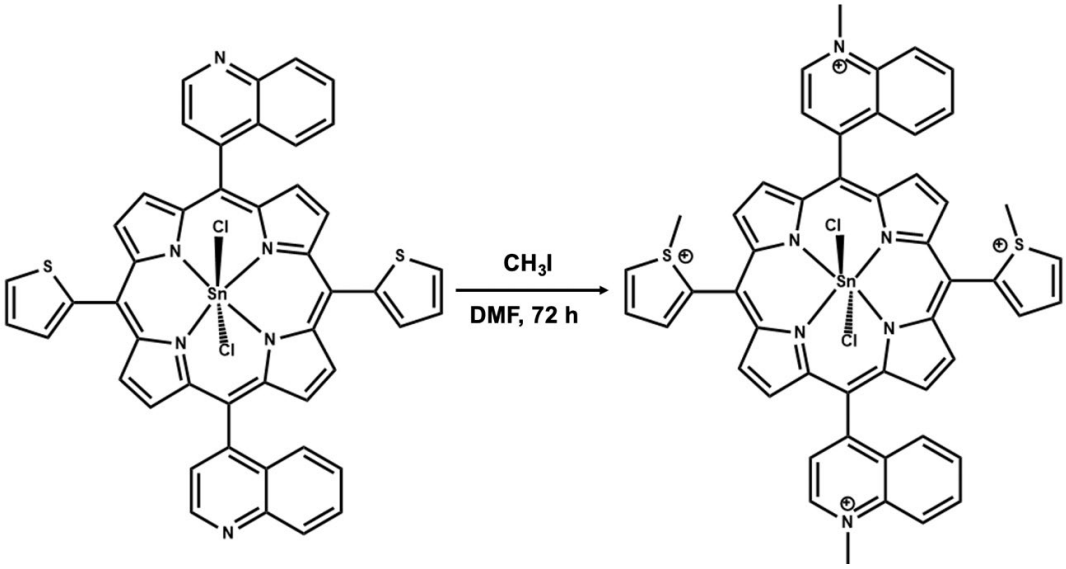

Scheme 2.3.9. The synthesis of **Sn(IV)T2Q2**$^{+}$ from **Sn(IV)T2Q**.[113]

2.3.10 5,15-bis(thien-2-yl)-10,20-bis(4-quinolinyl)porphyrinato indium(III)-chloride (In(III)T2Q2)

The free-base porphyrin (7 μmol, 5 mg) was dissolved in 7 mL of acetic acid and sodium acetate (400 mg) was added. Thereafter, Indium (III) chloride tetrahydrate (17.5 μmol, 5 mg) was added. The reaction mixture was refluxed for 72 h (**Scheme 2.3.10**). The reaction mixture was washed with water after dissolving in $CHCl_3$, and lastly washed with water that contained $NaHCO_3$. Chromatographic separation with a SiO_2 column and 4:1 $CHCl_3$/MeOH as eluent yielded 5 mg of **In(III)T2Q2.** Yield: 87%. UV-vis ($CHCl_3$) λ / nm (log ε) 433 (3.96), 564 (2.74), 606 (2.30). ^{1}H NMR ($CDCl_3$, 80 MHz) δ_H / ppm 9.25 (d, 2H, *J* = 3.43 Hz), 9.04 (d, 4H, *J* = 4.51 Hz), 8.59–8.86 (m, 4H), 8.27 ppm (s, 2H), 7.71–7.89 (m, 6H), 7.49–7.63 (m, 6H), 7.03 (s, 2 H). MS (MALDI-TOF): *m/z* for $[M–Cl]^-$ 841.76 amu and for $[M]^-$ 877.68; calculated 877.12 amu.

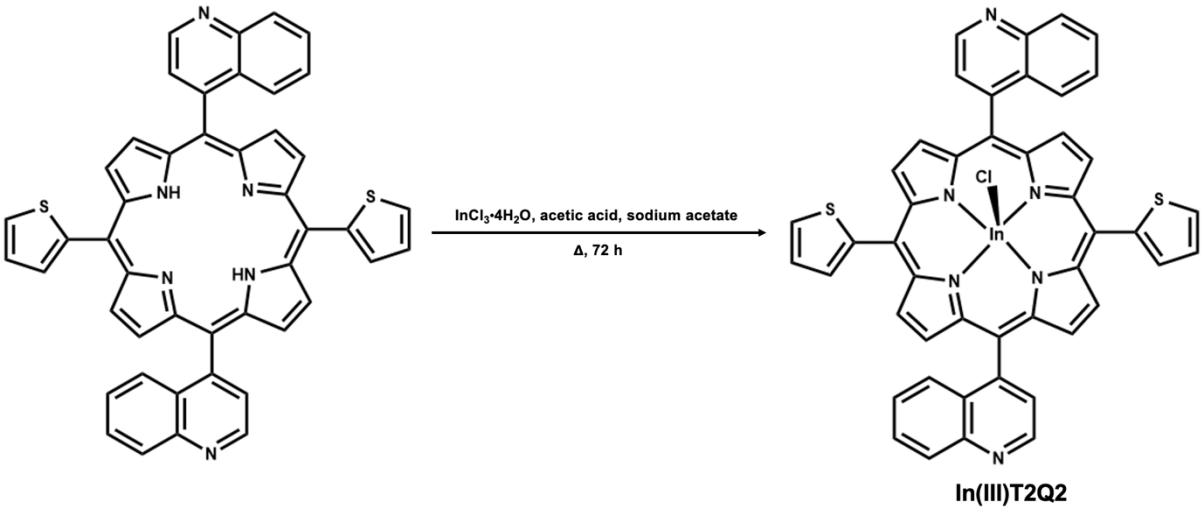

Scheme 2.3.10. The synthesis of **In(III)T2Q2** from **T2Q2**.[111]

2.3.11. 2,2'-(4-bromo-thien-2-ylmethylene)bis[1H-pyrrole]

To an aqueous mixture of HCl (a 100 mL 0.5% HCl solution), 1 eq of 4-bromo-2-thiophenecarboxaldehyde (15 mmol, 2.87 g) was added and stirred at room temperature while purging the solution with N_2 (g). After 10 min, 3 eq of freshly distilled pyrrole (45 mmol, 3.12 mL) was added to the reaction, and the solution turned cloudy. The reaction was monitored *via* TLC: the reaction mixture was spotted on a silica TLC plate, and chloroform was used as a mobile phase. After TLC, the silica plate was dipped into an iodine chamber and upon the blue staining of the primary band, the synthesis of the DPM can be confirmed and the reaction was stopped after 20 min upon extracting the dipyrromethene with chloroform. The short reaction time was used to limit oligomerisation past the target DPM product. The DPM was not purified *via* column chromatography due to its highly reactive nature and was advanced immediately to the subsequent synthesis to yield the low-symmetry molecules. **Scheme 2.3.11** details the synthesis of the DPM.

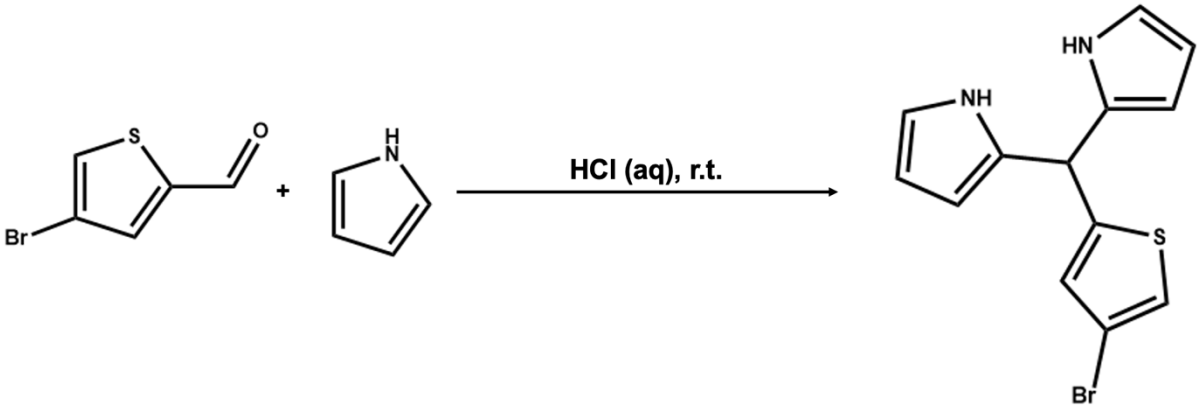

Scheme 2.3.11. The synthesis of the 4-bromo-thien-2-yl-substituted dipyrromethane precursor for low-symmetry porphyrins.[33]

2.3.12 5,15-bis(4-bromo-thien-2-yl)-10,20-bis(4-quinolinyl)porphyrin (T_{Br}2Q2)

Yielded from the low symmetry corrole synthesis of **T_{Br}2Q** (**Scheme 2.3.12**):[14] 2,2′-(4-bromo-thien-2-ylmethylene)bis[1*H*-pyrrole] (dipyrromethane) (8.25 mmol) and 4-quinoline carboxaldehyde (4.24 mmol, 0.67 g) were added to a 250 mL solution of CH_2Cl_2 and trifluoracetic acid (65 μmol, 7 mg, 5 μL). The reaction was stirred at room temperature for 5 hours. Afterwards, a solution of DDQ (4.5 mmol, 1.02 g) in 10 mL of toluene was added to the reaction mixture and the reaction was stirred for 5 min before allowing the solvent to dry. Chromatographic separation with a SiO_2 column and 1:3 Hexane/$CHCl_3$ as eluent and subsequently with an Al_2O_3 column and 7:3 hexane/ethyl acetate as eluent yielded 5 mg of T_{Br}2Q2. Yield: < 1%. UV-vis ($CHCl_3$) λ / nm (log ε) 422 (4.07), 516 (3.26), 564 (3.15). ^{1}H NMR ($CDCl_3$, 80 MHz) δ_H / ppm 9.41 (d, 2 H, *J* = 4.5 Hz), 9.04 (d, 4 H, *J* = 4.92 Hz), 8.55 (d, 4 H, *J* = 5.03 Hz), 8.31 (s, 2H), 7.46–7.95 (m, 12H), -2.57 (s, 2 H). MS (MALDI-TOF): *m/z* for $[M+H]^+$ 887.74 amu; calculated 886.69 amu.

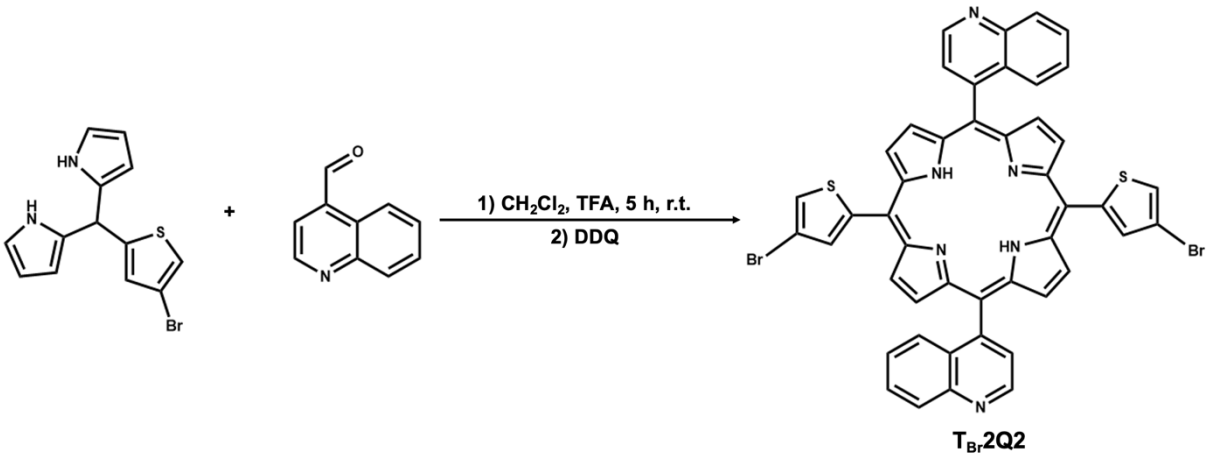

Scheme 2.3.12. The synthesis of the low-symmetry porphyrin **T_{Br}2Q2** from a secondary aromatic aldehyde and the 4-bromo-thien-2yl-substituted dipyrromethane.[14]

2.4 Synthesis of Corroles

2.4.1 5,10,15-tris(thien-2-yl)corrole (T3)

Yielded from the low-symmetry corrole synthesis of **T2Q** due to the residual presence of the primary aromatic aldehyde (**Scheme 2.4.1**): 2,2′-(thien-2-ylmethylene)bis[1*H*-pyrrole] (dipyrromethane) (8.25 mmol) and 4-quinoline carboxaldehyde (4.24 mmol, 0.67 g) were added to a 250 mL solution of CH_2Cl_2 and trifluoracetic acid (65 μmol, 7 mg, 5 μL)The reaction was stirred at room temperature for 5 hours. Afterwards, a solution of DDQ (4.5 mmol, 1.02 g) in 10 mL of toluene was added to the reaction mixture, and the reaction was stirred for 5 min before allowing the solvent to dry. Chromatographic separation (SiO_2, Hexane (1): $CHCl_3$ (3)) and, subsequently, with (Al_2O_3, hexane (7): ethyl acetate (3)) yielded 10 mg of **T3** as purple crystals. <1% yield. UV-vis ($CHCl_3$) λ / nm (log ε) 427 (4.00), 585 (3.15), 627 (3.08). ^{1}H NMR ($CDCl_3$, 80 MHz) δ_H / ppm 9.18 (s, 2H), 8.93 (s, 2H), 8.77 (s, 2H), 8.41 (s, 2H), 8,09 (s, 1H), 7.88–8.0 (m, 5H), 7.53–7.60 (m, 3H). MS (MALDI-TOF): *m/z* for $[M]^-$ 544.05 amu; calculated 544.72 amu.

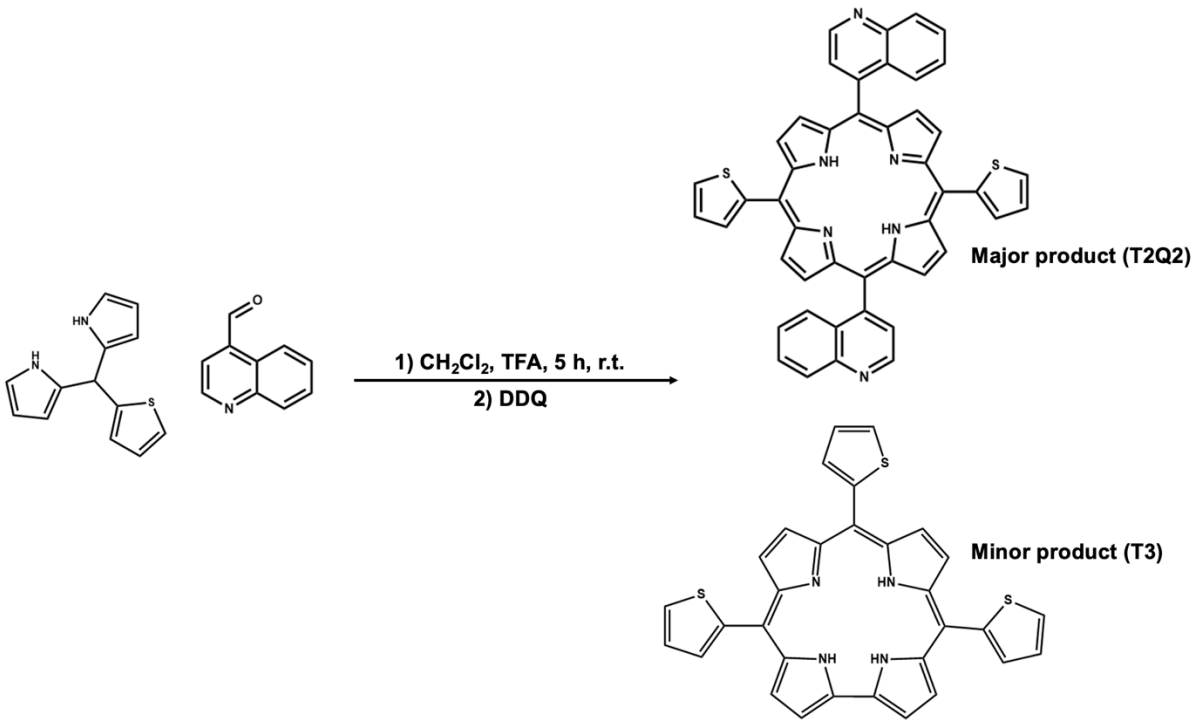

Scheme 2.4.1. The synthesis of the high-symmetry corrole **T3** as a minor product of the synthesis to yield the low-symmetry porphyrin and corrole, **T2Q2** and **T2Q**, respectively. This was possible due to the presence of the initial aromatic aldehyde, 2-thiophenecarboxaldehyde.[14]

2.4.2 5,10,15-tris(4-bromo-thien-2-yl)corrole ($T_{Br}3$)

$T_{Br}3$ was yielded according to Gryko *et al*.'s aqueous method (**Scheme 2.4.2**):[114] 2-thiophenecarboxaldehyde (5 mmol, 0.47 mL) and freshly distilled pyrrole (0.69 mL, 10 mmol) were dissolved in methanol (200 mL), and Millipore water (200 mL) was added afterwards. Subsequently, hydrochloric acid (32%, 4.5 mL) was added and the reaction was stirred for 3 h at room temperature. The mixture was extracted with $CHCl_3$ and the organic layer was washed thrice with water, filtered and dried over Na_2SO_4 and diluted to 300 mL with $CHCl_3$. *p*-Chloranil (5 mmol, 1.23 g) was added and the mixture was refluxed for 1 h. Purification was achieved *via* silica column chromatography with 1:1 CH_2Cl_2/cyclohexane as the eluent. All the fractions containing the corrole compounds were combined and chromatographed *via* DCVC twice (CH_2Cl_2 and hexane mixture). Yield: 5 mg of **$T_{Br}3$** as purple crystals**.** < 1% yield. UV-vis ($CHCl_3$) λ / nm (log ε) 427 (4.47), 589 (3.67). ^{1}H NMR ($CDCl_3$, 80 MHz) δ_H / ppm 9.15 (s, 2H),

8.99 (s, 2H), 8.81 (s, 4H), 8.01 (s, 1H), 7.70–7.82 (m, 5H). MS (MALDI-TOF): *m/z* for $[M+H]^+$ 782.49 amu; calculated 781.41 amu.

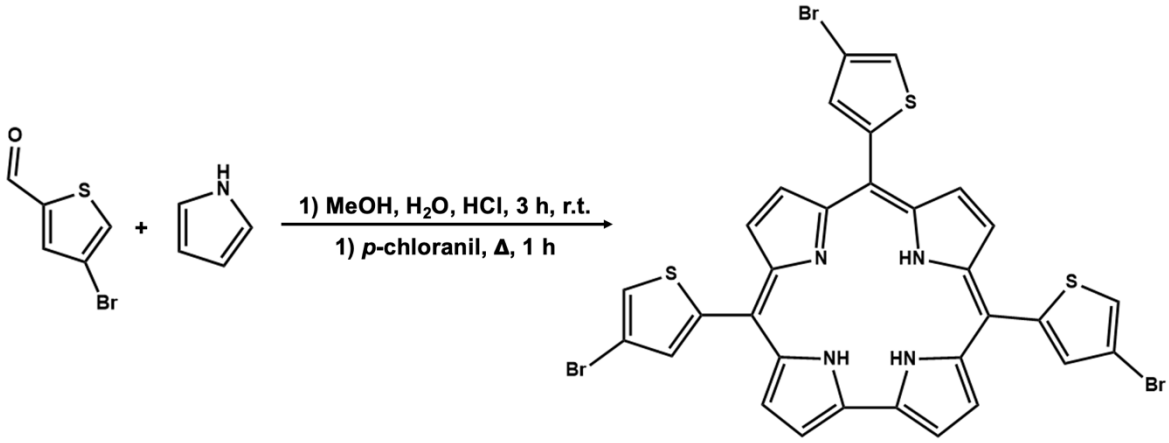

Scheme 2.4.2. The synthesis of the high-symmetry corrole $\mathbf{T_{Br}3}$.[114]

2.5 Preparation of the Sn(IV)T4 thin film (Sn(IV)T4-PBC)

Poly(bisphenol carbonate A) (PBS) (220 mg) (**Figure 1.10.2.1**) and of **Sn(IV)T4** (0.2 μmol, 0.2 mg) were dissolved in DCM (3 mL) and sonicated until a homogenous solution of the porphyrin-polymer mixture was obtained. **Sn(IV)T4-PBC** was then dropped onto glass substrates in a Petri dish, and the solvent was allowed to evaporate at room temperature. The average film thickness was determined to be 41 μm *via* SEM.[90]

2.6 Photostability experiments

Upon exposure to radiation in solution, a photosensitiser may undergo a photoinduced transformation that can, ultimately, alter its spectroscopic properties. Phototransformation of the photosensitised tissues during illumination can be responsible for an alteration of the photodynamic activity and overall efficacy.[115] Since this investigation employs light, this is an essential parameter to assess. The photostability experiments were conducted in a quartz cuvette (1 × 1 cm); the compounds were dissolved in PBS (5%DMSO) to mimic the *in vitro* experiments and irradiated with a 415 nm (360 mW/cm^2) Thorlabs LED lamp in 6 min intervals over a total time of 30 min. The experiment was done in a dark irradiation chamber so as to avoid ambient light. The bleaching of the dyes at the Soret absorption peak was monitored as a function of time, and the amount of dye remaining after the 30 min of irradiation is reported in **Table 3.4.1.**

2.7 Cell culturing and *in vitro* studies on MCF-7 cancerous cells

2.7.1 In vitro dark toxicity

In vitro dark toxicity studies were conducted on the MCF-7 (Michigan Cancer Foundation) human epithelial breast cancer cells before the PDT activity (light) studies. The cells were cultured in Dulbecco's modified Eagle's medium (DMEM) that was modified with 4.5 g.L^{-1} glucose, L-glutamine and phenol red. The DMEM was supplemented with 10% heat-inactivated FCS, penicillin-streptomycin-amphotericin B mix, 100 units.mL^{-1} penicillin and 100 μg.mL^{-1} streptomycin-amphotericin B were added. The cells were incubated at 37°C in a humidified atmosphere containing 5% CO_2 and grown in 75 cm^2 Porvair® flasks with vented caps. Regular subculturing was performed *via* trypsinisation, and the detached cells were treated with trypan blue (0.4%) and examined for viability. The cells were seeded in DMEM (modified with phenol red) at a density of 10000 cells per well in 96 well tissue culture plates (Porvair) and kept in a 5% CO_2 incubator maintained at 37°C for 24 h. When the cells were

confluent, the adherent cells were washed with 100 μL of DPBS. Subsequently, 100 μL of DMEM solution (modified with phenol red) containing the compounds under study at varying concentrations was added (2.5 μM – 80μM), and the solutions were incubated under the same conditions in the dark for 24 h. Control cells were incubated with the supplemented DMEM only.

After 24 h, the wells were rinsed with 100 μL of DPBS. The cytotoxicity of the compounds was assessed by the WST-1 assay.[116] The principle of this assay relies on the tetrazolium salt WST-1 being cleaved to a soluble formazan by a complex cellular mechanism that occurs primarily at the cell surface of viable cells; the amount of formazan formed is directly proportional to the number of metabolically viable cells in the cell culture.[117] The absorbance is measured at 450 nm to quantify the viability of the cells. The percentage of cell viability is given by:

$$\%\ Cell\ viability = \frac{Absorbance\ of\ sample\ at\ 450\ nm}{Absorbance\ of\ control\ at\ 450\ nm} \times 100 \qquad \textbf{(2.7.1)}$$

2.7.2 In vitro PDT

The cells were incubated with the same procedure described in **Section 2.6.1**, and the compounds (**Sn(IV)T4**, **In(III)T4**, **Sn(IV)T_{Br}4**, **Sn(IV)T2Q2**, **In(III)T2Q2** and **Sn(IV)T2Q2^{+}**) were added in the same range of concentrations (2.5 μM – 80 μM) dissolved in 2% DMSO. The controls were only incubated with DMEM modified with phenol red. After 24 h of incubation with the drugs, the media was replaced with DPBS and the plates were photoirradiated with a 625 nm Thorlabs M625L3 LED for 30 min (240 mW/cm^2). The LED was mounted into the housing of a Modulight 7710-680 medical laser system. After the irradiation, DPBS was replaced with DMEM modified with phenol red and incubated for 24 h. The cell viability was assayed using the previous protocol and equation described in **Section 2.6.1** with WST-1.

An important parameter for assessing the efficacy of photosensitisers during *in vitro* PDT is the IC_{50} value: the concentration of the photosensitiser that promotes 50% cell death after incubation and light treatment. Nonlinear regression analysis with GraphPad Prism was used to determine the IC_{50} values of the photosensitisers.

2.8 Bacterial Inactivation Studies (PACT)

The photodynamic antimicrobial chemotherapeutic activities of the photosensitisers were assessed against *Staphylococcus aureus* and *Escherichia coli*. The bacterial cultures were prepared by placing an aliquot of the commercially acquired bacterial crystals into 6 mL of freshly prepared Luria nutrient broth; these solutions were then briefly vortexed and incubated under agitation in a shaking incubator at 37°C to grow. The optical density at 600 nm of the bacterial stock solutions was tested regularly until an optical density of 0.6 was achieved for both of the individual solutions to ensure mid-logarithmic growth. The stock solutions were centrifuged at 3000 rpm for 15 min to remove the nutrient broth. The pellets of *S. aureus* and *E. coli* were washed thrice with PBS to remove any residual nutrient broth. The pellets of the individual bacteria were resuspended in 10 mL of PBS to afford the stock solutions (10^{-2}) for the subsequent studies.

Before the PACT studies were carried out, the bacterial stock solution was optimised to afford an appropriate working concentration of the bacteria. The bacterial solutions used throughout the study were 10^{-7} and these working concentrations were acquired via serial dilutions of the stock solutions. Drug concentration optimisation studies were also conducted, but the highest possible working concentration was used.

The PACT studies were conducted using the previously reported viable count method.[118] Stock solutions (5×10^{-4} M) of the following compounds were prepared in PBS (5% DMSO) and they were assessed for their photodynamic antimicrobial chemotherapeutic activities: **SnT4**, **InT4**, **$SnT_{Br}4$**, **SnT2Q2**, **InT2Q2**, **$T_{Br}2Q2$ and $SnT2Q2^{+}$**. The solutions that were used for the

experiments were prepared with 480 μL of the stock (to afford a final concentration of 40 μM for both *S. aureus* and *E. coli*) and 60 μL of the 10^{-5} bacterial dilution, and they were made up to 6 mL with PBS. The mixtures were placed in a shaking incubator at 37°C for 4 h to afford localisation of the dyes into the bacterial cells. Approximately 2.5 mL of these solutions were placed into individual wells of a 24-well plate and irradiated at 595 nm with a Thorlabs M595L3 LED (240 mW/cm^2) over predefined intervals (t_n, where n = 0, 30, 60, 90 and 120 min), while another 2.5 mL was placed in a different 24-well plate and kept in the dark for the same time intervals. After each of the subsequent experiments, 100 μL of the samples that were exposed to radiation or a lack thereof was inoculated onto agar plates in triplicate while maintaining a sterile environment. The plates were then inverted and placed into the incubator at 37°C for 18 h before the colony counts were determined. The colony-forming units (CFU/mL) of bacteria were counted using a Scan® 500 automatic colony counter.

2.9 *In silico* studies

Density functional theory (DFT) and time-dependent density functional theory (TD-DFT) were employed in the theoretical calculations conducted throughout this study. This was done by using the B3LYP exchange-correlation functional of the Gaussian 09 software package (version E01).[119] Geometry optimisations were conducted at the B3LYP/6-31G(d) level of theory. The obtained optimised B3LYP geometries were used to carry out excited state TD-DFT calculations by using the CAM-B3LYP functional, which introduces a long-range correction. The overall visualisation of the generated molecular orbitals was achieved using Chemcraft.

2.10 Failed syntheses

This section details the attempted syntheses of porphyrin compounds and their analogues and isomers. These compounds were selected to complete a trend set, but they could not be yielded upon synthesis and/or purification.

2.10.1 5,10,15,20-tetrakis(thien-2-yl)porphyrinato Phosphorous(V)-trichloride (P(V)T4)

The free base porphyrin (0.1 g, 0.16 mmol, 1 eq) was dissolved in 18 mL of pyridine under a nitrogen atmosphere and $POCl_3$ (2 mL, 21.96 mL, 135 eq) was added dropwise to the mixture while stirring. A solution of PCl_5 (0.1 g, 0.48 mmol, 3 eq) in 2 mL of pyridine was then added dropwise; the mixture was then refluxed under nitrogen for 24 h (**Scheme 2.10.1**). After cooling to room temperature and evaporating the pyridine under vacuum, the solid was dissolved in CH_2Cl_2 and subjected to column chromatography (SiO_2, CH_2Cl_2). After analysis of the fractions that eluted from the column, there was no evidence of the formation of **P(V)T4** upon analysis with MS and UV-visible spectroscopy. It was then decided that the Sn(IV) porphyrins would be compared to their In(III) counterparts experimentally, but P(V) the theoretical calculations of P(V) porphyrins and corroles are still reported in Chapter **8**.[120]

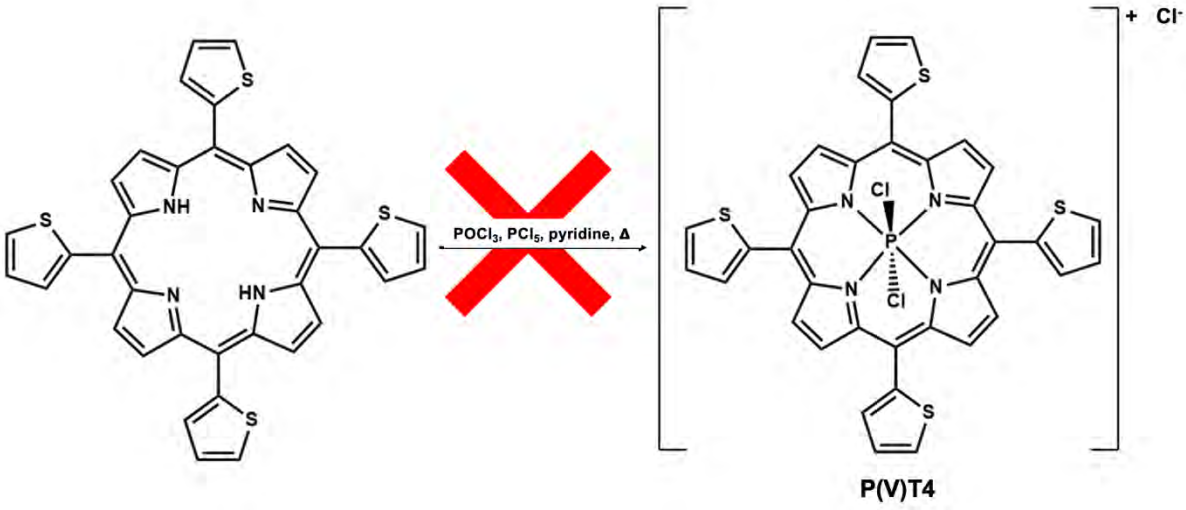

Scheme 2.10.1. The failed synthetic approach to yield **P(V)T4** from **T4**.[120]

2.10.2 5,10,15,20-tetrakis(4-bromo-thien-2-yl)porphyrinato Indium(III)-trichloride (In(III)T_{Br}4)

50 mg of the free-base porphyrin (5.4 μmol) was dissolved in 15 mL of acetic acid, and sodium acetate (400 mg) was added. Thereafter, Indium (III) chloride tetrahydrate (15 mg, 51.1 μmol) was added. The reaction mixture was refluxed for 72 h (**Scheme 2.10.2**). The reaction mixture was washed with water after dissolving in $CHCl_3$, and lastly washed with water that contained $NaHCO_3$. Upon analysis of the crude product and eluted fractions from chromatographic separation (SiO_2, $CHCl_3$ (4): MeOH (1)), there was no evidence of the formation of **Sn(IV)T_{Br}4.** The synthesis was attempted multiple times, but the target metalated product was not obtained.[111]

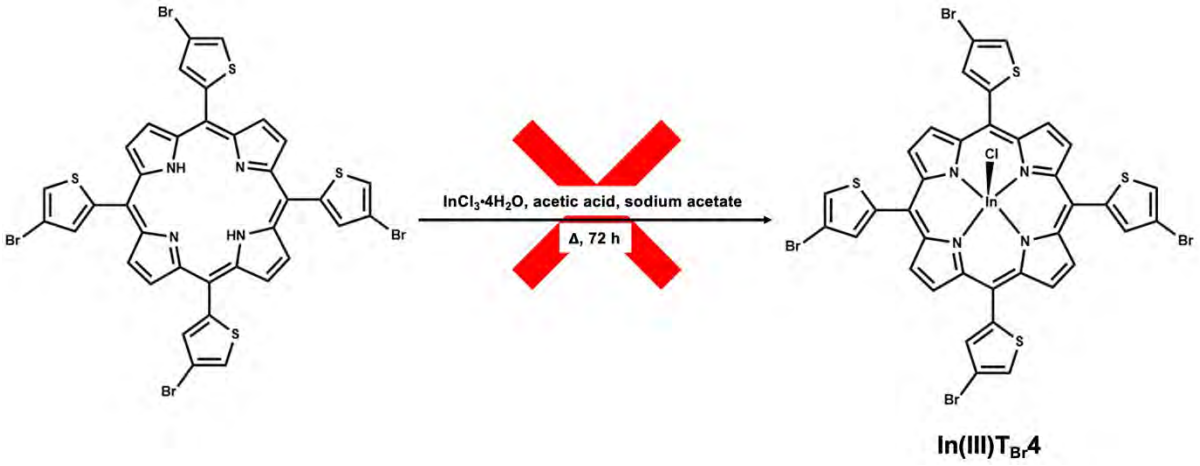

Scheme 2.10.2. The failed synthetic approach to yield **In(III)T_{Br}4** from **T_{Br}4**.[111]

2.10.3 Synthesis of 5,15-bis(thien-2-yl)-10-(4-quinolinyl)corrole (T2Q)

2,2′-(thien-2-ylmethylene)bis[1*H*-pyrrole] (dipyrromethane) (8.25 mmol) and 4-quinoline carboxaldehyde (4.24 mmol, 0.67 g) were added to a 250 mL solution of CH_2Cl_2 and trifluoracetic acid (65 μmol). The reaction was stirred at room temperature for 5 hours. Afterwards, a solution of DDQ (4.5 mmol, 1.02 g) in 10 mL of toluene was added to the reaction mixture and the reaction was stirred for 5 min before allowing the solvent to dry (**Scheme 2.10.3**). Chromatographic separation was attempted *via* SiO_2 gel chromatography with 1:3 Hexane/$CHCl_3$ as an eluent and subsequently with an Al_2O_3 column with 7:3 hexane/ethyl

acetate as the eluent. After the synthesis and column chromatography, the major product was found to be the low-symmetry porphyrin, **T2Q2**, and the low yield of the low-symmetry corrole, **T2Q**, could not be purified to a level sufficient for characterisation and subsequent application.[14]

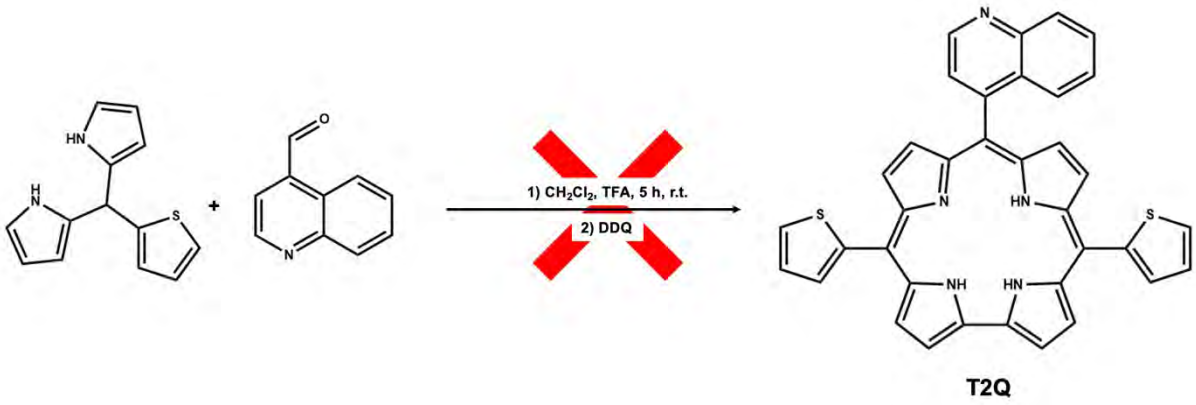

Scheme 2.10.3. The failed synthetic approach to yield **T2Q**.[14]

2.10.4 5,15-bis(4-bromo-thien-2-yl)-10-(4-quinolinyl)corrole ($T_{Br}2Q$)

2,2′-(4-bromo-thien-2-ylmethylene)bis[1*H*-pyrrole] (dipyrromethane) (8.25 mmol) and 4-quinoline carboxaldehyde (4.24 mmol, 0.67 g) were added to a 250 mL solution of CH_2Cl_2 and trifluoracetic acid (65 μmol). The reaction was stirred at room temperature for 5 hours (**Scheme 2.10.4**). Afterwards, a solution of DDQ (4.5 mmol, 1.02 g) in 10 mL of toluene was added to the reaction mixture and the reaction was stirred for 5 min before allowing the solvent to dry. Chromatographic separation was attempted *via* SiO_2 gel chromatography with 1:3 Hexane/$CHCl_3$ as an eluent and subsequently with an Al_2O_3 column with 7:3 hexane/ethyl acetate as the eluent. There was no fraction that eluted from the column that corresponded to **$T_{Br}2Q$** (in terms of UV-visible spectroscopy or mass spectrometry) and the major product was, once again, the low-symmetry porphyrin, **$T_{Br}2Q2$**.[14]

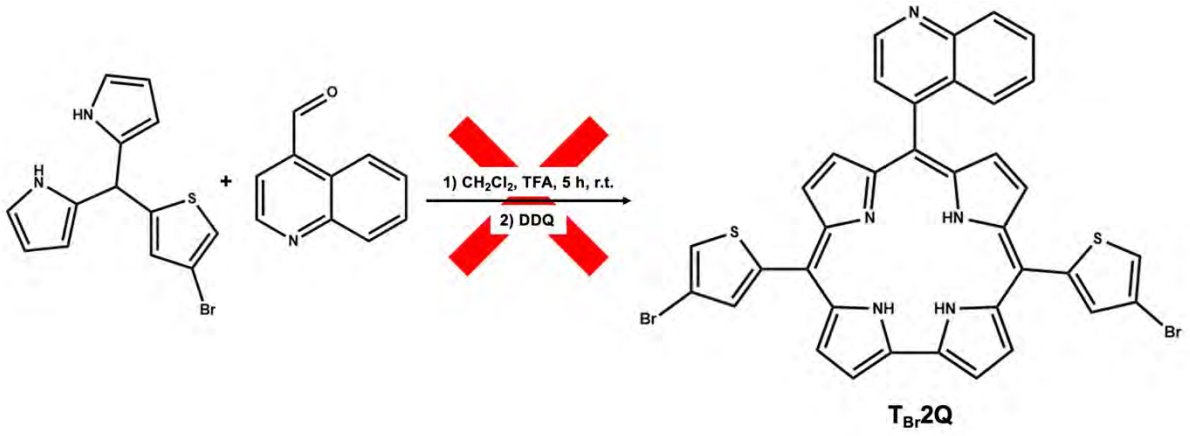

Scheme 2.10.4. The failed synthetic approach to yield **T_{Br}2Q**.[14]

2.10.5 5,10,15,20-tetrakis(4-quinolinyl)-2-aza-21-carbaporphyrin (NCQ4)

To a 1 L flask, dichloromethane (DCM) (750 mL), freshly distilled pyrrole (1.04 mL, 15 mmol) and 4-quinolinecarboxaldehyde (2.36 g, 15 mmol) were added. The reaction was initiated upon the addition of MSA (0.681 mL, 10.5 mmol). This was stirred at room temperature for 30 min with foil around the flask. DDQ (3.00 g, 13.2 mmol) was then added; the mixture was stirred for 1 min (**Scheme 2.10.5**). The acid was quenched upon the addition of TEA (5.8 mL; 42 mmol). Without solvent evaporation, the crude reaction mixture was passed through a 500 mL separatory funnel with basic alumina. This was rinsed thoroughly with DCM to yield maximum product. The dried product was added to a column containing basic alumina with petroleum ether. The polarity of the eluant was increased from 0% DCM in the petroleum ether to 50%. Upon analysis of the fractions that were eluted from the column, there were no fractions that exhibited the expected mass in MS or the typically N-confused UV-visible spectrum.[122]

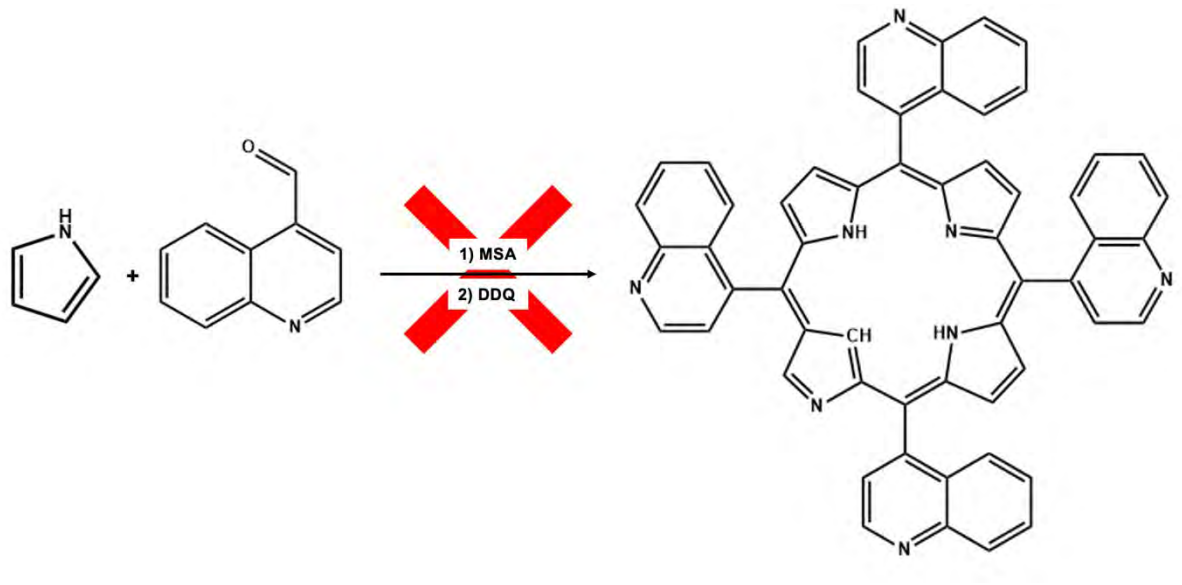

Scheme 2.10.5. The failed synthetic approach to yield **NCQ4**.[121]

CHAPTER THREE

STRUCTURAL CHARACTERISATION AND PHOTOPHYSICAL AND -CHEMICAL PROPERTIES

3.1 Structural characterisation of the porphyrins

^{1}H NMR, MALDI-TOF MS and UV-visible absorption spectroscopy were all used to confirm the successful synthesis of the dyes within this investigation.

3.1.1 Structural characterisation of the thien-2-yl substituted high-symmetry porphyrins

Mass spectrometry was used as the preliminary characterisation technique to determine whether the synthesis of the photosensitisers was successful. **T4**, **Sn(IV)T4**, and **In(III)T4** were all determined to be successfully synthesised and purified based on analyses by mass spectrometry and, later, ^{1}H NMR spectroscopy. **T4** was found to have a mass of 639.24 amu in MS, which is in an acceptable range for the expected mass of this molecule, which was 638.86 amu (**Figure 3.1.1.1**). Similarly, the metalated molecules, **Sn(IV)T4** and **In(III)T4** were found to have their respective masses that correlated to their structures without one chloride axial ligand, which is easily cleaved off during MS (**Figure 3.1.1.2** and **Figure 3.1.1.3**).

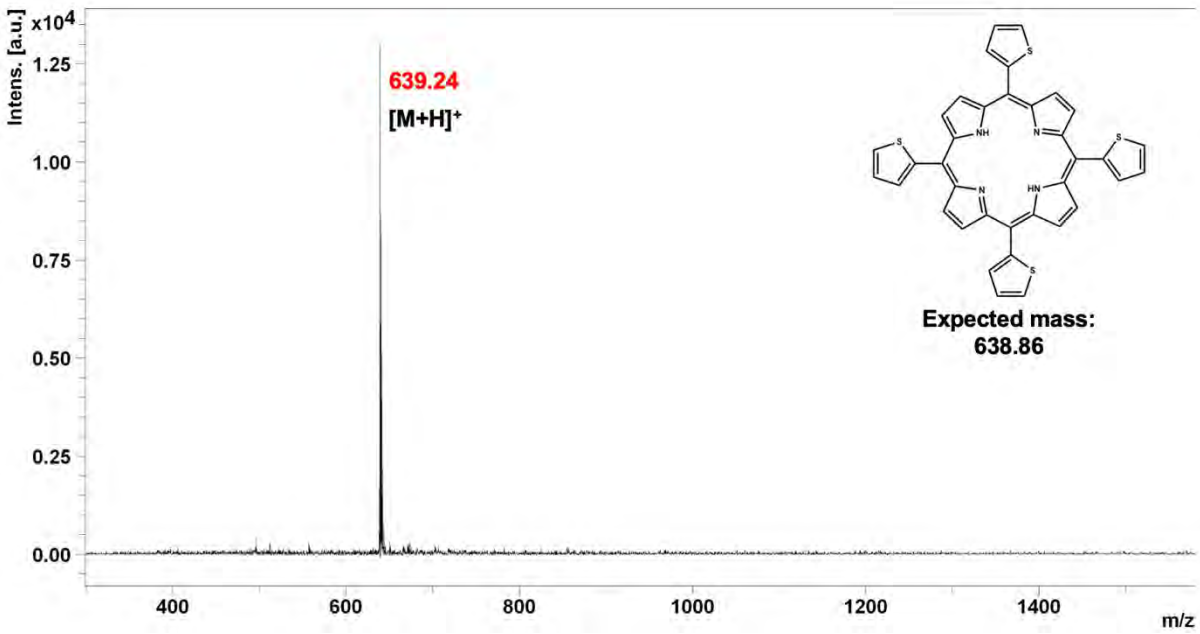

Figure 3.1.1.1. MALDI-TOF data for **T4**, with its mass obtained in red and the expected mass and structure alongside.

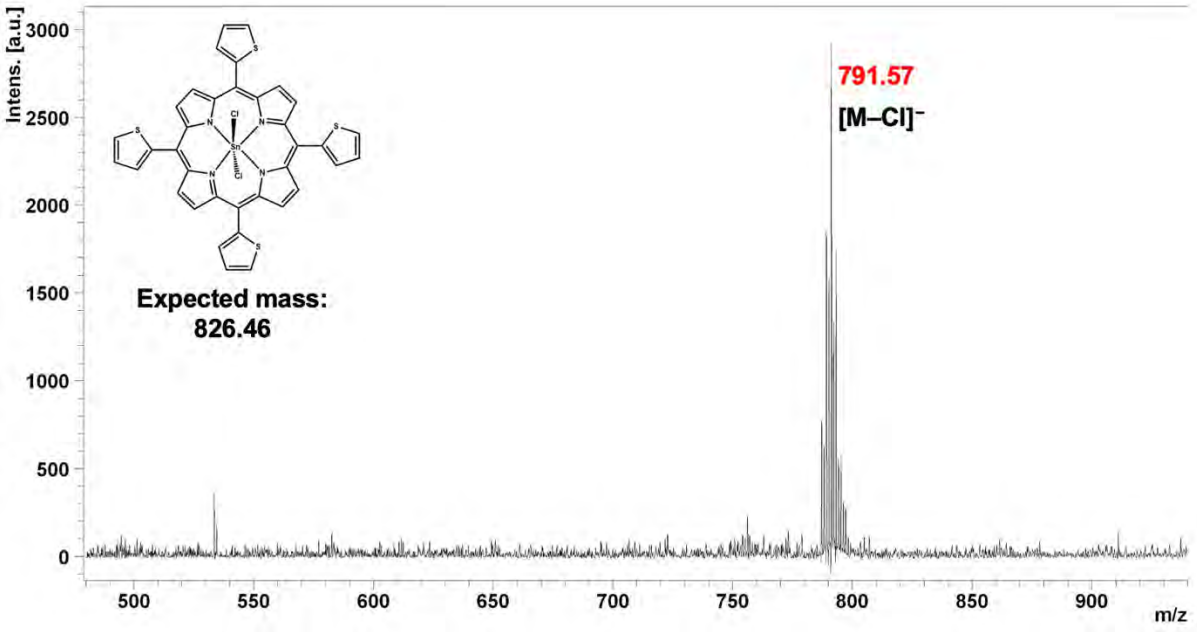

Figure 3.1.1.2. MALDI-TOF data for **Sn(IV)T4**, with its mass obtained in red and the expected mass and structure alongside.

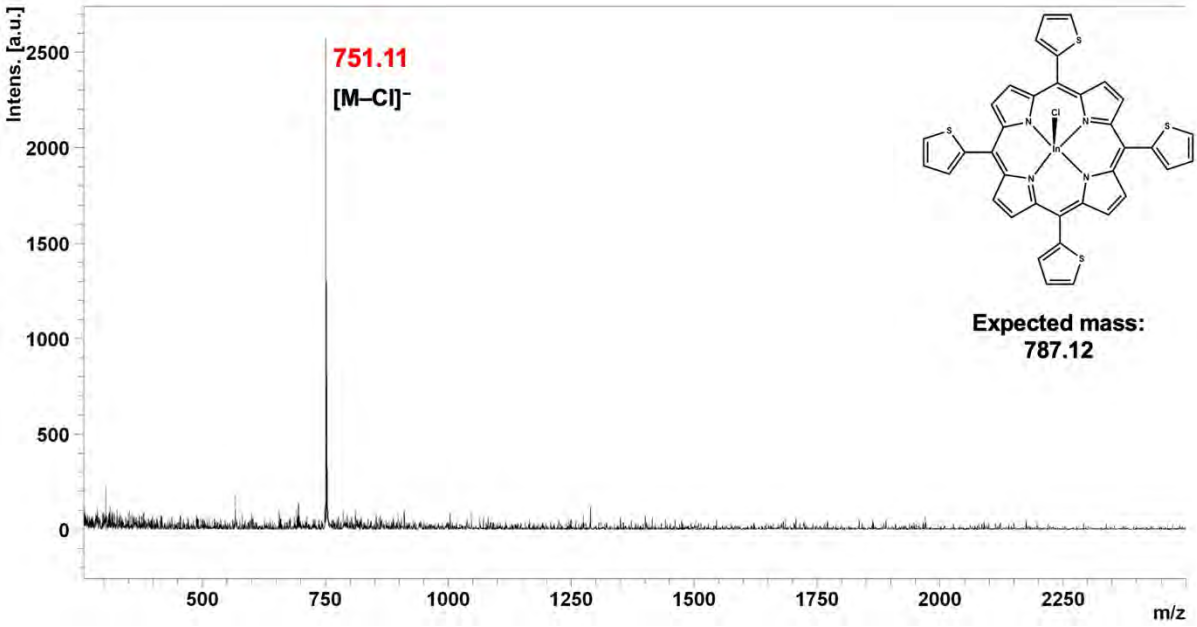

Figure 3.1.1.3. MALDI-TOF data for **In(III)T4**, with its mass obtained in red and the expected mass and structure alongside.

The signals for all 22 protons of **T4** could be readily assigned in the ^{1}H NMR spectrum (**Figure 3.1.1.4**). The singlet at -2.67 ppm integrates to 2 protons, and these account for the inner protons in **T4** (before metalation), which are significantly shielded from the external magnetic field by the aromatic system. The remaining signals account for the aromatic protons on either

on the thienyl ring or from the pyrrole groups. The lack of doublets could be accounted for by the high degree of symmetry within this molecule.

A similar ^{1}H NMR spectrum is seen for both **Sn(IV)T4** and **In(III)T4** (**Figure 3.1.1.5** and **Figure 3.1.1.6**), where there is a total aromatic integration of 20 protons, which again accounts for the aromatic protons within the molecule, i.e. on the pyrrole rings and the thiophene moiety. Both of these molecules lack a signal in the negative region of the spectrum due to the successful metalation event, which results in the deprotonation of the core electrons in the formation of a dianion for bonding to their respective metal ions.

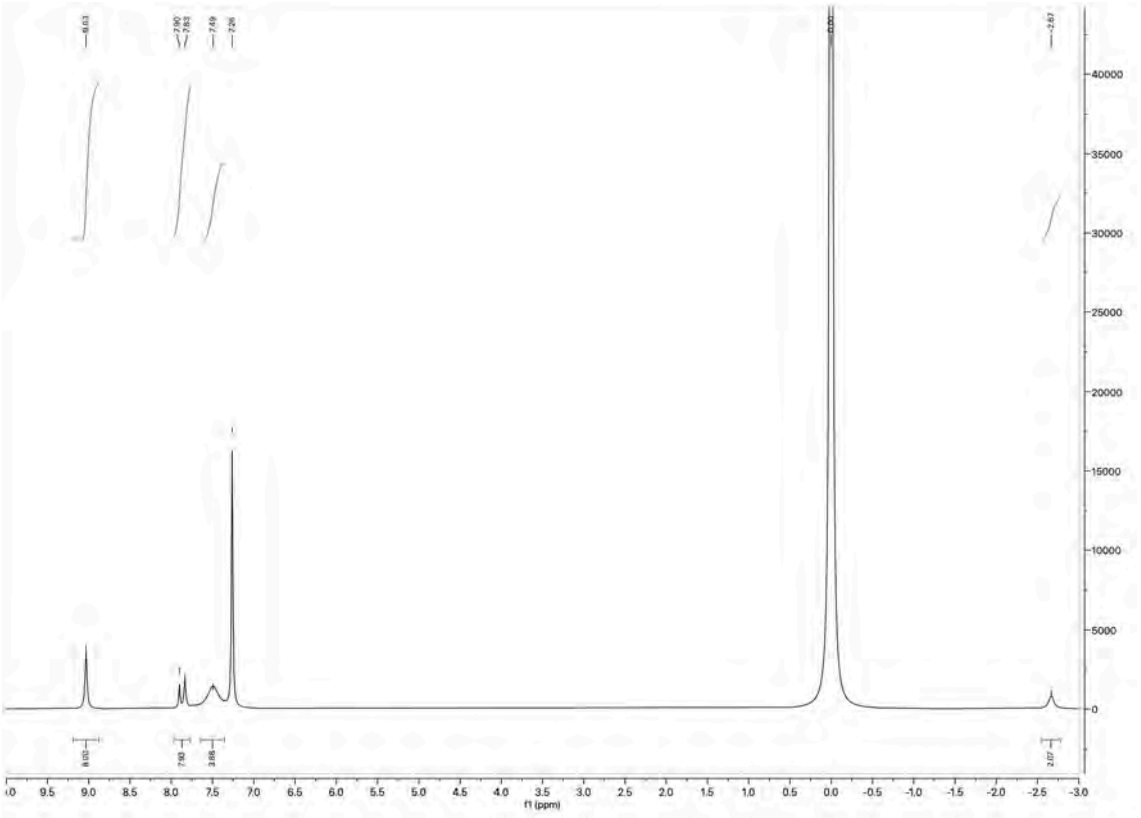

Figure 3.1.1.4. ^{1}H NMR spectrum of **T4** measured in $CDCl_3$.

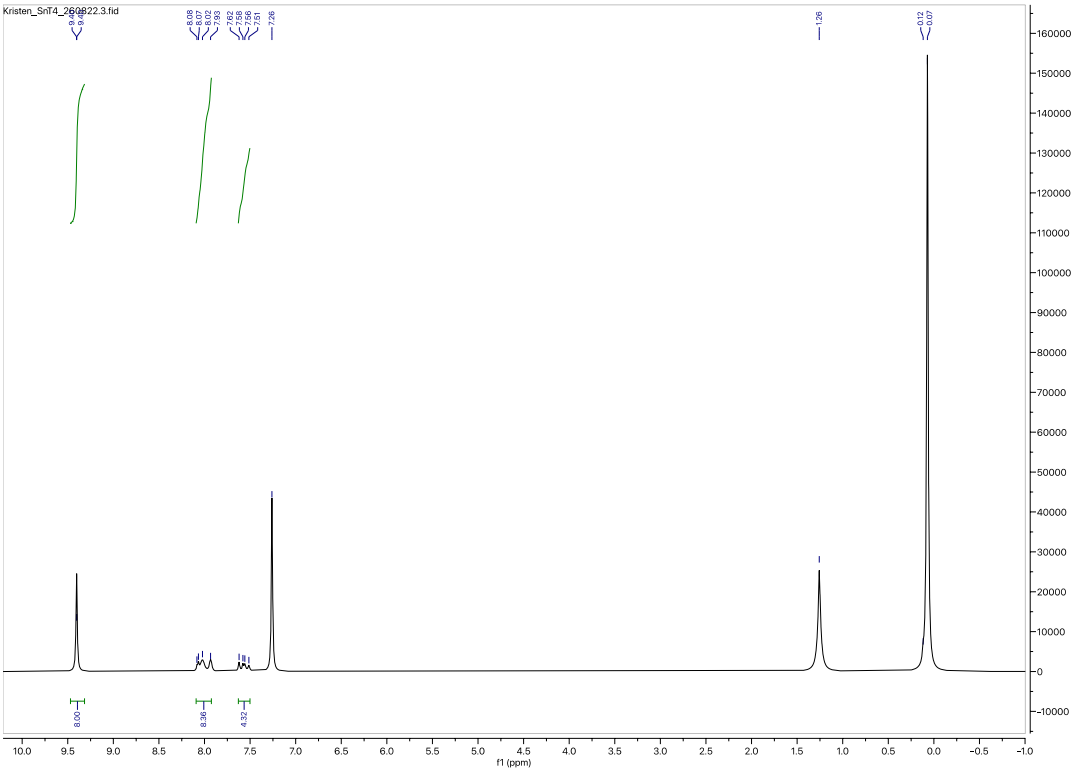

Figure 3.1.1.5. ^{1}H NMR spectrum of **Sn(IV)T4** measured in $CDCl_3$.

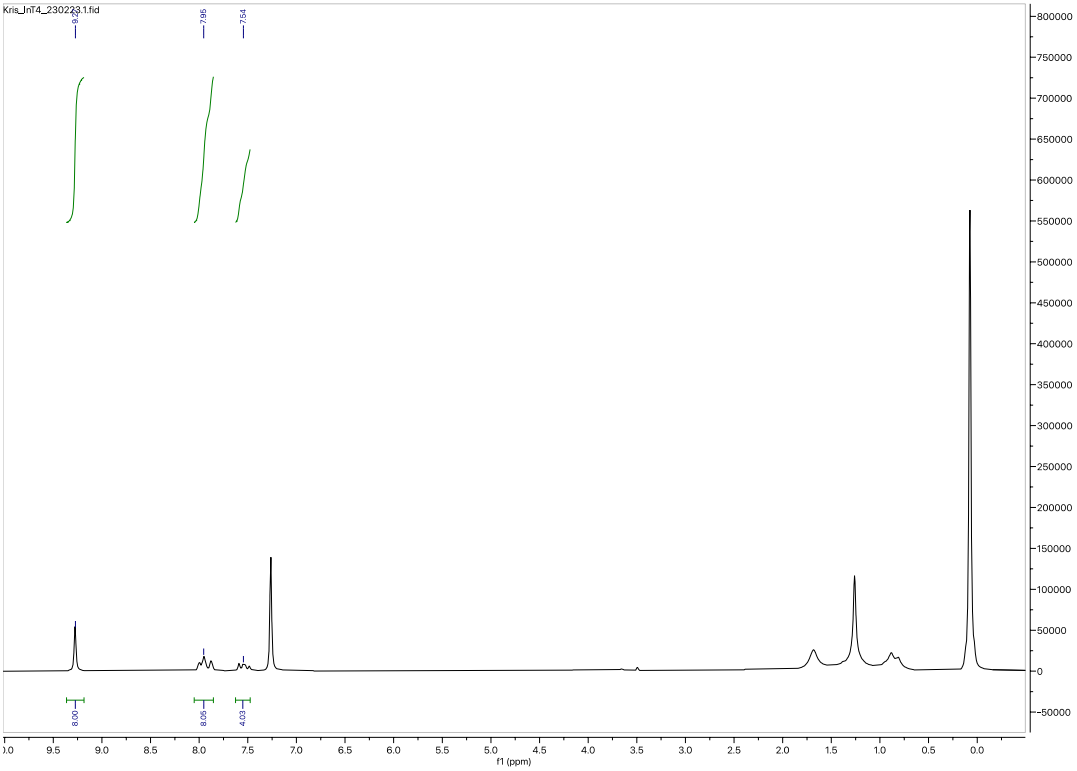

Figure 3.1.1.6. ^{1}H NMR spectrum of **In(III)T4** measured in $CDCl_3$.

T4, **Sn(IV)T4**, and **In(III)T4** all exhibited typical porphyrinoid UV-visible trends, with an intense and narrow Soret absorbance band and a relatively weak Q band envelope. It can be noted that **T4** has a relatively blue shifted B band compared to the metalated molecules, which was

expected. Additionally, **T4** has 4 Q bands. **Sn(IV)T4** and **In(III)T4** both have red-shifted Soret bands and blue-shifted Q bands, which is accounted for in **Chapter 8**. The experimental collapse of the 4 Q bands, as seen in the free base molecule (**Figure 3.1.1.7**), to 2 Q bands in the metalated molecules is apparent (**Figure 3.1.1.8** and **Figure 3.1.1.9**).

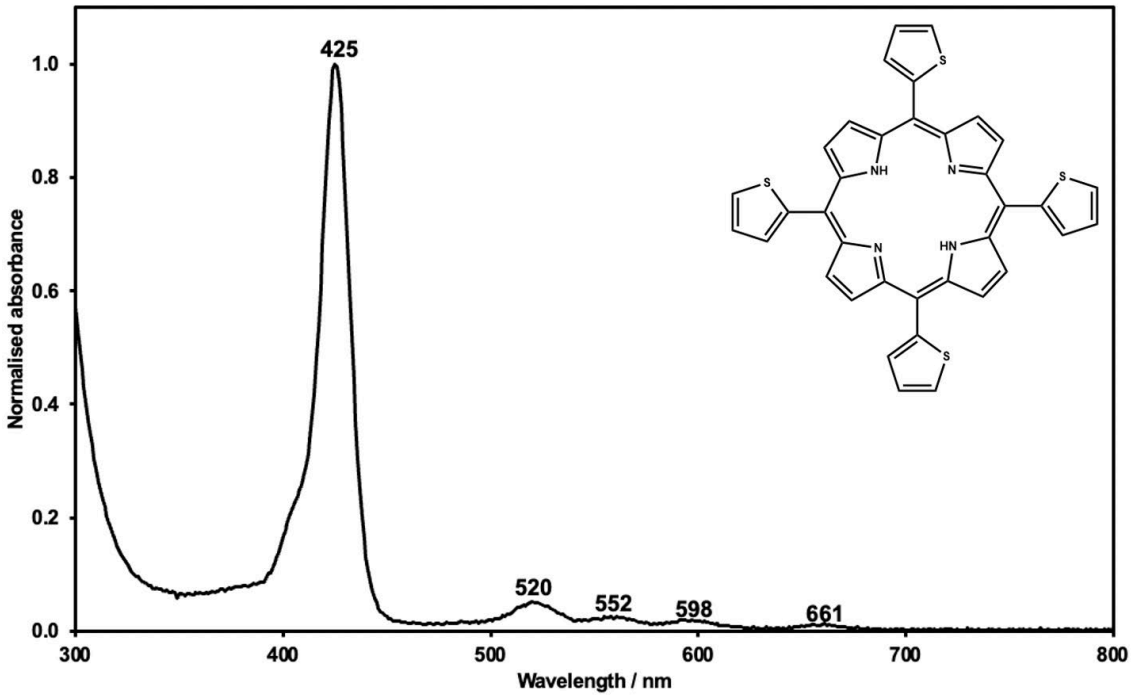

Figure 3.1.1.7. UV-visible absorption spectrum of **T4** measured in $CHCl_3$. Soret band: 425 nm ($\log\varepsilon = 5.57$).

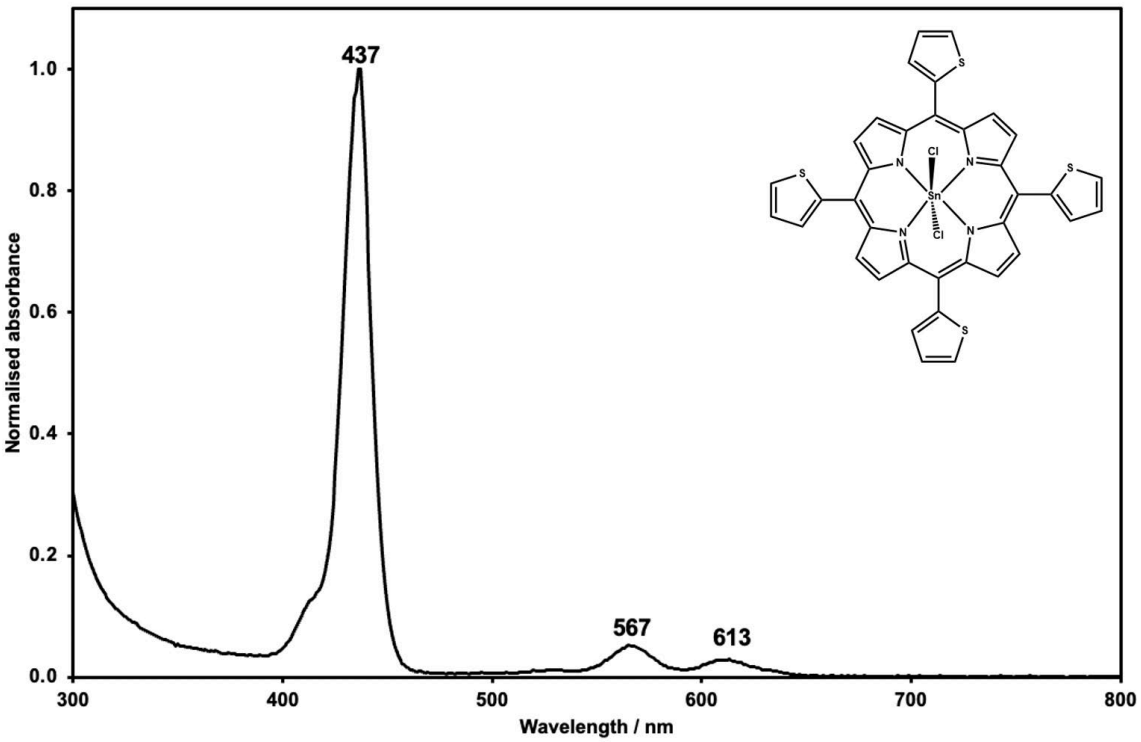

Figure 3.1.1.8. UV-visible absorption spectrum of **Sn(IV)T4** measured in $CHCl_3$. Soret band: 437 nm ($\log\varepsilon = 5.27$).

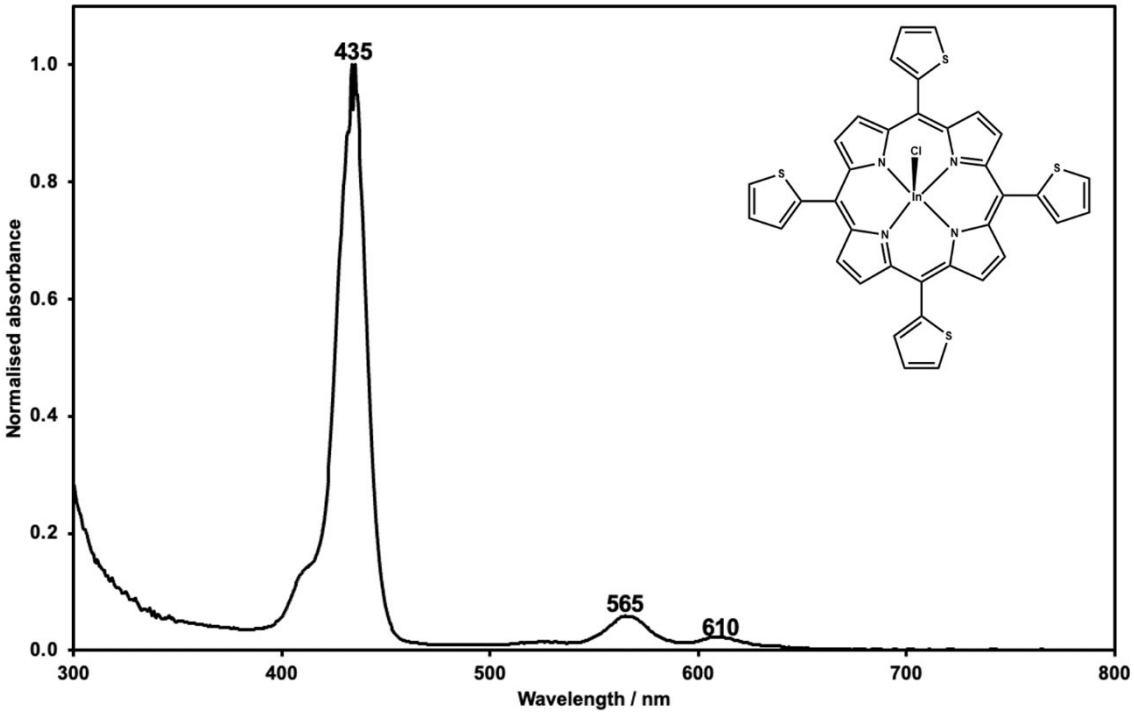

Figure 3.1.1.9. UV-visible absorption spectrum of **In(III)T4** measured in $CHCl_3$. Soret band: 435 nm ($\log\varepsilon$ = 4.80).

3.1.2 Structural characterisation of the 4-bromo-thien-2-yl substituted high-symmetry porphyrins

T_{Br}4 and **Sn(IV)T_{Br}4** were successfully synthesised and purified based on analyses by mass spectrometry and, later, ^{1}H NMR spectroscopy. **T_{Br}4** was found to have a mass of 954.99 amu in MS, which is in an acceptable range for the expected mass of this molecule, which was 954.45 amu (**Figure 3.1.2.1**). Similarly, the metalated molecule, **Sn(IV)T_{Br}4**, was found to have an experimentally determined mass that correlated to its structure without one chloride axial ligand, which is easily cleaved off during MS (**Figure 3.1.2.2**).

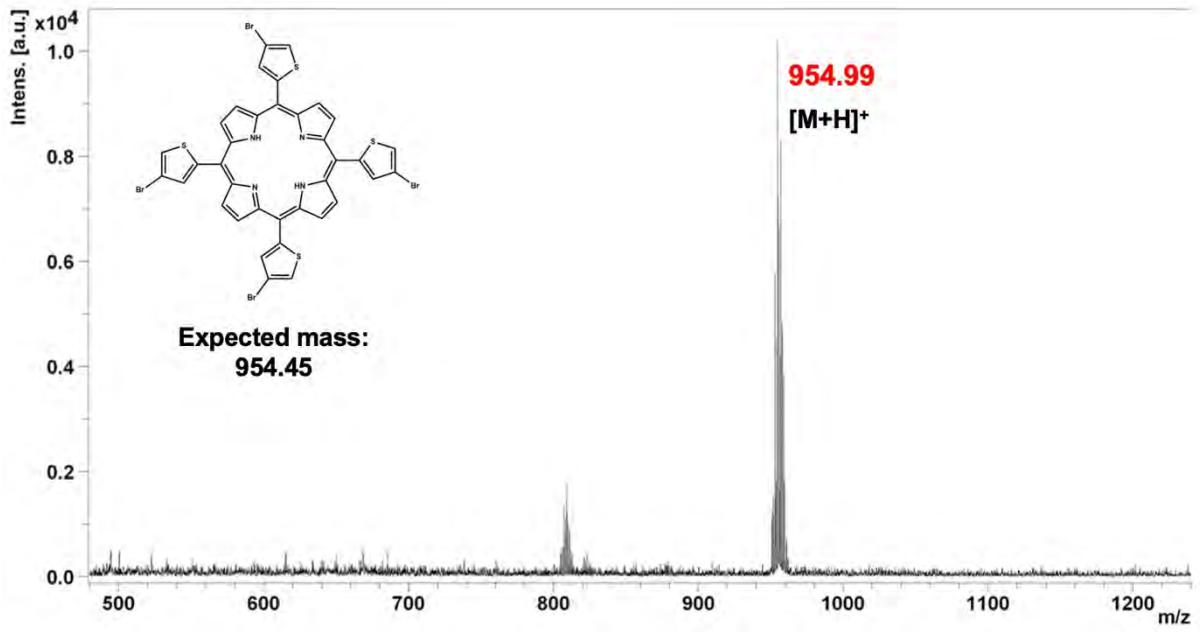

Figure 3.1.2.1. MALDI-TOF data for **T_{Br}4** with its mass obtained in red and its expected mass and structure alongside.

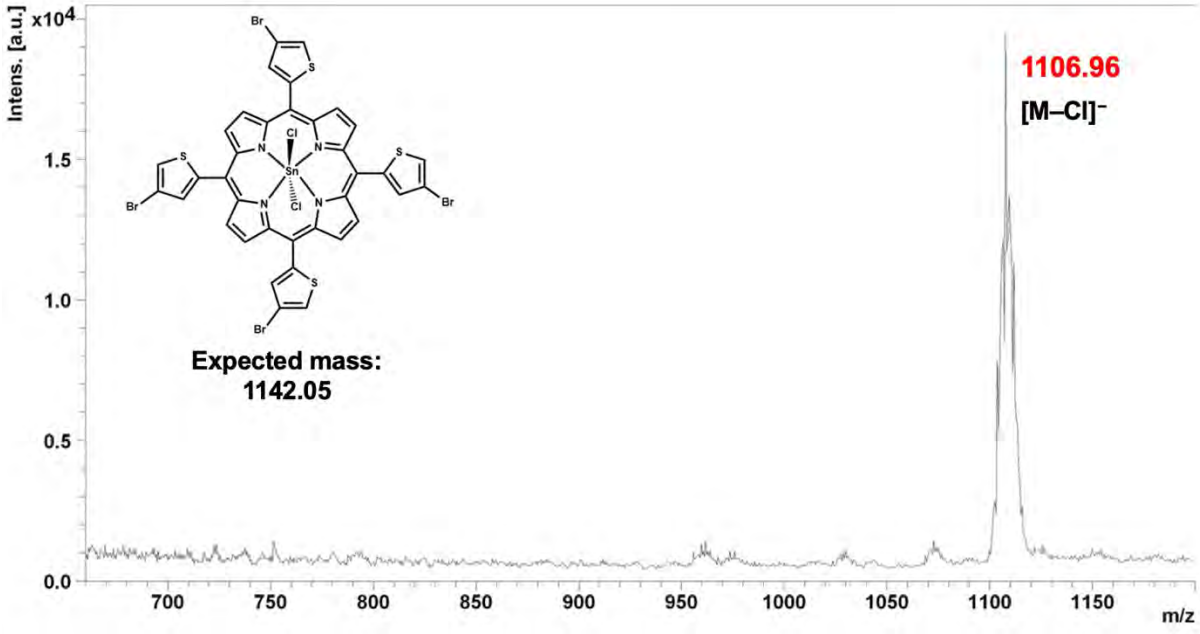

Figure 3.1.2.2 MALDI-TOF data for **Sn(IV)T_{Br}4** with its mass obtained in red and its expected mass and structure alongside.

The signals for all 18 protons of **T_{Br}4** could be readily assigned in the ^{1}H NMR spectrum (**Figure 3.1.2.3**). The singlet at -0.66 ppm integrates to 2 protons, and these account for the inner protons in **T_{Br}4** (before metalation), which are significantly shielded from the external magnetic field by the aromatic system. The remaining signals all account for the aromatic protons: the thienyl-proton signals appear as singlets at 8.65 and 9.08 ppm due to the lack of

a proton neighbour, and the doublets at 8.27 and 7.86 ppm account for the pyrrole protons, since these protons each have one neighbouring proton.

A similar ^{1}H NMR spectrum is seen for **Sn(IV)T4** (**Figure 3.1.2.4**), where there is a total aromatic integration of 16 protons, which again accounts for the aromatic protons within the molecule, i.e. on the pyrrole rings and the thiophene moiety. **Sn(IV)T_{Br}4** lack a signal in the negative region of the spectrum due to the successful metalation event, which results in the deprotonation of the core electrons in the formation of a dianion for bonding to Sn(IV). Additionally, **Sn(IV)T_{Br}4** only has two peaks. This can be accounted for by the high level of symmetry within this molecule.

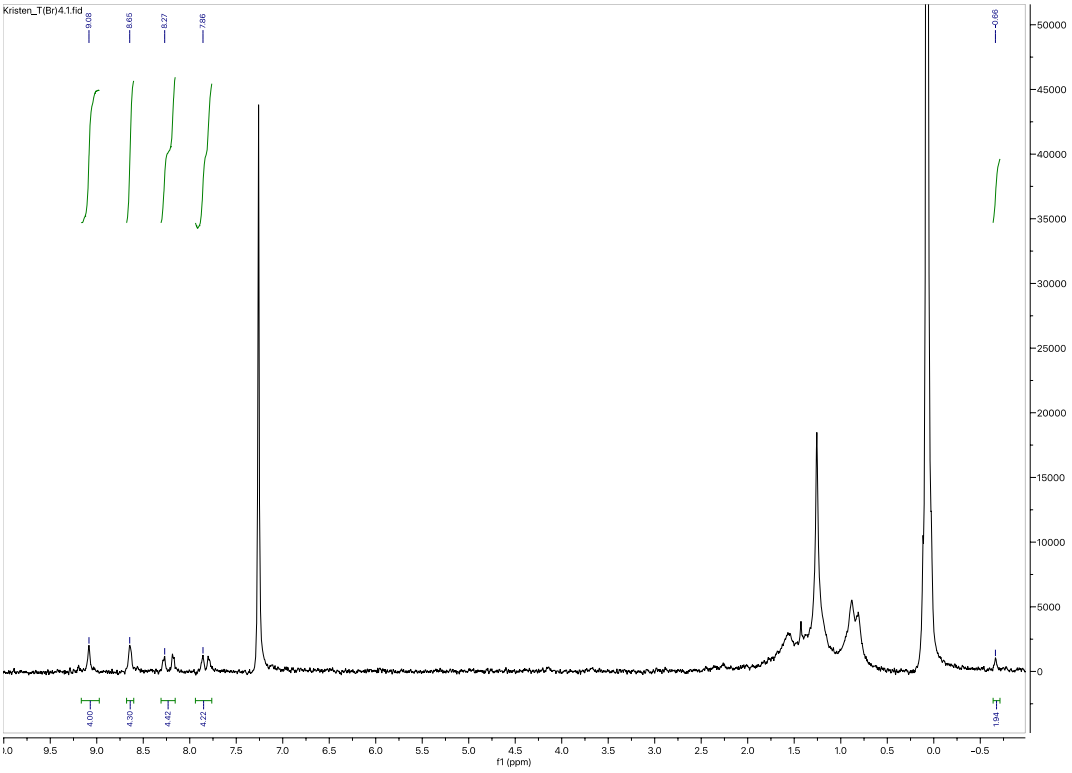

Figure 3.1.2.3. ^{1}H NMR spectrum of **T_{Br}4** measured in $CDCl_3$.

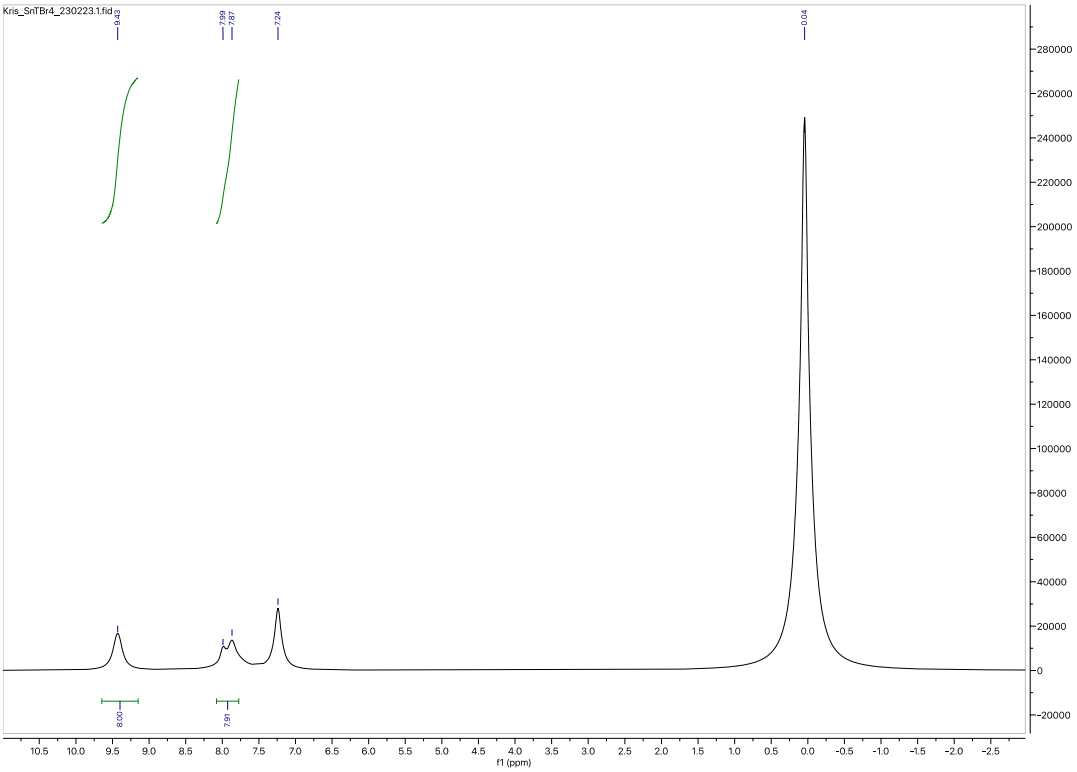

Figure 3.1.2.4. ^{1}H NMR spectrum of **Sn(IV)T_{Br}4** measured in $CDCl_3$.

T_{Br}4 and **Sn(IV)T_{Br}4** exhibited typical porphyrinoid UV-visible trends, with an intense and narrow Soret absorbance band and a relatively weak Q band envelope. It can be noted that **T_{Br}4** has a relatively blue shifted B band compared to the metalated molecules, which was expected. Additionally, **T_{Br}4** has 4 Q bands. **Sn(IV)T_{Br}4** has a red-shifted Soret band and blue-shifted Q bands, which is accounted for in **Chapter 8**. The experimental collapse of the 4 Q bands, as seen in the free base molecule (**Figure 3.1.2.5**), to 3 Q bands in the metalated molecules is apparent (**Figure 3.1.2.6**).

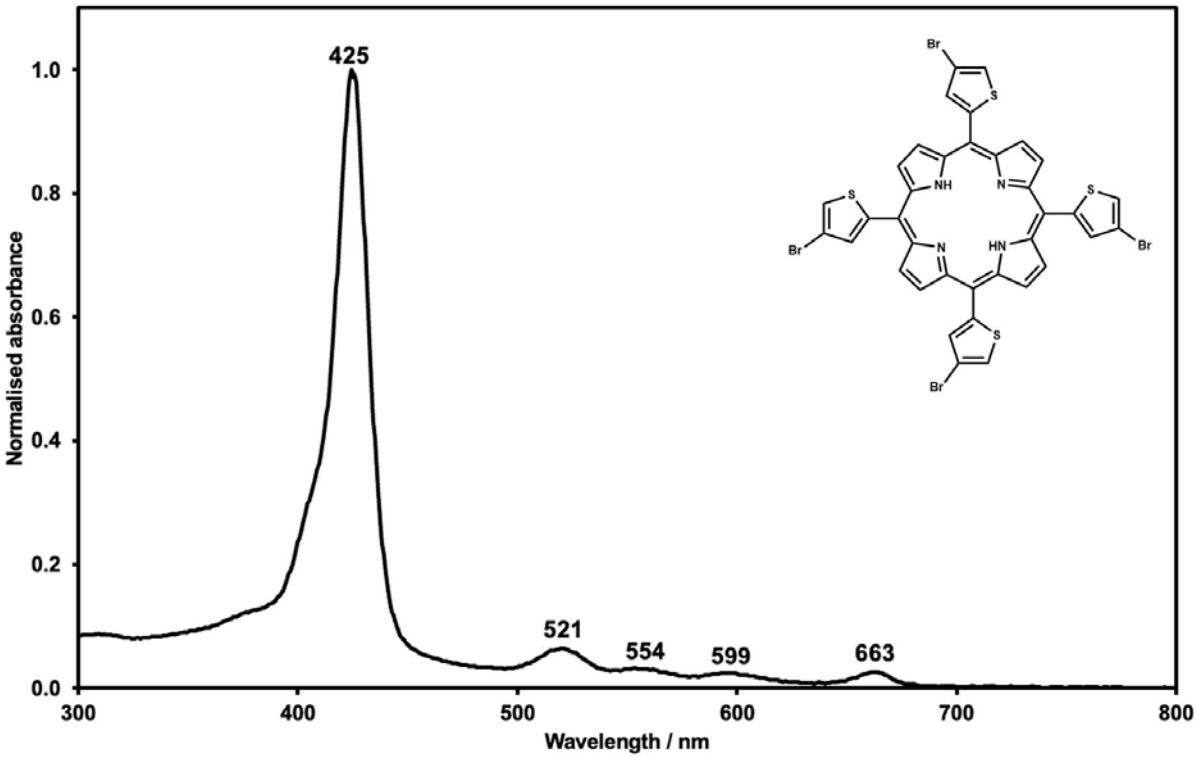

Figure 3.1.2.5. UV-visible absorption spectrum for **T_{Br}4** measured in $CHCl_3$. Soret band: 425 nm ($\log\varepsilon$ = 5.32).

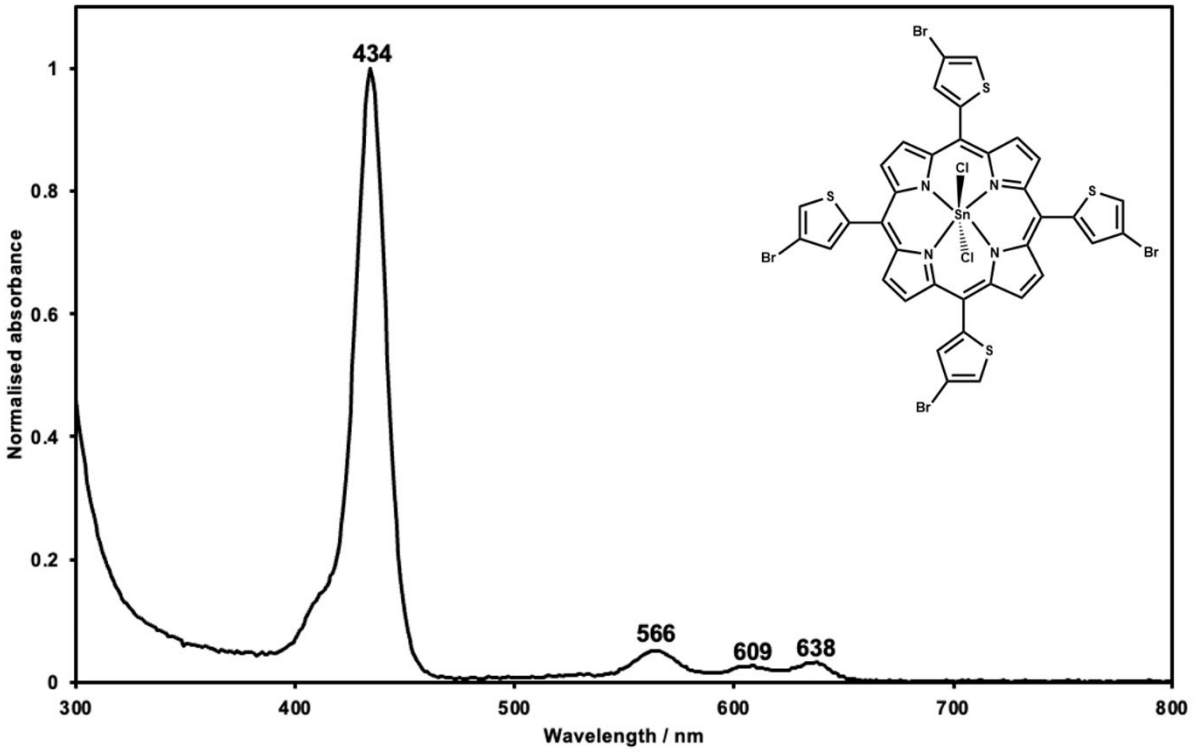

Figure 3.1.2.6. UV-visible absorption spectrum for **Sn(IV)T_{Br}4** measured in $CHCl_3$. Soret band: 434 nm ($\log\varepsilon$ = 4.68).

3.1.3 Structural characterisation of the thien-2-yl and 4-quinoline substituted low-symmetry trans-porphyrins

T2Q2, **Sn(IV)T2Q2**, and **In(III)T2Q2** were all determined to be successfully synthesised and purified based on analyses by mass spectrometry and, later, ^{1}H NMR spectroscopy. **T2Q2** was found to have a mass of 729.41 amu in MS, which is in an acceptable range to the expected mass of this molecule, which was 728.90 amu (**Figure 3.1.3.1**). Similarly, the metalated molecules, **Sn(IV)T2Q2** and **In(III)T2Q2**, were found to have their respective masses that correlated to their structures without one chloride axial ligand, which is easily cleaved off during MS (**Figure 3.1.3.2** and **Figure 3.1.3.3**). A second signal for **In(III)T2Q2** was found to lie within an acceptable range for the entire molecule with no loss of an axial ligand.

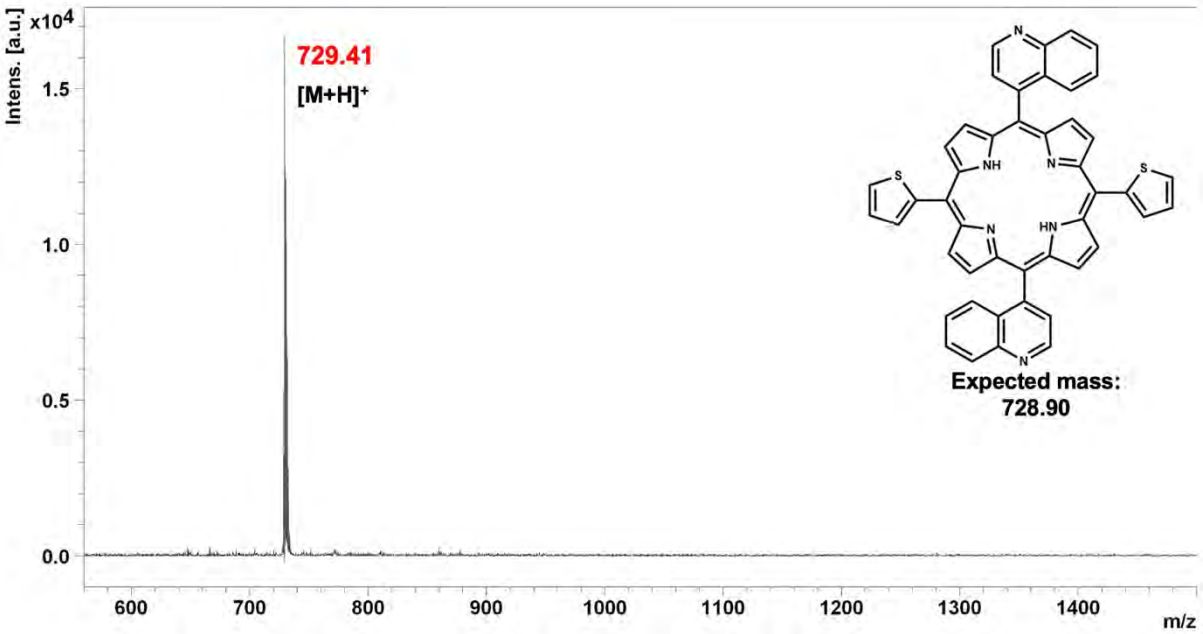

Figure 3.1.3.1. MALDI-TOF data for **T2Q2** with its mass obtained in red and its expected mass and structure alongside.

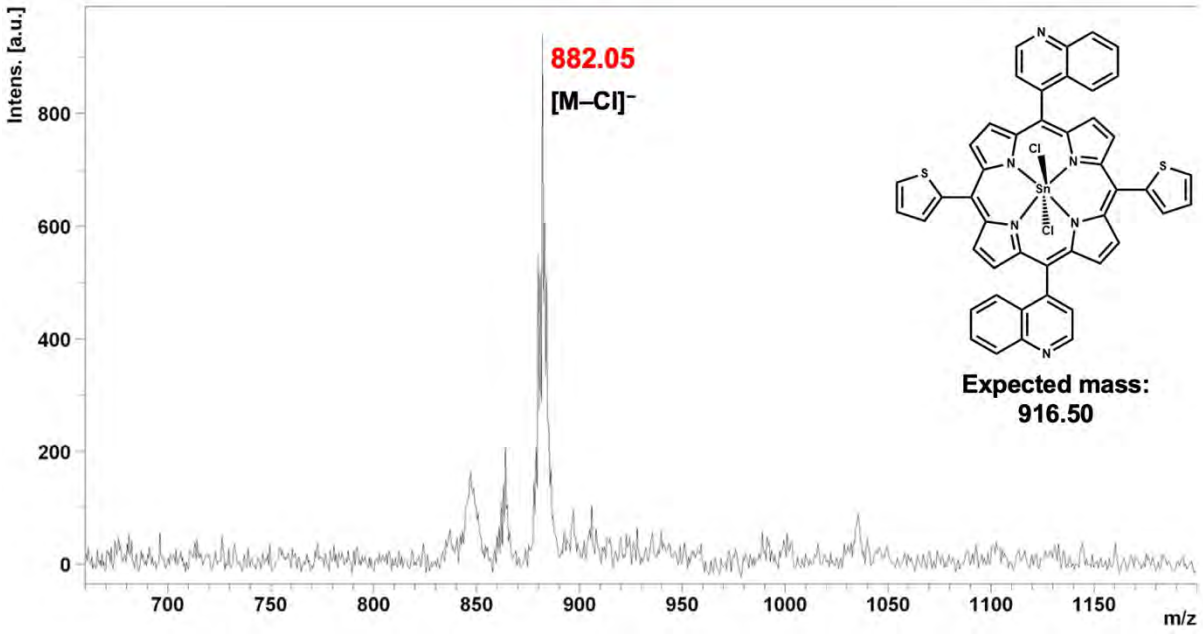

Figure 3.1.3.2. MALDI-TOF data for **Sn(IV)T2Q2** with its mass obtained in red and its expected mass and structure alongside.

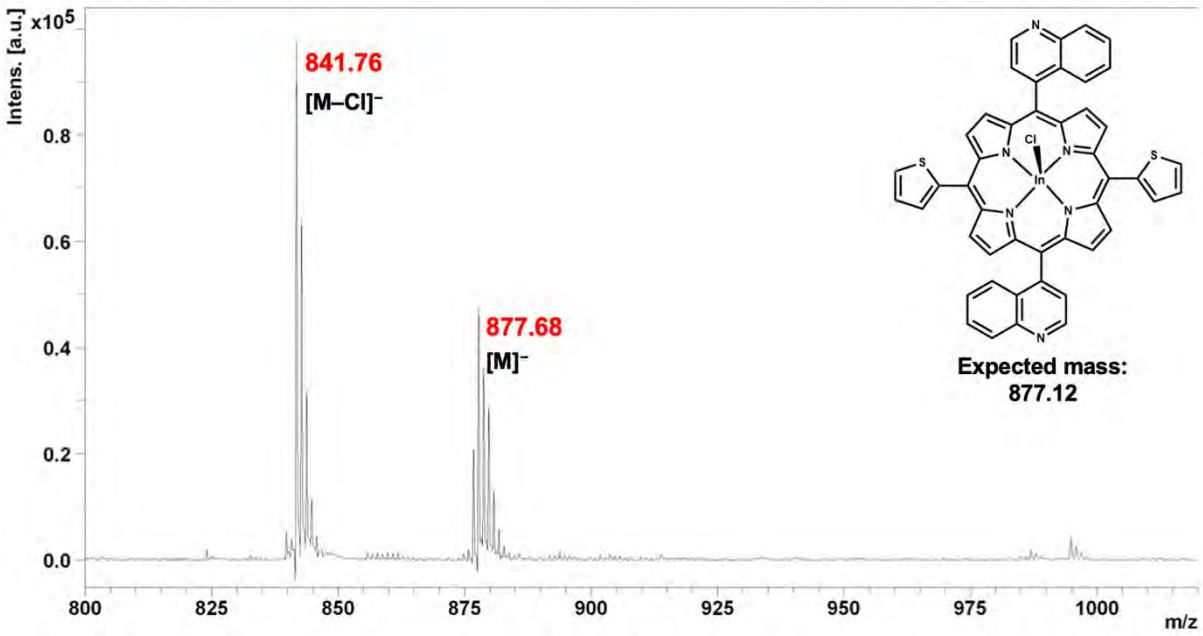

Figure 3.1.3.3. MALDI-TOF data for **In(III)T2Q2** with its masses obtained in red and its expected mass and structure alongside.

The signals for all 28 protons of **T2Q2** could be assigned in the ^{1}H NMR spectrum (**Figure 3.1.3.4**). The singlet at -2.49 ppm integrates to 2 protons, and these account for the inner protons in **T2Q2** (before metalation), which are significantly shielded from the external magnetic field by the aromatic system. The remaining signals all account for the aromatic protons, either on the thienyl rings, quinoline rings or from the pyrrole groups. Although it is

not safe or necessary to assign the peaks to specific protons within the molecule, it is likely that the multiplet from 7.57 – 8.0 ppm accounts for the quinoline protons, which are difficult to distinguish from each other. The other signals account for the thienyl and pyrrole protons.

A similar ^{1}H NMR spectrum is seen for both **Sn(IV)T2Q2** and **In(III)T2Q2** (**Figure 3.1.3.5** and **Figure 3.1.3.6**), where there is a total aromatic integration of 26 protons, which again accounts for the aromatic protons within the molecule, i.e. the thiophene and quinoline moieties, as well as the pyrrole rings. Both of these molecules lack a signal in the negative region of the spectrum due to the successful metalation event, which results in the deprotonation of the core electrons in the formation of a dianion for bonding to their respective metal ions. The aromatic region of **Sn(IV)T2Q2**, however, was challenging to integrate; there is a multiplet that integrates to 18 protons, which arise from a combination of the quinoline protons and some pyrrole protons. This NMR spectrum requires further investigation.

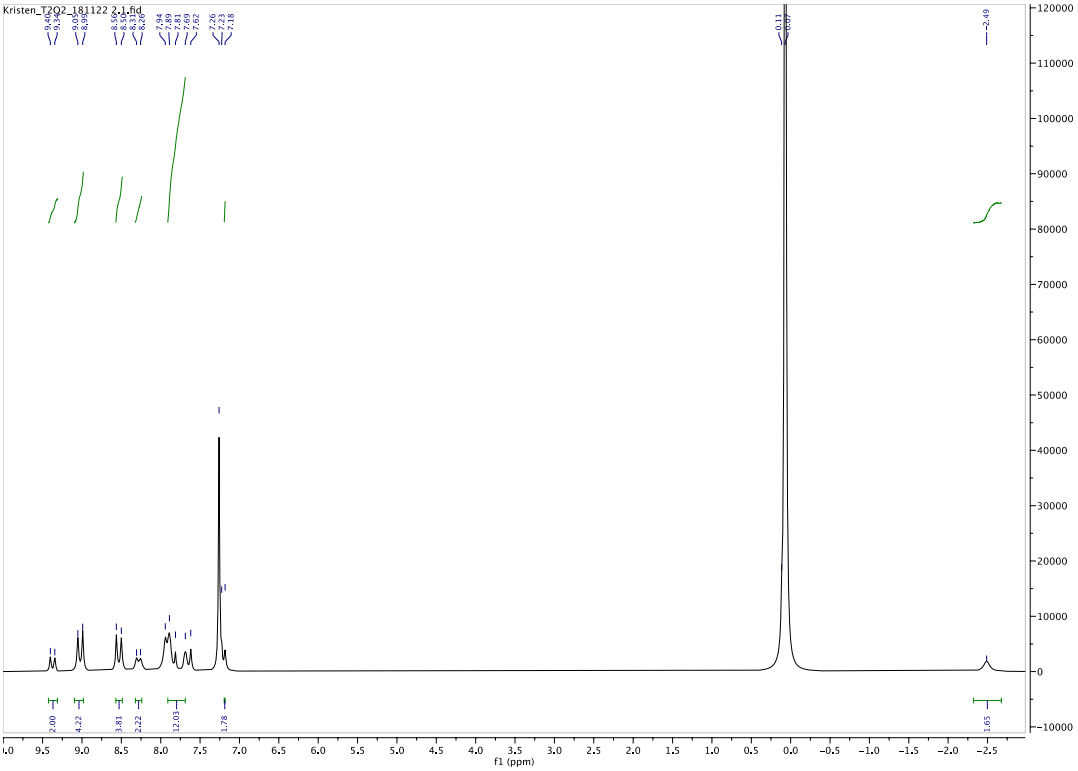

Figure 3.1.3.4. ^{1}H NMR spectrum of **T2Q2** measured in $CDCl_3$.

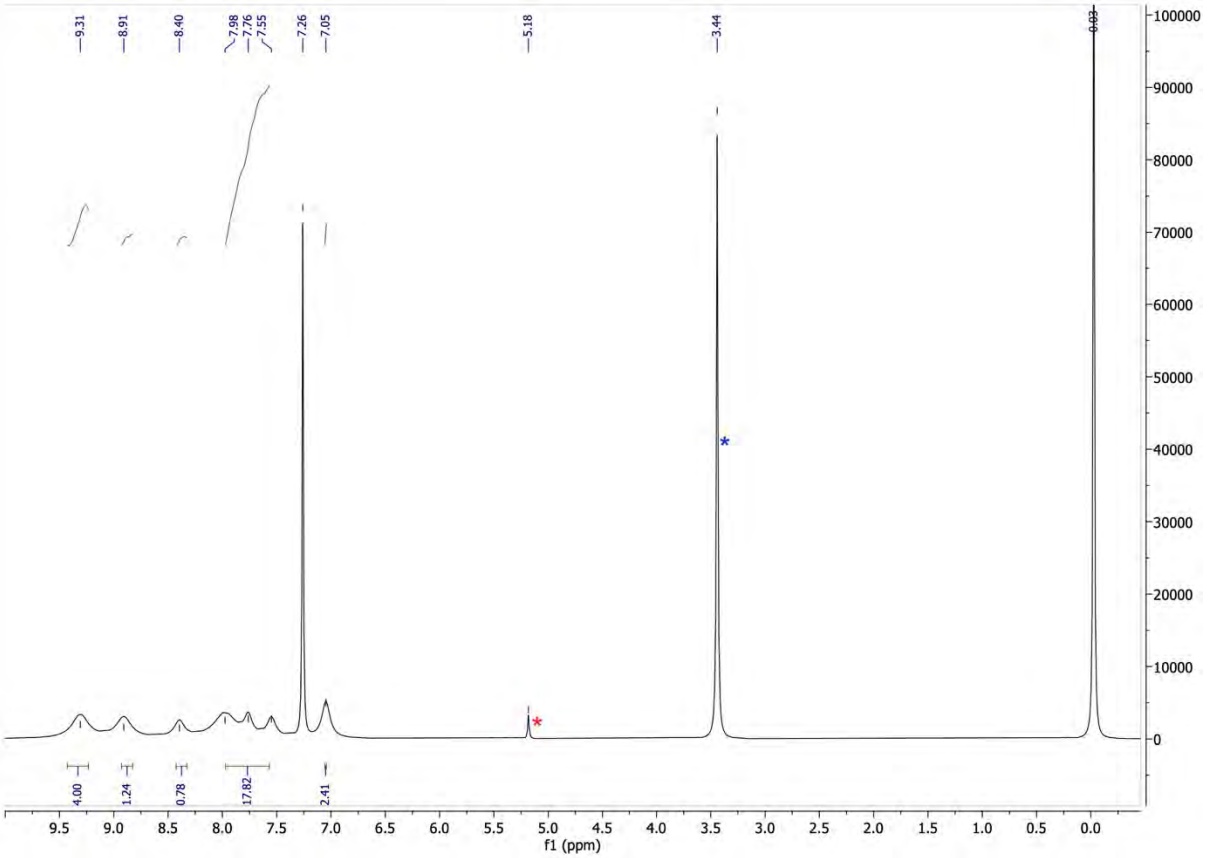

Figure 3.1.3.5. ^{1}H NMR spectrum of **Sn(IV)T2Q2** measured in $CDCl_3$.

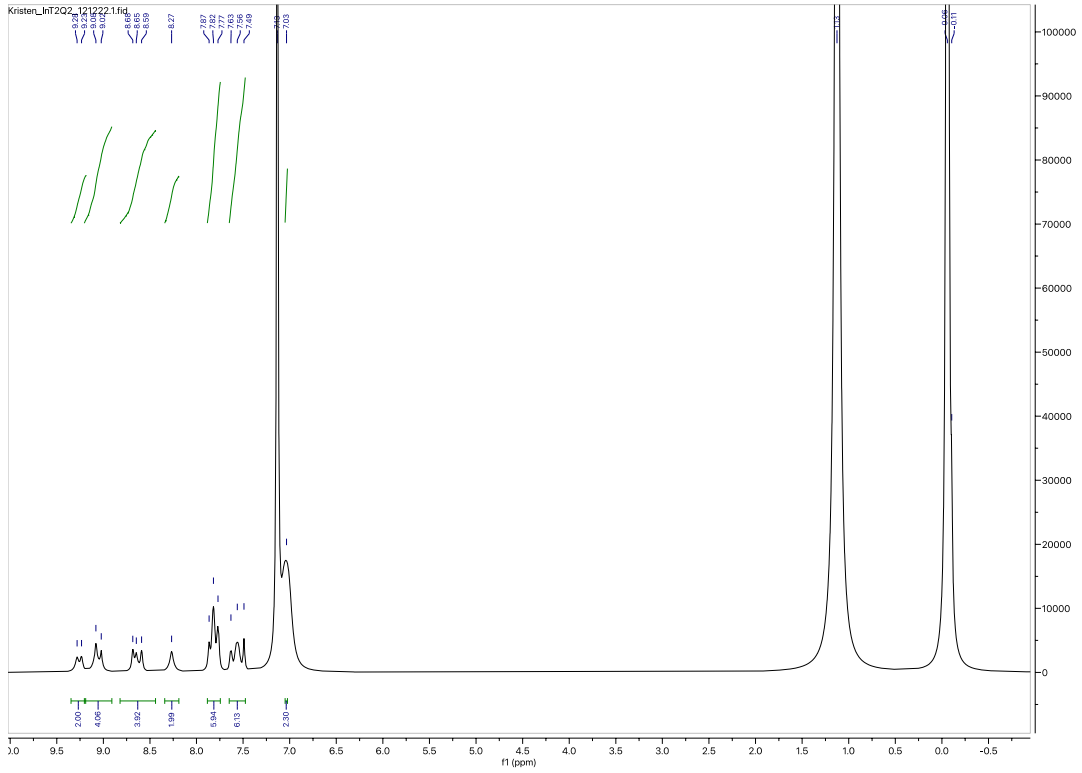

Figure 3.1.3.6. ^{1}H NMR spectrum of **In(III)T2Q2** measured in $CDCl_3$. The red asterisk denotes the residual DCM peak, while the blue asterisk denotes the residual MeOH peak.[122]

T2Q2, **Sn(IV)T2Q2**, and **In(III)T2Q2** exhibited typical porphyrinoid UV-visible trends, with an intense and narrow Soret absorbance band and a relatively weak Q band envelope. It can be noted that **T2Q2** has a relatively blue shifted B band compared to the metalated molecules, which was expected. Additionally, **T2Q2** has 4 Q bands. **Sn(IV)T2Q2** and **In(III)T2Q2** both have red-shifted Soret bands and blue-shifted Q bands, which is accounted for in **Chapter 8**. The experimental collapse of the 4 Q bands, as seen in the free base molecule (**Figure 3.1.3.7**), to 2 Q bands in the metalated molecules is apparent (**Figure 3.1.3.8** and **Figure 3.1.3.9**).

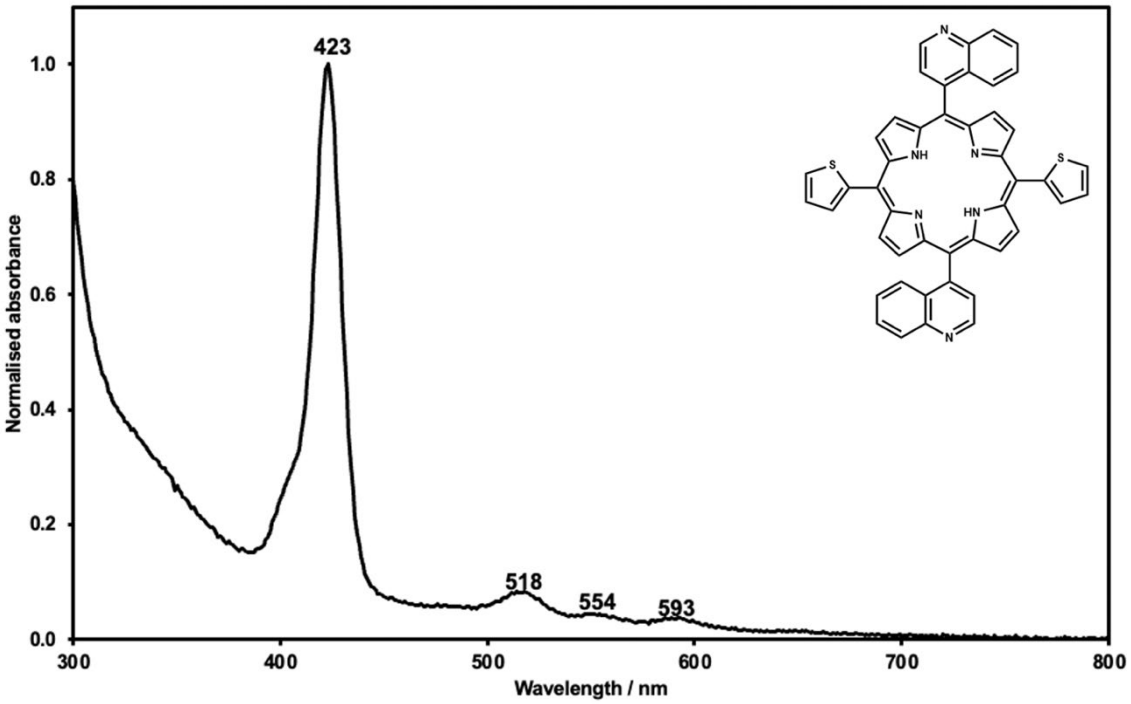

Figure 3.1.3.7. UV-visible absorption spectrum for **T2Q2** measured in $CHCl_3$. Soret band: 423 nm ($\log\varepsilon = 4.55$).

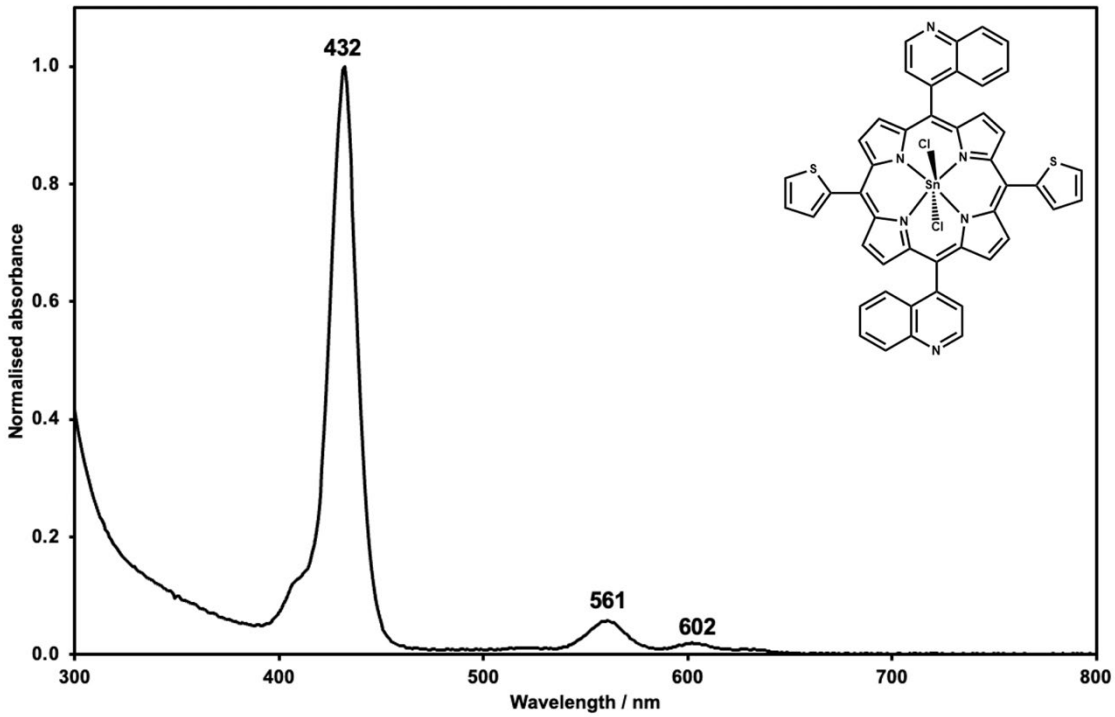

Figure 3.1.3.8. UV-visible absorption spectrum for **Sn(IV)T2Q2** measured in $CHCl_3$. Soret band: 432 nm ($\log\varepsilon = 4.53$).

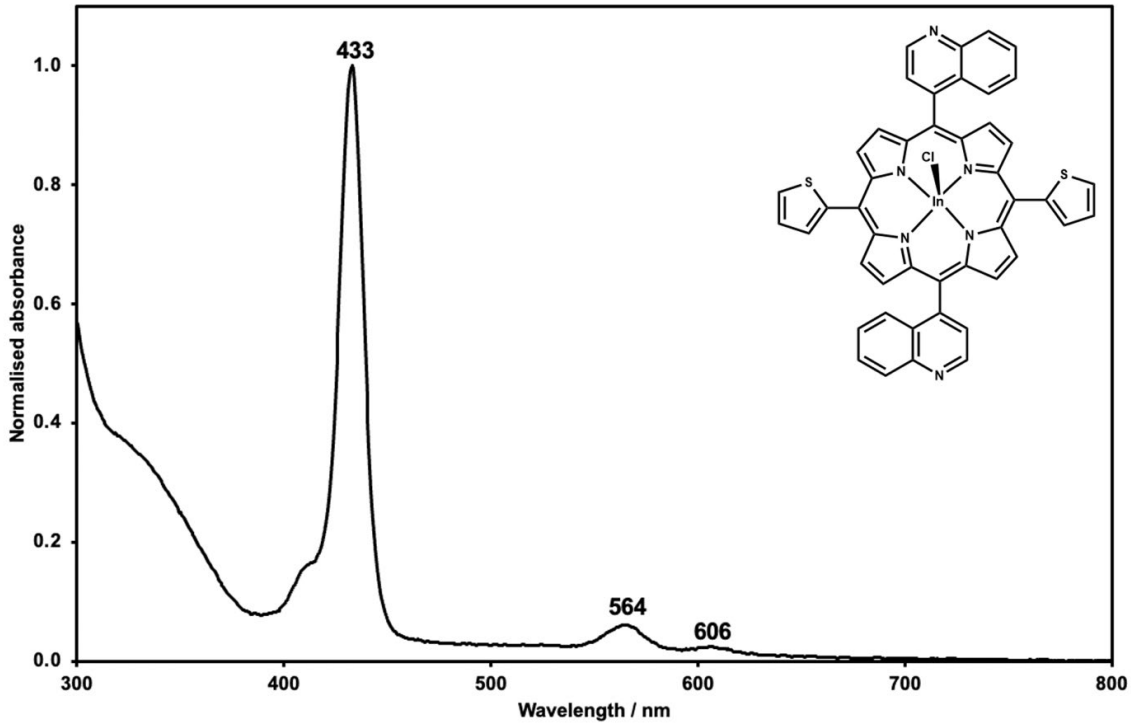

Figure 3.1.3.9. UV-visible absorption spectrum for **In(III)T2Q2** measured in $CHCl_3$. Soret band: 433 nm ($\log\varepsilon = 3.96$).

3.1.4 Structural characterisation of the 4-bromo-thien-2-yl and 4-quinoline substituted low-symmetry trans-porphyrins

T_{Br}2Q2 was determined to be successfully synthesised and purified based on analyses by mass spectrometry and, later, ^{1}H NMR spectroscopy. **T_{Br}Q2** was found to have a mass of 887.74 amu in MS, which is in an acceptable range for the expected mass of this molecule, which was 885.69 amu (**Figure 3.1.4.1**).

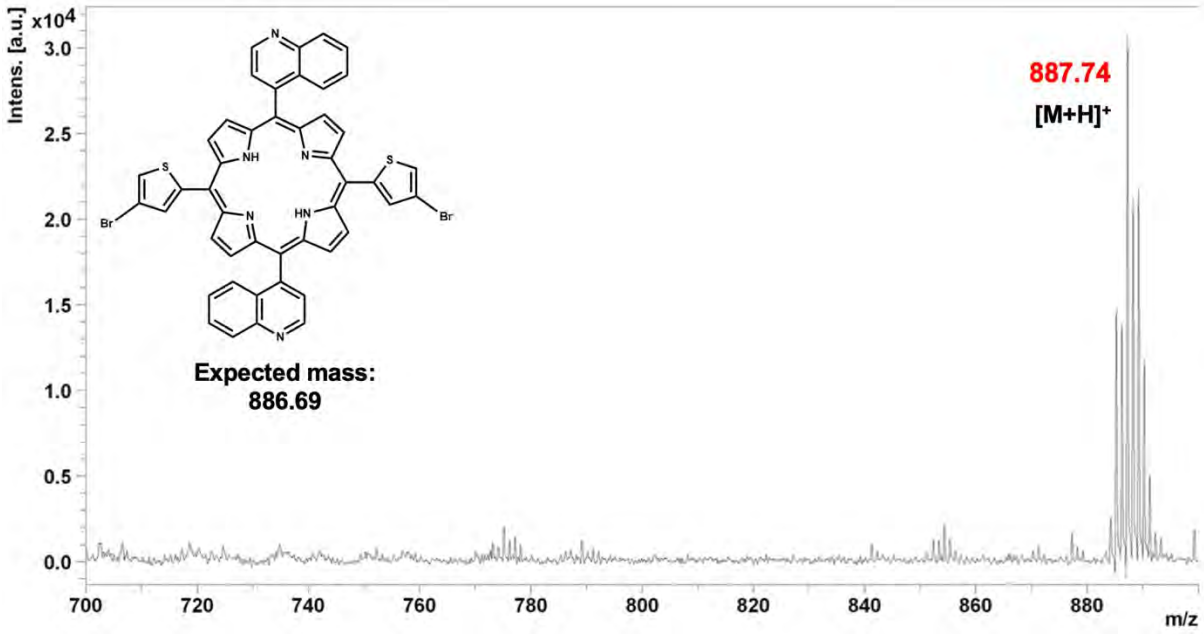

Figure 3.1.4.1. MALDI-TOF data for **T_{Br}2Q2** with its mass obtained in red and its expected mass and structure alongside.

The signals for all 26 protons of **T_{Br}2Q2** could be assigned in the ^{1}H NMR spectrum (**Figure 3.1.4.2**). The lack of a singlet at 7.17 ppm accounts for the bromines on the thienyl ring at position 4. The singlet at −2.57 ppm integrates to 2 protons, and these account for the inner protons in **T_{Br}2Q2** (before metalation), which are significantly shielded from the external magnetic field by the aromatic system. The remaining signals all account for the aromatic protons, either on the thienyl rings, quinoline rings or from the pyrrole groups. Although it is not safe or necessary to assign the peaks to specific protons within the molecule, it is likely that the multiplet from 7.46 to 7.95 ppm with an integration of 12 accounts for the quinoline protons, which are difficult to distinguish from each other. The other signals account for the thienyl and pyrrole protons.

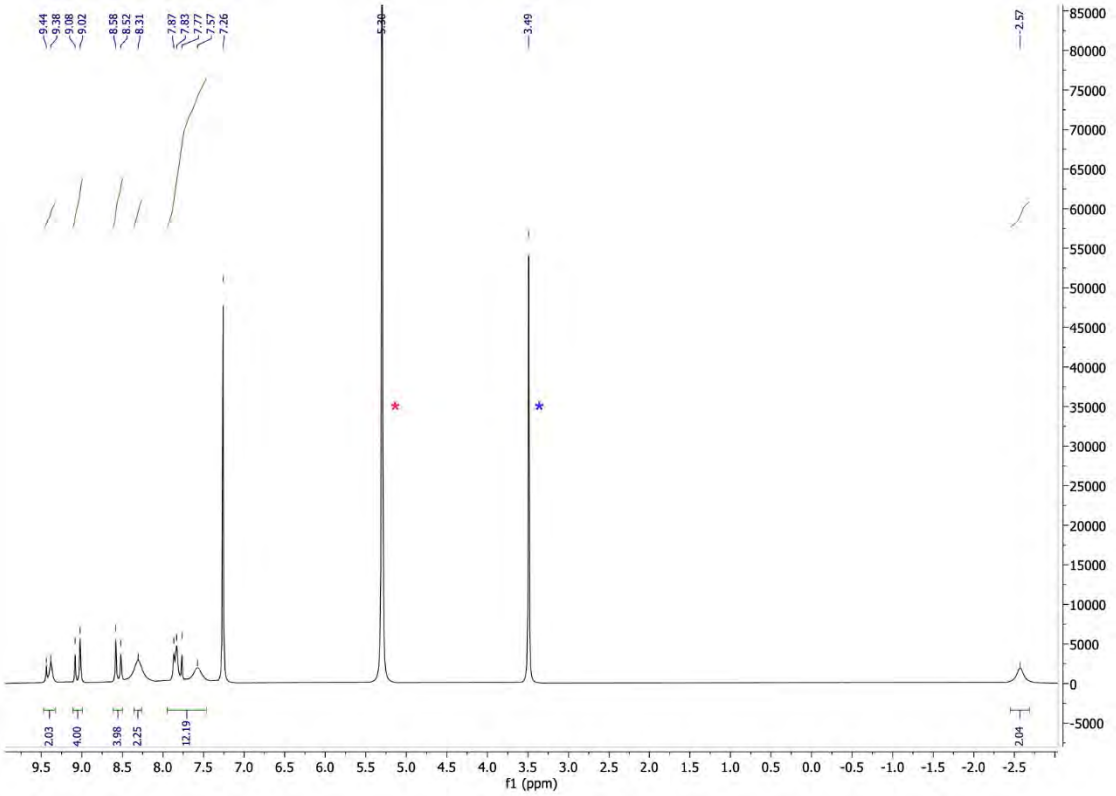

Figure 3.1.4.2. ^{1}H NMR spectrum of **T_{Br}2Q2** in $CDCl_3$. The red asterisk denotes the residual DCM peak, while the blue asterisk denotes the residual MeOH peak.[122]

Although **T_{Br}2Q2** has a typical porphyrin B band absorbance, the Q band envelope is rather abnormal: it has two, rather than four, relatively intense Q bands (**Figure 3.1.4.3**). This abnormality merits further investigation with a larger series of brominated low-symmetry porphyrins.

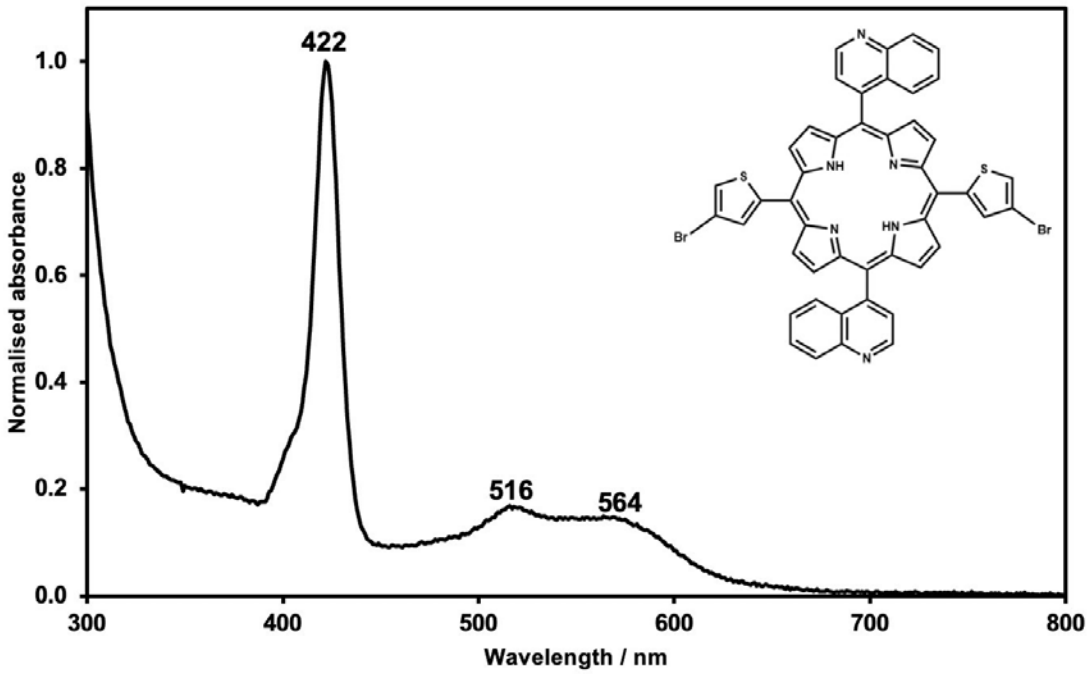

Figure 3.1.4.3. UV-visible absorption spectrum of **T_{Br}2Q2** measured in $CHCl_3$. Soret band: 422 nm (logε = 4.07).

3.2. Structural characterisation of the corroles

T3 and **T_{Br}3** were determined to be successfully synthesised and purified based on analyses by mass spectrometry and, later, ^{1}H NMR spectroscopy. **T3** was found to have a mass of 544.05 amu in MS, which is in an acceptable range for the expected mass of this molecule, which was 544.72 amu (**Figure 3.2.1**). **T_{Br}3** was found to have a mass of 782.49 amu in MS, which is in an acceptable range for the expected mass of this molecule, which was 781.41 amu (**Figure 3.2.2**).

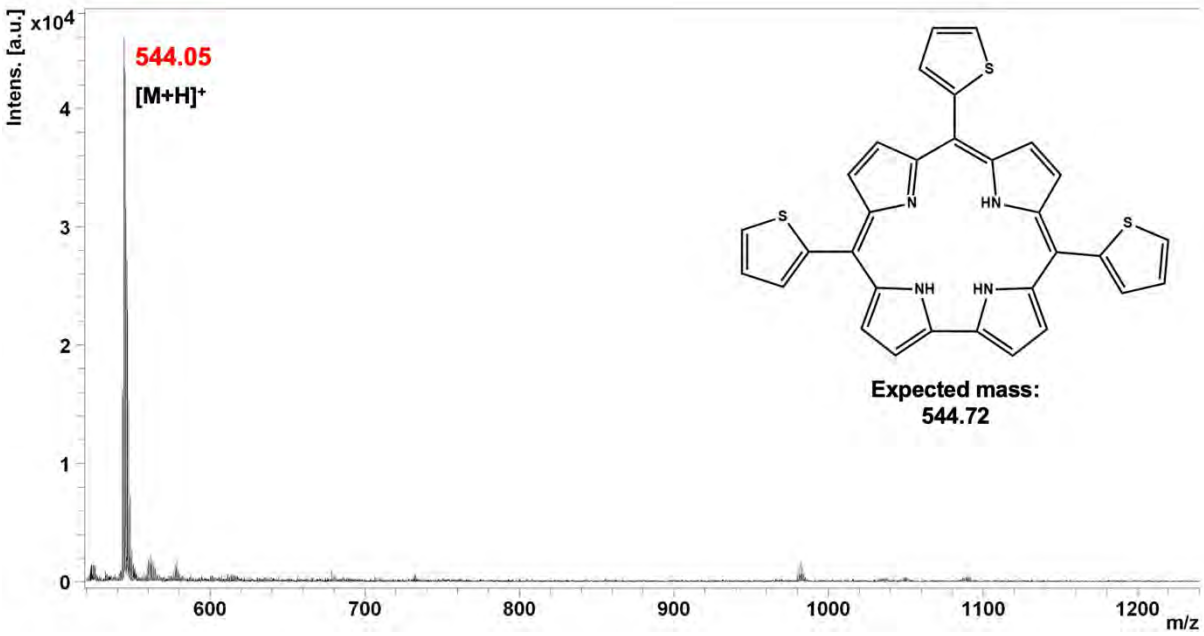

Figure 3.2.1. MALDI-TOF data for **T3** with its obtained mass in red and the expected mass and structure alongside.

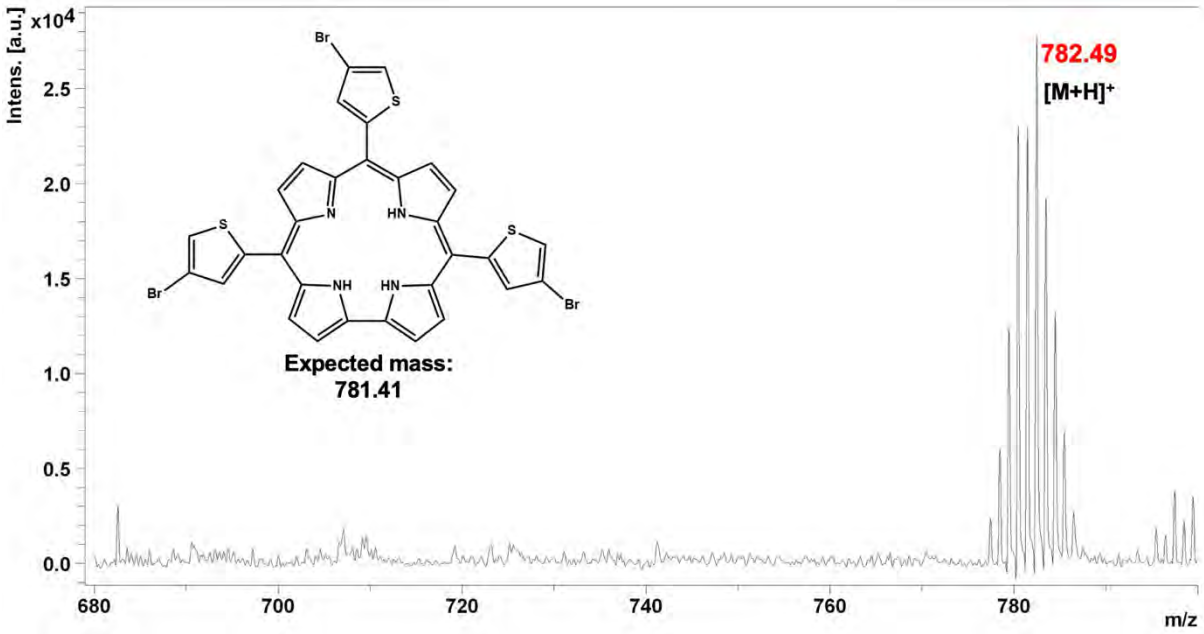

Figure 3.2.2. MALDI-TOF data for **T_{Br}3** with its obtained mass in red and the expected mass and structure alongside.

The ^{1}H NMR spectra of the corroles were consistent with Gryko *et al.*'s results:[114] the eight pyrrole protons are observed at higher frequencies, and the thiophene protons lie further downfield in the context of both **T3** and **T_{Br}3** (**Figure 3.2.3** and **Figure 3.2.4**). The additional multiplet seen from 7.53 – 7.60 ppm in **T3**, is due to the lack of a bromine atom (and the presence of a proton) at position 4 of each of the thiophene moieties.

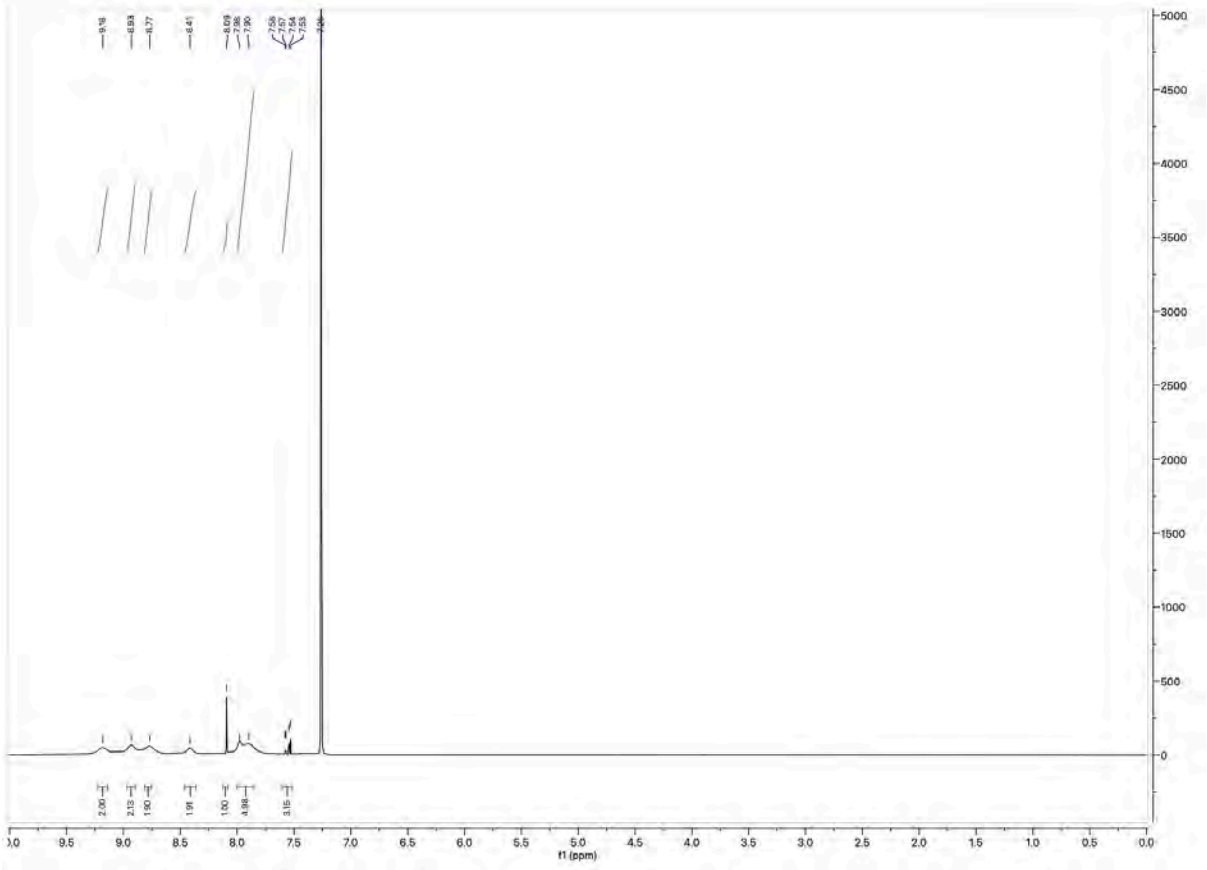

Figure 3.2.3. ^{1}H NMR spectrum of **T3** measured in $CDCl_3$.

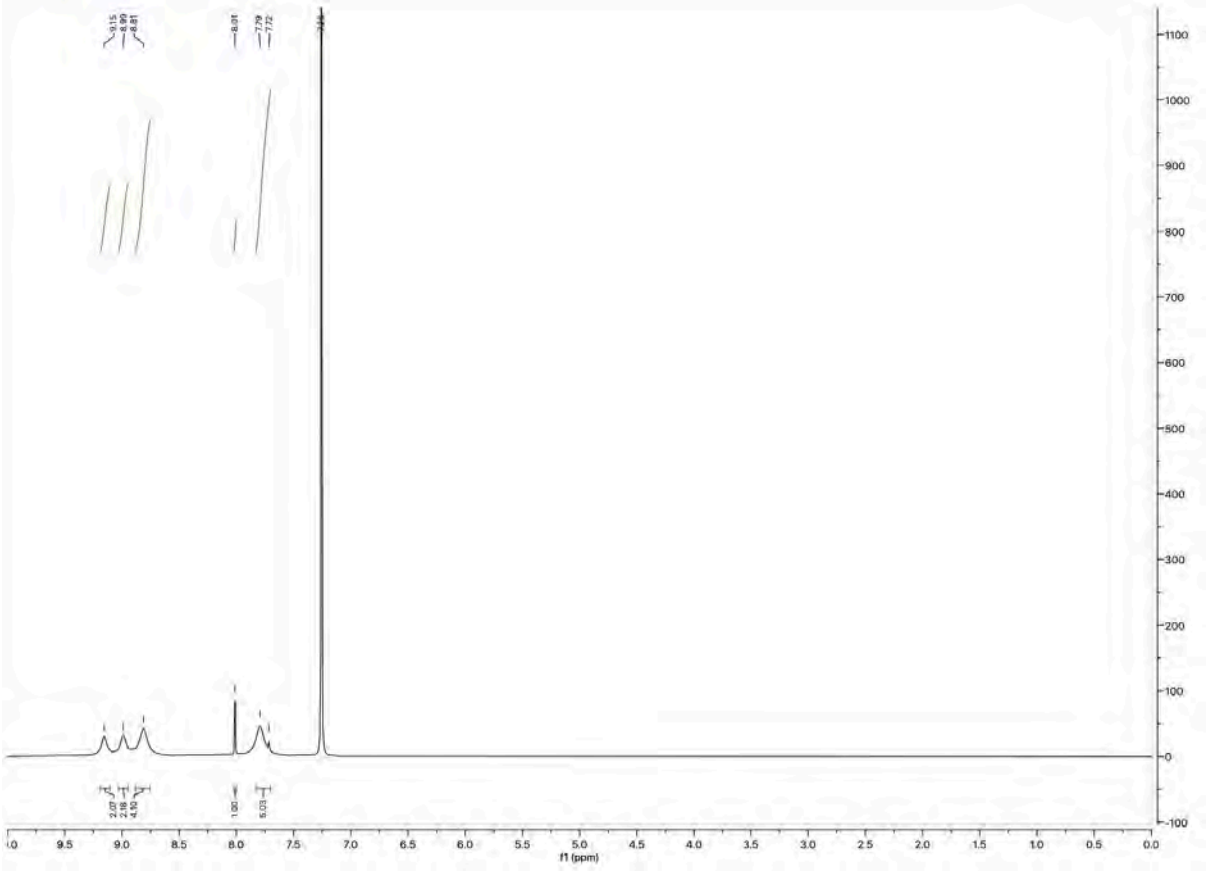

Figure 3.2.4. ^{1}H NMR spectrum of **T_{Br}3** measured in $CDCl_3$.

The UV visible spectra of the corroles were consistent with what has been reported in the literature: a wider B band than the porphyrins and three relatively intense Q bands, with **T_{Br}3** having slightly more red-shifted Q bands (**Figure 3.2.5** and **Figure 3.2.6**).

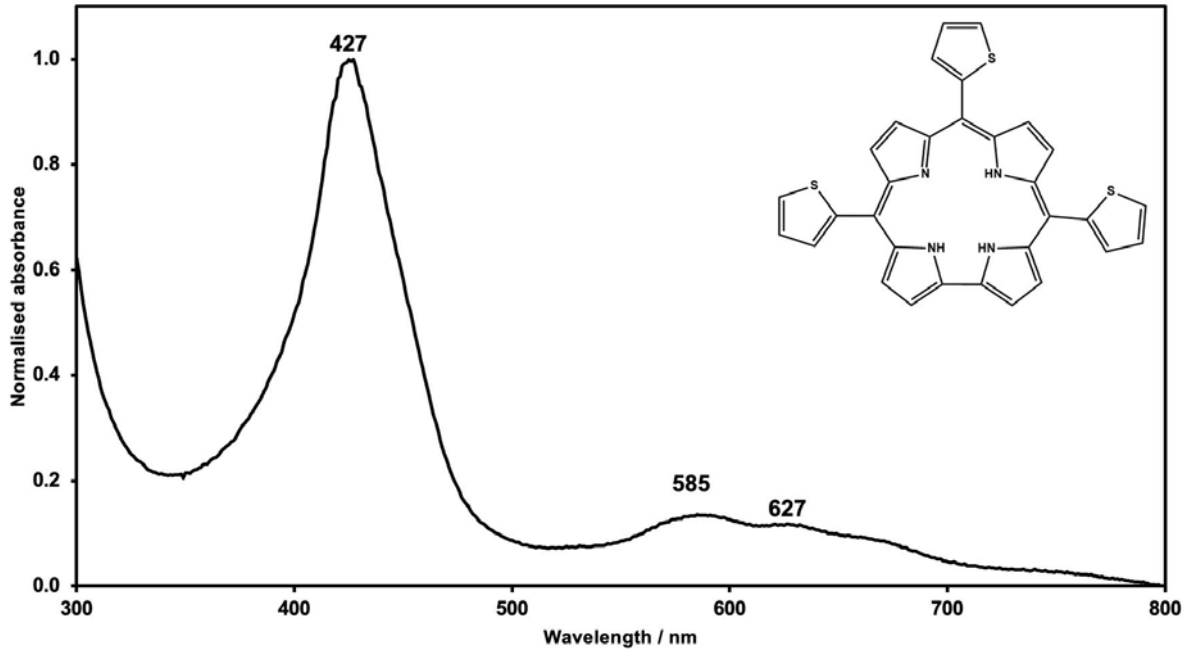

Figure 3.2.5. UV-visible absorption spectrum of **T3** measured in $CHCl_3$. Soret band: 427 nm ($\log\varepsilon$ = 4.00).

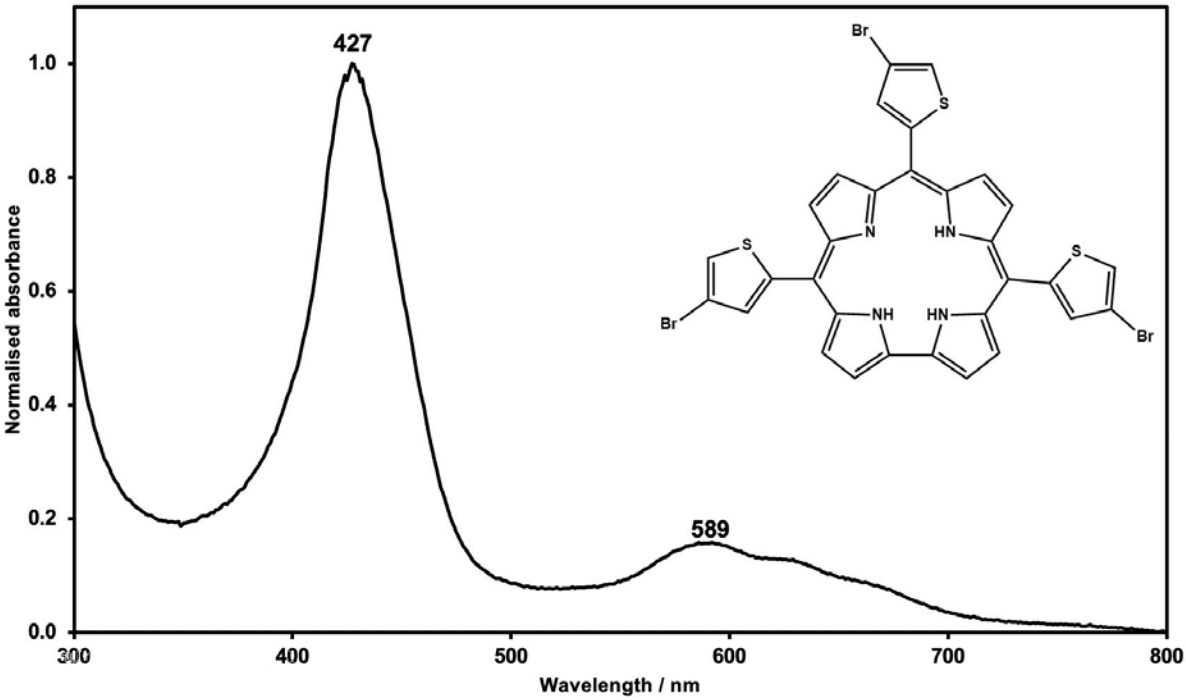

Figure 3.2.6. UV-visible absorption spectrum of **T_{Br}3** measured in $CHCl_3$. Soret band: 427 nm ($\log\varepsilon$ = 4.47).

3.3. Structural characterisation of the quaternised low-symmetry porphyrin

The quaternised molecule was characterised in the same manner that the other photosensitisers were. The MS of **Sn(IV)T2Q2^{+}** yielded a mass of 235.88 amu, which can be accounted for by the loss of an axial chloride ion from the entire complex (with an expected mass of 976.64), which leads to a mass of 941.19 amu and a subsequent division by the charge of 4 due to the quaternisation gives rise to an expected mass of 235.30 amu (**Figure 3.3.1**). This lies within ±1 amu for the experimentally determined mass/charge ratio.

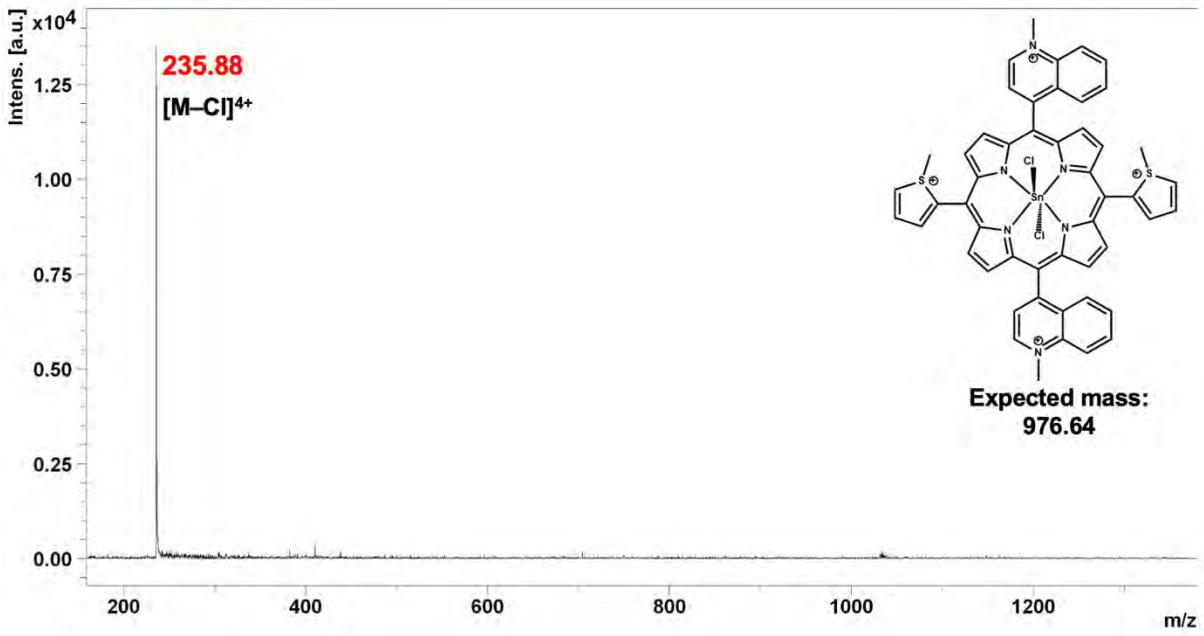

Figure 3.3.1. MALDI-TOF data for **SnT2Q2^{+}** with its obtained mass in red and the expected mass and structure alongside.

The ^{1}H NMR of the quaternised compound proved difficult to measure, particularly the aromatic region. There is a new signal at 3.53 ppm that is not observed in the unquaternised molecule (**Figure 3.1.3.5**), which can tentatively be assigned to the methyl protons (**Figure 3.3.2**). Integration of this peak was not possible due to the absence of aromatic peaks needed for a ratio in the normalisation and characterisation of the number of protons accounted for by each signal. The aromatic region was not intense enough to integrate and/or visualise.

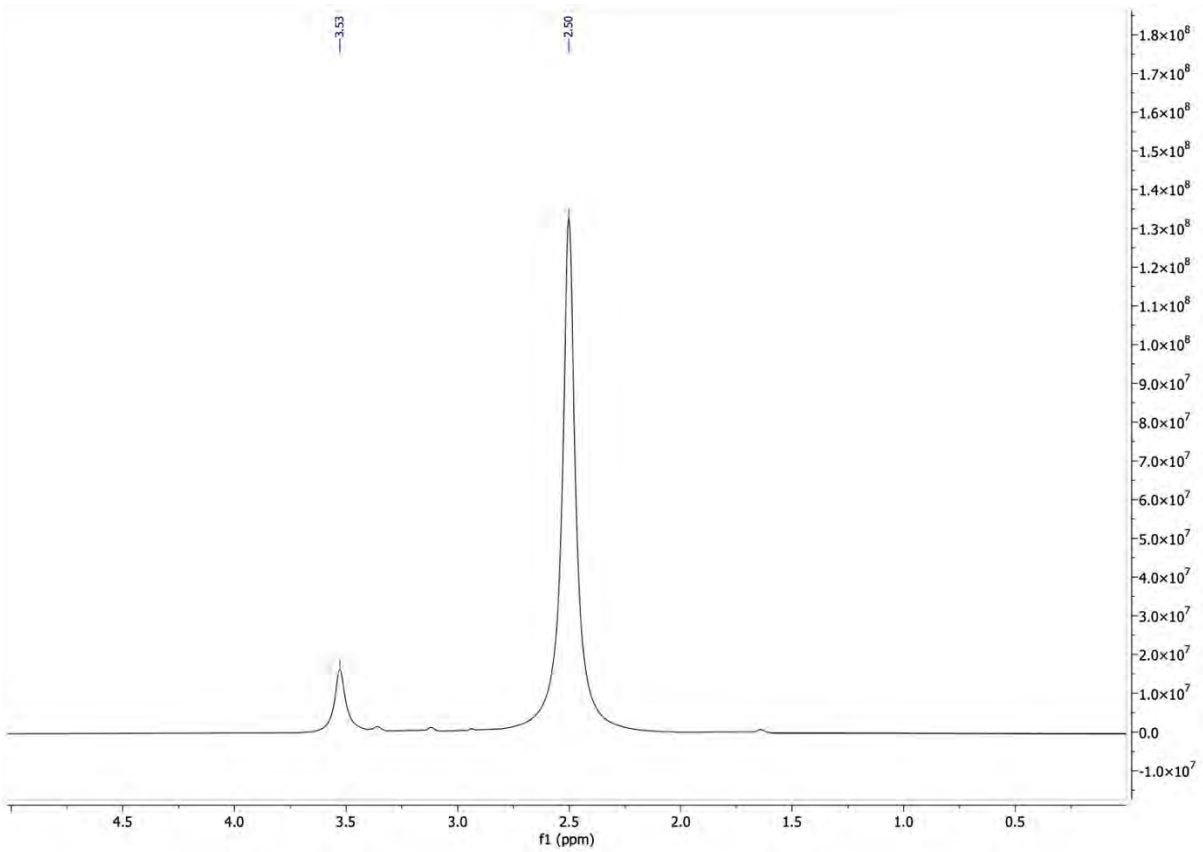

Figure 3.3.2. ^{1}H NMR spectrum of **SnT2Q2^{+}** measured in d_6-DMSO.

The UV visible absorption spectrum of the quaternised molecule, **Sn(IV)T2Q2^{+}**, was measured in DMF immediately after the synthesis (**Figure 3.3.3**). There is an apparent red-shifting of the Soret and Q band envelope of the cationic molecule, as opposed to its unquaternised counterpart, but the optical properties of the porphyrin are still maintained. This will be elaborated on further in **Chapter 8**.

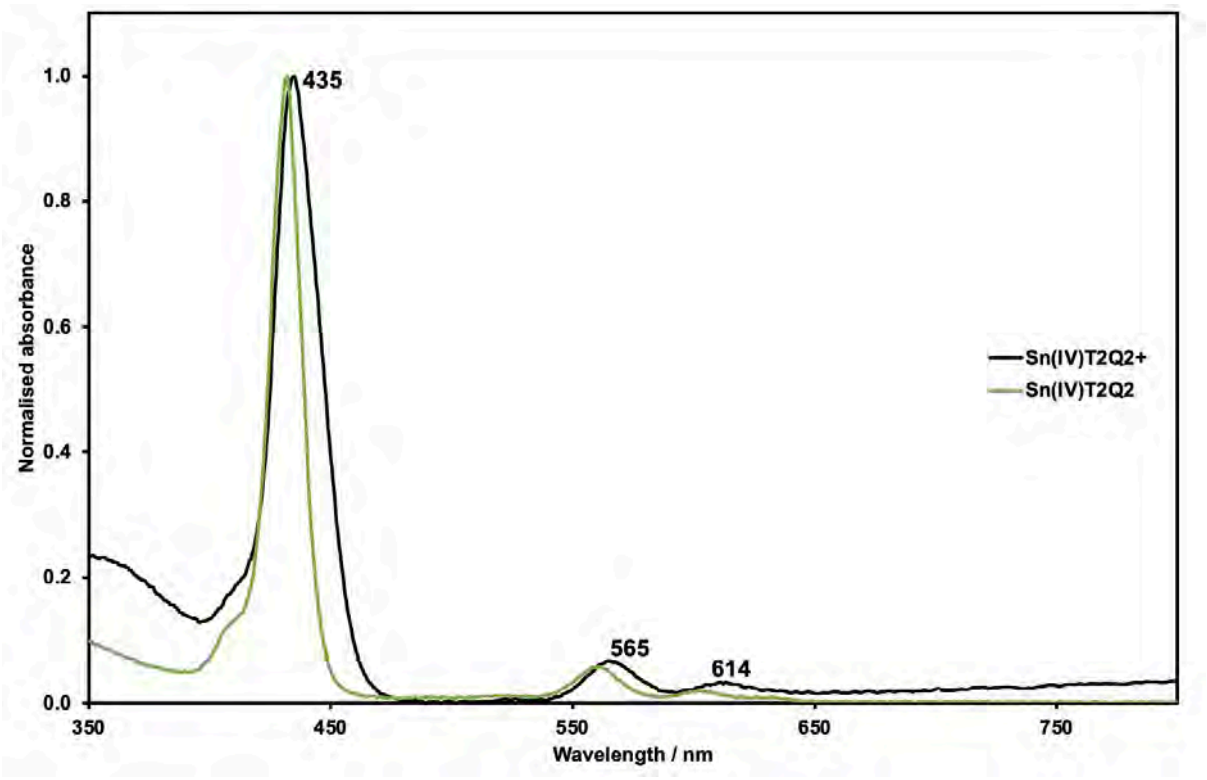

Figure 3.3.3. UV-visible absorption spectrum of **SnT2Q2**$^{+}$ measured in DMF compared to the unquaternised molecule, **Sn(IV)T2Q2**. Soret band: 435 nm (logε = 3.32).

3.4. Photophysical and -chemical properties of the porphyrinoids

This subsection details a comprehensive analysis of the photophysical properties of the photosensitisers, including singlet oxygen quantum yields (ϕ_Δ), fluorescent quantum yields (ϕ_F), triplet lifetimes, photostability and molar extinction coefficients.

In this thesis, the $\phi_\Delta$values were determined in DMSO with a comparative method: DMA (a singlet oxygen scavenger) was used to spectroscopically determine the $\phi_\Delta$of an unknown compound relative to a standard, which was ZnTPP in DMSO, in this case (ZnTPP in DMSO; ϕ_Δ = 0.55).[123]

Porphyrinoid compounds, such as porphyrins, themselves, and corroles, are slightly fluorescent. The ϕ_F values were determined in DMSO due to their complete solubility within this solvent and lack of solubility in water. The fluorescence quantum yields of the free base

and metalated molecules were quantified using a comparative method with ZnTPP as the reference molecule (ϕ_F = 0.039 in DMSO).[123]

The triplet lifetimes of the photosensitisers give insight into how long-lived the triplet manifolds of the photosensitisers are. This is an important parameter as this electronic state reacts with molecular oxygen in the surrounding biological environment to produce reactive oxygen species and/or singlet oxygen, which are the therapeutic agents in the context of PDT and PACT (see **Figures 1.8.2** and **1.9.1**).

Photosensitiser drugs are prone to degradation by the singlet oxygen formed upon the photoexcitation event. It is, thus, important to assess the degree of photodegradation that occurs under the conditions used in PDT and PACT activity experiments.

The above photophysical and -chemical properties are summarised in **Table 3.4.1.**

Table 3.4.1. A summary of the photophysicochemical properties (singlet oxygen quantum yields, fluorescence quantum yields, triplet lifetimes and photostability) of the photosensitisers within this investigation. The molecules that were not synthetically achievable within this thesis are denoted with N/A, as their photophysicochemical properties could not be quantified.

	Compound	Φ_{Δ}	Φ_F	**T_T (μs)**	**Photostability (%)**
Free base compounds	**T4**	0.55	0.03	28	90
	T_{Br}4	0.59	0.02	14	92
	T2Q2	0.61	0.02	56	91
	T_{Br}2Q2	0.67	0.01	48	94
	T3	0.14	0.02	12	86
	T_{Br}3	0.09	0.02	10	92
	T2Q	--	--	--	--
	T_{Br}2Q	--	--	--	--
Sn(IV) complexes	**Sn(IV)T4**	0.52	0.02	130	94
	Sn(IV)T_{Br}4	0.58	0.01	110	98
	Sn(IV)T2Q2	0.85	<0.01	170	87
	Sn(IV)T2Q2$^+$	0.68	0.03	40	96
	Sn(IV)T_{Br}2Q2	--	--	--	--
	Sn(IV)T3	--	--	--	--
	Sn(IV)T_{Br}3	--	--	--	--
	Sn(IV)T2Q	--	--	--	--
	Sn(IV)T_{Br}2Q	--	--	--	--
In(III) complexes	**In(III)T4**	0.82	0.01	83	87
	In(III)T_{Br}4	--	--	--	--
	In(III)T2Q2	0.72	0.02	100	84

In the context of the porphyrin photosensitisers, incorporating of heavy atoms into the molecules, such as bromine, tin or indium, generally increases the singlet oxygen quantum yields and decreases the fluorescence quantum yields, as expected. This is due to the heavy atom effect and the increased rate of ISC to populate the triplet manifold of the photosensitiser. The free bases exhibited lower singlet oxygen quantum yields than their metalated counterparts, and the brominated compounds generally exhibited higher singlet oxygen quantum yields than their non-brominated counterparts. The Sn(IV) complexes of the thienyl- and 4-bromo-thienyl-substituted exhibited slightly lower singlet oxygen quantum yields than their free base counterparts, which could possibly be attributed to increased rates of phosphorescence with the heavy atoms.

An exception was noted for the corroles: **T3** had a higher singlet oxygen quantum yield than its brominated counterpart, $\mathbf{T_{Br}3}$, and these photosensitisers had the same fluorescence quantum yields. It has been noted that the presence of heavy atoms can increase the rate of phosphorescence, which may account for the decreased singlet oxygen quantum yields observed in the brominated corrole.[124] Additionally, the brominated corrole, $\mathbf{T_{Br}3}$, has a shorter-lived triplet state than **T3**. This merits further investigation and needs to be compared across a larger range of non-brominated and brominated corroles.

The low-symmetry porphyrins had improved singlet oxygen quantum yields than their high-symmetry counterparts, and asymmetry was explored within this thesis specifically to exploit these favourable photophysical properties for their therapeutic efficacy in PDT and PACT.[125]

For the low-symmetry porphyrin, **In(IV)T4** exhibited a higher singlet oxygen quantum yield than **Sn(IV)T4**, but in the low-symmetry porphyrin, the Sn(IV) complex had the higher singlet oxygen quantum yield. Again, this merits further investigation across a larger series of high- and low-symmetry porphyrins.

Sn(IV)T2Q2 had the highest singlet oxygen quantum yield, the lowest fluorescence quantum yield, the longest-lived triplet state and a reasonable photostability and, due to these favourable photophysicochemical properties, was quaternised for application in PDT and PACT.

The triplet lifetimes followed the same trends as the singlet oxygen quantum yields, which was expected. The photosensitisers had reasonable photostabilities, with **Sn(IV)T_{Br}4** exhibiting the highest photostability.

3.5 Summary of chapter

The synthesis of the free base porphyrin, as well as three Sn(IV) complexes and two In(III) complexes were synthesised sucessfully. Additionally, two free base corrole molecules were synthesised. Characterisations were successfully carried out by analysing their UV-visible absorption and ^{1}H NMR spectra and MALDI-TOF MS data. The porphyrins became the primary interest due to the significant challenges experienced with the corrole syntheses, which should be further optimised.

Additionally, the photophysical and -chemical properties of the porphyrins and corroles were quantified in this chapter. The porphyrins exhibited superior properties to the corrole dyes from the standpoint of PDT and PACT applications, and in addition to the challenging synthesis and purification of the corroles, only the porphyrins were advanced to the biological applications.

CHAPTER FOUR

PHOTODYNAMIC ANTIMICROBIAL CHEMOTHERAPY

4.1. PACT studies against *Staphylococcus aureus* and *Escherichia coli*

There is potential to use this therapy against bacterial infections that affect the skin and soft tissue layers, and such an application would employ a wavelength of light within the deep-red region of the spectrum to exploit the phototherapeutic window and avoid the development of adverse side effects. This investigation assessed the potential of the photosensitisers as a soft tissue infection treatment, as well as a water purification agent.[126,127] Water-bourne diseases caused by microbes pose both an environmental and health hazard, specifically *Escherichia col*.[126] Although there are other means to treat wastewater, such as disinfection with chlorine, ozone or ultraviolet light, this has been known to lead to the formation of toxic by-products, which leads to other health hazards.[127] PACT, therefore, has proven to be an effective alternative to treat wastewater and disinfect it, as well as to treat microbial infections that affect the skin.

The compounds that were assessed in this study were: **Sn(IV)T4**, **In(III)T4**, **Sn(IV)T_{Br}4**, **Sn(IV)T2Q2**, **In(III)T2Q2** and later in the study, **Sn(IV)T2Q2^{+}**, the quaternised compound.

Concentration optimisation studies of the photosensitisers against *Staphylococcus aureus* were initially conducted with a 60 min irradiation time interval after 30 min of localisation and the irradiation was achieved with a 565 nm LED, as depicted by **Figure 4.1.1.**

The compounds that were initially employed in this investigation all exhibited relatively low activities against the bacterial colonies, so the optimal concentrations employed in the time studies shown later in the chapter was 40 μM for both *Staphylococcus aureus* and *Escherichia coli*.

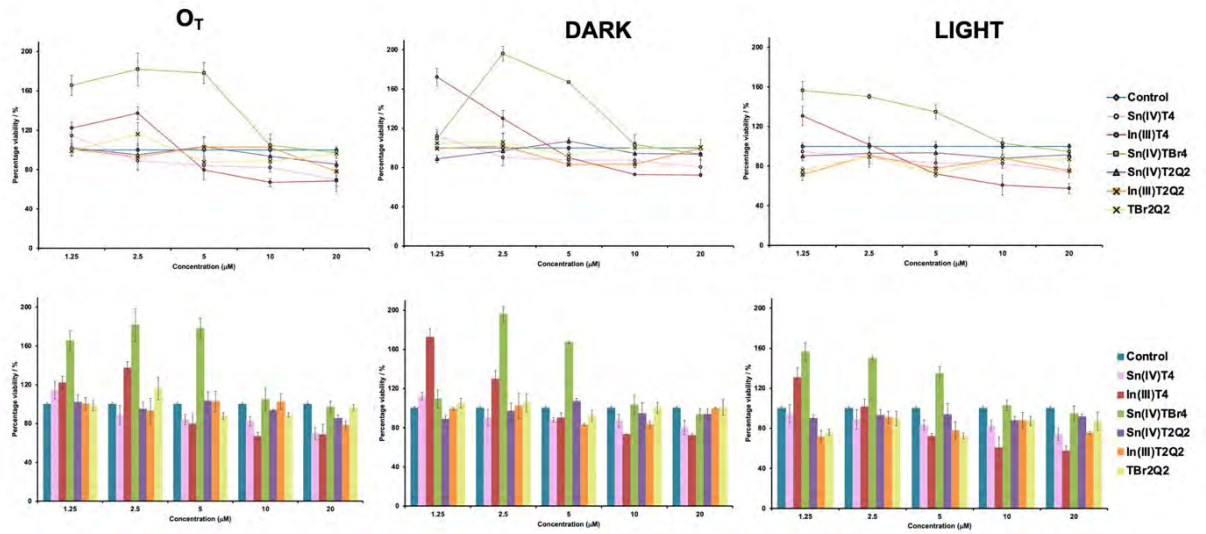

Figure 4.1.1. The initial concentration optimisation investigation against *Staphylococcus aureus* using 1.25, 2.5, 5, 10 and 20 μM as the drug concentrations. The experiment is represented as the percentage viability of the bacteria versus the concentration of the drug. O_T was inoculated immediately after 30 min of incubation of the bacteria with the drug, the dark experiment after 1 h of no exposure to light, and the light experiment after 1 h of irradiation with a 565 nm Thorlabs M565L3 LED (270 mW/cm^2).

It is evident from the results represented in **Figure 4.1.1.** that the compounds did not display a high level of photoactivity. The increasing concentrations did prove effective in reducing the bacterial survival rate, particularly in the case of **In(III)T4**, which is also the only compound that showed any difference between the light experiment and the O_T and dark experiments and was able to reduce approximately 45% of the bacterial growth at the highest concentration in the light experiment. **Sn(IV)T4** and **In(III)T2Q2** were able to reduce approximately 25% of bacterial growth after irradiation with the 565 nm Thorlabs M565L3 LED (270mW/cm^2) at a concentration of 20 μM.

It is also evident that some excess bacterial growth was observed in the presence of the photosensitiser, particularly in the case of **Sn(IV)T$_{Br}$4**, which had close to 200% of the bacterial colonies present compared to the control. This may be because the bromine present within this compound aids in bacterial growth. This could, however, be attributed to anomalous results.

Overall, the compounds exhibited relatively low activities against *Staphylococcus aureus.* Another investigation was conducted whereby a working concentration of 20 μM was employed, and the activities were reassessed with an LED closer to the therapeutic window: Thorlabs M595L3 LED (240 mW/cm^2). This was done to enhance the PACT activity and to assess whether the longer wavelength LED was more appropriate for the studies. In addition to this, a longer localisation time of 1 h was used to facilitate increased uptake of the drugs into the bacterial cell membrane.

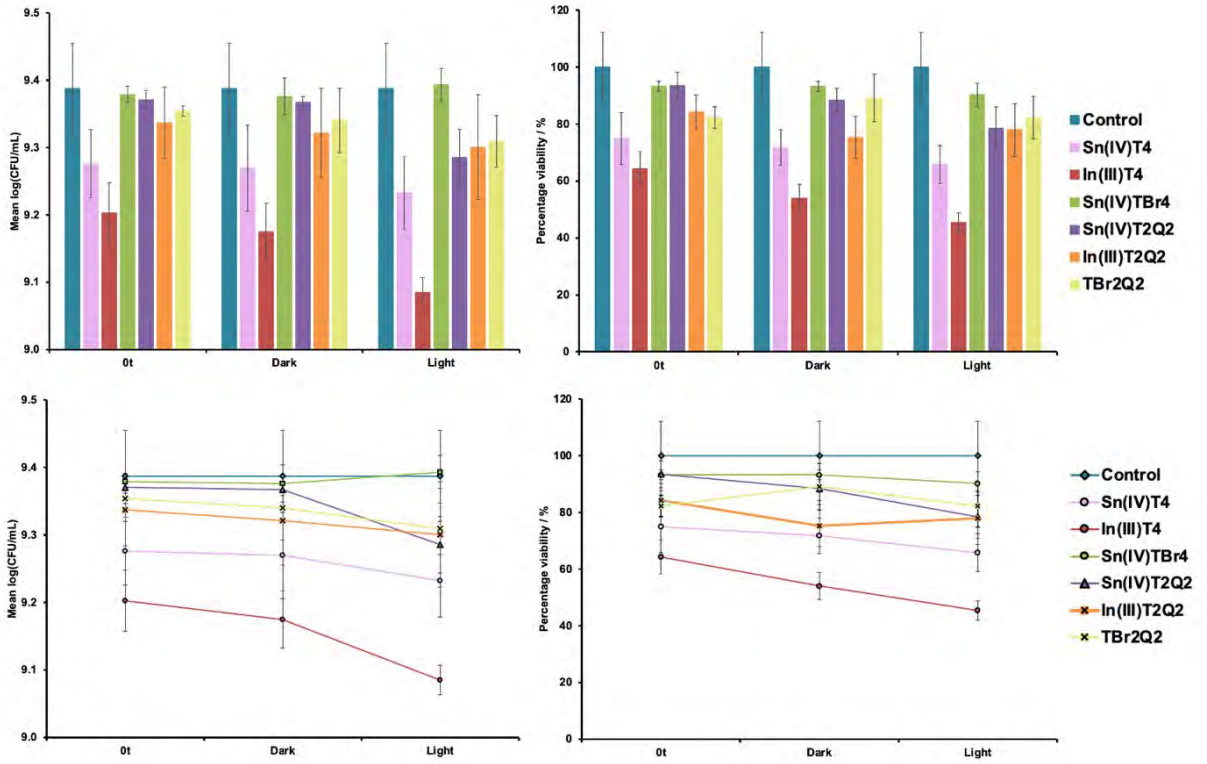

Figure 4.1.2. A repeated concentration optimisation investigation against *Staphylococcus aureus* using 20 μM as the drug concentration. The data is reported as both mean log(CFU/mL) and percentage viability of the bacteria versus the type of experiment. O_T was plated immediately after 1 h of incubation of the bacteria with the drug, the dark experiment was inoculated after 1 h of no exposure to light, and the light experiment was inoculated after 1 h of irradiation with a 595 nm Thorlabs M595L3 LED (240 mW/cm^2).

In **Figure 4.1.2**, it can be noted that **In(III)T4** was the most active compound against *Staphylococcus aureus* within this experiment as well. A 55% bacterial reduction was observed within this experiment after 60 min of irradiation with the Thorlabs M595L3 LED (240mW/cm^2), as opposed to the 45% reduction seen in the first experiment with the shorter wavelength LED. **In(III)T4** still exhibited a 45% reduction in the dark conditions, implying that

it has an inherent antibiotic activity and exhibits slight photoactivity. In addition, none of the compounds within this experiment contributed to the bacterial growth suggesting that the previous results may have been anomalous, particularly in the case of **Sn(IV)T_{Br}4**. **Sn(IV)T4** reduced bacterial growth by approximately 35%, which was also an improvement from the previous experiment. On this basis, it was decided that the Thorlabs M595L3 LED (240 mW/cm^2) would be employed for the subsequent studies and that a 1 h localisation time was more appropriate.

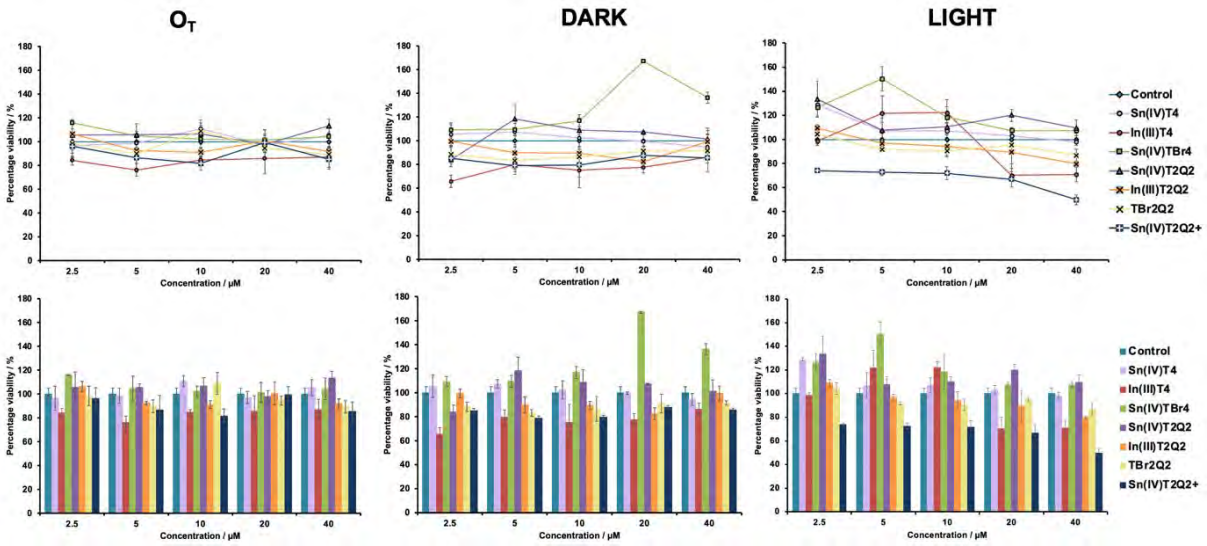

Figure 4.1.3. The concentration optimisation studies against *Escherichia coli*. The data represents the percentage viability as a function of the drug concentration, which ranges from 2.5 μM–40 μM. A 1 h localisation was employed within this investigation. The graphs on the left-hand side represent the percentage viability of the bacteria immediately after incubation with the drug at these varying concentrations (0_T), those in the middle represent the viability of the bacteria after 1 h of being placed in the dark, and those on the right-hand side represent the viability of the drugs after irradiation with a Thorlabs M595L3 LED (240 mW/cm^2) for 1 h.

The first experiment conducted against *Escherichia coli* is outlined in **Figure 4.1.3**. Higher concentrations of the photosensitisers were employed within this investigation (2.5–40 μM) since this is a gram-(–) bacterium and, thus, more of a challenge to inhibit its growth,[86] as well as the fact that the photosensitisers exhibited lower than expected activities against *Staphylococcus aureus*.

This was the first time that the quaternised compound was introduced into the study as a possible means of improving the observed PACT activity. As expected, it exhibited the highest

activity against the bacteria, as well as the greatest photoactivity. It reduced bacterial growth by 50% in the light experiment, as opposed to the 15% reduction observed in both the O_T and dark experiments. This was a promising improvement, particularly when considering it was against a gram-(–) bacterium. As previously, **Sn(IV)T4** displayed the highest PACT activity among the other compounds. There was a 30% reduction in the bacterial growth observed in the light experiment at the highest concentration and only an approximate 15% reduction in the bacterial growth in both the 0_T and dark experiments.

In(III)T2Q2 was the third-best-performing compound in this investigation, but only exhibited a 20% reduction in bacterial growth and did not exhibit any bacterial toxicity in the dark at the highest concentration.

Sn(IV)T2Q2 and **Sn(IV)T_{Br}4** were the worst-performing compounds in this experiment, as they both contributed slightly to the bacterial growth throughout all three experiments, 0_T, dark and light.

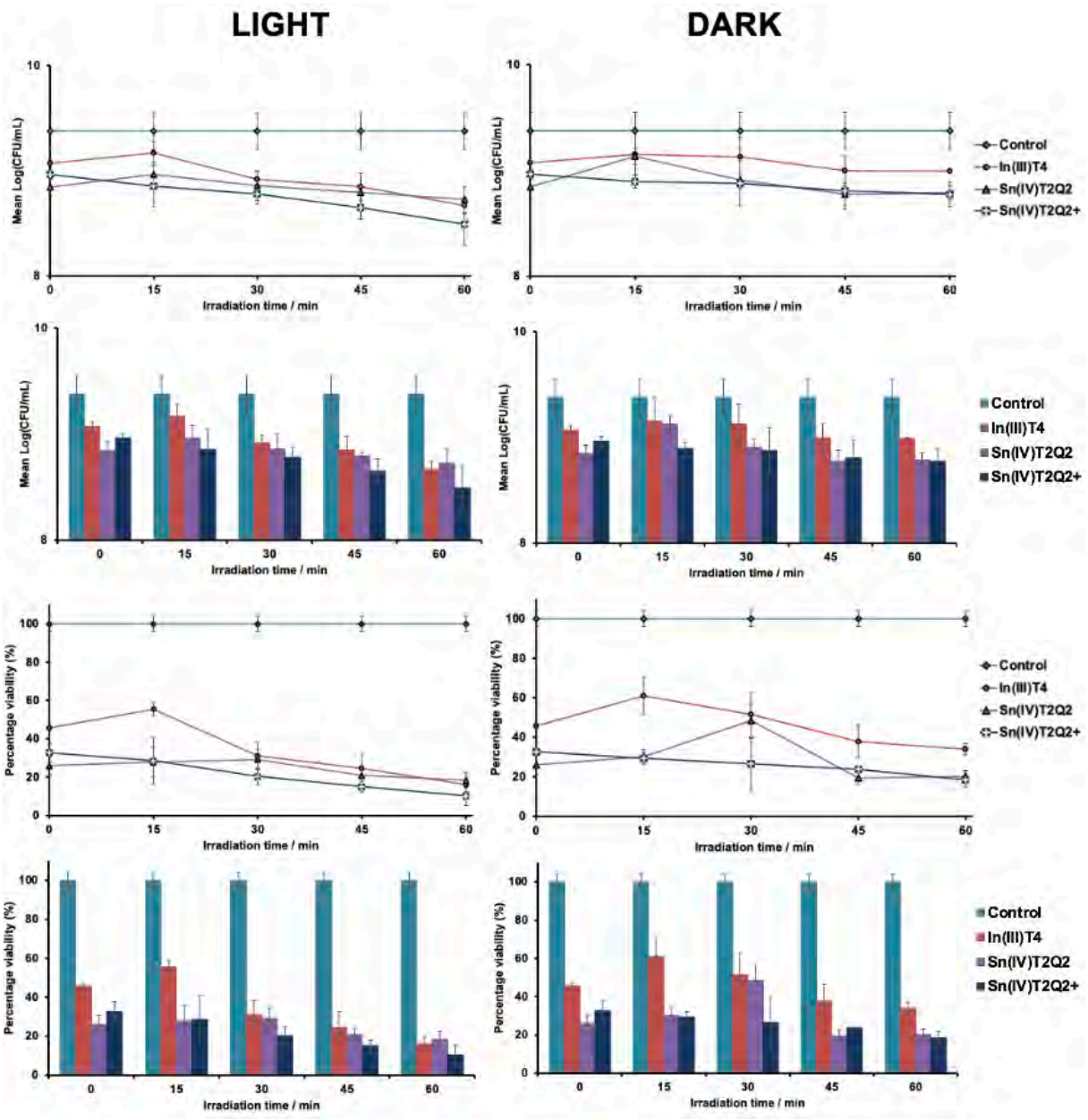

Figure 4.1.4. The preliminary time studies conducted against *Staphylococcus aureus* with the most promising compounds, **In(III)T4**, **Sn(IV)T2Q2** and **Sn(IV)T2Q2^{+}**. The drugs were at a concentration of 40 μM, a 2 h localisation time was employed, and the irradiation was done over 60 min. The graphs on the left-hand side of the figure represent the light experiments that were exposed to a 595 nm Thorlabs M595L3 LED (240 mW/cm^2) over the relevant time intervals, whereas those on the right-hand side represent the dark toxicity experiments, which had no light exposure. The top four graphs are Log(CFU/mL) versus time of irradiation in min and the bottom four are percentage viability (%) versus time of irradiation in min. The data is given as both line and bar graphs.

This experiment was conducted as a preliminary time study against *Staphylococcus aureus*, with the quaternised compound, **Sn(IV)T2Q2+**, and the second-most promising compound

from the previous studies, **In(III)T4**. The unquaterrnised **Sn(IV)T2Q2** was also included within this study as a means to assess the effect of quaternisation on the photodynamic antimicrobial chemotherapeutic activity of the photosensitisers. A 2 h localisation time was employed to further improve the uptake of the drug into the bacterial cell membrane (**Figure 4.1.4**).

It is noteworthy that all of the compounds studied exhibited an inherent antimicrobial activity in the absence of light, as there was a percentage reduction of at least 40% in all cases during the dark toxicity experiments. In addition to this, the bacterial reduction improved with longer irradiation times, as expected. Once again, the quaternised compound was the most promising photosensitiser and had an approximate 90% reduction in bacterial growth in the light experiment and an approximate 80% reduction in the dark experiment.

In general, **Sn(IV)T2Q2** exhibited higher antimicrobial activity than **In(III)T4** in this particular study. This could be attributed to the longer localisation times and its higher singlet oxygen quantum yield. The one exception to this observation is after 60 min of irradiation in the light experiment: **In(III)T4** reduced the bacterial growth by approximately 84%, whereas **Sn(IV)T2Q2** reduced the bacterial growth by only 82%. It can be rationalised that **In(III)T4** has a greater photoactivity after extended periods of irradiation, as they both have the same photostability (87%).

None of the compounds in this experiment, however, achieved a satisfactory $\log_{10}$ reduction, as all of the $\log_{10}$ reductions observed throughout the experiment were less than 1. In this regard, an even longer localisation time of 4 h was employed for the final time studies against both *Staphylococcus aureus* and *Escherichia coli*. It should be noted that Malá *et al.* incubated their photosensitisers with the bacteria for up to 5 h in a similar study.[128]

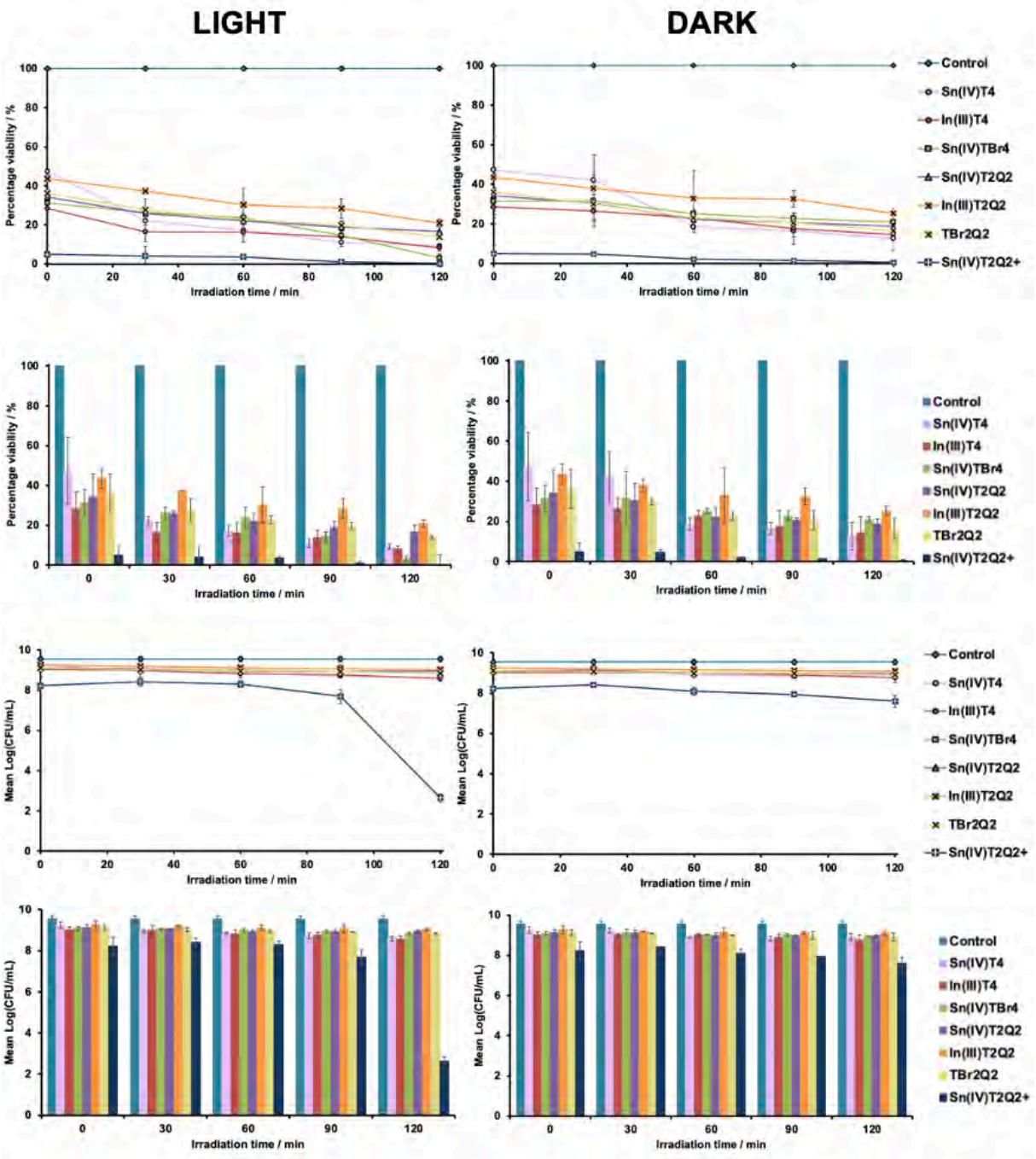

Figure 4.1.5. The final time studies against *Staphylococcus aureus* with the following compounds: **Sn(IV)T4**, **In(III)T4**, **Sn(IV)TBr4**, **Sn(IV)T2Q2**, **In(III)T2Q2**, **T_{Br}2Q2** and **Sn(IV)T2Q2^{+}.** The drugs were at a concentration of 40 μM, a 4 h localisation time was employed and the irradiation was done over 120 min. The graphs on the left-hand side of the figure represent the light experiments that were exposed to a 595 nm Thorlabs M595L3 LED (240 mW/cm^2) over the relevant time intervals, whereas those on the right-hand side represent the dark toxicity experiments, which had no light exposure. The top four graphs are Log(CFU/mL) versus time of irradiation in min, and the bottom four are percentage viability (%) versus time of irradiation in min. The data is given as both line and bar graphs.

A 2 h irradiation time over 30 min intervals, as well as a 4 h localisation was employed within this experiment to further enhance the results (**Figure 4.1.5**).

The final time studies against *Staphylococcus aureus* provided much more promising results, especially in the context of **Sn(IV)T2Q2**$^{+}$: this compound exhibited a bacterial viability reduction of >99% and a $\log_{10}$ reduction of 6.91 in the light experiments. Considering that a 3-$\log_{10}$ in the CFU/mL value is deemed the desirable level of antibacterial activity, this compound performed well.[110,129] In the dark, It still reduced the bacterial viability by approximately 99%, but only had an approximate 2-$\log_{10}$ reduction. This, again, speaks to the inherent antimicrobial activity of the compound, as is observed for all the compounds in each of the experiments undertaken. Another confirming factor that the compounds exhibit antibiotic activity is that all the compounds achieved at least a 50% reduction, even in the dark.

Interestingly, **Sn(IV)T$_{Br}$4** was the second-best-performing compound in the light studies and reduced bacterial growth by approximately 97% after 120 min of irradiation with the 595 nm Thorlabs M595L3 LED (240 mW/cm^2). This improvement in activity could be attributed to the increased localisation time and the long irradiation, showing that this compound requires at least 2 h of irradiation to perform well in PACT. It also had the second-lowest dark toxicity.

In(III)T4 had an approximate 92% bacterial reduction in the light experiment and an approximate 85% reduction in the dark experiment. This compound did, however, have the second-highest $\log_{10}$ reduction in both the light and dark experiments, since the colonies that grew were smaller than those that were able to form in the presence of **Sn(IV)T$_{Br}$4**.

In this experiment, the only free-base molecule that was applied, **T$_{Br}$2Q2**, exhibited the lowest activity in the light and dark experiments, which was the anticipated trend. Precipitation issues were experienced with this compound, and the lack of metalation, regardless of the incorporation of bromines into the atoms, reduces its ability to have high singlet oxygen quantum yields and without the axial ligands associated with metalation, π-π stacking of the

organic macrocycles is more likely, leading to aggregation and solubility problems in aqueous media. In order to improve the potential of the compound as a photosensitising agent, metalation and quartenisation should be considered for future work.

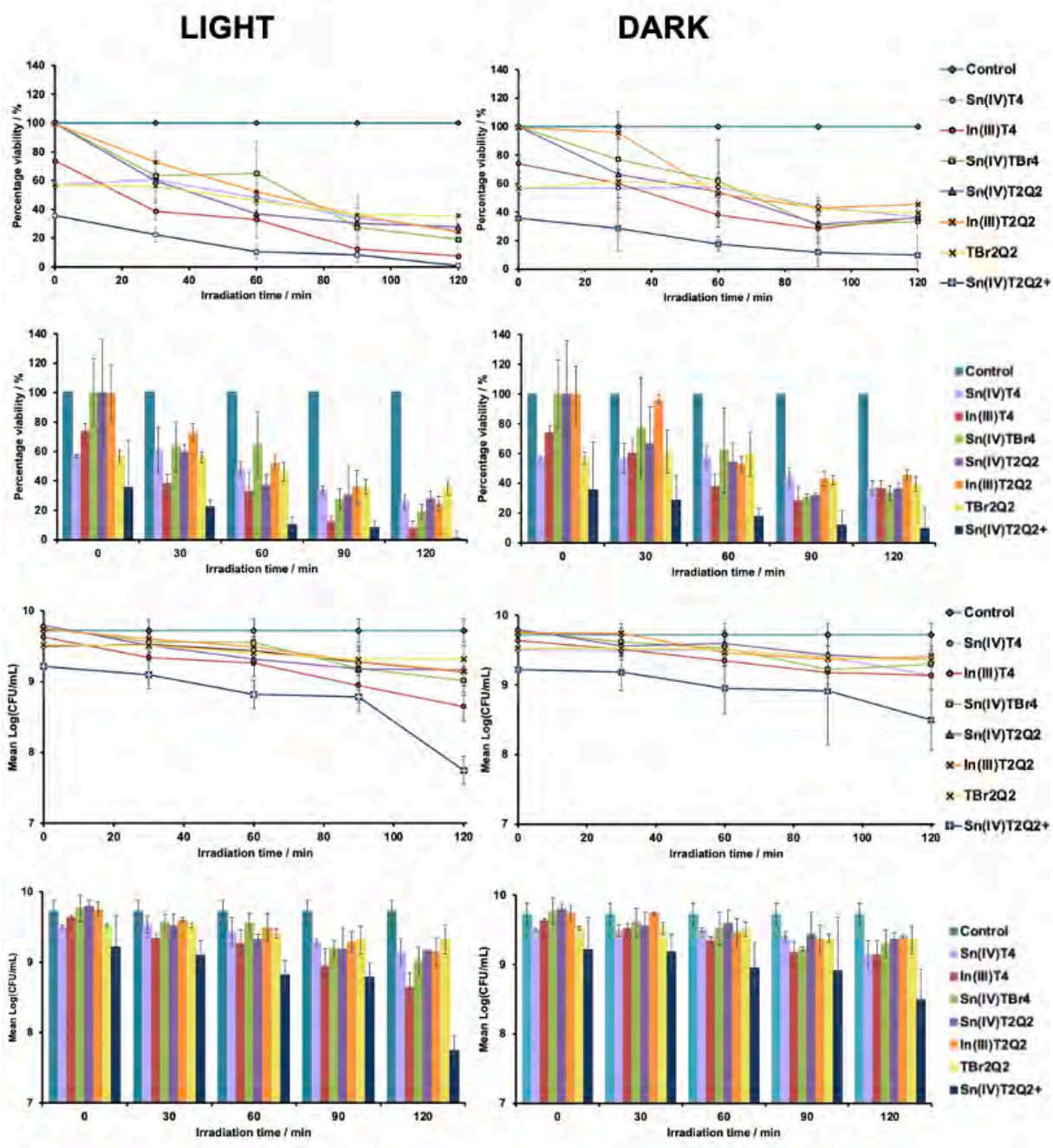

Figure 4.1.6. The final time studies conducted against *Escherichia coli* with the following compounds: **Sn(IV)T4, In(III)T4**, **Sn(IV)TBr4**, **Sn(IV)T2Q2**, **In(III)T2Q2**, **T_{Br}2Q2** and **Sn(IV)T2Q2^{+}.** The drugs were at a concentration of 40 μM, a 4 h localisation time was employed and the irradiation was done over 120 min. The graphs on the left-hand side of the figure represent the light experiments that were exposed to an LED of 595 nm over the relevant time intervals, whereas those on the right-hand side represent the dark experiments, which had no light exposure. The top four graphs are Log(CFU/mL) versus time of irradiation in min and the bottom four are percentage viability (%) versus time of irradiation in min. The data is given as both line and bar graphs.

The same experimental conditions for the final time studies against *Staphylococcus aureus* were employed against *Escherichia coli*: 4 h localisation and 2 h irradiation over 30 min intervals with a working concentration of 40 μM of the photosensitisers. The results of this experiment are outlined in **Figure 4.1.6**.

Sn(IV)T2Q2^{+} was again, the most active compound within this experiment: it achieved a >99% bacterial reduction in the light and a 90% bacterial reduction in the dark. Despite these promising results in the percentage reduction against the gram-negative bacterium, the disparity between the activity of this photosensitiser against *Staphylococcus aureus* and *Escherichia coli* is clear when comparing its $\log_{10}$ reductions. **Sn(IV)T2Q2^{+}** had an approximate 2-$\log_{10}$ reduction against *Escherichia coli* in the light and a 1.2-$\log_{10}$ reduction in the dark, which is much less than the 6.9-$\log_{10}$ and 3-$\log_{10}$ reductions observed against *Staphylococcus aureus* in the light and dark, respectively. This is expected due to the more resistant nature of gram-negative bacteria, as opposed to gram-positive bacteria.

In(III)T4 was seen to be the second-best-performing compound within this experiment, too. It reduced bacterial growth by approximately 92% in the light experiments after 2 h and 65% in the dark experiments, speaking to the most noticeable photoactivity of this compound, when compared to the other photosensitisers.

Sn(IV)T$_{Br}$4 exhibited much higher activities than the early experiments within this investigation, which again rationalises the concept that a longer localisation and irradiation time is required for this compound to exhibit decent activity against the bacterium. It exhibited an 80% reduction in bacterial growth in the light experiment after 2 h and a 65% reduction in the dark experiment.

It is evident that **T$_{Br}$2Q2** was the worst-performing compound after extended periods of irradiation: after 0, 30 and 60 min of irradiation, this compound was outperforming **In(III)T2Q2**

but after a longer exposure to the LED, the metalated asymmetric macrocycle, ultimately, caused a greater reduction in the bacterial growth, despite the greater photostability of **T_{Br}2Q2**.

Table 4.1.1. A summary of the log_{10} reductions and percentage viability of the photosensitisers (at a working concentration 40 μM) against *Staphylococcus aureus* and *Escherichia coli* after 120 minutes of irradiation with a 595 nm Thorlabs M595L3 LED (240 mW/cm^2).

	Log_{10} reduction		***Percentage viability***	
	Staphylococcus aureus	*Escherichia coli*	*Staphylococcus aureus*	*Escherichia coli*
Sn(IV)T4	0.91	0.58	9.26	25.75
In(III)T4	0.97	1.07	8.23	7.66
Sn(IV)T_{Br}4	0.71	0.71	3.06	19.03
Sn(IV)T2Q2	0.61	0.55	16.8	27.84
In(III)T2Q2	0.52	0.58	20.92	24.36
T_{Br}2Q2	0.72	0.40	13.89	35.2
Sn(IV)T2Q2$^+$	6.91	1.97	0.23	0.93

4.2. Summary of chapter

This chapter focussed on the application of the porphyrins in an *in vitro* analysis of their photodynamic antimicrobial chemotherapeutic activities against both *Staphylococcus aureus* and *Escherichia coli*.

The compounds, overall, did not exhibit incredibly high activities against the bacteria, particularly in the case of *Escherichia coli.* The only exception to this was **Sn(IV)T2Q2$^+$**, which had a 6.91-log_{10} reduction against *Staphylococcus aureus* and a 1.97-log_{10} reduction against *Escherichia coli*, as well as exhibiting a bacterial percentage reduction of >99% against both bacterial strains, as outlined in **Table 4.1.1**. Additionally, to achieve a significant reduction in bacterial growth, long localisation times are not usually required, and this merits further investigation, particularly in the context of cellular uptake.[111]

In general, the compounds performed better against *Staphylococcus aureus* than *Escherichia coli*, which was not unusual due to the resistant cell membrane that the latter presents. The only exception to this was seen in the indium compounds: **In(III)T4** and **In(III)T2Q2.** This could be due to the molecular geometry of the molecules and increased permeation through the complex gram-(–) cell wall. **In(III)T2Q2**, however, did not exhibit a higher percentage reduction in *Escherichia coli* than *Staphylococcus aureus*.

Sn(IV)T_{Br}4 produced identical $\log_{10}$ reductions for both bacterial strains. It did, however, have a higher percentage viability reduction against *Staphylococcus aureus*, which is consistent with the expected results.

In(III)T4 exhibited the second-highest $\log_{10}$ reduction against both of the bacterial strains and exhibited the best photoactivity. Surprisingly, however, **Sn(IV)T_{Br}4** was able to reduce a higher percentage of the bacterial colonies with the increased localisation time and longer exposure to the 595 nm Thorlabs M595L3 LED (240 mW/cm^2) LED, compared to the results from the early experiments of the investigation, which were not promising for this compound. It is clear that the increased localisation times and longer irradiation improve the photodynamic antimicrobial chemotherapeutic activities of the photosensitising agents.

Generally, it would seem as if the symmetric molecules performed better in this investigation than the asymmetric molecules, despite the improved singlet oxygen quantum yields of the latter, which is known to be the main cytotoxic agent within this therapeutic approach. There are other factors, such as localisation, to take into account when considering the success of photosensitising agents in PACT, however. Additionally, the thiophene moiety could have a higher bacterial toxicity than the quinoline.

The dark toxicity that the compounds presented is not a major concern due to the inherent antimicrobial activity that the compounds present, which is promising in itself.

The ability of the indium compounds to yield improved $\log_{10}$ reductions against *Escherichia coli* compared to *Staphylococcus aureus* is interesting and cannot be attributed to singlet oxygen quantum yield trends within this thesis. It is also rather unexpected since a reduced π-π stacking should be observed in the Sn(IV) complexes due to the presence of two axial ligands. This observed phenomenon merits further investigation across a broader series of photosensitisers.

Upon comparison with other work of a similar nature, it is apparent that the results obtained in this study of the photodynamic antimicrobial chemotherapeutic activities of porphyrins were not favourable. The rationale behind this series of porphyrins was to exploit the improved singlet oxygen quantum yields of the dyes upon the incorporation of the sulfur in the thiophene, as well as the observed red shift of the UV-visible absorption trends of the porphyrins, compared to **TPP**, which will be further elaborated on in **Chapter 7**. Additionally, the loss of symmetry was explored to improve the singlet oxygen quantum yields of the dyes, which is detailed in **Section 3.4**. Although improved singlet oxygen quantum yields were observed in the low-symmetry porphyrins, they exhibited lower $\log_{10}$-reductions than their symmetric counterparts.

Babu *et al.* observed a significant reduction of bacterial growth and relatively high $\log_{10}$-reductions of both *S. aureus* and *E. coli* for brominated thienyl porphyrinoids (chlorins) of 7.42 and 8.32, respectively, as well as minimal observed dark toxicity.[129] Additionally, Sn(IV) 4-thiolmethylphenyl chlorins and N-confused porphyrins exhibited high $\log_{10}$-reductions (>10) against *S. aureus,* and the chlorin analogue also exhibited a high $\log_{10}$-reduction (>8) against *E. coli* after 75 min of irradiation with a 660 nm Thorlabs (280 mW/cm^2) LED.[110] As a result, a more significant reduction in bacterial growth within this study was anticipated.

Although there is not much available literature on the PACT activities of triaryl corroles with the *meso*-substituents reported in this thesis, the low singlet oxygen quantum yields of these molecules may hinder their potential in this particular application, but this merits further

investigation. The initial aim of this thesis was to study the photodynamic antimicrobial chemotherapeutic activities of the corroles within the synthetic trend, but due to synthetic difficulties, the porphyrins were the main focus of the biological application.

Overall, it is evident that the thienyl substitution of porphyrinoids and the loss of symmetry is promising, but this should be explored with other porphyrin analogues and isomers, such as corroles, chlorins and N-confused porphyrins to enhance the PACT activities of these photosensitisers.

CHAPTER FIVE

PHOTODYNAMIC THERAPY

5.1 Anticancer Photodynamic Activities

In this chapter, the *in vitro* cytotoxicities and phototoxicities of **Sn(IV)T4**, **In(III)T4**, **Sn(IV)T_{Br}4**, **Sn(IV)T2Q2**, **In(III)T2Q2** and **Sn(IV)T2Q2^{+}** were assessed against the MCF-7 breast cancer cell line.

All PDT studies were carried out in 2% DMSO due to the photosensitisers' poor solubility in aqueous media, besides from **Sn(IV)T2Q2^{+}**. The *in vitro* studies were conducted in triplicate against the MCF-7 breast cancer cell line for validation and improved reliability of the results. The WST-1 assay was used to determine the cell viability of the cells after treatment with the photosensitisers without/with light irradiation. Both the light and dark toxicity of the drugs were evaluated, and the half-maximal inhibitory concentration (IC_{50}) values were determined. The IC_{50} value is the concentration of the drug that is required for 50% inhibition of a specific biological/biochemical process and is essentially a measure of the quantity of the pharmacological agent that is required to inhibit the biological activity by half.[131]

The percentage viabilities of the cells were determined with the following equation (**Equation 2.7.1**):

$$\%\ Cell\ viability = \frac{Absorbance\ of\ sample\ at\ 450\ nm}{Absorbance\ of\ control\ at\ 450\ nm}\ x\ 100$$

The *in vitro* toxicity studies against the MCF-7 breast cancer cell lines were conducted in the absence and presence of light to determine the suitability of the porphyrins for PDT. Ideally, the photosensitisers should exhibit minimal dark toxicity and a high phototoxicity to be promising PDT agents and limit the development of adverse side effects.

The concentration range of the drugs was 2.5–80 μM and the irradiation was done with a 625 nm Thorlabs M625L3 light-emitting diode (LED) with an irradiance value of 240 mW/cm^2, which was mounted on the Modulight® Medical 7710-860 laser. The irradiation period was 30 min, and the cells were then incubated with the activated dyes for 24 h. Although there was

dark toxicity observed, particularly in the case of **In(III)T4** and **Sn(IV)T2Q2** (**Figure 5.1.1**), significantly higher phototoxicities were observed in all the drugs except for **Sn(IV)T2Q2^{+}** (**Table 5.1.1**).

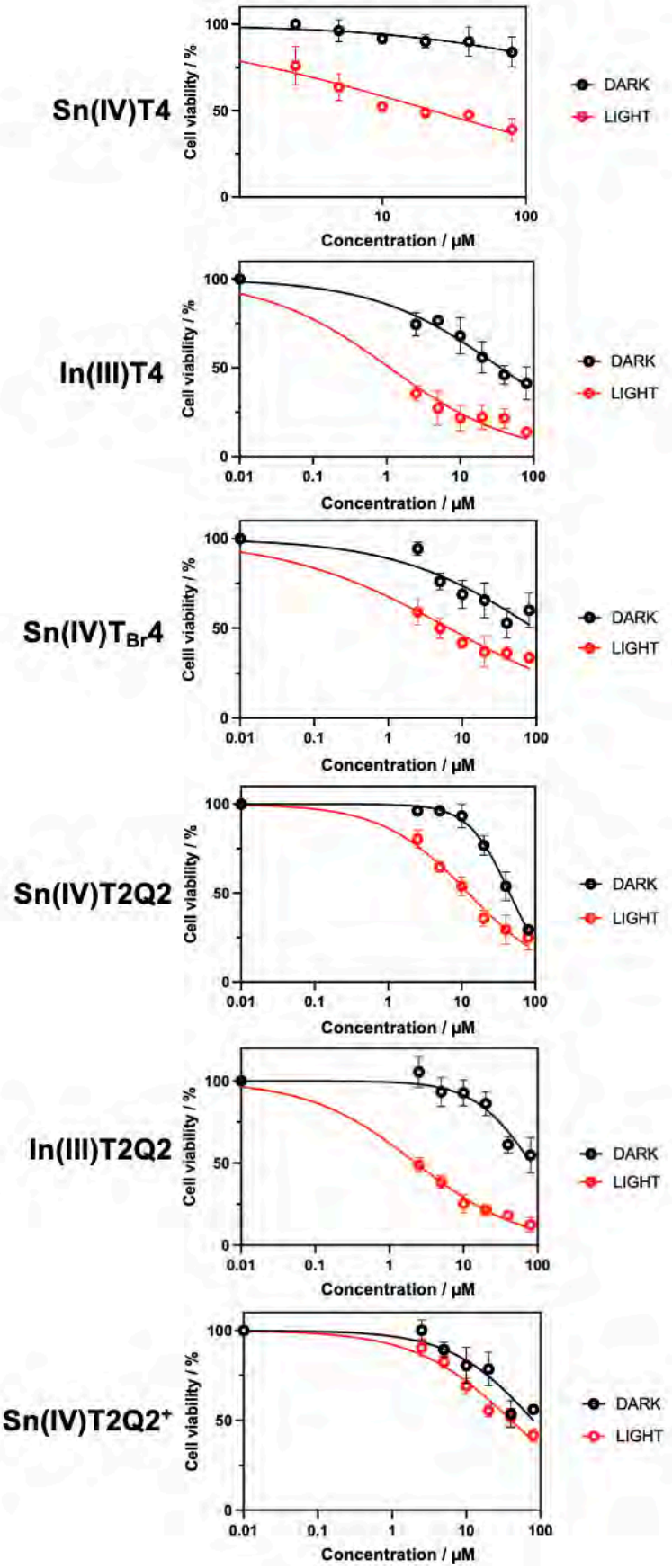

Figure 5.1.1. Dose-dependent photocytotoxicity of the porphyrins against the MCF-7 breast cancer cell line in the dark (black) and after irradiation with a 625 nm Thorlabs M625L3 LED (240 mW/cm^2) (red). The error bars denote the standard deviation.

Table 5.1.1. A summary of the IC_{50} values of the porphyrins against the MCF-7 breast cancer cell line in the light experiment (photocytotoxicity) and the dark experiment (cytotoxicity).

	IC_{50} (μM)	
	Light[a]	Dark[b]
Sn(IV)T4	22.3	>>80
In(III)T4	1.10	35.3
Sn(IV)T_{Br}4	6.67	>80
Sn(IV)T2Q2	12.3	44.8
In(III)T2Q2	2.29	>80
Sn(IV)T2Q2^{+}	40.5	>80

[a]24 h of incubation after 30 min of irradiation with a 625 nm Thorlabs M625L3 LED (240 mW/cm^2).

[b]24 h of incubation in the dark.

5.2 Cellular imaging

Figure 5.2.1. provides a visual representation of the effect of the photosensitisers on the MCF-7 cells at the highest and lowest concentration studied after irradiation with the 625 nm Thorlabs M625L3 LED (240 mW/cm^2). It is evident that the control well had fully confluent cells that appeared healthy, but upon treatment with the photosensitisers, there was a decrease in the MCF-7 confluence, due to the phototoxicity of the photosensitisers. The higher concentration caused a more significant disruption of the cellular confluence, but this effect is still visible even at the lowest concentration.

It is apparent that there is precipitation of the drug at the highest concentration (80 μM), particularly in the case of **Sn(IV)T_{Br}4**. This is a potential limitation to the photosensitiser efficacy because it limits uptake and overall bioavailability.

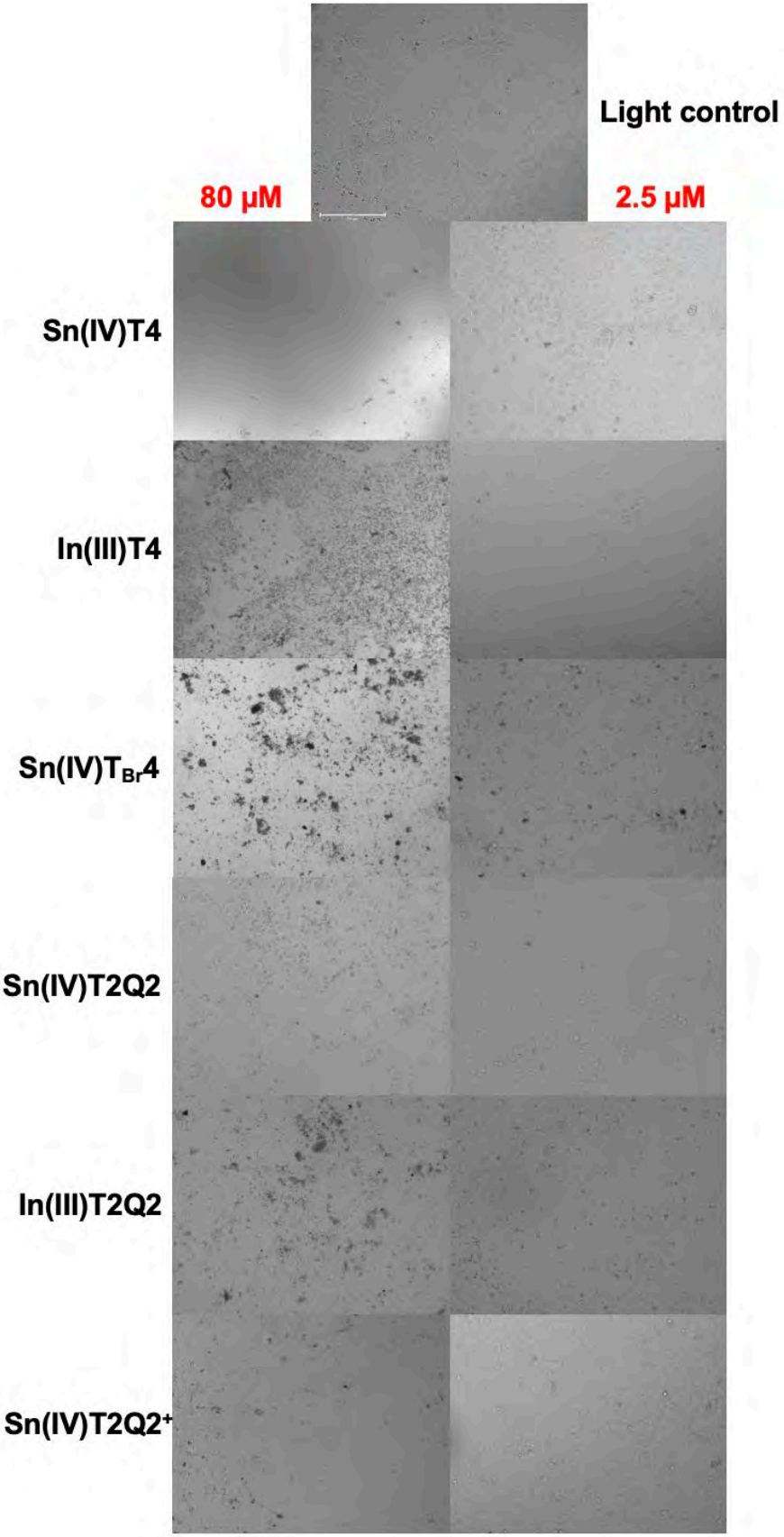

Figure 5.2.1. MCF-7 morphological changes observed upon treatment with the photosensitisers and irradiation with a 625 nm Thorlabs M625L3 LED (240 mW/cm^2) compared to the control well. A comparison is made between the highest dosage (80 μM) on the left and the lowest dosage (2.5 μM) on the right. The scale bar in the control panel represents 275 μm and applies to all of the images.

5.3 Summary of chapter

In(III)T4 is the best-performing compound in the context of light study IC_{50} values, but this molecule exhibits significant dark toxicity issues. **Sn(IV)T4** exhibits the highest dark IC_{50} value and minimal dark toxicity.

The neutral low-symmetry porphyrins (**Sn(IV)T2Q2** and **In(III)T2Q2**) show low dark toxicity at low concentrations but significant phototoxicity, as both of their IC_{50} values are well below 50 μM, as depicted in **Table 5.1.1**. It is likely that this is a result of their higher singlet oxygen quantum yields, but this needs further investigation as **In(III)T2Q2** has a lower IC_{50} value, but a lower singlet oxygen quantum yield. Other factors determine the efficacy of a photosensitiser for PDT, however, and uptake studies should be conducted in the future to assess the effect differing *meso*-aryl rings and the central metal ions. The overall photodynamic activity of the *trans*-A_2B_2 porphyrins is promising and merits further investigation to assess their suitability for PDT.

The quaternised molecule, **Sn(IV)T2Q2$^+$**, showed a significant dark toxicity. Quaternisation of low-symmetry porphyrins with sulfurs and/or nitrogens needs further investigation.

The *meso*-aryl rings of the dyes provide scope for conjugation to silver or gold nanoparticles for improved cellular uptake and overall PDT activity. Further in-depth study is merited in this context.

Upon comparison with other studies of a similar nature, it is evident that there is scope for improvement of the photodynamic activities of these photosensitisers. The light IC_{50} value of **Sn(IV)T4** has been reported (> 25 μM) against the MCF-7 cell line, but the chlorin analogue of this photosensitiser has a significantly lower light IC_{50} value of 0.9 μM. Additionally, the Sn(IV) 4-thiolmethylphenyl substituted porphyrin exhibited a light IC_{50} value of 12.4 against the MCF-7 cell line, whereas its corrole analogue exhibited an improved light IC_{50} value of 8.9

μM, with both having minimal dark toxicity.[131] Lastly, a study between Sn(IV) 4-thiolmethylphenyl substituted porphyrins, corroles and chlorins reported light IC_{50} values against the MCF-7 cell line of 12.4 μM, 8.9 μM and 3.9 μM, respectively.[132]

Sn(IV)T3 has been reported in literature, and it exhibited a light IC_{50} value of 3.2 μM against the MCF-7 cell line after 30 min of irradiation with a 625 nm Thorlabs M625L3 LED (240 mW/cm^2) LED.[133] This is a significant improvement to the light IC_{50} value of **Sn(IV)T4** (22.3 μM) reported in **Table 5.1.1**, as well as the light IC_{50} value of 13.1 μM reported for **Sn(IV)TPC**.[133] Corroles are, therefore, still promising for PDT applications, despite their relatively unfavourable photophysicochemical properties, and this merits an in-depth investigation within this synthetic trend.

N-confused porphyrins are also promising for PDT applications: **NCTPP** exhibited a light IC_{50} value of 1.6 μM, while that of **TPP** was >25 μM after irradiation with a 660 nm Thorlabs M660L3 LED (280 mW/cm^2) LED due to the significant spectral red shift and improved singlet oxygen quantum yield of the former.[133]

Conjugation of P(V) and Ga(III) trithienylcorroles to gold nanoparticles has been reported to afford improved PDT activity and IC_{50} values, as reported by Soy *et al*.[134] Time constraints made it impossible to explore this possibility in the context of this study.

Overall, the thiophene moieties are promising for red shifting the spectral bands of porphyrinoids deeper into the phototherapeutic window, improved singlet oxygen quantum yields and facilitating nanoparticle conjugation *via* affinity. For future work, an in-depth investigation of this series of high- and low-symmetry porphyrins should be extended to other analogues and isomers, including but not limited to corroles, chlorins and N-confused porphyrins.

CHAPTER SIX

OPTICAL LIMITING

6.1 Porphyrinoids for NLO studies

It has been previously demonstrated that π-conjugated systems possess large electronic polarisabilities.[136] In this work, a series of porphyrin macrocycles and two corrole molecules were investigated for their optical limiting properties (**Figure 6.1.1** and **Figure 6.1.2**). Additionally, the most promising compound, **Sn(IV)T4**, was embedded in poly(bisphenol carbonate A) to improve the optical limiting properties of the dye and to conduct OL measurements in the solid state, which is important for real-world applications.

The nonlinear optical parameters were determined using the open aperture z-scan technique described in **Chapter 2**. The studies were carried out in solution, except for **Sn(IV)T4-PBC**, which was conducted in the solid state. The studies were carried out in different organic solvents (either $CHCl_3$ or DMSO) for each compound to optimise the solubility and eliminate aggregation in solution, and the refractive index of the solvent was incorporated into the calculation of the optical limiting parameters. The open aperture z-scan profiles of the porphyrins and the corroles are given in **Figure 6.1.3.1** and **Figure 6.1.3.2**, respectively. The plots of output fluence (I_{out}) *vs* input fluence (I_0) of the porphyrins and corroles are given in **Figure 6.1.4.1** and **Figure 6.1.4.2**, respectively. The normalised transmittance *vs* input fluence (I_0) of the porphyrins and corroles are given in **Figure 6.1.5.1** and **Figure 6.1.5.2**, respectively. Lastly, the optical limiting parameters of the porphyrins and corroles are summarised in **Table 6.1**. The parameters that were reported included concentration, α, the effective nonlinear absorption coefficient (β_{eff}), the imaginary third-order susceptibility ($Im\{\chi^3\}$), the second-order hyperpolarisability (γ), and the optical limiting threshold (I_{lim}). Although there is not a single parameter that will determine the efficacy of an optical limiting material, the second-order hyperpolarisability (γ) is a particularly useful parameter to compare the photosensitisers with, as it is independent of concentration and hence allows for a meaningful comparison.

Since nanosecond laser pulses are employed and the fact that the absorbance of the molecules at 532 nm is nonzero, the RSA responses that are observed cannot be attributed strictly to 2PA.[90,97] As a result, the 2PA intrinsic β value cannot be measured, which would be possible in the context of femtosecond laser pulses. Instead, the effective nonlinear absorption coefficient (β_{eff}) is obtained.[97]

It is expected that the incorporation of heavy atoms, including and not limited to bromine, tin (IV) and indium (III), promotes intersystem crossing to the triplet manifold. Linear single-photon absorption populates the excited states enabling ESA from either the S_1 state and /or the T_1. Hence the RSA responses are due to a combination of 2PA and ESA.

A good optical limiting material should display a significant decrease in transmittance at increased fluence values.

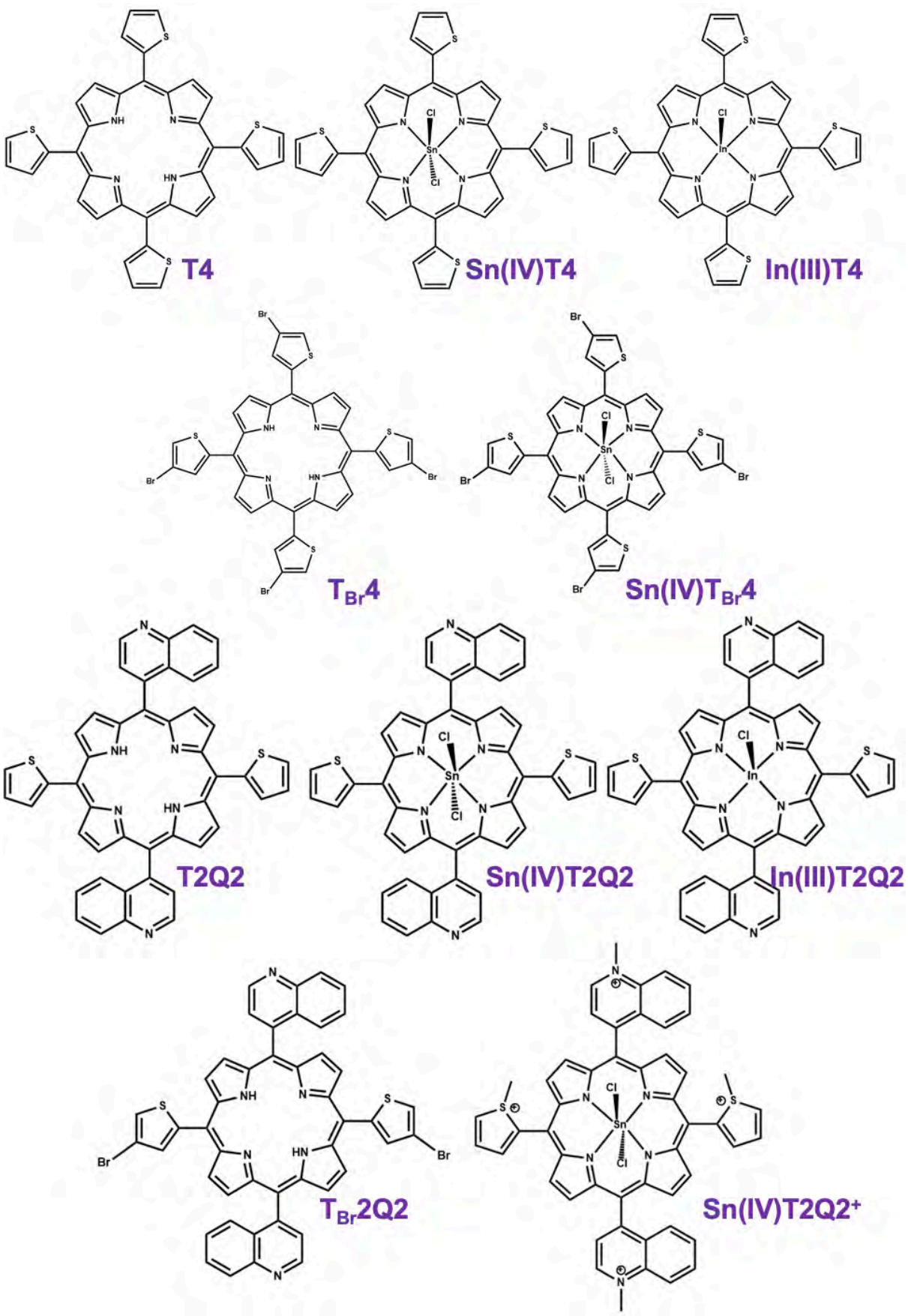

Figure 6.1.1. The porphyrin molecules that were assessed for their optical limiting properties within this chapter. A thin film of **Sn(IV)T4** (embedded in poly(bisphenol carbonate A)) was also investigated.

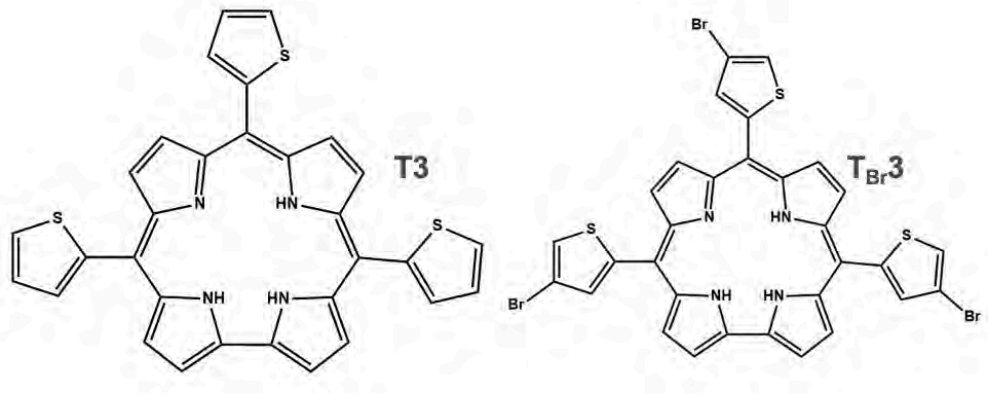

Figure 6.1.2. The corrole molecules that were assessed for their optical limiting properties within this chapter.

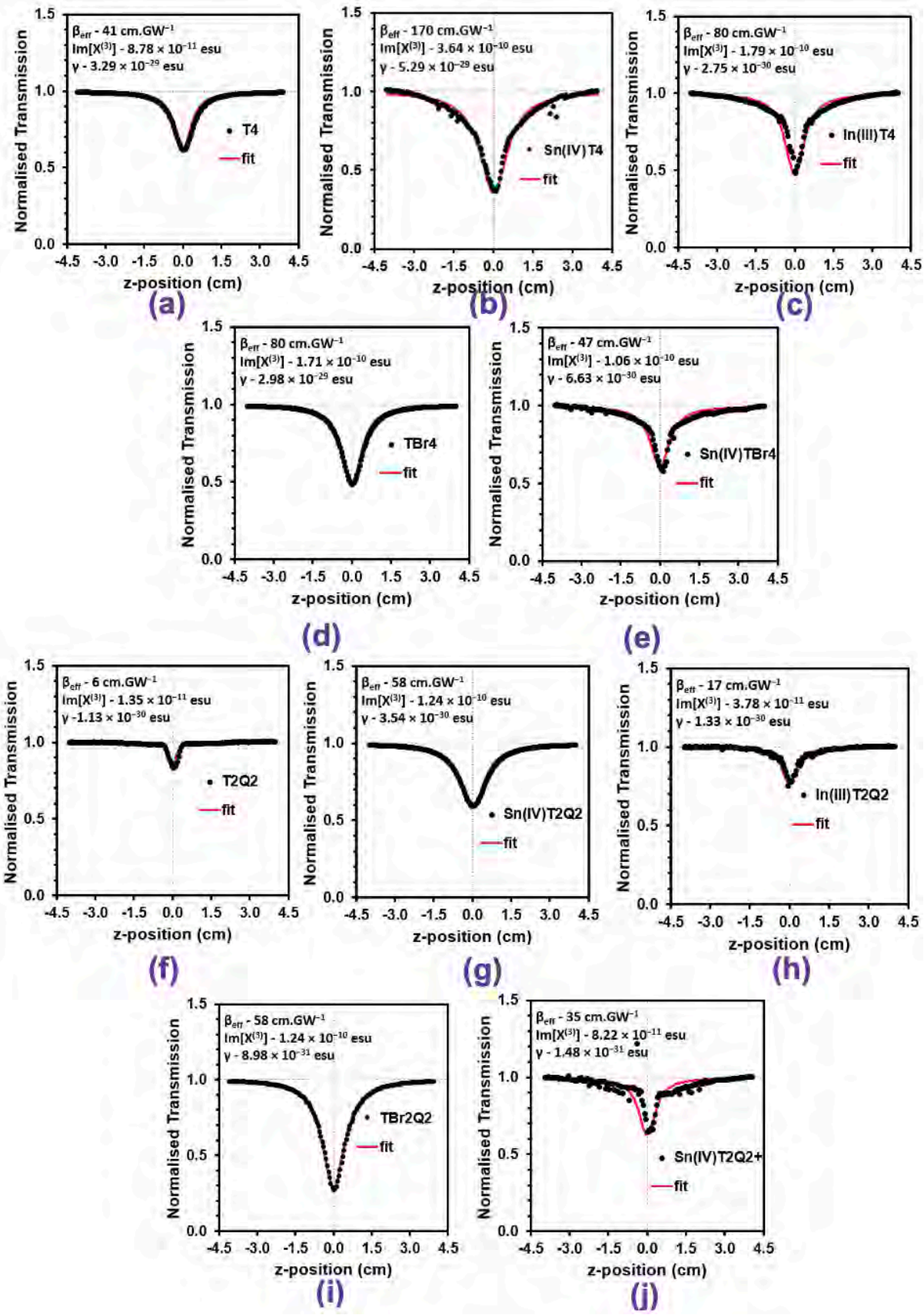

Figure 6.1.3.1. Open aperture z-scan profiles of porphyrins (**T4** (**a**), **Sn(IV)T4** (**b**), **In(III)T4** (**c**), **T_{Br}4** (**d**), **Sn(IV)T_{Br}4** (**e**), **T2Q2** (**f**), **Sn(IV)T2Q2** (**g**), **In(III)T2Q2** (**h**), **T_{Br}2Q2** (**i**), and **Sn(IV)T2Q2^{+}** (**j**).

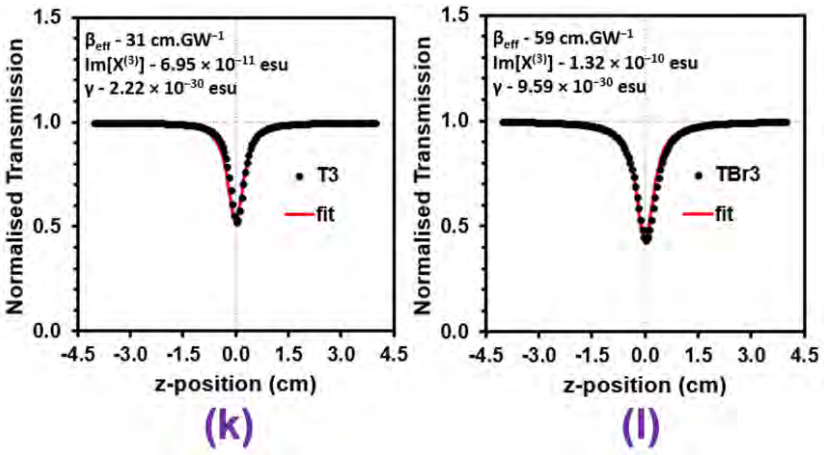

Figure 6.1.3.2. Open aperture z-scan profiles of the free base corroles (**T3** (k) and **T_{Br}3** (l)).

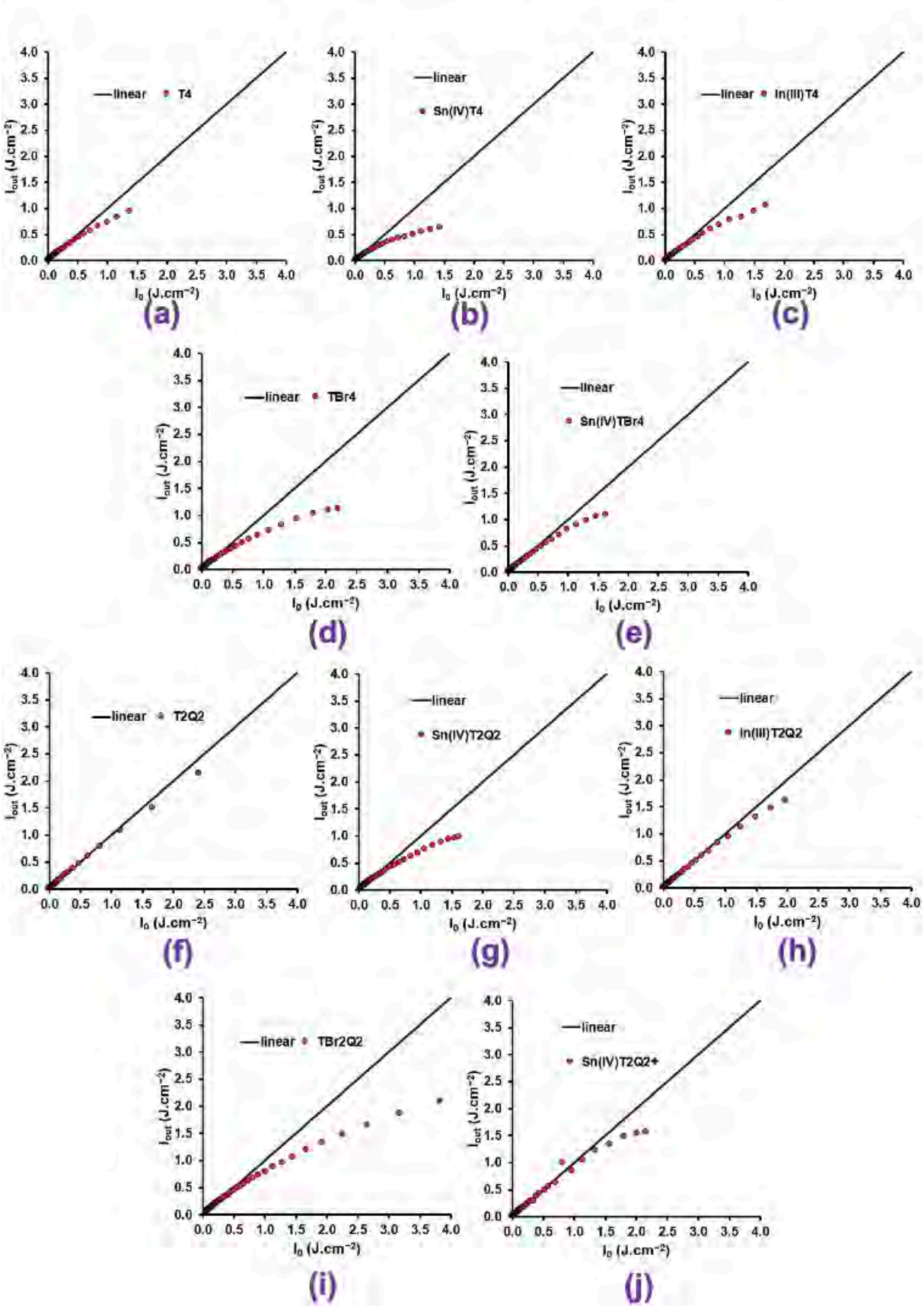

Figure 6.1.4.1. Plots of output fluence (I_{out}) *vs* input fluence (I_0) of the porphyrins: **T4** (**a**), **Sn(IV)T4** (**b**), **In(III)T4** (**c**), **T_{Br}4** (**d**), **Sn(IV)T_{Br}4** (**e**), **T2Q2** (**f**), **Sn(IV)T2Q2** (**g**), **In(III)T2Q2** (**h**), **T_{Br}2Q2** (**i**), and **Sn(IV)T2Q2$^+$** (**j**).

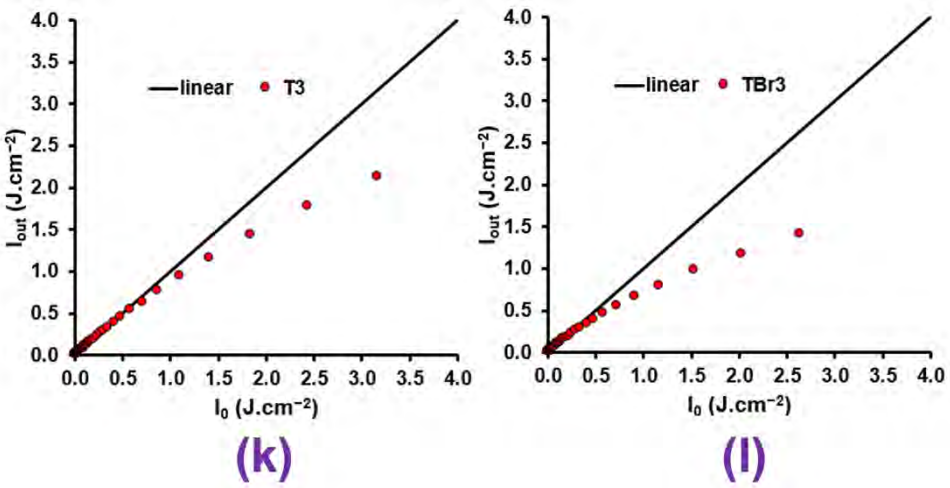

Figure 6.1.4.2. Plots of output fluence (I_{out}) *vs* input fluence (I_0) of the corroles: **T3** (**k**) and **T_{Br}3** (**l**).

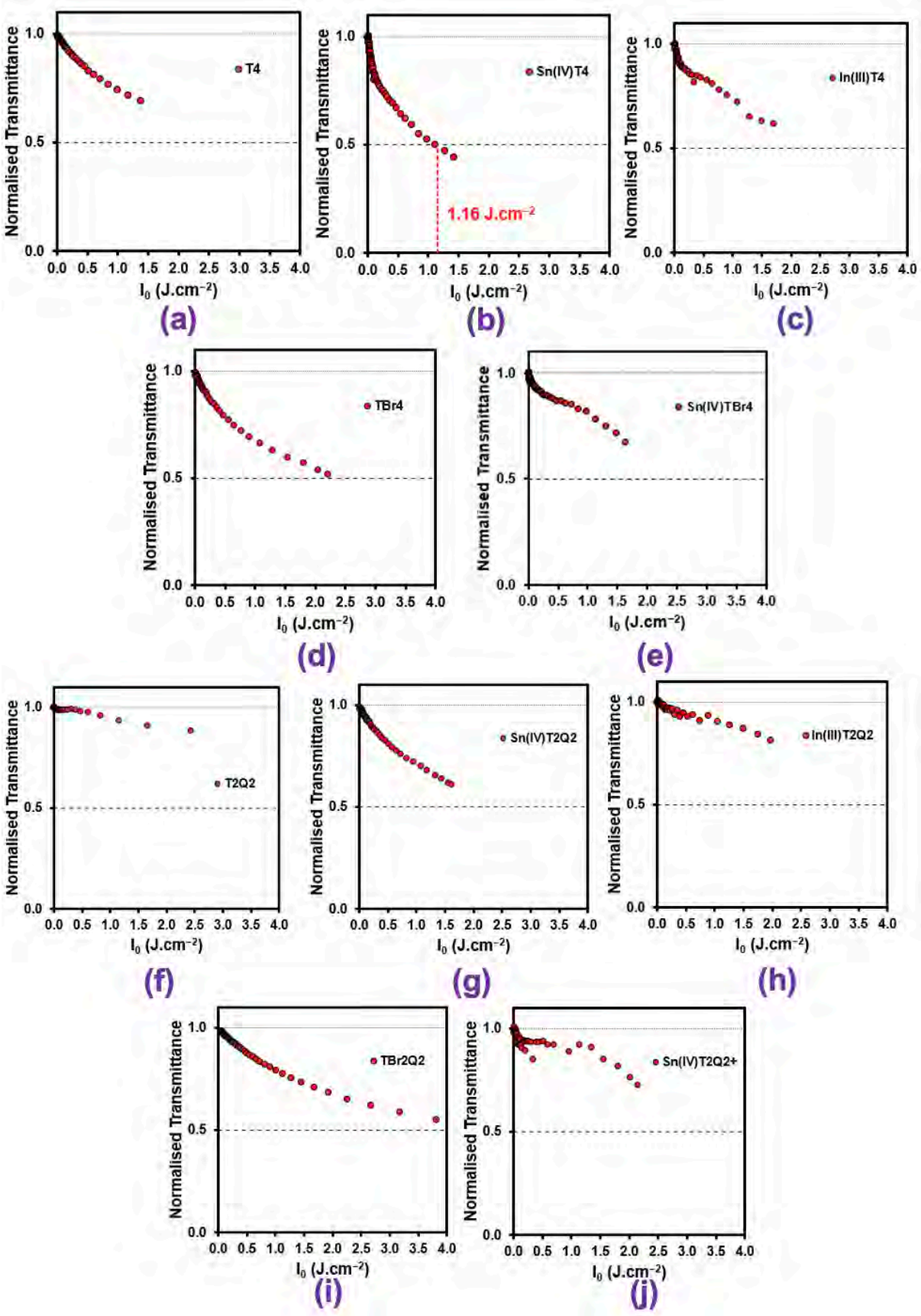

Figure 6.1.5.1. Normalised transmittance *vs* input fluence (I_0) of the porphyrins: **T4** (**a**), **Sn(IV)T4** (**b**), **In(III)T4** (**c**), **T_{Br}4** (**d**), **Sn(IV)T_{Br}4** (**e**), **T2Q2** (**f**), **Sn(IV)T2Q2** (**g**), **In(III)T2Q2** (**h**), **T_{Br}2Q2** (**i**), and **Sn(IV)T2Q2$^+$** (**j**).

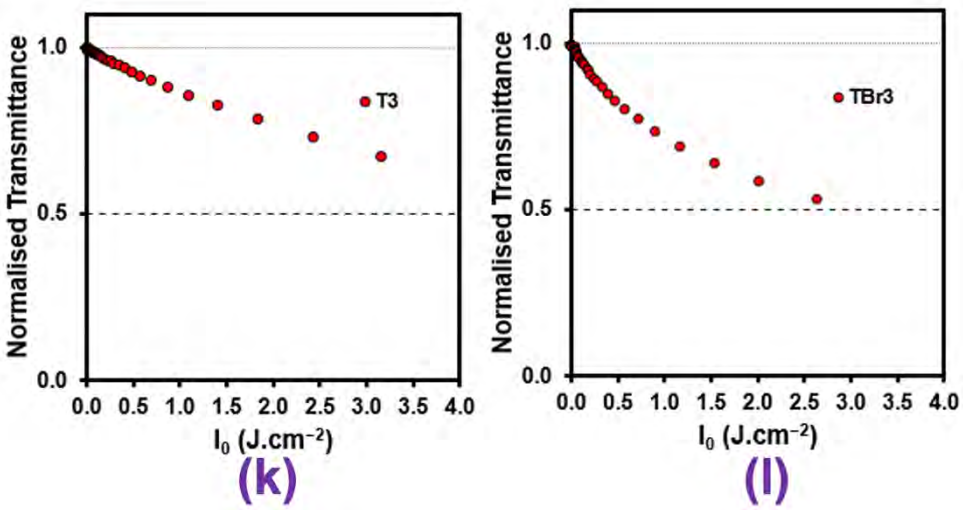

Figure 6.1.5.2. Normalised transmittance *vs* input fluence (I_0) of the corroles: **T3** (**k**) and **T_{Br}3** (**l**).

6.2. Porphyrin-PBC thin film

The ground state absorption spectrum of the thin film in solution was obtained to investigate the effect of embedding the dye in a solid support, poly(bisphenol A carbonate) (PBC). **Figure 6.2.1** shows the absorption trends of **Sn(IV)T4**, the most promising compound from the previous study of the macrocycles alone, and **Sn(IV)T4-PBC**. It is evident that the spectrum of **Sn(IV)T4-PBC** in solution is slightly red-shifted. The average film thickness of **Sn(IV)T4-PBC** was determined using SEM (**Figure 6.2.2**).

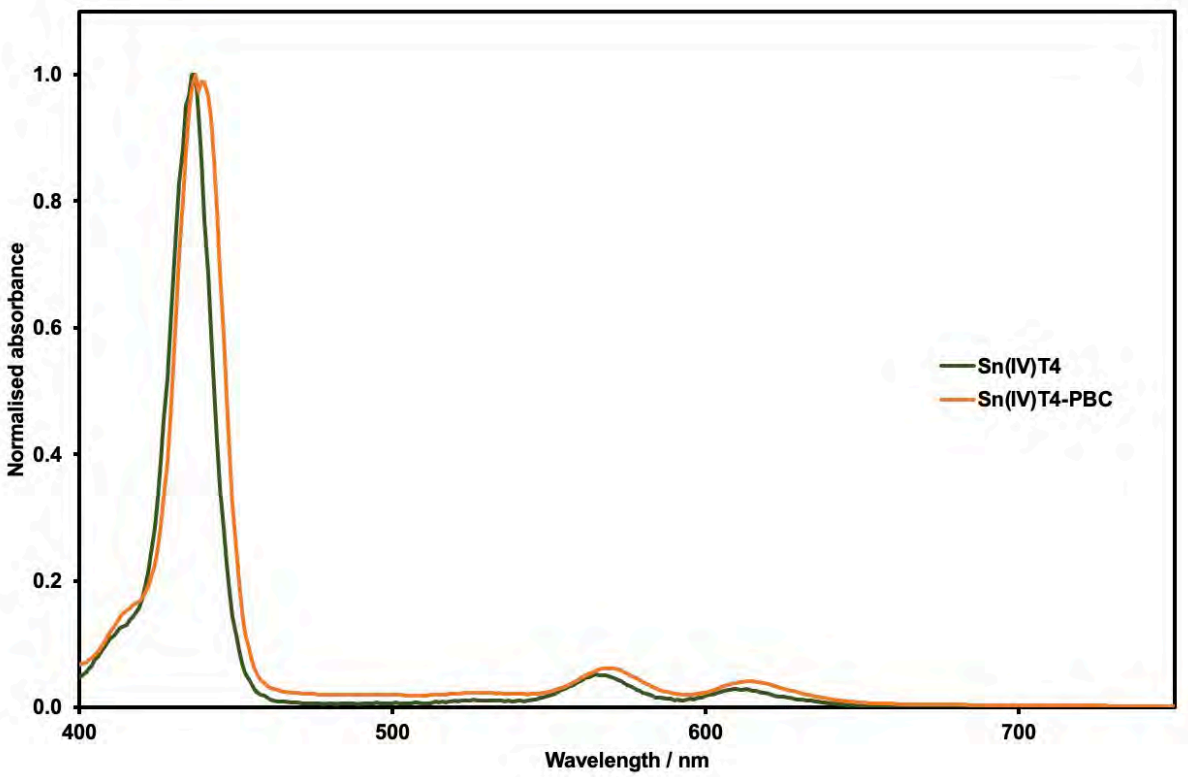

Figure 6.2.1 Ground state absorption spectra for **Sn(IV)T4** and **Sn(IV)T4-PBC** in solution, which was measured in CH_2Cl_2.

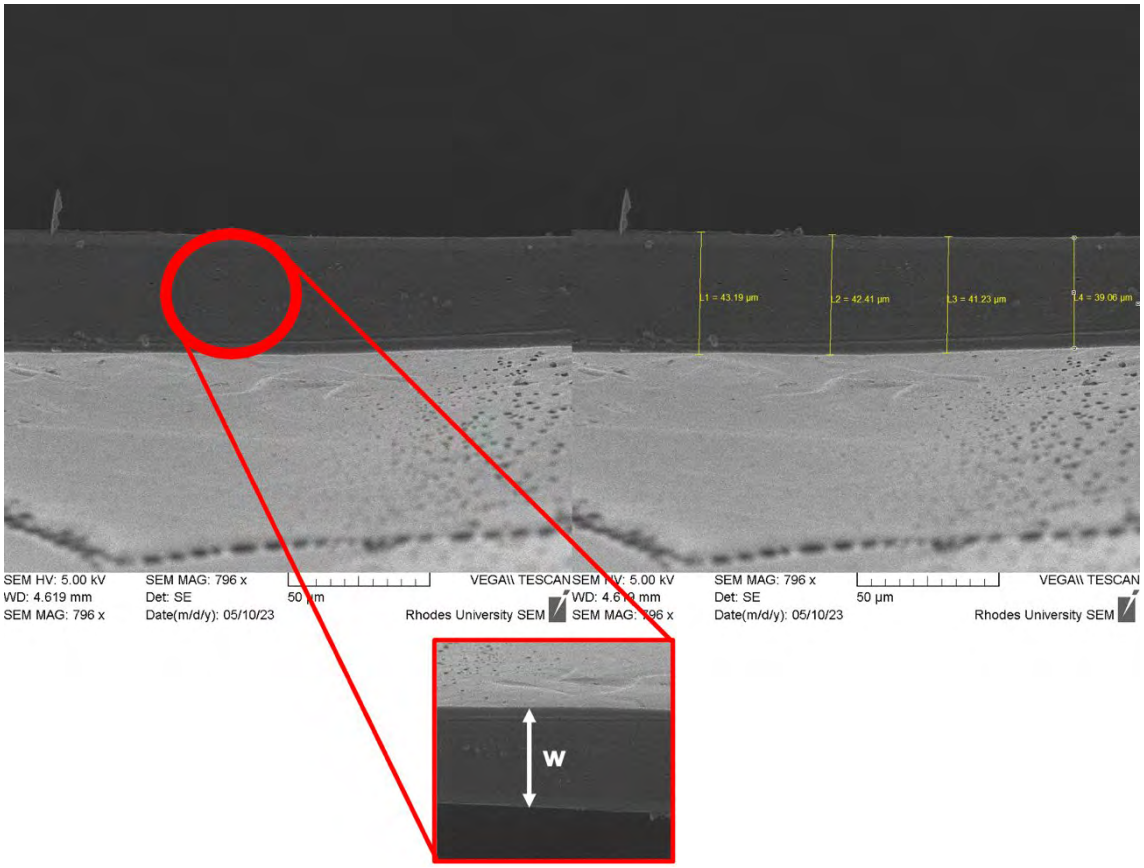

Figure 6.2.2. Scanning electron microscopy images of the PBC thin films embedded with **Sn(IV)T4**. The width of the thin film was measured transversely, and an average film thickness of ca. 41 μm was obtained.

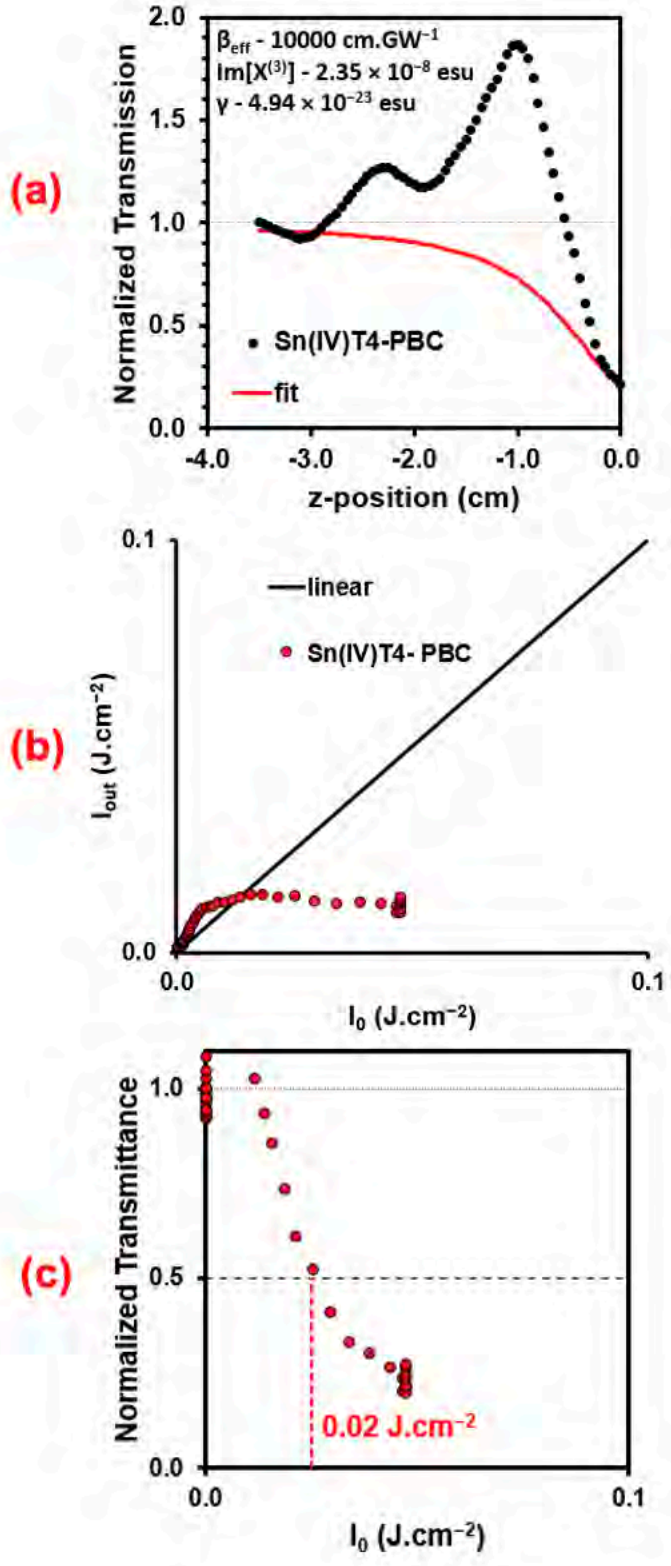

Figure 6.2.3. (a) Open aperture z-scan profile of **Sn(IV)T4-PBC** until z = 0. (b) Plots of output fluence (I_{out}) *vs* input fluence (I_0) of **Sn(IV)T4-PBC**, and (c) Normalised transmittance *vs* input fluence (I_0) of **Sn(IV)T4-PBC**.

The thin film displayed unusual optical limiting properties, as seen in **Figure 6.2.3**, likely due to thermal effects and a lack of transparency of the film, despite multiple synthetic attempts.

As a proof of concept, a porphyrin or corrole being embedded in a polymer to form a thin film for application in the solid state is promising as there is a substantial reduction in the transmission towards z = 0. There is a need to optimise the thin film preparation process before further progress will be possible, however.

Table 6.1. A summary of the optical limiting parameters of **T4**, **Sn(IV)T4**, **In(III)T4**, **T_{Br}4**, **Sn(IV)T_{Br}4**, **T2Q2**, **Sn(IV)T2Q2**, **In(III)T2Q2**, **T_{Br}2Q2**, **T3**, **T_{Br}3**, **Sn(IV)T2Q2^{+}** and **Sn(IV)T4-PBC** at a fixed pulse energy of 35 kJ.

	Solvent used	**[ ] / M**	**α / cm^{-1}**	**β_{eff} / cm.GW^{-1}**	**Im{X^3} / esu**	**γ / esu**	**I_{lim} / J.cm^{-2}**
T4	DMSO	1.41×10^{-6}	1.36	41	8.78×10^{-11}	3.29×10^{-29}	–
Sn(IV)T4	$CHCl_3$	3.63×10^{-6}	1.08	170	3.64×10^{-10}	5.29×10^{-29}	1.16
In(III)T4	$CHCl_3$	6.26×10^{-6}	0.81	80	1.79×10^{-10}	1.38×10^{-29}	–
T_{Br}4	DMSO	3.04×10^{-6}	2.47	80	1.71×10^{-10}	2.98×10^{-29}	–
Sn(IV)T_{Br}4	$CHCl_3$	7.71×10^{-6}	1.39	47	1.06×10^{-10}	6.63×10^{-30}	–
T2Q2	$CHCl_3$	5.72×10^{-6}	0.83	6	1.35×10^{-11}	1.13×10^{-30}	–
Sn(IV)T2Q2	DMSO	1.85×10^{-5}	0.86	58	1.24×10^{-10}	3.54×10^{-30}	–
In(III)T2Q2	$CHCl_3$	1.37×10^{-5}	0.77	17	3.78×10^{-11}	1.33×10^{-30}	–
T_{Br}2Q2	DMSO	7.30×10^{-5}	6.71	58	1.24×10^{-10}	8.98×10^{-31}	–
Sn(IV)T2Q2^{+}	DMSO	2.42×10^{-4}	1.11	35	8.22×10^{-11}	1.48×10^{-31}	–
T3	$CHCl_3$	1.51×10^{-5}	1.86	31	6.95×10^{-11}	2.22×10^{-30}	–
T_{Br}3	$CHCl_3$	6.63×10^{-6}	2.36	59	1.32×10^{-10}	9.59×10^{-30}	–
Sn(IV)T4-PBC	Solid state	--	--	$\approx$ 10000	$\approx 2 \times 10^{-8}$	--	$\approx$ 0.02

6.3. Summary of chapter

It is evident that all of the dyes studied exhibit promising optical limiting properties and a significant decrease in transmittance at increased fluence values, with the apparent exceptions of **T2Q2** and **In(III)T2Q2**. They all have optimal ranges of second-order hyperpolarisability (γ) and the imaginary third-order susceptibility ($Im\{\chi^3\}$), as reported in **Chapter 1.10.1**.

Generally, the optical limiting properties of the dyes improve upon the incorporation of heavy atoms: **Sn(IV)T2Q2** and **In(III)T2Q2** both had better RSA responses than **T2Q2**, as well as **T_{Br}4** having a better RSA response than **T4**. One exception to this general trend was apparent: **Sn(IV)T_{Br}4** did not exhibit better OL properties than **T_{Br}4**. **Sn(IV)T_{Br}4** did not exhibit such a significant decrease in the normalised transmittance with an increased input fluence and **T_{Br}4** had a better RSA response. In **Chapter 4**, it was noted that **Sn(IV)T_{Br}4** did exhibit a surprisingly low singlet oxygen quantum yield compared to **T_{Br}4**, which could explain the reduced optical limiting properties due to reduced ESA.

Sn(IV)T4 was chosen as the most promising compound, due to its promising RSA response, a significant decrease in transmittance at higher input fluence and obtainable I_{lim} value. It was thus embedded in poly(bisphenol carbonate A). The thin film showed a significant reduction in transmission towards z = 0 and a strong RSA response, but was not sufficiently transparent under ambient light conditions and had an abnormal optical limiting response due to the thermal effects and hence needs to be further optimised.

CHAPTER SEVEN

THEORETICAL CALCULATIONS

7.1 Molecular structures and TD-DFT calculations

In accordance with Gouterman's 4-orbital theory (**Figure 1.6.4**), the degenerate excited singlet configurations of normal porphyrins (i.e. $(a_{2u})^1(e_g)^1$ and $(a_{1u})^1(e_g)^1$) are responsible for the typical spectroscopic trends: an intense Soret band and relatively weak Q band absorption band envelope. Time-dependent density functional theory (TD-DFT) was used in this thesis to establish the relationship between structural modifications to the porphyrin core and the resultant bathochromic shift and intensification of the Q bands. All the theoretical calculations conducted in this chapter involved a geometry optimisation calculated at the B3LYP/SDD level of theory.

A time-dependent density functional theory (TD-DFT) treatment is provided for the optical properties of the molecules of synthetic interest within this thesis: free base, Sn(IV) and P(V) high- and low-symmetry porphyrins and corroles, as well as In(III) high- and low-symmetry porphyrins. Calculations were performed at the CAM-B3LYP/SDD level to obtain the 40 lowest singlet-singlet transitions. The SDD basis sets account for the relativistic heavy atoms such as tin, indium, sulfur and bromine.[136] The *in vacuo* results presented in this chapter provide insight into the effect of structural modification on the parent porphyrin complex to the lower symmetry analogue, corroles, as well as that of substitution with different *meso*-substituents.

The first series of molecules include the reference compound, tetraphenylporphyrin (**TPP**) and its thienyl-substituted counterpart (**T4**) and their corrole analogues (**TPC** and **T3**) (**Figure 7.1**). This is done to provide a theoretical explanation of the observed groundstate absorption spectra in accordance with Gouterman's 4-orbital model and Michl's perimeter model.[41,42,46-49] A secondary goal was to provide insight into the optical and electronic properties of the molecules upon replacing the phenyl ring with a thien-2-yl substituent.

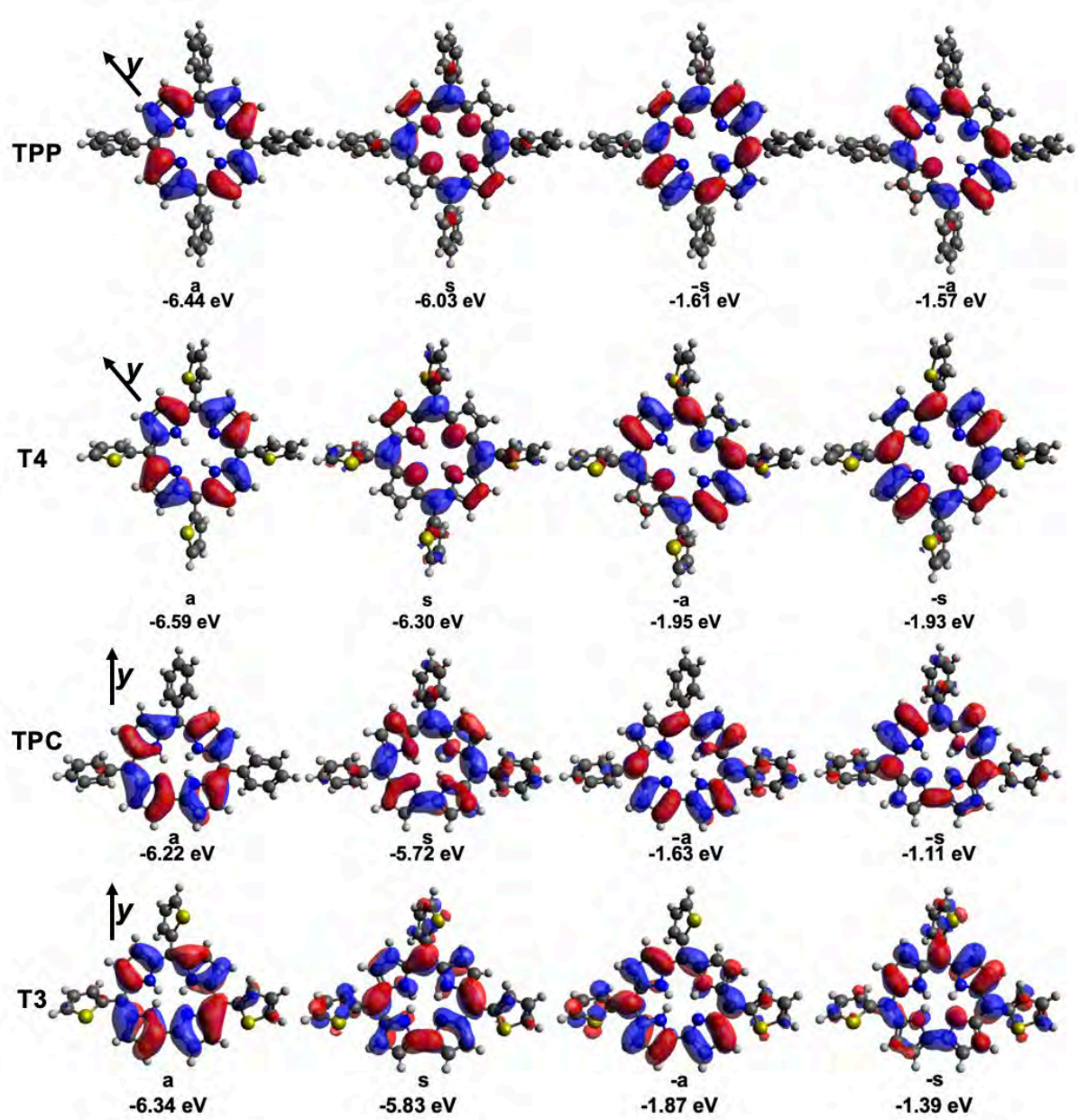

Figure 7.1. The nodal patterns of tetraphenylporphyrin (**TPP**), **T4**, triphenylcorrole (**TPC**) and **T3** at an isosurface value of 0.02 a.u., and the MO energies of the **a, s, -a,** and **-s** MOs.

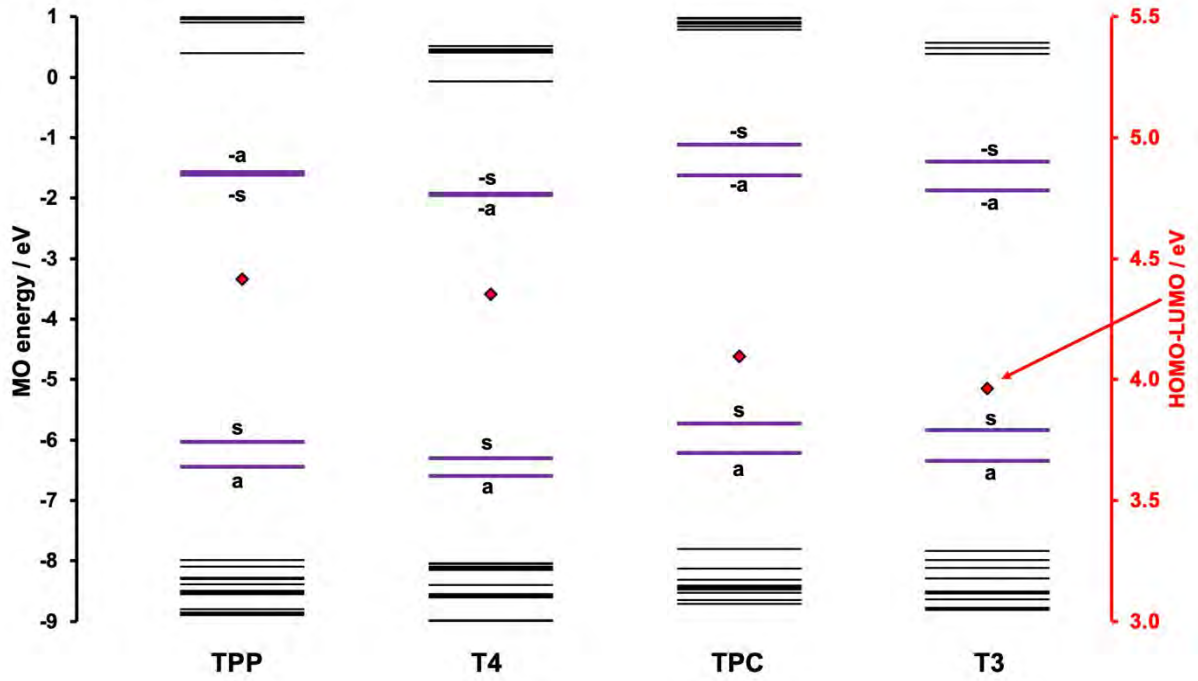

Figure 7.2. The relative energies of the molecular orbitals of the phenyl- and thienyl-substituted symmetric porphyrins **(TPP** and **T4**, respectively) and corroles (**TPC** and **T3**, respectively). The four-frontier molecular orbitals energies are bolded and in purple, and the occupied orbitals are denoted by circular black markers. A secondary axis is used to plot the HOMO–LUMO energy gap in red diamonds.

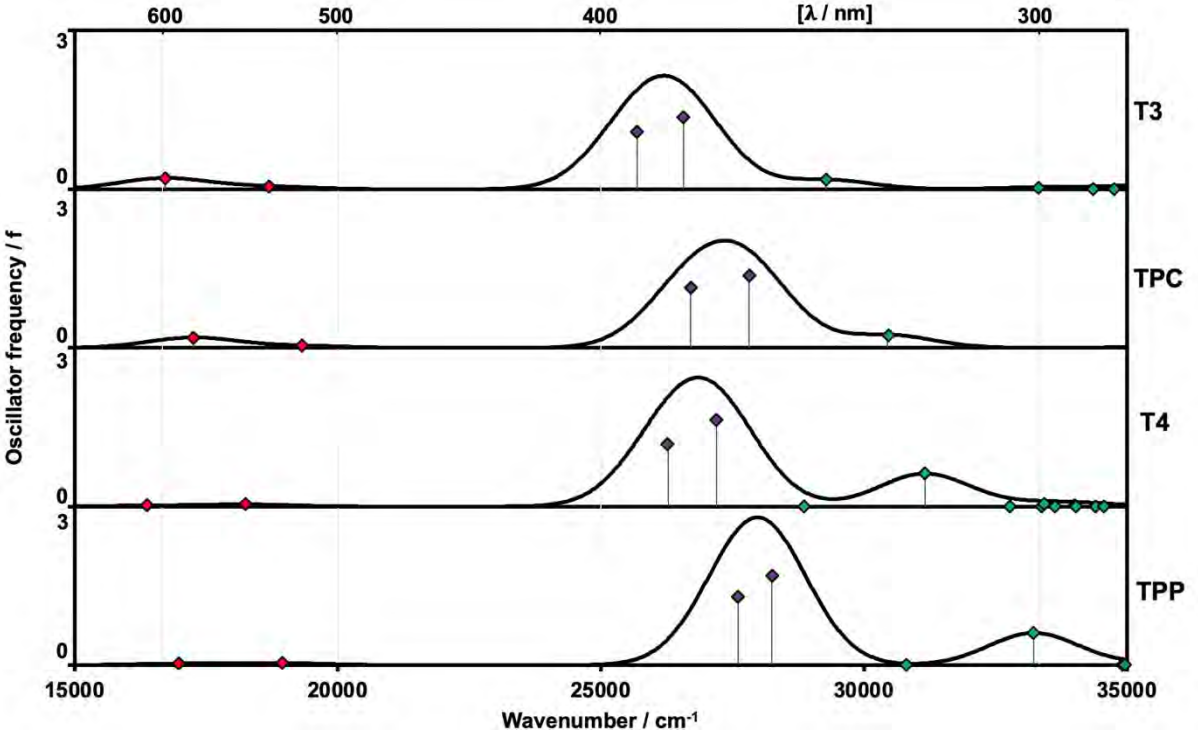

Figure 7.3. The simulated UV-visible spectra comparing the thienyl-substituted symmetric porphyrin (**T4**) and corrole (**T3**) to the phenyl-substituted tetraphenylporphyrin (**TPP**) and triphenylcorrole (**TPC**) as well as the TD spectral bands depicted as purple diamonds for the B (allowed) band and red diamonds for the Q (forbidden) transitions. A wavelength scale is included for reference.

Upon comparison of the experimental ground state absorption spectra of the porphyrins and corroles, key trends can be discerned. The lowering of the corroles symmetry lifts the degeneracy of the LUMO orbitals (i.e. **-s** and **-s**), as seen in **Figure 7.2**. There is a significant intensification of the Q bands of the corrole compared to those of the porphyrins (**Figure 7.3**). This increase in ΔLUMO cause a mixing of the allowed and forbidden properties of the B and Q transitions. Additionally, there is a decrease in the HOMO–LUMO gap in the corrole analogues, which leads to a red-shifted spectrum of the corroles, specifically in the Q bands. Ding *et al.* observed a relative blue shift of the B band of **TPC** compared to **TPP**, which was not consistent with what was found in the theoretical calculations.[137] The ground-state absorption spectra of porphyrinoids are highly dependent on the solvent system, however.[138]

The thiophene substituent was explored to red shift the absorption spectra of the porphyrins and corroles, as can be observed in **Figure 7.3.** Additionally, **Figure 7.2.** shows the decreased HOMO–LUMO gap, which gives rise to the observed red shift, which is further emphasized by the trends in the experimental data provided in **Table 7.1**.[133] This makes the thiophene substituent more suitable for PDT applications since the aim is to excite the molecules with a wavelength of light within the therapeutic window. A summary of the calculated UV-visible absorption spectra is given in **Table 7.1**.

Table 7.1. The calculated UV-visible absorption spectra of the B3LYP optimised geometries of **TPP**, **T4**, **TPC**, and **T3** obtained using the CAM-B3LYP functional of the Gaussian 09 software packages[108] with SDD basis sets.

			TPP		
	#[a]	**λ_{exp}[b]**	**λ_{calc}[c]**	***f*[d]**	**Wavefunction =[e]**
Q	1	549[133]	589	0.03	**65% s → -s; 35% a → -a; …**
Q	2	514[133]	528	0.04	**61% s → -a; 38% a → -s; …**
B	3	419[133]	362	1.30	**62% a → -a; 20% s → -s; …**
B	4		354	1.69	**62% a → -s; 41% s → -a; …**
			T4		
	#[a]	**λ_{exp}[b]**	**λ_{calc}[c]**	***f*[d]**	**Wavefunction =[e]**
Q	1	552	611	0.02	**60% s → -s; 39% a → -a; …**
Q	2	520	548	0.04	**59% s → -a; 40% a → -s; …**
B	3	425	381	1.17	**55% a → -a; 32% s → -s; …**
B	4		368	1.64	**59% a → -s; 51% s → -a; …**
			TPC		
	#[a]	**λ_{exp}[b]**	**λ_{calc}[c]**	***f*[d]**	**Wavefunction =[e]**
Q	1	615[133]	579	0.19	**68% s → -a; 19% a → -s; …**
Q	2	572[133]	518	0.04	**46% a → -a; 41% s → -s; …**
B	3	414[133]	374	1.14	**51% s → -s; 46% a → -a; …**
B	4		359	1.36	**71% a → -s; 20% s → -a; …**
			T3		
	#[a]	**λ_{exp}[b]**	**λ_{calc}[c]**	***f*[d]**	**Wavefunction =[e]**
Q	1	627	598	0.21	**67% s → -a; 18% a → -s; …**
Q	2	585	535	0.05	**43% a → -a; 42% s → -s; …**
B	3	427	389	1.09	**49% s → -s; 47% a → -a; …**
B	4		376	1.36	**71% a → -s; 19% s → -a; …**

[a]Excited state number assigned in increasing energy in the TD-DFT calculations. [b]Experimental wavelengths in nanometers. [c]Calculated wavelengths in nanometers. [d]Calculated oscillator strengths. [e]Wavefunctions describing the MOs involved in the transition based on eigenvectors predicted by TD-DFT. Only one-electron transition contributions of more than 5% are included. **a**, **s**, **-a**, and **-s** refer to the MO nomenclature of Michl's perimeter model.[46-49] One-electron transitions between these orbitals are highlighted in bold.

The second series of molecules compares the initial synthetic goal of this thesis: free base, Sn(IV) and P(V) high- and low-symmetry porphyrins and corroles (**T4**, **Sn(IV)T4**, **P(V)T4**, **T3**, **Sn(IV)T3**, **P(V)T3**, **T2Q2**, **Sn(IV)T2Q2**, **P(V)T2Q2**, **T2Q**, **Sn(IV)T2Q** and **P(V)T2Q**) (**Figure 7.4.1** and **Figure 7.4.2**).

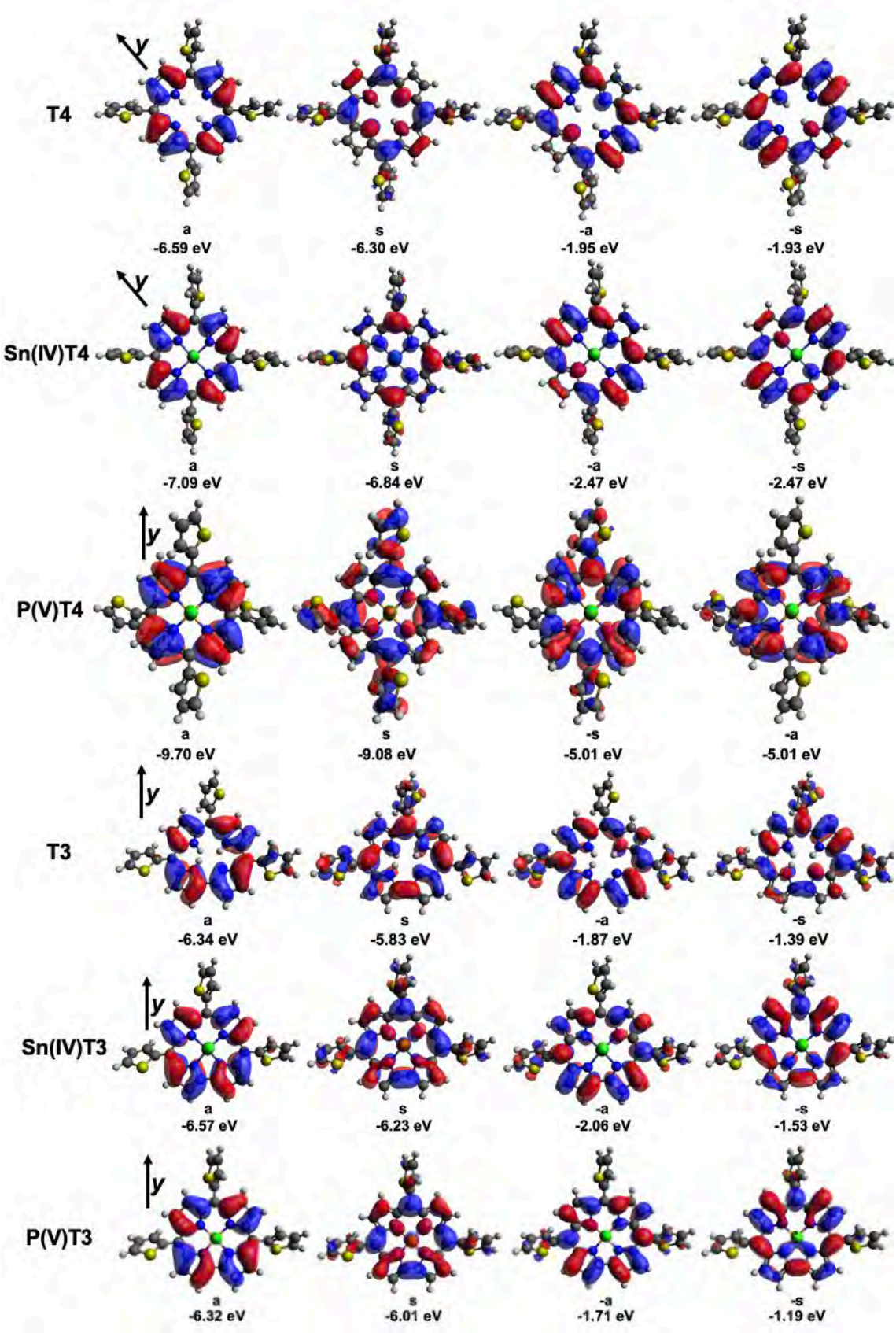

Figure 7.4.1. The nodal patterns of the high-symmetry molecules in the non-brominated series of molecules: **T4**, **Sn(IV)T4**, **P(V)T4**, **T3**, **Sn(IV)T3** and **P(V)T3** at an isosurface value of 0.02 a.u., and the MO energies of the **a**, **s**, **-a**, and **-s** MOs. The black arrow indicates the orientation of the axis along which the orbitals were assigned according to Michl's perimeter model.

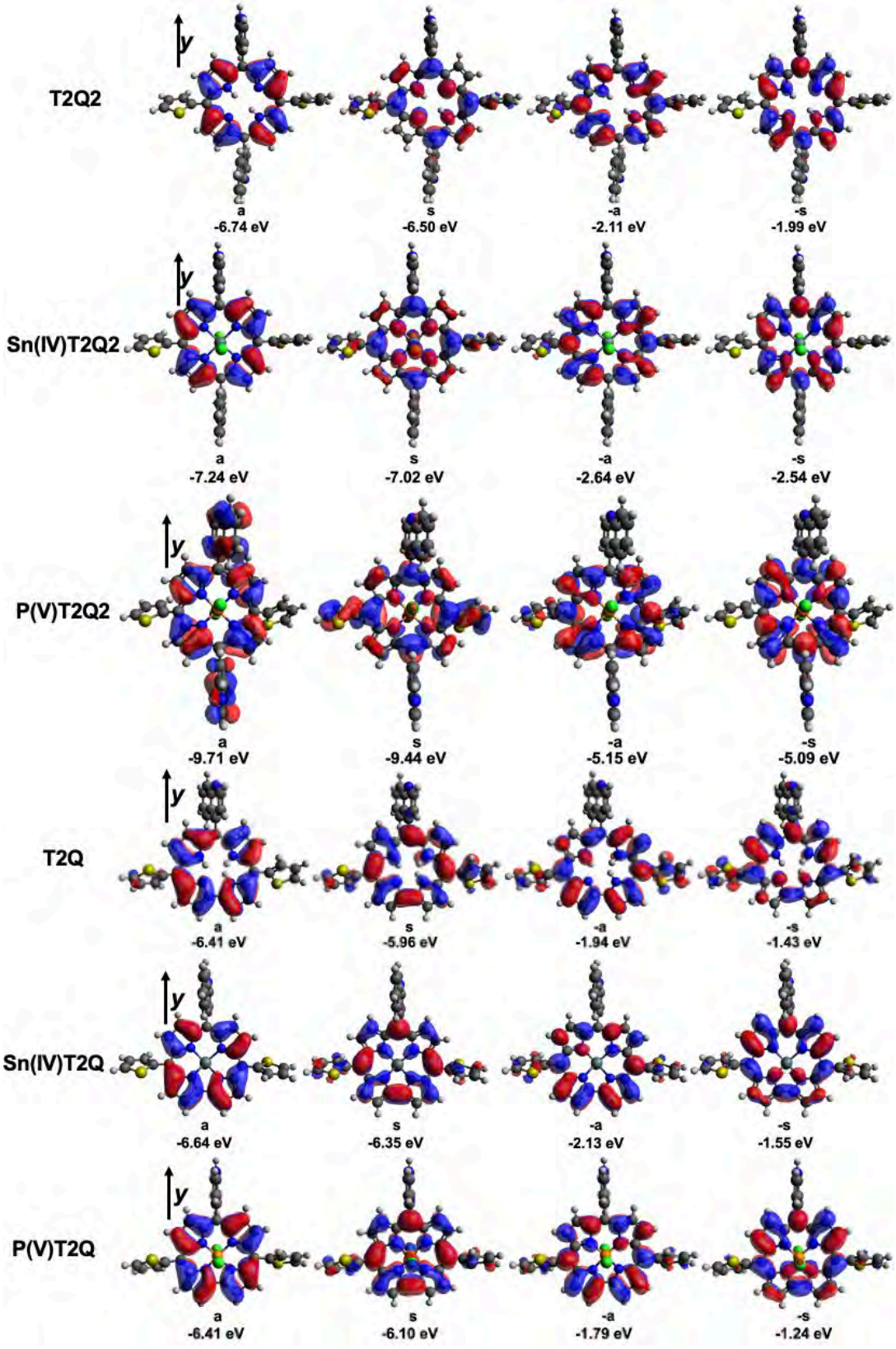

Figure 7.4.2. The nodal patterns of the low-symmetry molecules in the non-brominated series of molecules: **T2Q2**, **Sn(IV)T2Q2**, **P(V)T2Q2**, **T2Q**, **Sn(IV)T2Q** and **P(V)T2Q** at an isosurface value of 0.02 a.u., and the MO energies of the **a**, **s**, **-a**, and **-s** MOs. The black arrow indicates the orientation of the axis along which the orbitals were assigned according to Michl's perimeter model.

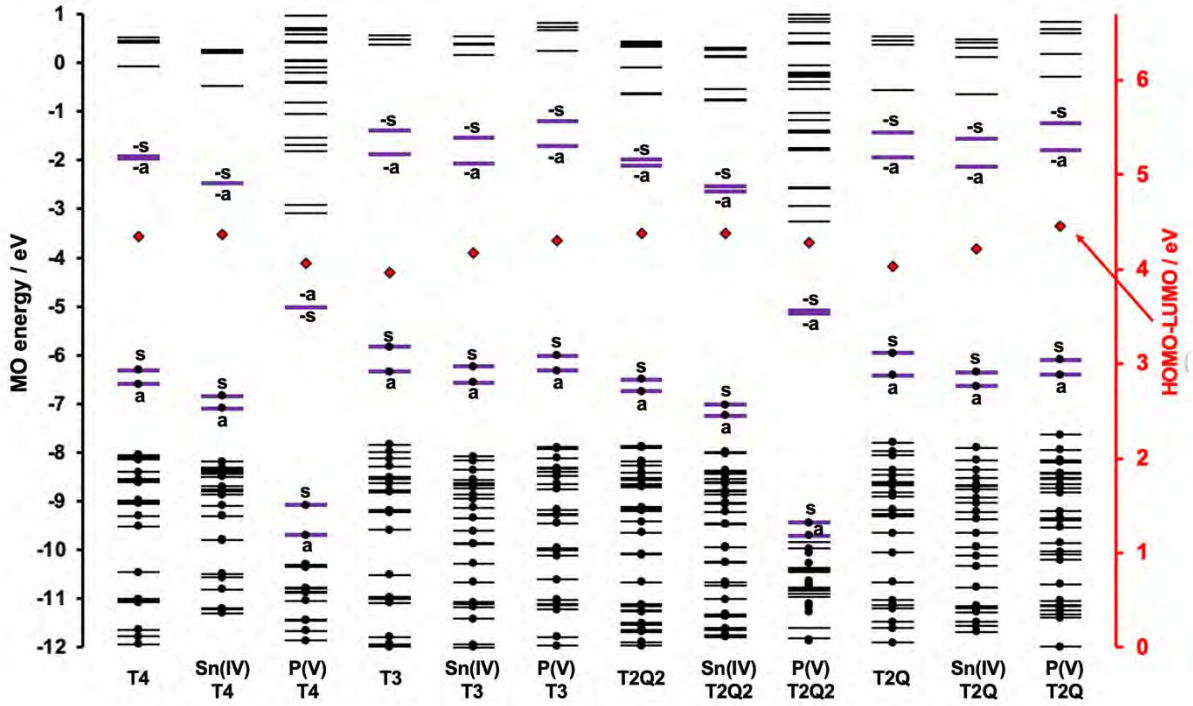

Figure 7.5. The relative energies of the molecular orbitals comparing the series of non-brominated compounds: **T4**, **Sn(IV)T4**, **P(V)T4**, **T3**, **Sn(IV)T3**, **P(V)T3**, **T2Q2**, **Sn(IV)T2Q2**, **P(V)T2Q2**, **T2Q**, **Sn(IV)T2Q**, and **P(V)T2Q**. The four-frontier molecular orbitals energies are bolded and in purple, and the occupied orbitals are denoted by circular black markers. A secondary axis is used to plot the HOMO–LUMO energy gap in red diamonds.

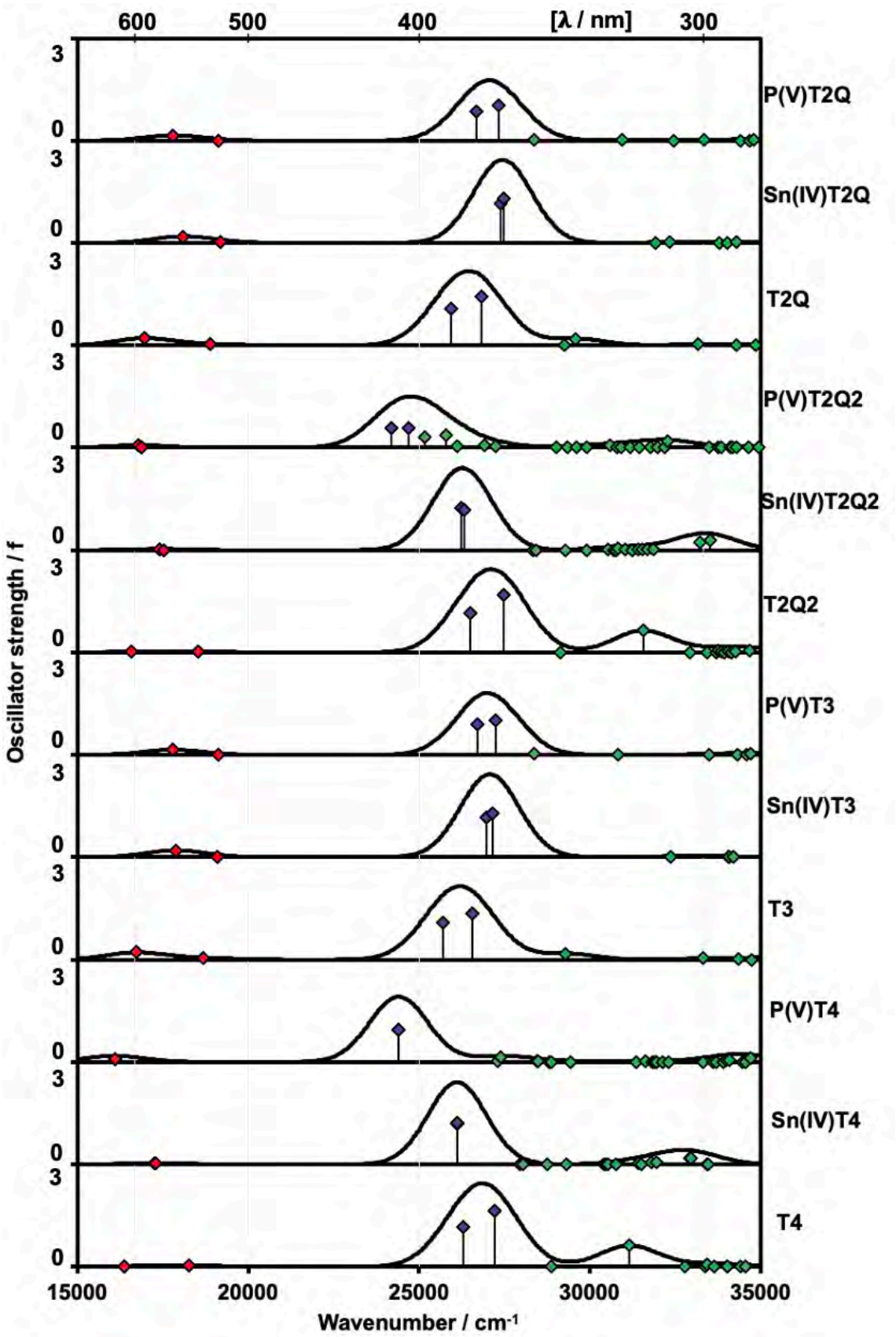

Figure 7.6. The simulated UV-visible spectra comparing the series of non-brominated porphyrins and corroles: **T4**, **Sn(IV)T4**, **P(V)T4**, **T3**, **Sn(IV)T3**, **P(V)T3**, **T2Q2**, **Sn(IV)T2Q2**, **P(V)T2Q2**, **T2Q**, **Sn(IV)T2Q**, and **P(V)T2Q**, as well as the TD spectral bands depicted as purple diamonds for the B (allowed) band and red diamonds for the Q (forbidden) transitions. A wavelength scale is included for reference.

Table 7.2. The calculated UV-visible absorption spectra of the B3LYP optimised geometry of **T4**, **Sn(IV)T4**, **P(V)T4**, **T3**, **Sn(IV)T3**, **P(V)T3**, **T2Q2**, **Sn(IV)T2Q2**, **P(V)T2Q2**, **T2Q**, **Sn(IV)T2Q**, and **P(V)T2Q** obtained using the CAM-B3LYP functional of the Gaussian 09 software packages[108] with SDD basis sets.

			T4		
	#[a]	**λ_{exp}[b]**	**λ_{calc}[c]**	***f*[d]**	**Wavefunction =[e]**
Q	1	552	611	0.02	**60% s → -s; 39% a → -a; …**
Q	2	520	548	0.04	**59% s → -a; 40% a → -s; …**
B	3	425	381	1.17	**55% a→ -a; 32% s → -s; …**
B	4		368	1.64	**59% a → -s; 41% s → -a; …**
			Sn(IV)T4		
	#[a]	**λ_{exp}[b]**	**λ_{calc}[c]**	***f*[d]**	**Wavefunction =[e]**
Q	1	613	579	0.02	**58% s → -a; 39% a → -s; …**
Q	2	567	579	0.02	**57% s → -s; 39% a → -a; …**
B	3	437	383	1.20	**55% a → -s; 37% s → -a; …**
B	4		383	1.21	**55% a → -a; 37% s → -s; …**
			P(V)T4		
	#[a]	**λ_{exp}[b]**	**λ_{calc}[c]**	***f*[d]**	**Wavefunction =[e]**
Q	1	--	622	0.09	**57% s → -a; 25% a → -s; …**
Q	2	--	621	0.09	**57% s → -s: 25% a → -a; …**
B	3	--	410	0.95	**46% a → -s; 21% s → -a; …**
B	4	--	410	0.95	**46% a → -a; 21% s → -s; …**
			T3		
	#[a]	**λ_{exp}[b]**	**λ_{calc}[c]**	***f*[d]**	**Wavefunction =[e]**
Q	1	627	598	0.21	**67% s → -a; 18% a → -s; …**
Q	2	585	535	0.05	**43% a → -a; 42% s → -s; …**
B	3	427	389	1.09	**49% s → -s; 47% a → -a; …**
B	4		376	1.36	**71% a → -s; 19% s → -a; …**
			Sn(IV)T3		
	#[a]	**λ_{exp}[b]**	**λ_{calc}[c]**	***f*[d]**	**Wavefunction =[e]**
Q	1	--	560	0.20	**74% s → -a; 25% a → -s; …**
Q	2	--	524	0.00	**60% a → -a; 38% s → -s; …**
B	3	--	371	1.15	**58% s → -s; 36% a → -a; …**
B	4	--	368	1.29	**67% a → -s; 24% s → -a; …**
			P(V)T3		
	#[a]	**λ_{exp}[b]**	**λ_{calc}[c]**	***f*[d]**	**Wavefunction =[e]**
Q	1	--	562	0.15	**75% s → -a; 24% a → -s; …**
Q	2	--	523	0.00	**57% a → -a; 42% s → -s; …**
B	3	--	374	0.88	**57% s → -s; 42% a → -a; …**
B	4	--	367	1.01	**72% a → -s; 23% s → -a; …**

			T2Q2		
	#[a]	**λ_{exp}[b]**	**λ_{calc}[c]**	***f*[d]**	**Wavefunction =[e]**
Q	1	554	603	0.02	**34% s → -a; 26% s → -s; …**
Q	2	518	540	0.03	**29% s → -s; 28% s → -a; …**
B	3	423	377	1.16	**29% a → -a; 26% a → -s; …**
B	4		364	1.68	**32% a → -s; 25% a → -a; …**
			Sn(IV)T2Q2		
	#[a]	**λ_{exp}[b]**	**λ_{calc}[c]**	***f*[d]**	**Wavefunction =[e]**
Q	1	602	575	0.03	**62% s → -a; 37% a → -s; …**
Q	2	561	571	0.00	**56% s → -s; 43% a → -s; …**
B	3	432	381	1.25	**54% a → -a; 41% s → -s; …**
B	4		380	1.16	**59% a → -s; 35% s → -s; …**
			P(V)T2Q2		
	#[a]	**λ_{exp}[b]**	**λ_{calc}[c]**	***f*[d]**	**Wavefunction =[e]**
Q	1	--	596	0.06	**60% s → -a; 25% a → -s; …**
Q	2	--	595	0.01	**56% s → -s; 28% a → -a; …**
B	3	--	413	0.58	**66% a → -s; 24% s → -a; …**
B	4	--	405	0.58	**31% a → -a; 27% s → -s; …**
			T2Q		
	#[a]	**λ_{exp}[b]**	**λ_{calc}[c]**	***f*[d]**	**Wavefunction =[e]**
Q	1	--	590	0.21	**67% s → -a; 19% a → -s; …**
Q	2	--	529	0.04	**47% a → -a; 39% s → -s; …**
B	3	--	386	1.08	**52% s → -s; 44% a → -a; …**
B	4	--	373	1.41	**71% a → -s; 20% s → -a; …**
			Sn(IV)T2Q		
	#[a]	**λ_{exp}[b]**	**λ_{calc}[c]**	***f*[d]**	**Wavefunction =[e]**
Q	1	--	553	0.19	**74% s → -a; 25% a → -s; …**
Q	2	--	521	0.02	**63% a → -a; 36% s → -s; …**
B	3	--	365	1.15	**61% s → -s; 35% a → -s; …**
B	4	--	364	1.29	**68% a → -s; 24% s → -a; …**
			P(V)T2Q		
	#[a]	**λ_{exp}[b]**	**λ_{calc}[c]**	***f*[d]**	**Wavefunction =[e]**
Q	1	--	562	0.15	**75% s → -a; 23% a → -s; …**
Q	2	--	523	0.01	**56% a → -a; 42% s → -s; …**
B	3	--	375	0.85	**55% s → -s; 42% a → as; …**
B	4	--	366	1.04	**73% a → -s; 23% s → -a; …**

[a]Excited state number assigned in increasing energy in the TD-DFT calculations. [b]Experimental wavelengths in nanometers. [c]Calculated wavelengths in nanometers. [d]Calculated oscillator strengths. [e]Wavefunctions describing the MOs involved in the transition based on eigenvectors predicted by TD-DFT. Only one-electron transition contributions of more than 5% are included. **a**, **s**, **-a**, and **-s** refer to the MO nomenclature of Michl's perimeter model.[46-49] One-electron transitions between these orbitals are highlighted in bold.

The P(V) porphyrins exhibit a marked stabilisation in their MO energies because they are cationic (**Figure 7.5**): they retain two axial ligands and bond ionically to the third, existing with an overall positive charge in solution. In addition, they have relatively red-shifted calculated absorption spectra (**Figure 7.6**). P(V) corroles, on the other hand, are destabilised compared to their free base and Sn(IV) counterparts. This is due to the trianion that this porphyrin analogue forms upon deprotonation and metalation; the corrole can coordinate central metal ions in higher oxidation states and retains two axial ligands, so there is no overall charge.

Upon the introduction of Sn(IV), a heavy atom, into the centre of the ligands, there is a relative stabilisation of the MO energies and a blue-shifting of the Q band envelopes. The blue shift observed in the Q bands can be attributed to the increased HOMO–LUMO gap seen upon metalation (**Figure 7.5**). The metalation is done to improve the singlet oxygen quantum yields of the molecules to facilitate a more efficacious therapy.

There is no significant difference in the electronic and spectral properties of the high- and low-symmetry molecules.

A summary of the calculated UV-visible absorption spectra is given in **Table 7.2**.

The third series of molecules compares the non-brominated thiophene-substituted porphyrin to its brominated counterpart (substituted at the 4-position of the thiophene ring) (**Figure 7.7**).

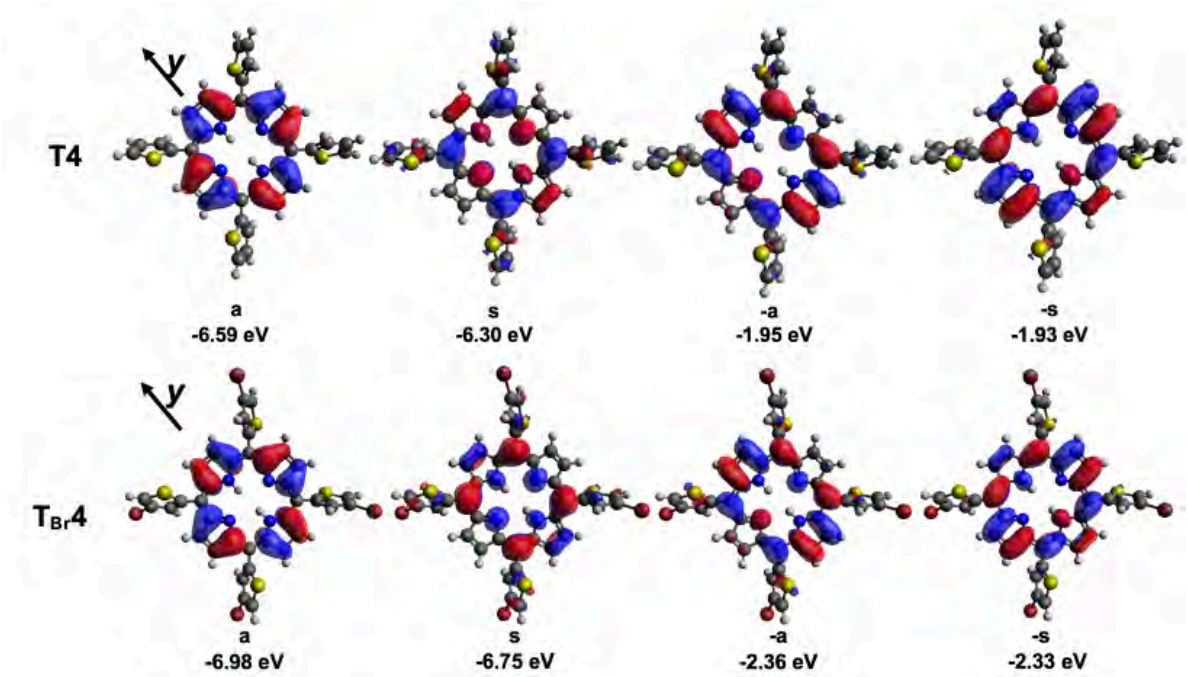

Figure 7.7. The nodal patterns of **T4** and **$T_{Br}4$** at an isosurface value of 0.02 a.u., and the MO energies of the **a**, **s**, **-a**, and **-s** MOs.

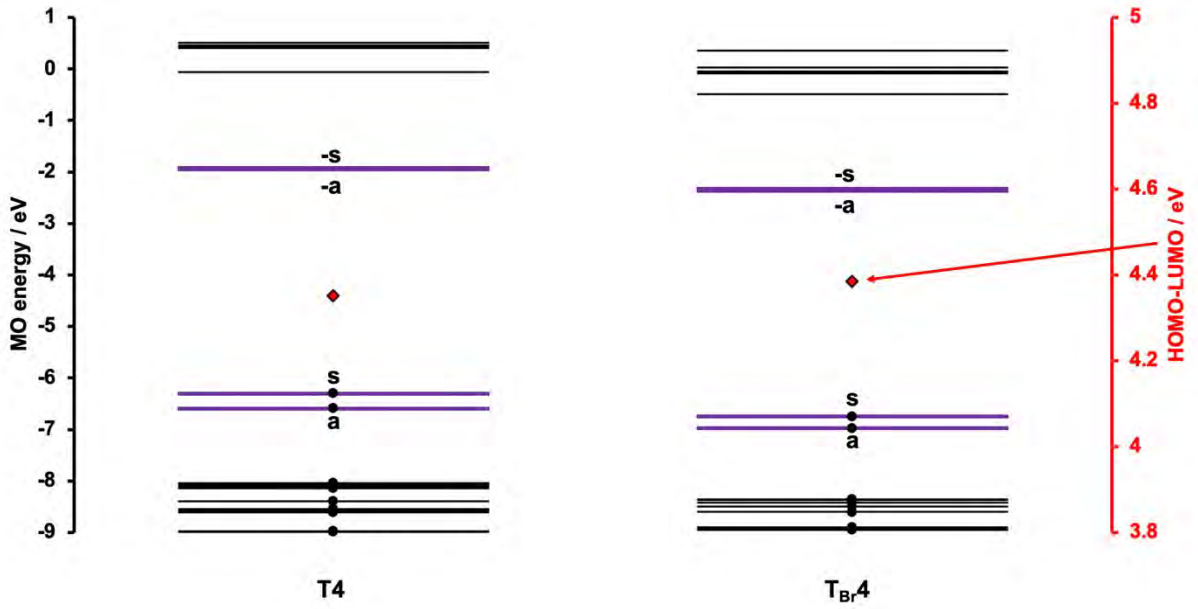

Figure 7.8. The relative energies of the molecular orbitals comparing the non-brominated thienyl-substituted high-symmetry porphyrin (**T4**) and brominated thienyl-substituted porphyrin (**$T_{Br}4$**). The four-frontier molecular orbitals energies are bolded and in purple, and the occupied orbitals are denoted by circular black markers. A secondary axis is used to plot the HOMO–LUMO energy gap in red diamonds.

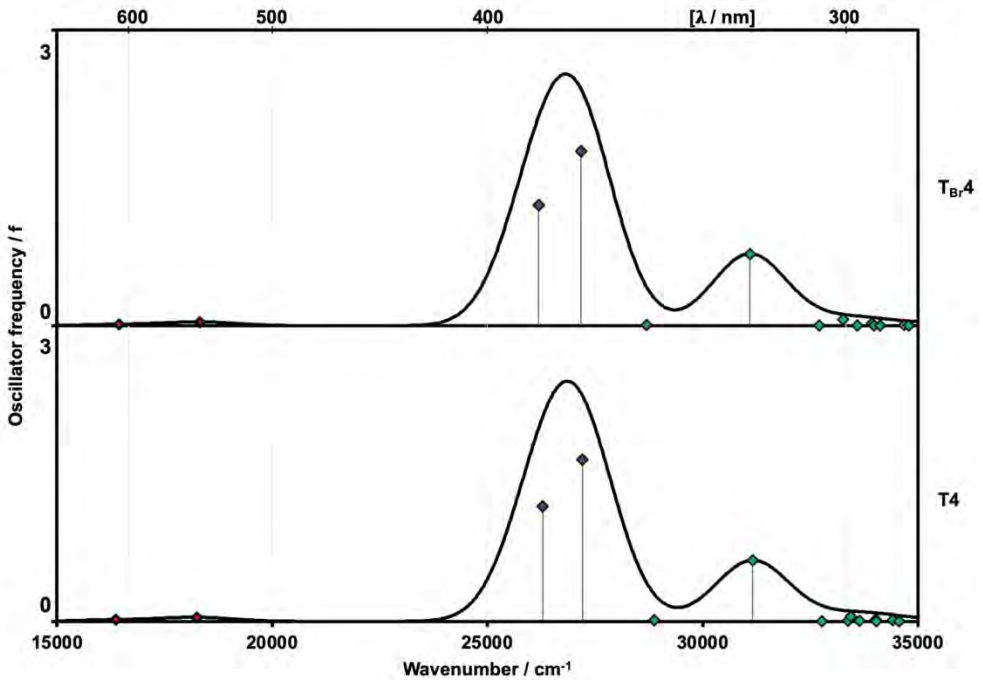

Figure 7.9. The simulated UV-visible spectra comparing the non-brominated thienyl-substituted high-symmetry porphyrin (**T4**) and brominated thienyl-substituted porphyrin (**T_{Br}4**), as well as the TD spectral bands depicted as purple diamonds for the B (allowed) band and red diamonds for the Q (forbidden) transitions. A wavelength scale is included for reference.

Table 7.3. The calculated UV-visible absorption spectra of the B3LYP optimised geometry of **T4** and **T_{Br}4** obtained using the CAM-B3LYP functional of the Gaussian 09 software packages[108] with SDD basis sets.

			T4		
	#[a]	**λ_{exp}[b]**	**λ_{calc}[c]**	***f*[d]**	**Wavefunction =[e]**
Q	1	552	611	0.02	**60% s → -s; 39% a → -a; …**
Q	2	520	548	0.04	**59% s → -a; 40% a → -s; …**
B	3	425	381	1.17	**55% a→ -a; 32% s → -s; …**
B	4		368	1.64	**59% a → -s; 41% s → -a; …**
			T_{Br}4		
	#[a]	**λ_{exp}[b]**	**λ_{calc}[c]**	***f*[d]**	**Wavefunction =[e]**
Q	1	554	608	0.01	**58% s → -s; 41% a → -a; …**
Q	2	521	546	0.04	**58% s → -a; 41% a → -s; …**
B	3	425	382	1.23	**54% a → -a; 33% s → -s; …**
B	4		368	1.77	**58% a → -s; 43% s → -a; …**

[a]Excited state number assigned in increasing energy in the TD-DFT calculations. [b]Experimental wavelengths in nanometers. [c]Calculated wavelengths in nanometers. [d]Calculated oscillator strengths. [e]Wavefunctions describing the MOs involved in the transition based on eigenvectors predicted by TD-DFT. One-electron transition contributions of more than 5% are included. **a**, **s**, **-a**, and **-s** refer to the MO nomenclature

of Michl's perimeter model.[46-49] One-electron transitions between these orbitals are highlighted in bold.

A slightly increased HOMO–LUMO gap is predicted in the brominated porphyrin, which leads to blue-shifted spectral bands, as observed specifically in the Q band region (**Figure 7.8**), but this was not observed experimentally (**Table 7.3**). There is no significant difference in the simulated UV-visible spectra of the porphyrin upon incorporation of the heavy atom, bromine (**Figure 7.9**). The rationale for including the bromines was to improve the rate of ISC to populate the triplet manifold of the photosensitiser more effectively, leading to the generation of more singlet oxygen.

The fourth series of molecules compare the brominated high- and low-symmetry porphyrins and corroles: **T_{Br}4**, **Sn(IV)T_{Br}4**, **P(V)T_{Br}4**, **T_{Br}3**, **Sn(IV)T_{Br}3**, **P(V)T_{Br}3**, **T_{Br}2Q2**, **Sn(IV)T_{Br}2Q2**, **P(V)T_{Br}2Q2**, **T_{Br}2Q**, **Sn(IV)T_{Br}2Q**, and **P(V)T_{Br}2Q** (**Figure 7.10.1** and **Figure 7.10.2**).

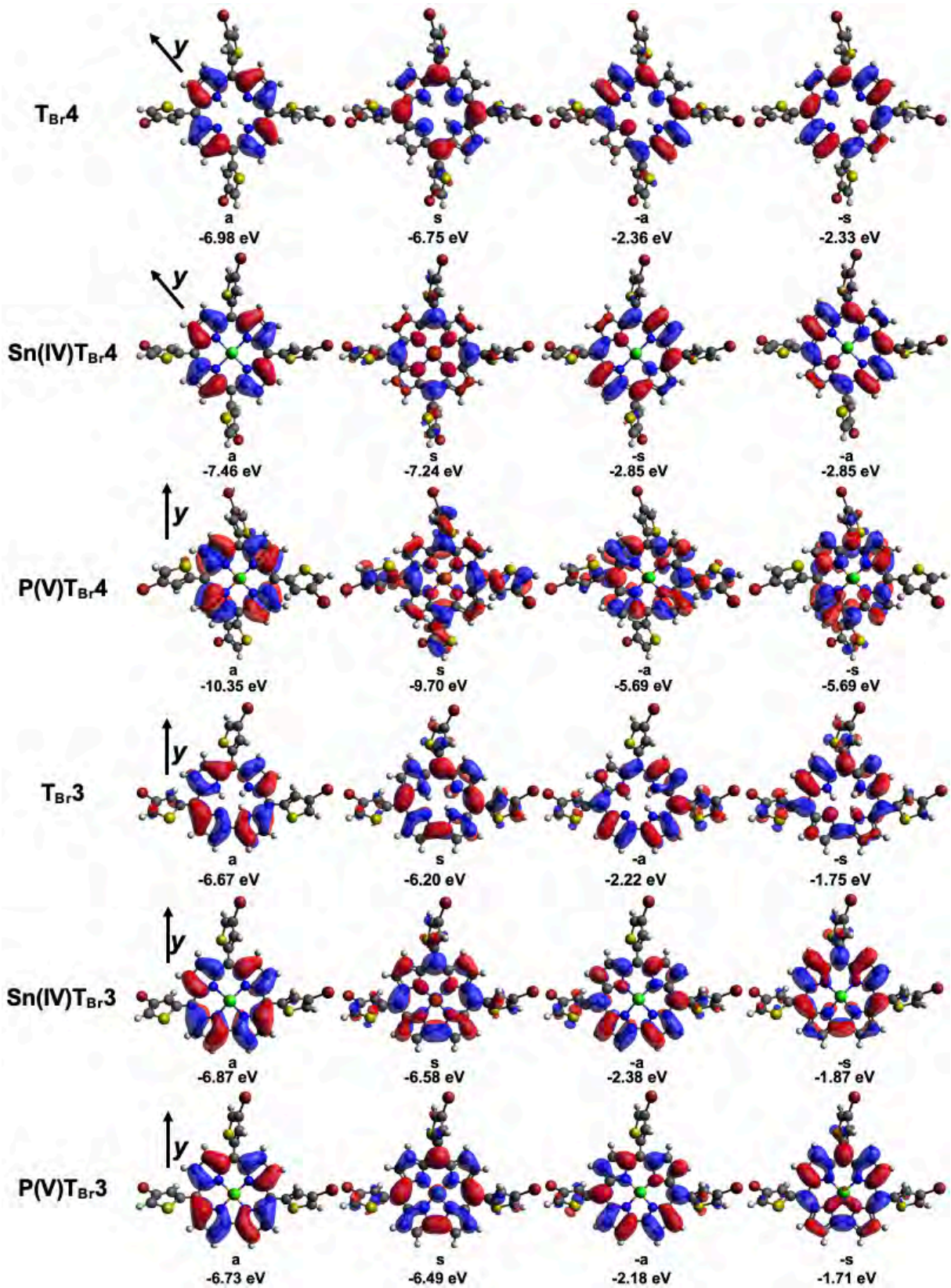

Figure 7.10.1. The nodal patterns of the high-symmetry molecules in the brominated series of molecules: **T$_{Br}$4**, **Sn(IV)T$_{Br}$4**, **P(V)T$_{Br}$4**, **T$_{Br}$3**, **Sn(IV)T$_{Br}$3**, and **P(V)T$_{Br}$3** at an isosurface value of 0.02 a.u., and the MO energies of the **a**, **s**, **-a**, and **-s** MOs. The black arrow indicates the orientation of the axis along which the orbitals were assigned according to Michl's perimeter model.

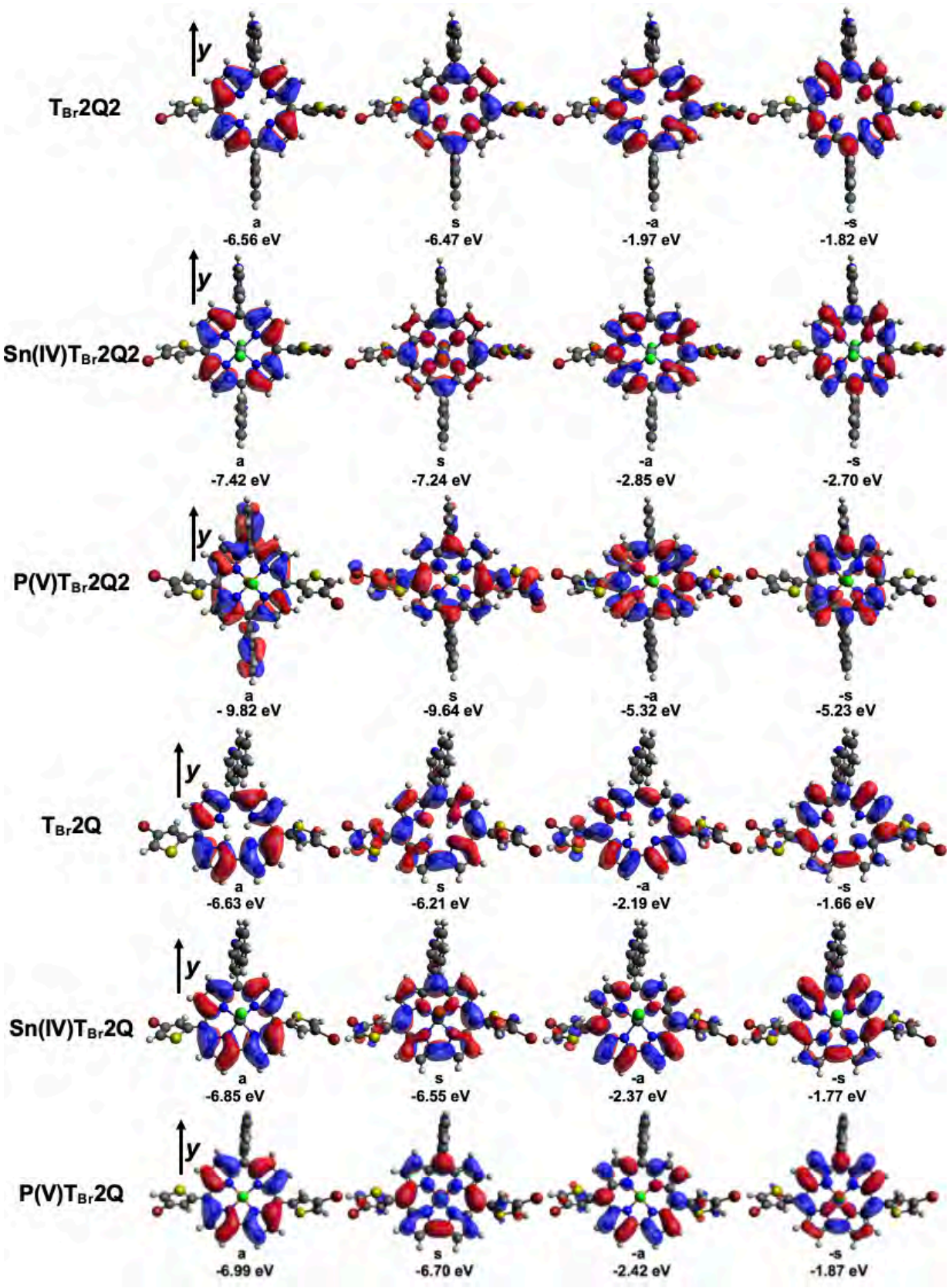

Figure 7.10.2. The nodal patterns of the high-symmetry molecules in the brominated series of molecules: **T$_{Br}$2Q2**, **Sn(IV)T$_{Br}$2Q2**, **P(V)T$_{Br}$2Q2**, **T$_{Br}$2Q**, **Sn(IV)T$_{Br}$2Q**, and **P(V)T$_{Br}$2Q** at an isosurface value of 0.02 a.u., and the MO energies of the **a**, **s**, **-a**, and **-s** MOs. The black arrow indicates the orientation of the axis along which the orbitals were assigned according to Michl's perimeter model.

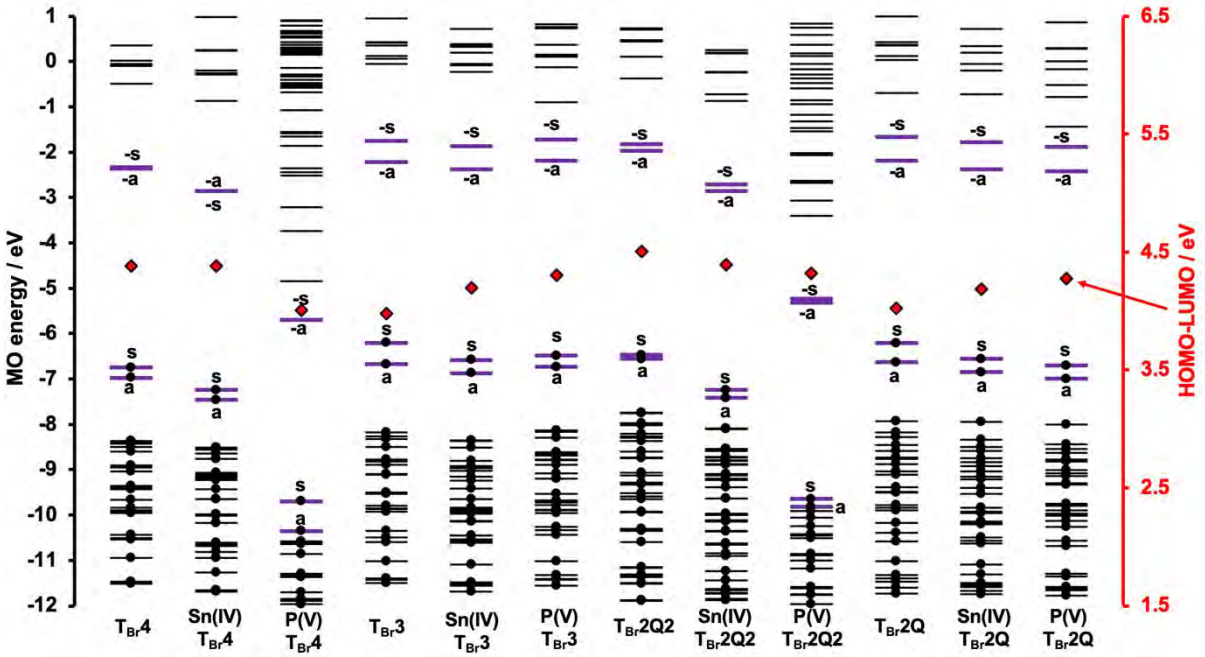

Figure 7.11. The relative energies of the molecular orbitals comparing the series of brominated compounds (**$T_{Br}4$**, **Sn(IV)$T_{Br}4$**, **P(V)$T_{Br}4$**, **$T_{Br}3$**, **Sn(IV)$T_{Br}3$**, **P(V)$T_{Br}3$**, **$T_{Br}2Q2$**, **Sn(IV)$T_{Br}2Q2$**, **P(V)$T_{Br}2Q2$**, **$T_{Br}2Q$**, **Sn(IV)$T_{Br}2Q$**, and **P(V)$T_{Br}2Q$**). The four-frontier molecular orbitals energies are bolded and in purple, and the occupied orbitals are denoted by circular black markers. A secondary axis is used to plot the HOMO–LUMO energy gap in red diamonds.

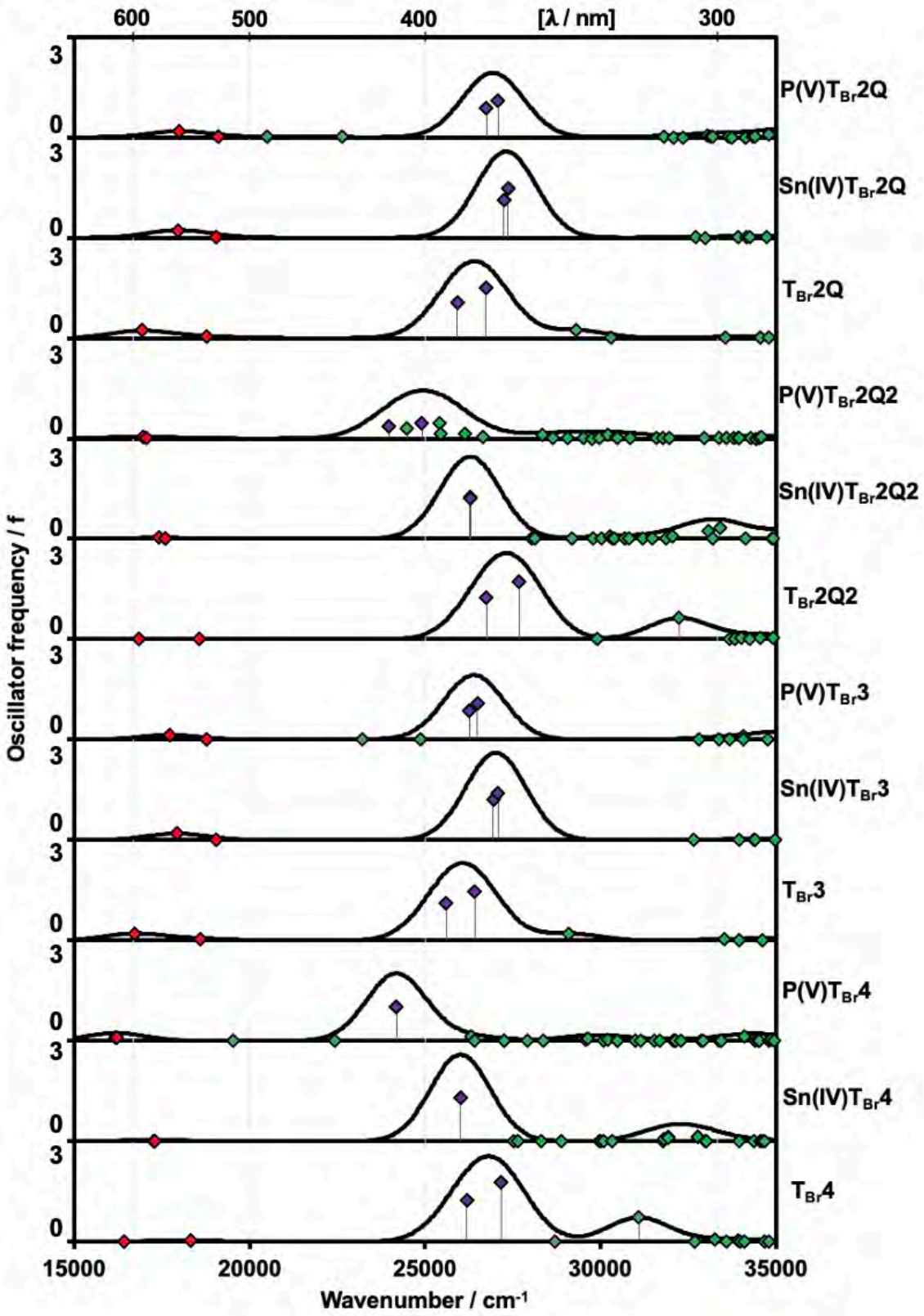

Figure 7.12. The simulated UV-visible spectra comparing the series of brominated porphyrins and corroles: **T$_{Br}$4**, **Sn(IV)T$_{Br}$4**, **P(V)T$_{Br}$4**, **T$_{Br}$3**, **Sn(IV)T$_{Br}$3**, **P(V)T$_{Br}$3**, **T$_{Br}$2Q2**, **Sn(IV)T$_{Br}$2Q2**, **P(V)T$_{Br}$2Q2**, **T$_{Br}$2Q**, **Sn(IV)T$_{Br}$2Q**, and **P(V)T$_{Br}$2Q**, as well as the TD spectral bands depicted as purple diamonds for the B (allowed) band and red diamonds for the Q (forbidden) transitions. A wavelength scale is included for reference.

Table 7.4. The calculated UV-visible absorption spectra of the B3LYP optimised geometry of **$T_{Br}4$**, **Sn(IV)$T_{Br}4$**, **P(V)$T_{Br}4$**, **$T_{Br}3$**, **Sn(IV)$T_{Br}3$**, **P(V)$T_{Br}3$**, **$T_{Br}2Q2$**, **Sn(IV)$T_{Br}2Q2$**, **P(V)$T_{Br}2Q2$**, **$T_{Br}2Q$**, **Sn(IV)$T_{Br}2Q$**, and **P(V)$T_{Br}2Q$** obtained using the CAM-B3LYP functional of the Gaussian 09 software packages[108] with SDD basis sets.

			$T_{Br}4$		
	#[a]	**λ_{exp}[b]**	**λ_{calc}[c]**	***f*[d]**	**Wavefunction =[e]**
Q	1	554	608	0.01	**58% s → -s; 41% a → -a; …**
Q	2	521	546	0.04	**58% s → -a; 41% a → -s; …**
B	3	425	382	1.23	**54% a → -a; 33% s → -s; …**
B	4		368	1.77	**58% a → -s; 43% s → -a; …**
			Sn(IV)$T_{Br}4$		
	#[a]	**λ_{exp}[b]**	**λ_{calc}[c]**	***f*[d]**	**Wavefunction =[e]**
Q	1	609	579	0.02	**59% s → -s; 41% a → -a; …**
Q	2	566	579	0.02	**58% s → -a; 41% a → -s; …**
B	3	434	384	1.29	**57% a → -a; 39% s → -s; …**
B	4		384	1.29	**57% a → -s; 39% s → -s; …**
			P(V)$T_{Br}4$		
	#[a]	**λ_{exp}[b]**	**λ_{calc}[c]**	***f*[d]**	**Wavefunction =[e]**
Q	1	--	618	0.12	**45% s → -a; 23% s → -s; …**
Q	2	--	617	0.12	**45% s → -s; 23% s → -a; …**
B	5	--	414	1.01	**43% a → -a; 20% a → -s; …**
B	6	--	413	1.01	**43% a → -s; 20% a → -a; …**
			$T_{Br}3$		
	#[a]	**λ_{exp}[b]**	**λ_{calc}[c]**	***f*[d]**	**Wavefunction =[e]**
Q	1	-	597	0.21	**64% s → -a; 18% a → -s; …**
Q	2	589	538	0.06	**42% a → -a; 40% s → -s; …**
B	3	427	391	1.12	**48% s → -s; 46% s → -s; …**
B	4		379	1.47	**69% a → -s; 19% s → -a; …**
			Sn(IV)$T_{Br}3$		
	#[a]	**λ_{exp}[b]**	**λ_{calc}[c]**	***f*[d]**	**Wavefunction =[e]**
Q	1	--	558	0.20	**72% s → -a; 26% a → -s; …**
Q	2	--	525	0.01	**61% a → -a; 37% s → -s; …**
B	3	--	371	1.22	**57% s → -s; 34% a → -s; …**
B	4	--	369	1.40	**64% a → -s; 24% s → -a; …**
			P(V)$T_{Br}3$		
	#[a]	**λ_{exp}[b]**	**λ_{calc}[c]**	***f*[d]**	**Wavefunction =[e]**
Q	1	--	564	0.14	**72% s → -a; 26% a → -s; …**
Q	2	--	533	0.00	**57% a → -a; 41% s → -s; …**
B	5	--	381	0.86	**56% s → -s; 41% a → -a; …**
B	6	--	369	1.08	**69% a → -s; 26% s → -a; …**

			$T_{Br}2Q2$		
	#[a]	λ_{exp}[b]	λ_{calc}[c]	*f*[d]	Wavefunction =[e]
Q	1	564	594	0.01	**33% s → -s; 29% a → -a; …**
Q	2	516	538	0.02	**35% s → -a; 26% a → -s; …**
B	3	422	374	1.23	**37% a → -a; 32% s → -s; …**
B	4		361	1.73	**44% a → -s; 33% s → -a; …**
			$Sn(IV)T_{Br}2Q2$		
	#[a]	λ_{exp}[b]	λ_{calc}[c]	*f*[d]	Wavefunction =[e]
Q	1	--	574	0.04	**62% s → -a; 37% a → -s; …**
Q	2	--	568	0.00	**53% s → -s; 46% a → -a; …**
B	3	--	381	1.26	**50% a → -a; 42% s → -s; …**
B	4	--	380	1.20	**58% a → -s; 33% s → -a; …**
			$P(V)T_{Br}2Q2$		
	#[a]	λ_{exp}[b]	λ_{calc}[c]	*f*[d]	Wavefunction =[e]
Q	1	--	590	0.05	**55% s → -a; 20% a → -s; …**
Q	2	--	586	0.01	**49% s → -s; 23% a → -a; …**
B	3	--	417	0.37	**67% a → -s; 18% s → -a; …**
B	5	--	401	0.47	**59% a → -a; 23% s → -s; …**
			$T_{Br}2Q$		
	#[a]	λ_{exp}[b]	λ_{calc}[c]	*f*[d]	Wavefunction =[e]
Q	1	--	591	0.22	**66% s → -a; 18% a → -s; …**
Q	2	--	533	0.05	**48% a → -a; 37% s → -s; …**
B	3	--	386	1.08	**52% s → -s; 41% a → -a; …**
B	4	--	374	1.49	**69% a → -s; 19% s → -a; …**
			$Sn(IV)T_{Br}2Q$		
	#[a]	λ_{exp}[b]	λ_{calc}[c]	*f*[d]	Wavefunction =[e]
Q	1	--	557	0.22	**74% s → -a; 24% a → -s; …**
Q	2	--	525	0.01	**63% a → -a; 35% s → -s; …**
B	3	--	367	1.12	**64% s → -s; 36% a → -a; …**
B	4	--	365	1.46	**72% a → -s; 25% s → -a; …**
			$P(V)T_{Br}2Q$		
	#[a]	λ_{exp}[b]	λ_{calc}[c]	*f*[d]	Wavefunction =[e]
Q	1	--	555	0.18	**75% s → -a; 24% a → -s; …**
Q	2	--	524	0.01	**56% a → -a; 41% s → -s; …**
B	5	--	374	0.87	**57% s → -s; 40% a → -a; …**
B	6	--	369	1.10	**70% a → -s; 23% s → -a; …**

[a]Excited state number assigned in increasing energy in the TD-DFT calculations. [b]Experimental wavelengths in nanometers. [c]Calculated wavelengths in nanometers. [d]Calculated oscillator strengths. [e]Wavefunctions describing the MOs involved in the transition based on eigenvectors predicted by TD-DFT. One-electron transition contributions of more than 5% are included. **a**, **s**, **-a**, and **-s** refer to the MO nomenclature of Michl's perimeter model.[46-49] One-electron transitions between these orbitals are highlighted in bold.

The same trends were observed for the brominated compounds compared to their non-brominated counterparts: the stabilisation of the P(V) porphyrins due to their overall positive charge and the destabilisation of **P(V)T$_{Br}$3** is seen within this series of molecules (**Figure 7.11**). Interestingly, there is a notable stabilisation of the HOMO orbital of **P(V)T$_{Br}$2Q** in comparison to that of the free base and Sn(IV) complexes of this low-symmetry corrole.

Upon the introduction of Sn(IV), a heavy atom, into the centre of the ligands, there is a relative stabilisation of the MO energies and a blue-shifting of the Q band envelopes. The blue shift observed in the Q bands can be attributed to the increased HOMO–LUMO gap predicted upon metalation (**Figure 7.12**). The metalation is done to improve the singlet oxygen quantum yields of the molecules to facilitate a more efficacious therapy.

There is no significant difference in the electronic or spectral properties of the high- and low-symmetry molecules, as noted in the second series of molecules, despite slightly blue-shifted spectral bands in the low-symmetry molecules (**Table 7.4**) that can be attributed to an increased HOMO–LUMO gap (**Figure 7.12**).

The fifth series of molecules compares the free base and In(III) high- and low-symmetry porphyrins: **T4**, **In(III)T4**, **T_{Br}4**, **In(III)T_{Br}4**, **T2Q2**, **In(III)T2Q2**, **T_{Br}2Q2**, and **In(III)T_{Br}2Q2**. This was done to assess the effect of metalation with In(III) on the optical and electronic properties of the porphyrins (**Figure 7.13.1** and **Figure 7.13.2**).

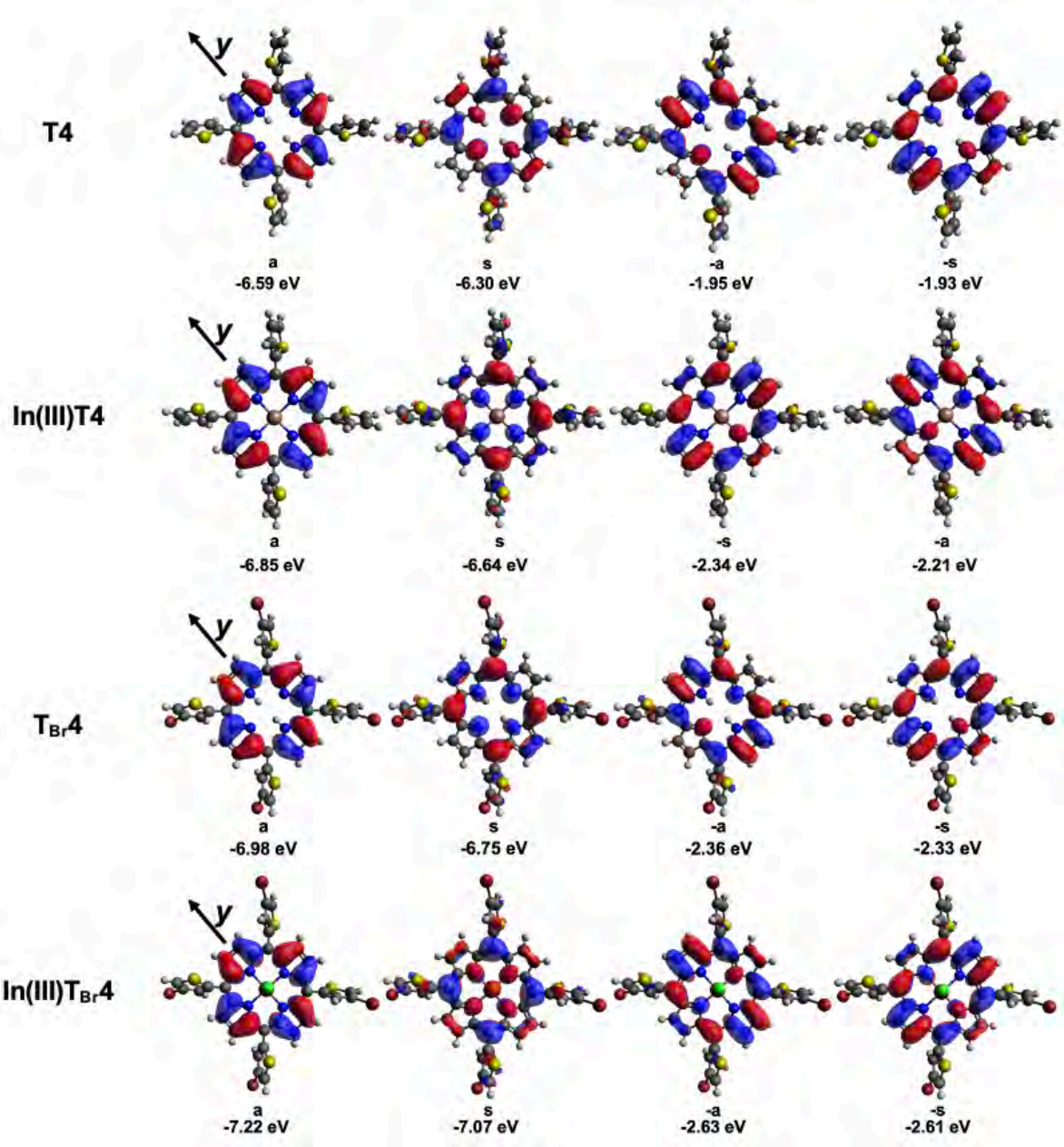

Figure 7.13.1. The nodal patterns of the high-symmetry molecules in the Indium (III) series of porphyrins: **T4**, **In(III)T4**, **T_{Br}4**, and **In(III)T_{Br}4** at an isosurface value of 0.02 a.u., and the MO energies of the **a**, **s**, **-a**, and **-s** MOs. The black arrow indicates the orientation of the axis along which the orbitals were assigned according to Michl's perimeter model.

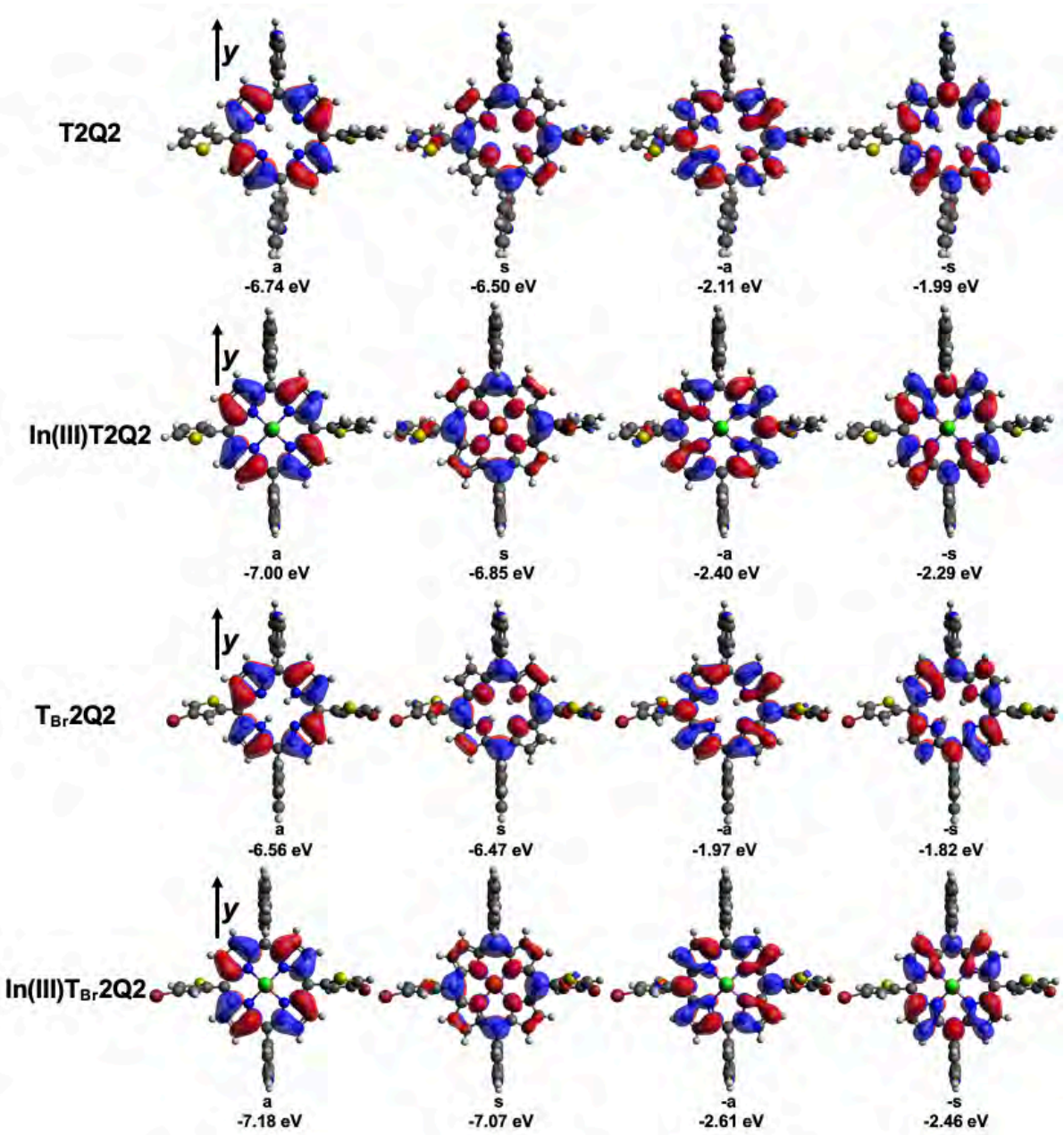

Figure 7.13.2. The nodal patterns of the low-symmetry molecules in the Indium (III) series of porphyrins: **T2Q2**, **In(III)T2Q2**, **T$_{Br}$2Q2**, and **In(III)T$_{Br}$2Q2** at an isosurface value of 0.02 a.u., and the MO energies of the **a**, **s**, **-a**, and **-s** MOs. The black arrow indicates the orientation of the axis along which the orbitals were assigned according to Michl's perimeter model.

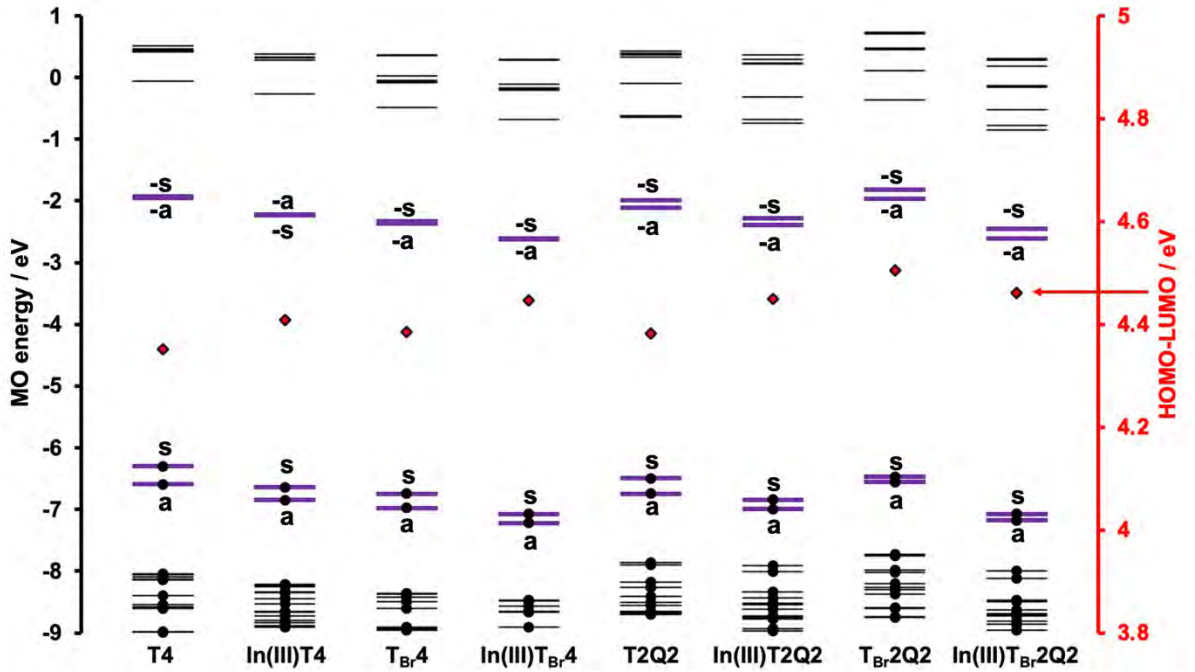

Figure 7.14. The relative energies of the molecular orbitals comparing the series of free base and Indium (III) porphyrins (**T4**, **In(III)T4**, **T_{Br}4**, **In(III)T_{Br}4**, **T2Q2**, **In(III)T2Q2**, **T_{Br}2Q2**, and **In(III)T_{Br}2Q2**). The four-frontier molecular orbitals energies are bolded and in purple, and the occupied orbitals are denoted by circular black markers. A secondary axis is used to plot the HOMO–LUMO energy gap in red diamonds.

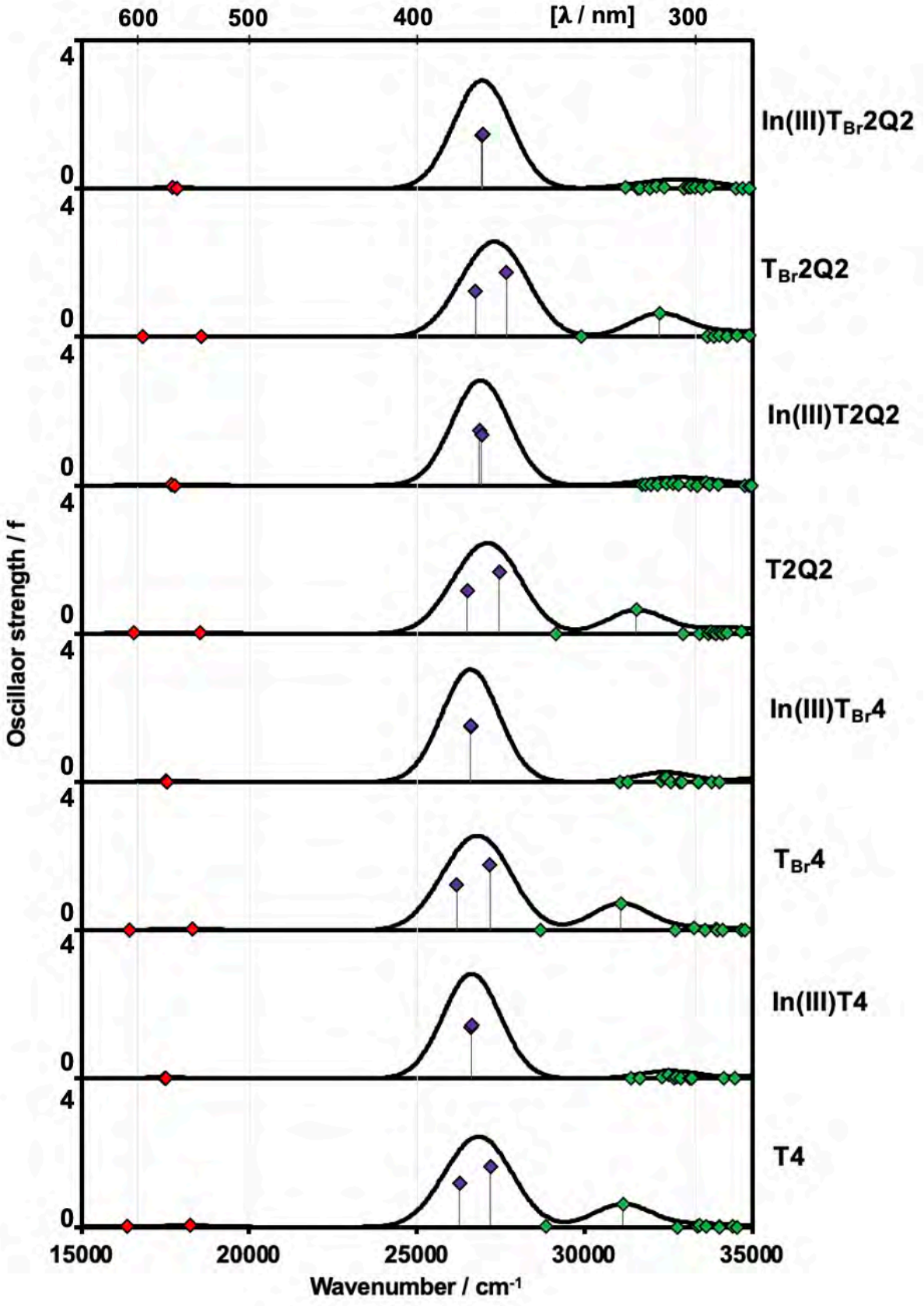

Figure 7.15. The simulated UV-visible spectra comparing the series of free base and Indium (III) porphyrins (**T4**, **In(III)T4**, **T$_{Br}$4**, **In(III)T$_{Br}$4**, **T2Q2**, **In(III)T2Q2**, **T$_{Br}$2Q2**, and **In(III)T$_{Br}$2Q2**) as well as the TD spectral bands depicted as purple diamonds for the B (allowed) band and red diamonds for the Q (forbidden) transitions. A wavelength scale is included for reference.

Table 7.5. The calculated UV-visible absorption spectra of the B3LYP optimised geometry of **T4**, **In(III)T4**, **T_{Br}4**, **In(III)T_{Br}4**, **T2Q2**, **In(III)T2Q2**, **T_{Br}2Q2**, **In(III)T_{Br}2Q2**, obtained using the CAM-B3LYP functional of the Gaussian 09 software packages[108] with SDD basis sets.

			T4		
	#[a]	**λ_{exp}[b]**	**λ_{calc}[c]**	***f*[d]**	**Wavefunction =[e]**
Q	1	552	611	0.02	**60% s → -s; 39% a → -a; …**
Q	2	520	548	0.04	**59% s → -a; 40% a → -s; …**
B	3	425	381	1.17	**55% a→ -a; 32% s → -s; …**
B	4		368	1.64	**59% a → -s; 41% s → -a; …**
			In(III)T4		
	#[a]	**λ_{exp}[b]**	**λ_{calc}[c]**	***f*[d]**	**Wavefunction =[e]**
Q	1	610	572	0.02	**57% s → -s; 42% a → -a; …**
Q	2	565	571	0.01	**55% s → -a; 44% a → -s; …**
B	3	435	376	1.40	**56% a → -a; 42% s → -s; …**
B	4		375	1.43	**55% a → -s; 43% s → -a; …**
			T_{Br}4		
	#[a]	**λ_{exp}[b]**	**λ_{calc}[c]**	***f*[d]**	**Wavefunction =[e]**
Q	1	554	608	0.01	**58% s → -s; 41% a → -a; …**
Q	2	521	546	0.04	**58% s → -a; 41% a → -s; …**
B	3	425	382	1.23	**54% a → -a; 33% s → -s; …**
B	4		368	1.77	**58% a → -s; 43% s → -a; …**
			In(III)T_{Br}4		
	#[a]	**λ_{exp}[b]**	**λ_{calc}[c]**	***f*[d]**	**Wavefunction =[e]**
Q	1	--	570	0.02	**55% s → -a; 44% a → -s; …**
Q	2	--	569	0.01	**54% s → -s; 45% a → -a; …**
B	3	--	376	1.50	**55% a → -s; 43% s → -a; …**
B	4	--	376	1.53	**53% a → -a; 44% s → -s; …**
			T2Q2		
	#[a]	**λ_{exp}[b]**	**λ_{calc}[c]**	***f*[d]**	**Wavefunction =[e]**
Q	1	554	603	0.02	**34% s → -a; 26% s → -s; …**
Q	2	518	540	0.03	**29% s → -s; 28% s → -a; …**
B	3	423	377	1.16	**29% a → -a; 26% a → -s; …**
B	4		364	1.68	**32% a → -s; 25% a → -a; …**
			In(III)T2Q2		
	#[a]	**λ_{exp}[b]**	**λ_{calc}[c]**	***f*[d]**	**Wavefunction =[e]**
Q	1	606	565	0.02	**58% s → -a; 41% a → -s; …**
Q	2	564	560	0.01	**51% s → -s; 47% a → -a; …**
B	3	433	371	1.46	**52% a → -a; 46% s → -s; …**
B	4		371	1.37	**57% a → -s; 40% s → -a; …**

			$T_{Br}2Q2$		
	#[a]	λ_{exp}[b]	λ_{calc}[c]	*f*[d]	**Wavefunction =**[e]
Q	1	564	594	0.01	**33% s → -s; 29% a → -a; …**
Q	2	516	538	0.02	**35% s → -a; 26% a → -s; …**
B	3	422	374	1.23	**37% a → -a; 32% s → -s; …**
B	4		361	1.73	**44% a → -s; 33% s → -a; …**
			In(III)T_{Br}2Q2		
	#[a]	λ_{exp}[b]	λ_{calc}[c]	*f*[d]	**Wavefunction =**[e]
Q	1	--	564	0.03	**58% s → -a; 41% a → -s; …**
Q	2	--	560	0.00	**50% a → -a; 49% s → -s; …**
B	3	--	371	1.44	**37% a → -s; 25% s → -a; …**
B	4	--	371	1.48	**32% a → -a; 31% s → -s; …**

[a]Excited state number assigned in increasing energy in the TD-DFT calculations. [b]Experimental wavelengths in nanometers. [c]Calculated wavelengths in nanometers. [d]Calculated oscillator strengths. [e]Wavefunctions describing the MOs involved in the transition based on eigenvectors predicted by TD-DFT. Only one-electron transition contributions of more than 5% are included. **a**, **s**, **-a**, and **-s** refer to the MO nomenclature of Michl's perimeter model.[46-49] One-electron transitions between these orbitals are highlighted in bold.

All of the porphyrins in the fifth series show a marked stabilisation of the MO upon coordination to In(III) (**Figure 7.14)**. With the exception of **In(III)T_{Br}2Q2**, which has a decreased HOMO–LUMO gap compared to its free base counterpart, the In(III) molecules have an increased HOMO–LUMO gap compared to the free base molecules. The In(III) molecules generally have relatively blue-shifted spectra due to the increased HOMO–LUMO gap (**Figure 7.15**).

A summary of the calculated UV-visible absorption spectra is given in **Table 7.5**.

The sixth series of molecules compares the free base reference compound (**T4**) to the metalated molecules (**Sn(IV)T4** and **In(III)T4**) and the molecule that is coordinated to P(V), **P(V)T4** (**Figure 7.16**).

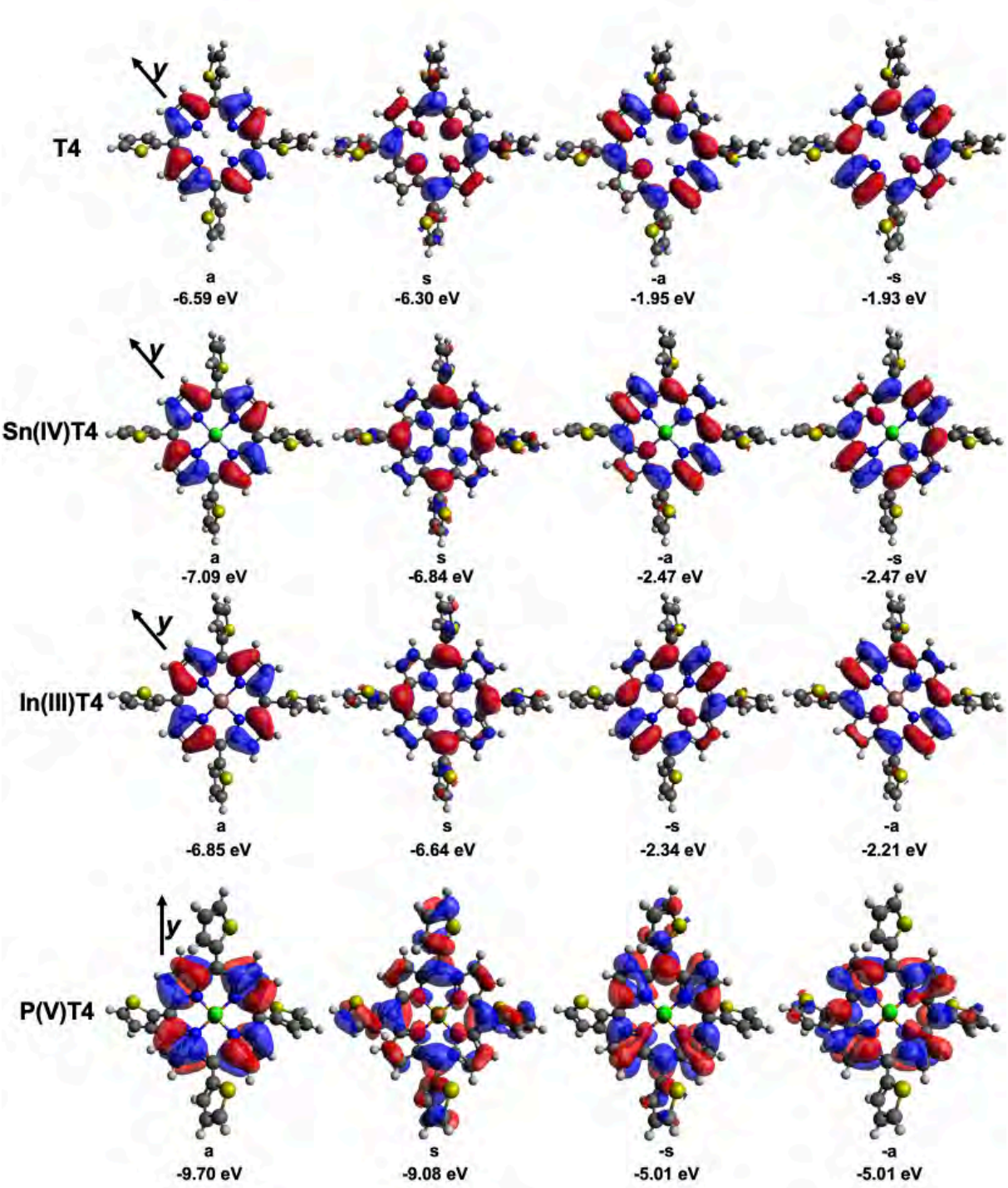

Figure 7.16. The nodal patterns of the series of free base and metalated porphyrins (**T4**, **Sn(IV)T4**, **In(III)T4**, **P(V)T4**) at an isosurface value of 0.02 a.u., and the MO energies of the **a**, **s**, **-a**, and **-s** MOs. The black arrow indicates the orientation of the axis along which the orbitals were assigned according to Michl's perimeter model.

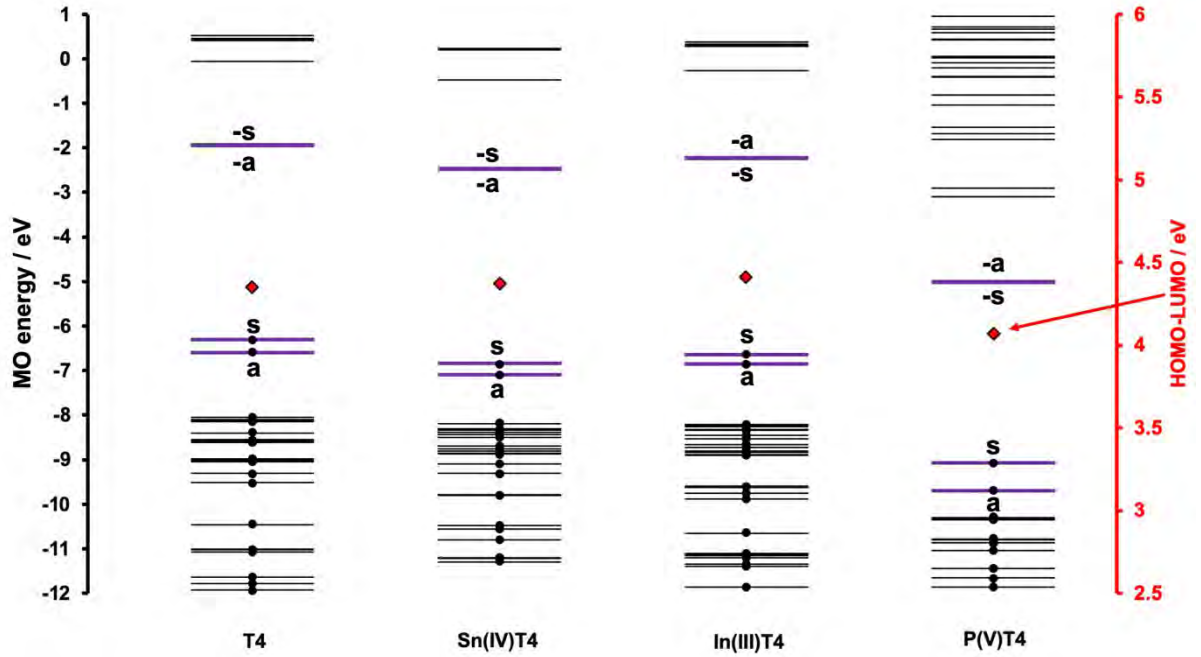

Figure 7.17. The relative energies of the molecular orbitals comparing the series of free base and metalated porphyrins (**T4**, **Sn(IV)T4**, **In(III)T4**, **P(V)T4**). The four-frontier molecular orbitals energies are bolded and in purple, and the occupied orbitals are denoted by circular black markers. A secondary axis is used to plot the HOMO–LUMO energy gap in red diamonds.

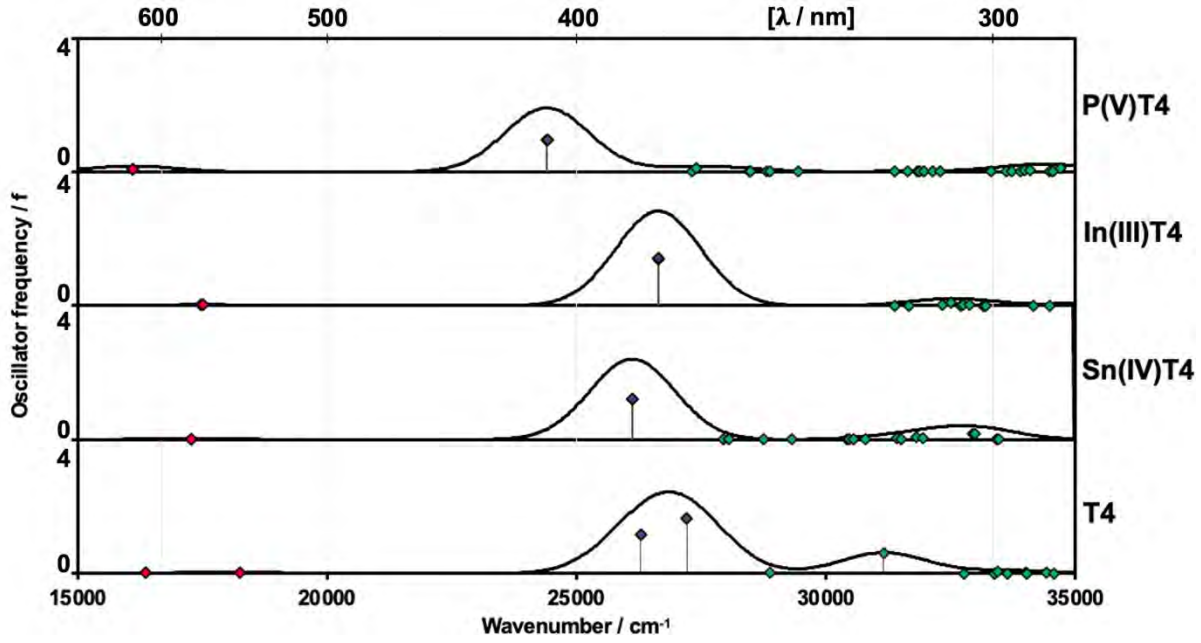

Figure 7.18. The simulated UV-visible spectra comparing the series of free base and metalated porphyrins (**T4**, **Sn(IV)T4**, **In(III)T4**, and **P(V)T4**), as well as the TD spectral bands depicted as purple diamonds for the B (allowed) band and red diamonds for the Q (forbidden) transitions. A wavelength scale is included for reference.

Table 7.6. The calculated UV-visible absorption spectra of the B3LYP optimised geometry of **T4**, **Sn(IV)T4**, **In(III)T4**, and **P(V)T4**, obtained using the CAM-B3LYP functional of the Gaussian 09 software packages[108] with SDD basis sets.

			T4		
	#[a]	**λ_{exp}[b]**	**λ_{calc}[c]**	***f*[d]**	**Wavefunction =[e]**
Q	1	552	611	0.02	**60% s → -s; 39% a → -a; …**
Q	2	520	548	0.04	**59% s → -a; 40% a → -s; …**
B	3	425	381	1.17	**55% a→ -a; 32% s → -s; …**
B	4		368	1.64	**59% a → -s; 41% s → -a; …**
			Sn(IV)T4		
	#[a]	**λ_{exp}[b]**	**λ_{calc}[c]**	***f*[d]**	**Wavefunction =[e]**
Q	1	613	579	0.02	**58% s → -a; 39% a → -s; …**
Q	2	567	579	0.02	**57% s → -s; 39% a → -a; …**
B	3	437	383	1.20	**55% a → -s; 37% s → -a; …**
B	4		383	1.21	**55% a → -a; 37% s → -s; …**
			In(III)T4		
	#[a]	**λ_{exp}[b]**	**λ_{calc}[c]**	***f*[d]**	**Wavefunction =[e]**
Q	1	610	572	0.02	**57% s → -a; 42% a → -a; …**
Q	2	565	571	0.01	**55% s → -a; 44% a → -s; …**
B	3	435	376	1.40	**56% a → -a; 42% s → -s; …**
B	4		375	1.43	**55% a → -s; 43% s → -a; …**
			P(V)T4		
	#[a]	**λ_{exp}[b]**	**λ_{calc}[c]**	***f*[d]**	**Wavefunction =[e]**
Q	1	--	622	0.09	**57% s → -a; 25% a → -s; …**
Q	2	--	621	0.09	**57% s → -s; 25% a → -a; …**
B	3	--	410	0.95	**46% a → -s; 21% s → -a; …**
B	4	--	410	0.95	**46% a → -a; 21% s → -s; …**

[a]Excited state number assigned in increasing energy in the TD-DFT calculations. [b]Experimental wavelengths in nanometers. [c]Calculated wavelengths in nanometers. [d]Calculated oscillator strengths. [e]Wavefunctions describing the MOs involved in the transition based on eigenvectors predicted by TD-DFT. Only one-electron transition contributions of more than 5% are included. **a**, **s**, **-a**, and **-s** refer to the MO nomenclature of Michl's perimeter model.[46-49] One-electron transitions between these orbitals are highlighted in bold.

The free base molecule, **T4**, is the least stable molecule with the most destabilised HOMO energy due to the lack of the heavy atom in the centre of the macrocycle (**Figure 7.17**). **P(V)T4** is the most stable due to its overall cationic charge. Additionally, **P(V)T4** has red-shifted

spectral bands due to the decreased HOMO–LUMO gap (**Figure 7.18**). The free base molecule has Q bands with significantly different calculated wavelengths, which give rise to four Q bands, experimentally, due to the presence of vibrational overtones in addition to the main electronic bands. **Sn(IV)**, **In(III)T4**, and **P(V)T4** are predicted to have Q spectral bands that have identical or near-identical calculated wavelengths, which causes the experimentally observed collapse of the four Q bands of the free base dye into two bands in the context of metal complexes. A summary of the calculated UV-visible absorption spectra is given in **Table 7.6**.

The seventh and final series of molecules aims to assess the effect of the quaternisation of the porphyrin on the electronic and optical properties (**Figure 7.19**).

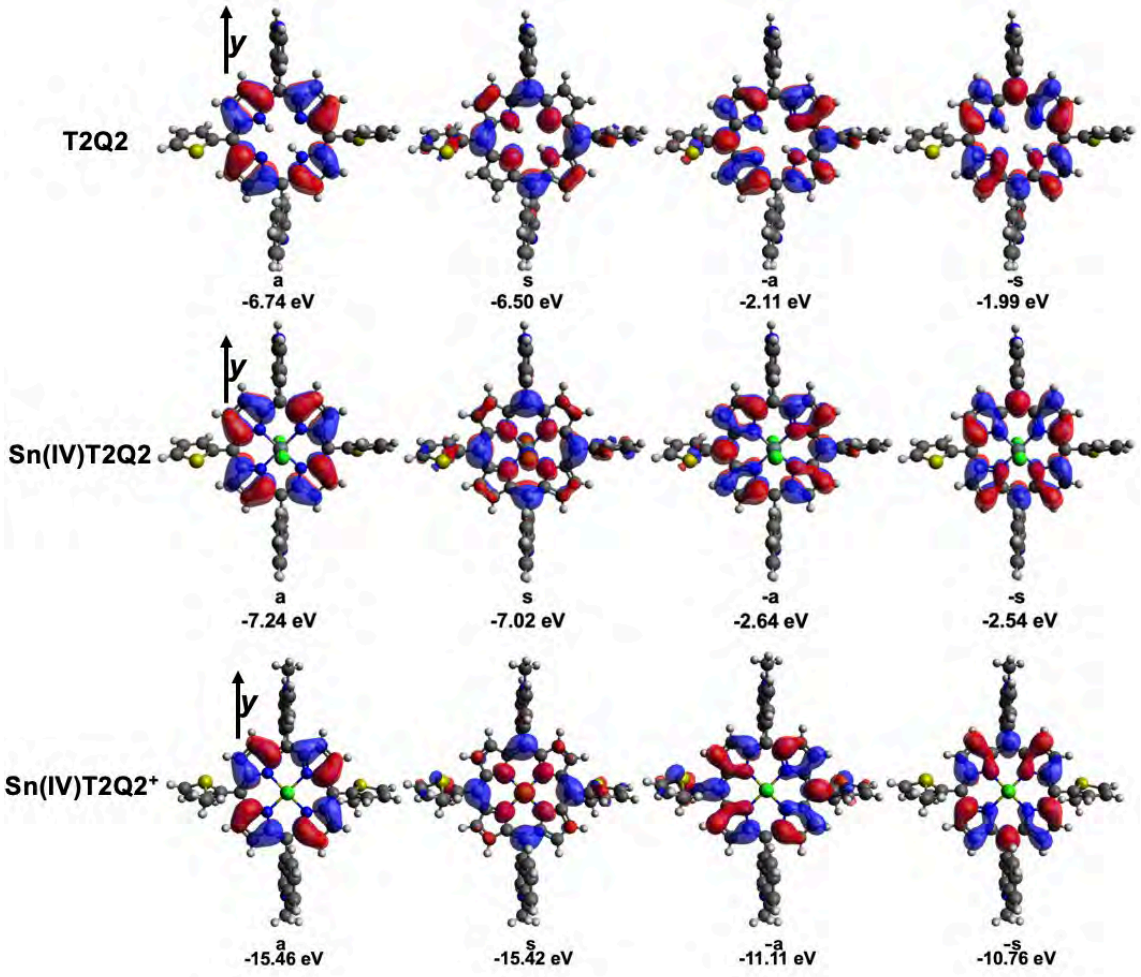

Figure 7.19. The nodal patterns of the series of the free base, metalated and quaternised molecules (**T2Q2**, **SnT2Q2**, and **SnT2Q2^{+}**, respectively) at an isosurface value of 0.02 a.u., and the MO energies of the **a**, **s**, **-a**, and **-s** MOs. The black arrow indicates the orientation of the axis along which the orbitals were assigned according to Michl's perimeter model.

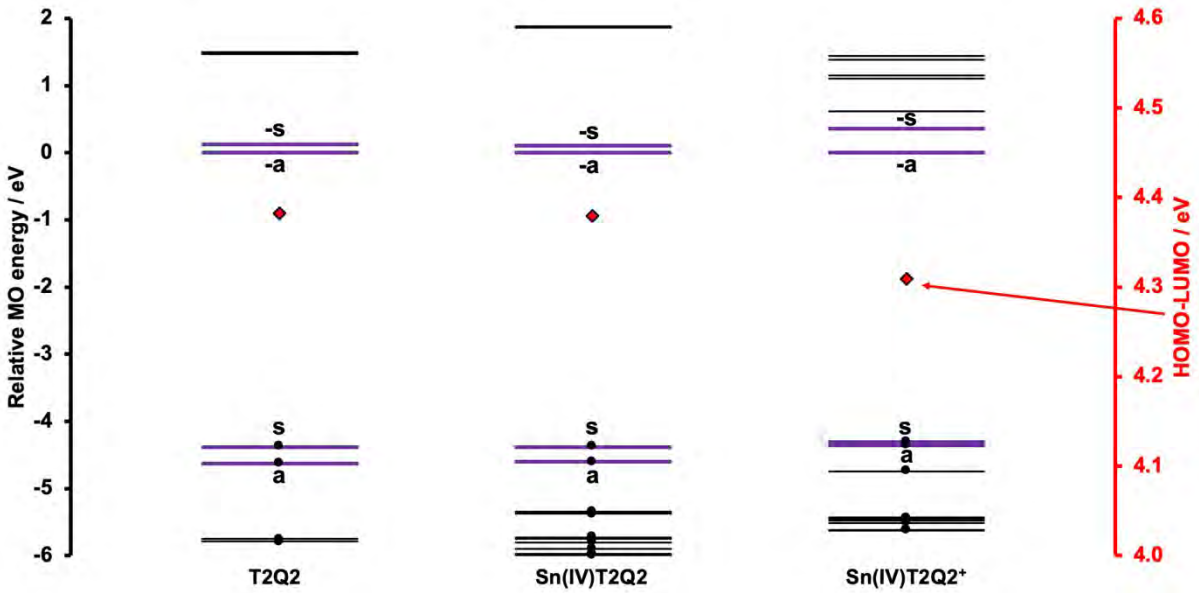

Figure 7.20. The relative energies (LUMO = 0) of the molecular orbitals comparing the series of free base, metalated and quaternised low-symmetry porphyrins (**T2Q2**, **Sn(IV)T2Q2**, **Sn(IV)T2Q2**$^{+}$). The four-frontier molecular orbitals energies are bolded and in purple, and the occupied orbitals are denoted by circular black markers. A secondary axis is used to plot the HOMO–LUMO energy gap in red diamonds.

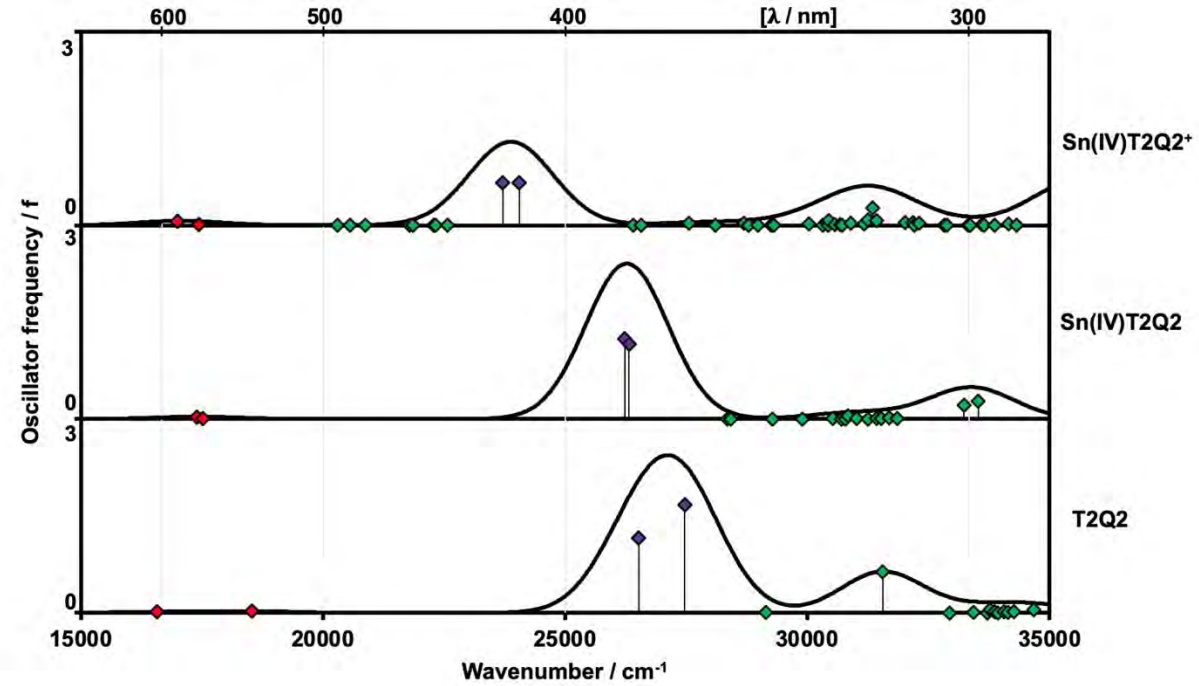

Figure 7.21. The simulated UV-visible spectra comparing the series of the free base, metalated and quaternised low-symmetry porphyrins (**T2Q2**, **SnT2Q2**, **SnT2Q2**$^{+}$), as well as the TD spectral bands depicted as purple diamonds for the B (allowed) band and red diamonds for the Q (forbidden) transitions. A wavelength scale is included for reference.

Table 7.7. The calculated UV-visible absorption spectra of the B3LYP optimised geometry of **T2Q2**, **Sn(IV)T2Q2**, and **SnT2Q2^{+}**, obtained using the CAM-B3LYP functional of the Gaussian 09 software packages[108] with SDD basis sets.

			T2Q2		
	#[a]	**λ_{exp}[b]**	**λ_{calc}[c]**	***f*[d]**	**Wavefunction =[e]**
Q	1	554	603	0.02	**34% s → -a; 26% s → -s; …**
Q	2	518	540	0.03	**29% s → -s; 28% s → -a; …**
B	3	423	377	1.16	**29% a → -a; 26% a → -s; …**
B	4		364	1.68	**32% a → -s; 25% a → -s; …**
			Sn(IV)T2Q2		
	#[a]	**λ_{exp}[b]**	**λ_{calc}[c]**	***f*[d]**	**Wavefunction =[e]**
Q	1	602	575	0.03	**62% s → -a; 37% a → -s; …**
Q	2	561	571	0.00	**56% s → -s; 43% a → -a; …**
B	3	434	381	1.25	**54% a → -a; 41% s → -s; …**
B	4		380	1.16	**59% a → -s; 35% s → -a; …**
			Sn(IV)T2Q2^{+}		
	#[a]	**λ_{exp}[b]**	**λ_{calc}[c]**	***f*[d]**	**Wavefunction =[e]**
Q	1	614	588	0.06	**68% s → -a; 29% a → -s; …**
Q	2	565	574	0.01	**56% a → -a; 42% s → -s; …**
B	3	435	422	0.66	**50% s → -s; 37% a → -a; …**
B	4		416	0.66	**61% a → -s; 25% s → -a; …**

[a]Excited state number assigned in increasing energy in the TD-DFT calculations. [b]Experimental wavelengths in nanometers. [c]Calculated wavelengths in nanometers. [d]Calculated oscillator strengths. [e]Wavefunctions describing the MOs involved in the transition based on eigenvectors predicted by TD-DFT. Only one-electron transition contributions of more than 5% are included. **a**, **s**, **-a**, and **-s** refer to the MO nomenclature of Michl's perimeter model.[46-49] One-electron transitions between these orbitals are highlighted in bold.

Upon incorporating a methyl group onto two nitrogen atoms and two sulphur atoms, the porphyrin possesses an overall charge of +4. This is done to improve the efficacy of therapy by improving the bioavailability with improved hydrophilicity and permeation through the target cells, due to their overall negative charge. This leads to a significant stabilisation of the MOs (**Figure 7.20**), in a similar but more exaggerated manner to the P(V) porphyrins. A reduced HOMO–LUMO gap gives rise to the marked red shift in the spectral bands of the quaternised

molecule, which makes this molecule more suitable for PDT. There is also an intensification of the Q bands in the quaternised species due to an increased ΔLUMO value (**Figure 7.21**). A summary of the calculated UV-visible absorption spectra is given in **Table 7.7**.

7.2 Summary of chapter

The goal of this chapter was to provide a theoretical explanation of the observed groundstate absorption spectra in accordance with conceptual frameworks, such as Gouterman's 4-orbital model and Michl's perimeter model, based on trends in the relative energies of the four frontier π-MOs.[41,41,46-49]

It can be concluded that the bromination of the thiophene did not significantly alter the electronic or optical properties of the molecules but was used for the heavy atom effects to improve the efficacy of the photosensitisers in PDT and PACT. Metalation of porphyrins and corroles blue shifted the Q band envelopes and was done for improved singlet oxygen quantum yields and bioavailability due to axial ligation. The corroles have more intense Q bands than the porphyrins due to their increased ΔLUMO due to the decreased symmetry of this analogue. This is in agreement with the observations made in Chapter 3.

CHAPTER EIGHT

DISCUSSION

8.1. Conclusions

The main aim of this thesis was to synthesise and characterise a series of high- and low-symmetry porphyrins and corroles for their application during *in vitro* PDT and PACT. Additionally, their Sn(IV) and In(IV) complexes were compared.

The novel low-symmetry porphyrins, **T2Q2** and **T_{Br}2Q2**, were synthesised and purified from Gryko *et al.*'s 2001 low-symmetry corrole synthesis, and the former was metalated with Sn(IV) and In(IV), thereafter. The high-symmetry corrole, **T3**, was purified from the same synthesis that yielded the low-symmetry porphyrin, **T2Q2**. **T_{Br}3**, on the other hand, was synthesised using Gryko *et al*.'s 2006 method.

There were synthetic challenges experienced with the corroles, and the low-symmetry corroles could not be synthesised and/or purified to a level that is required for the subsequent characterisation, quantification of the photophysical and-chemical properties and subsequent application-related studies of the molecules. Additionally, the corroles did not exhibit favourable photophysical and -chemical properties suitable for PDT and PACT, and subsequently, it was decided that porphyrins would be the main focus of this thesis.

Sn(IV)T2Q2 was found to have the most promising photophysicochemical properties, as it exhibited the highest singlet oxygen quantum yield of 0.85, as well as a low fluorescence quantum yield and a long-lived triplet state. For this reason, this photosensitiser was chosen to be quaternised to afford a cationic charge and improved bioavailability due to enhanced solubility in aqueous solutions.

In(III)T4, **Sn(IV)T_{Br}4**, **Sn(IV)T2Q2**, **In(III)T2Q2** and **Sn(IV)T2Q2^{+}** all displayed significant dark toxicity, but the neutral low-symmetry porphyrins were promising due to their high phototoxicity and low dark toxicity at low concentrations. This is promising and merits further investigation to assess their suitability for PDT applications. The indium (III) complexes had relatively high

activities (low IC_{50}) values, and this is preferential for PDT applications. Quaternisation of the molecule seemed to increase the dark toxicity but not the overall photoactivity to a significant extent. This merits further investigation in the context of nitrogen and sulfur quaternisation and the suitability of these molecules for PDT.

The PACT studies revealed that the quaternised molecule, **Sn(IV)T2Q2^{+}**, exhibited the best antimicrobial activity. **Sn(IV)T2Q2^{+}** achieved a $\log_{10}$ reduction of 6.91 against *Staphylococcus aureus*, which is suitable in the context of PACT, and a $\log_{10}$ reduction of 1.97 against *Escherichia coli*. Overall, the other photosensitisers did not perform very well against either *S. aureus* or *E. coli,* and this is likely due to the lack of a positive charge and the resultant low bioavailability and uptake into the bacterial cell membrane. Dark toxicity was observed in all the photosensitisers, which is not necessarily problematic due to the inherent antimicrobial activities of these molecules.

The porphyrins and corroles all exhibited nonlinear optical properties, but the two most promising molecules were **Sn(IV)T4** (with an obtainable I_{lim}) and **T_{Br}2Q2**, since they exhibited the most pronounced RSA responses. In general, the incorporation of heavy atoms did improve the nonlinear optical properties of the molecules, and this trend should be investigated across a larger series of molecules. **Sn(IV)T4** was embedded in a polymer (poly(bisphenol carbonate A)) in order to assess its solid state properties. Although the response was anomalous due to thermal effects and a lack of transparency, there was a significant reduction in transmittance towards $z = 0$. This is promising for future applications, despite the need to optimise the transparency of the thin film.

The theoretical calculations provided insight into the optical and electronic properties of the molecules, even those that could not be yielded synthetically. This chapter gave insight into the intensification of the Q bands of the corrole molecules relative to the analogous porphyrins, as well as the experimentally observed red shift of their spectral bands. This was the initial premise for their inclusion in this investigation due to the excitation of the molecules in the

phototherapeutic window in the context of PDT and PACT. As previously mentioned, the synthetic challenges and undesirable photophysicochemical properties that the synthetically viable corroles presented resulted in their lack of application in PDT and PACT.

8.2. Future outlook

Nevertheless, there is still more work to be carried out in exploiting low-symmetry porphyrins and corroles for their applications in PDT, PACT and optical limiting. Specifically, the following recommendations are made for future work:

i. The optimisation of the low-symmetry porphyrin synthesis and the high- and low-symmetry corrole synthesis, as well as purification.

ii. To explore the photodynamic and optical limiting properties of this synthetic trend across more low symmetry porphyrinoids and isomers, prepared from dipyrromethanes in a similar manner to the ABAB porphyrins in this study, including but not limited to corroles, chlorins and N-confused porphyrins in a similar manner to other recent research by Mack and coworkers.[18]

iii. To quaternise porphyrinoids at the nitrogens and/or sulfurs for their application in PDT and PACT.

iv. To explore other heavy atoms, including iodine, for improved photophysicochemical and optical limiting properties.

v. To compare symmetrical porphyrins to their A_3B, *trans*-A_2B_2 and AB_3 counterparts across a larger series of *meso*-substituents.

vi. To incorporate nanoparticles by taking advantage of the Au-S affinity to improve the photodynamic activity of the thienyl-substituted dyes and localisation into the target cells to improve their efficacy.

vii. To optimise the thin film synthesis in the context of the optical limiting studies.

REFERENCES

1. UK National Health Service, “Overview: Cancer”, **2019**, https://www.nhs.uk/conditions/cancer/, accessed 2nd October 2022.
2. S.H. Hassanpour & M. Dehghani, “Review of Cancer from the Perspective of Molecular”, *Journal of Cancer Research and Practice* **2017**, 4, 127-129.
3. World Health Organisation, “Cancer”, **2022**, https://www.who.int/news-room/fact-sheets/detail/cancer, accessed 2nd October 2022.
4. A.G. Renehan, C. Booth & C.S. Potten, “What is Apoptosis, and Why is it Important?”, *The British Medical Journal* **2001**, 322, 1536-1538. doi: 10.1136/bmj.322.7301.1536
5. S. Booth, “Common Carcinogens You Should Know”, WebMD. **2022**, https://www.webmd.com/cancer/know-common-carcinogens, accessed 2nd October 2022.
6. R. Sharma, Aashima, M. Nanda, C. Fronterre, P. Sewagudde, A.E. Ssentongo, K. Yenney, N.D. Arhin, J. Oh, F. Amponsah-Manu & P. Ssentongo, “Mapping Cancer in Africa: a Comprehensive and Comparable Characterisation of 34 Cancer Types Using Estimates from GLOBOCAN 2020”, *Frontiers in Public Health* **2022**, 10, 839835.
7. H. Hamdi, I. Abdeljaoued-Tej, A.A Zatchi, S. Abdelhak, S. Boubaker, J.S. Brown & A. Benkahla, “Cancer in Africa: The Untold Story”, *Frontiers in Oncology* **2021**, 11, 650117.
8. M. Aydin & D.L. Akins, “Geometric and Electronic Properties of Porphyrins and its Derivatives”, *Applications of Molecular Spectroscopy to Current Research in the Chemical and Biological Sciences.* **2016**, Intechopen: London, UK.
9. H. Huang, W. Song, J. Rieffel & J.F. Lovell, “Emerging Applications of Porphyrins in Photomedicine”, *Frontiers in Physics* **2015**, 3, 23.
10. M. Imran, M. Ramzan, A.K. Qureshi, M.A. Khan & M. Tariq, “Emerging Applications of Porphyrins and Metalloporphyrins in Biomedicine and Diagnostic Magnetic Resonance Imaging”, *Biosensors* **2018**, 8, 95.
11. M.G.H. Vincente & K.M. Smith, “Syntheses and Functionalizations of Porphyrins Macrocycles”, *Current Organic Synthesis* **2014**, 11, 3-28.
12. A. Galdoni, “Porphyrins: Fascinating Molecules with Biological Significance”, *Atomic, Molecular and Supramolecular Studies* **2002**, Elettra highlights: Trieste, Italy.
13. J.E. Merritt & K.L. Loening, “International Union of Pure and Applied Chemistry: Nomenclature of Tetrapyrroles”, *Pure and Applied Chemistry* **51**, 2251-2304.
14. D. Gryko & K. Jadach, “A Simple and Versatile One-Pot Synthesis of *Meso*-Substituted *Trans*-A_2B-Corroles”, *The Journal of Organic Chemistry* **2001**, 66, 4267-4275.
15. L. You, H. Shen, L. Shi, G. Zhang, H. Liu, H. Wang & L. Ji, “Photophysical Properties of The Corrole Photosensitizers”, *Science China: Physics, Mechanics and Astronomy* **2010**, 53, 1491-1496.
16. J. Mack, “Expanded, Contracted, and Isomeric Porphyrins: Theoretical Aspects”, *Chemical Reviews* **2017**, 117, 3444-3478.

17. S.M.M. Lopes, M. Pineiro & T.M.V.D. Pinho e Melo, “Corroles and Hexaphyrins: Synthesis and Applications in Cancer Photodynamic Therapy”, *Molecules* **2020**, 25, 3450.
18. B. Babu, J. Mack & T. Nyokong, “Sn(IV)-Porphyrinoids for Photodynamic Anticancer and Antimicrobial Chemotherapy”, *Dalton Transactions* **2023**, 52, 5000-5018.
19. N. Siraj, P.E. Kolic, B.P. Regmi & I.M. Warner, “Strategy for Tuning the Photophysical Properties of Photosensitizers for Use in Photodynamic Therapy”, *Chemistry: A European Journal* **2015**, 21, 14440-14446.
20. J.M. Dabrowski, B. Pucelik, A. Regiel-Futyra, M. Brindell, O. Mazuryk, A. Kyzioł, G. Stochel, W. Macyk & L.G. Arnaut, “Engineering of Relevant Photodynamic Processes Through Structural Modifications of Metallotetrapyrrolic Photosensitizers”, *Coordination Chemistry Reviews* **2016**, 325, 67-101.
21. C. Zipp, J.P. Michael, M.A. Fernandes & H.M. Marqeus, “The Synthesis and Characterisation of Several Corroles”, *South African Journal of Chemistry* **2013**, 66, 158-166.
22. M. König, F. Faschinger, L.M. Reith & W. Schöfberger, “The Evolution of Corrole Synthesis – from Simple One-Pot Strategies to Sophisticated ABC-corroles”, *Journal of Porphyrins and Phthalocyanines* **2016**, 20, 96-107.
23. D. Shemin, “The Biosynthesis of Porphyrins”, *National Academy of Sciences (US) and National Research Council (US) Division of Medical Sciences. Conference on Hemoglobin* **1957**, National Academies Press: Washington DC, USA.
24. K. Arja, “Multimodal Porphyrin-Based Conjugates”, **2018**, PhD thesis, Linköping University, Sweden.
25. V. Patwardhan, “Hans Fischer (1881-1945) Pathbreaking Research on Blood, Bile and Plant Pigments”, *Chemical Industry Digest* **2018**. https://chemindigest.com/hans-fischer-1881-1945/, accessed 3rd June 2023.
26. P. Rothemund, “Formation of Porphyrins from Pyrrole and Aldehydes”, *Journal of the American Chemical Society* **1935**, 57, 2010-2011.
27. P. Rothemund, “A New Porphyrin Synthesis. The Synthesis of Porphin”, *Journal of American Chemical Society* **1936**, 58. 625-627.
28. H. Shy, P. Mackin, A.S. Orvieto, D. Gharbharan, G.R. Peterson, N. Bampos & T.D. Hamilton, “Two-step Mechanochemical Synthesis of Porphyrins”, *Faraday Discussions* **2014**, 19, 59-69.
29. P. Rothemund & A.R. Menotti, “Porphyrin Studies. IV. 1 The Synthesis of α,β,γ,δ-Tetraphenylporphine”, *Journal of the American Chemical Society* **1941**, 61, 267-270.
30. F.R. Longo & J.D. Finarelli, “A Simplified Synthesis for *Meso*-Tetraphenylporphyrin”, *The Journal of Organic Chemistry* **1966**, 32, 476.
31. J.S. Lindsey, “Synthetic Routes to *Meso*-Patterned Porphyrins”, *Accounts of Chemical Research* **2009**, 43, 300-311.

32. H. Hölzel, M. Muth, D. Lungerich & N. Jux, “Addressing Environmental Challenges of Porphyrin Mixtures Obtained from Statistical Syntheses”, *Chemistry – Methods* **2021**, 1, 142-147.
33. T. Rohand, E. Dolusic, T.H. Ngo, W. Maes & W. Dehaen, “Efficient Synthesis of Aryldipyrromethanes in Water and Their Application in the Synthesis of Corroles and Dipyrromethenes”, *Arkivoc* **2007**, 10, 307-324.
34. R. Orłowski, D. Gryko & D.T. Gryko, “Synthesis of Corroles and their Heteroanalogs”, *Chemical Reviews* **2017**, 117, 3102-3137.
35. M.K. Tse, Z. Zhang & K.S. Chang, “Synthesis of an Oxorhenium(V) Corrolate from Porphyrin with Detrifluromethylation and Ring Contraction”, *Chemical Communications* **1998**, 1199-1200.
36. Z. Gross, N. Galili & I. Saltsman, “The First Direct Synthesis of Corroles for Pyrrole”, *Angewandte Chemie International Edition* **1999**, 38, 1427-1429.
37. R. Giovannetti, “The Use of Spectrophotometry UV-vis for the Study of Porphyrins”, *Macro to Nano Spectroscopy* **2023**. https://cdn.intechopen.com/pdfs/37656/InTech-The_use_of_spectrophotometry_uv_vis_for_the_study_of_porphyrins.pdf, accessed 27th September 2022.
38. M. Prushan, “Absorption and Fluorescence Spectroscopy of Tetraphenylporphyrin and Metallo-Tetraphenylporphyrin”, **2005**, La Salle University, Philadelphia, USA.
39. A. Zhang, L. Kwan & M. Stillman, “The Spectroscopic Impact of Interactions with the Four Gouterman Orbitals from Peripheral Decoration of Porphyrins with Simple Electron Withdrawing and Donating Groups”, *Organic & Biomolecular. Chemistry* **2017**, 15, 9081-9094.
40. J.R. Platt, “Classification of Spectra of Cata-Condensed Hydrocarbons”, *The Journal of Chemical Physics* **1949**, 17, 484-495.
41. M. Gouterman, “Optical Spectra and Electronic Structure of Porphyrins and Related Rings”, *The Porphyrins, Vol. III*, D. Dolphin (Ed.), **1978**, Academic Press: Cambridge, Massachusetts, United States, pp 1-165.
42. M. Gouterman, “Spectra of Porphyrins”, *Journal of Molecular Spectroscopy* **1961**, 6, 138-163.
43. B. Babu, J. Mack & T. Nyokong, “Sn(IV) N-Confused Porphyrins as Photosensitizer Dyes for Photodynamic Therapy in the Near IR Region”, *Dalton Transactions* **2020**, *49*, 15180-15183.
44. B. Babu, J. Mack & T. Nyokong, “A Heavy-Atom-Free π-Extended N-Confused Porphyrin as a Photosensitizer for Photodynamic Therapy”, *New Journal of Chemistry* **2021**, *45*, 5654-5658.
45. J. Mack, Y. Asano, N. Kobayashi & M.J. Stillman, “Application of MCD Spectroscopy and TD-DFT to a highly Non-Planar Porphyrinoid Ring System. New Insights on Red-

Shifted Porphyrinoid Spectral Bands", *Journal of the American Chemical Society* **2005**, 127, 17697-17711.

46. J. Michl, "Magnetic Circular Dichroism of Cyclic π-electron Systems. 1. Algebraic Solution of the Perimeter Model for the A and B terms of High-Symmetry Systems with a (*4N+2)*-Electron [*n*]Annulene Perimeter", *Journal of the American Chemical Society* **1978**, 100, 6801-6811.
47. J. Michl, "Magnetic Circular Dichroism of Cyclic π-electron Systems. 1. Algebraic Solution of the Perimeter Model for the B terms of Systems with a (*4N+2)*-Electron [*n*]Annulene Perimeter", *Journal of the American Chemical Society* **1978**, 100, 6812-6818.
48. J. Michl, "Electronic Structure of Aromatic π-electron Systems as reflected in their MCD Spectra", *Pure and Applied Chemistry* **1980**, 52, 1549-1563.
49. J. Michl, "Magnetic Circular Dichroism of Aromatic Molecules", *Tetrahedron* **1984**, 40, 3845-3934.
50. L.C.P. Gonçalves, "Photophysical Properties and Therapeutic Use of Natural Photosensitizers", *Journal of Photochemistry and Photobiology* **2021**, 7, 100052.
51. K. Berg, "Photosensitizers in Medicine", *Photobiological Sciences Online*, J. Lee, K.C. Smith (Eds), **2009**. http://photobiology.info/Berg.html, accessed 3rd June 2023.
52. T. Itoh, "Fluorescence and Phosphorescence from Higher Excited States of Organic Molecules", *Journal of the American Chemical Society* **2012**, 112, 4541-4568.
53. J. Berlanda, T. Kiesslich & F. Berr, "Photophysics and Photochemistry of Photodynamic Therapy: Fundamental Aspects", *Lasers in Medical Science* **2008**, 24, 259-268.
54. T-B. Ren, W. Zu, W. Zhang, X-X. Zhang, Z-Y. Wang, Z. Xiang, L. Yuan & X-B. Zhang, "A General Method to Increase Stokes Shift by Introducing Alternation Vibronic Structures", *Journal of the American Chemical Society* **2018**, 140, 7716-7722.
55. Z. Yang, Z. Zhang, Y. Sun, Z. Lei, D. Wang, H. Ma & B.Z. Tang, "Incorporating Spin-Orbit Coupling Promoted Functional Group into an Enhanced Electron D-A System: A Useful Designing Concept for Designing Efficient Photosensitizer and Imaging-Guided Photodynamic Therapy", *Biomaterials* **2021**, 275, 120934.
56. M. Einzinger, T. Zhu, P. de Silva, C. Belger, T.M. Swager, T. Van Voorhis & M.A. Baldo, "Shorter Exciton Lifetime via an External Heavy Atom Effect: Alleviating the Effects of Bimolecular Processes in Organic Light Emitting Diodes", *Advanced Materials* **2017**, 29, 1701987.
57. J.C. Koziar and D.O. Cowan, "Photochemical Heavy-Atom Effects", *Accounts of Chemical Research* **1977**, 11, 334-341.

58. M.T. Jarvi, M.S. Patterson & B.C. Wilson, “Insights into Photodynamic Therapy Dosimetry: Simultaneous Singlet Oxygen Luminescence and Photosensitizer Photobleaching Measurements”, *Biophysical Journal* **2012**, 102, 661-671.
59. R. Castro-Olivares, G. Günther, A.L. Zanocco & E. Lemp, “Linear Free Energy Relationship Analysis of Solvent Effects on Singlet Oxygen Reactions with Mono- and Disubstituted Anthracene Derivatives”, *Journal of Photochemistry and Photobiology A: Chemistry* **2009**, 207, 160-166.
60. Y. Hao, B.M. Liu, T.F. Bennett, C.G. Monsour, M. Selke & Y. Liu, “Determination of Singlet Oxygen Quantum Yield of a Porphyrinic Metal-Organic Framework”, *The Journal of Physical Chemistry* **2021**, 125, 7392-7400.
61. T.S. Mang, R. Allison, G. Hewson, W. Snider & R. Moskowitz, “A Phase II/III Clinical Study of Tin Ethyl Etiopurpurin (Purlytin) – Induced Photodynamic Therapy for the Treatment of Recurrent Cutaneous Metastatic Breast Cancer”, *The Cancer Journal from Scientific American* **1998**, 4, 378-384.
62. R. Lincoln, L. Kohler, S. Monro, H. Yin, M. Stephenson, R. Zong, A. Chouai, C. Dorsey, R. Hennigar, R.P. Thummel & S.A. McFarland, “Exploitation of Long-Lived ^{3}IL Excited States for Metal-Organic Photodynamic Therapy: Verification in a Metastatic Melanoma Model”, *Journal of the American Chemical Society* **2013**, 135, 17161-17175.
63. Z. Wang, A. Toffoletti, Y. Hou, J. Zhao, A. Barbon & B. Dick, “Insight into the Drastically Different Triplet Lifetimes of BODIPY Obtained by Optical/Magnetic Spectroscopy and Theoretical Computations”, *Chemical Science* **2021**, 12, 2829-2840.
64. O. Elbjeirami, M.A. Rawashdeh-Omary & M.A. Omary, “Phosphorescence Sensitization via Heavy-Atom Effects in d^{10} complexes”, *Research on Chemical Intermediates* **2011**, 37, 691-703.
65. J. Clark, “The Beer-Lambert Law”, *LibreTexts Chemistry* **2022**. https://chem.libretexts.org/Bookshelves/Physical_and_Theoretical_Chemistry_Textbook_Maps/Supplemental_Modules_(Physical_and_Theoretical_Chemistry)/Spectroscopy/Electronic_Spectroscopy/Electronic_Spectroscopy_Basics/The_Beer-Lambert_Law, accessed 26th September 2022.
66. J.P. McCormack, G.M. Allen & A.S. Virani, “Is Bigger Better? An Argument for Very Low Starting Doses”, *Canadian Medical Association Journal* **2011**, 183, 65-69.
67. P. Agostinis, K, Berg, K.A. Cengel, T.H. Foster, A.W. Girotti, S.O. Gollnick, S.M. Hahn, M.R. Hamblin, A. Juzeniene, D. Kessel, M. Korbelik, J. Moan, P. Mroz, D. Nowis, J. Piette, B.C. Wilson & J. Golab, “Photodynamic Therapy of Cancer: an Update”, *American Cancer Society Journals* **2011**, 61, 250-281.
68. M. Triesscheijn, P. Baas, J.H.M. Schellens & F.A. Stewart, “Photodynamic Therapy in Oncology”, *The Oncologist* **2006**, 11, 1043-1044.

69. T. Kocki, B. Czarczynska-Goslinksa, K. Kocha, M. Stolarska, D. Wachowska, S. Lijewski, T. Koczorowski & T. Goslinski, "Nurses and Pharmacists in Interdisciplinary Team of Health Care Providers in Photodynamic Therapy", *Photomedicine– Advances in Clinical Practice* **2016**, Intechopen: London, UK.

70. R.R. Allison & K. Moghissi, "Photodynamic Therapy (PDT): PDT Mechanisms", *Clinical Endoscopy* **2013**, 46, 24-29.

71. J.G. Levy, "Photosensitizers in Photodynamic Therapy", *Seminars in Oncology* **1994**, 21, 4-10.

72. J.M. Dabrowski, B. Pucelik, A. Regiel-Futyra, M. Brindell, O. Mazuryk, A. Kyziol, G. Stochel, W. Macyk & L.G. Arnaut, "Engineering of Relevant Photodynamic Processes through Structural Modifications of Metallotetrapyrollic Photosensitizers", *Coordination Chemistry Reviews* **2016**, 325, 67-101.

73. P. Liang, D. Kolodieznyi, Y. Cregger, B. Ballou & M.P. Bruchez, "Subcellular Singlet Oxygen and Cell Death: Location Matters", *Frontiers in Chemistry* **2020**, 8, 592491.

74. J. Zhang, C. Jiang, J.P.F. Longo, R.B. Azevedo, H. Zhang and L.A. Muehlmann, "An Updated Overview on the Development of New Photosensitizers for Anticancer Photodynamic Therapy", *Acta Pharmaceutica Sinica B* **2018**, 8, 137-146.

75. H. Maeda & M. Khatami, "Analyses of Repeated Failures in Cancer Therapy for Solid Tumours: Poor Tumour-Selective Drug Delivery, Low Therapeutic Efficacy and Unsustainable Costs", *Clinical and Translational Medicine* **2018**, 7, 11.

76. Stanford Healthcare, "Risk and Side Effects of Cancer Treatments", **2022**. https://stanfordhealthcare.org/medical-treatments/c/cancer-surgery/complications.html, accessed 27th April 2022.

77. National Cancer Institute, "Radiation Therapy Side Effects", **2022**. https://www.cancer.gov/about-cancer/treatment/types/radiation-therapy/side-effects, accessed 27th April 2022.

78. H. Nesbitt, K. Logan, K. Thomas, B. Callan, J. Gao, T. McKaig, M. Taylor, M. Love, E. Stride, A.P. McHale & J.F. Callan, "Sonodynamic Therapy Complements PD-L1 Immune Checkpoint Inhibition in a Murine Model of Pancreatic Cancer", *Cancer Letters* **2021**, 517, 88-95.

79. S. Rajesh, E. Koshi, K. Philip & A. Mohan, "Antimicrobial Photodynamic Therapy: An Overview", *Journal of Indian Society of Periodontology* **2011**, 15, 323-327.

80. X. Hu, Y-Y. Huang, Y. Wang, X. Wang & M.R. Hamblin, "Antimicrobial Photodynamic Therapy to Control Clinically Relevant Biofilm Infections", *Frontiers in Microbiology* **2018**, 9, 1299.

81. C.L. Ventola, "The Antibiotic Resistance Crisis", *Pharmacy and Therapeutics* **2015**, 40, 277-283.

82. J. Oyim., C.A. Omolo & E.K. Amuhaya, “Photodynamic Antimicrobial Chemotherapy: Advancements in Porphyrin-Based Photosensitize Development”, *Frontiers in Chemistry* **2021**, 9, 635344.
83. J. O’Neill, “Antimicrobial Resistance: Tackling a Crisis for the Health and Wealth of Nations”, *Review on Antimicrobial Resistance* **2014**, Wellcome Trust: London, UK.
84. S. Sharma, T. Dai, G. Kharkwal, Y-Y. Huang, L. Huang, V. Arce, G. Tegos & M. Hamblin, “Drug Discovery of Antimicrobial Photosensitizers using Animal Models”, *Current Pharmaceutical Design* **2011**, 17, 1303.
85. T.J. Silhavy, D. Kahne & S. Walker, “The Bacterial Cell Envelope”, *Cold Spring Harbor Perspectives in Biology* **2010**, 2, a000414.
86. Z. Breijyeh, B. Jubeh & R. Karaman, “Resistance of Gram-Negative Bacteria to Current Antibacterial Agents and Approaches to Resolve It”, *Molecules* **2020**, 25, 1340.
87. A. Howes, Z. Zhu, D. Curie, J.R. Avila, V.D. Wheeler, R.F. Hagland & J.G. Valentine, “Optical Limiting Based on Huygens’ Metasurfaces”, *Nanoletters* **2020**, 20, 4638-4644.
88. A. Zheltikov, A. L’Huillier & F. Krausz, “Nonlinear Optics”, *Springer Handbook of Lasers and Optics* **1970**, Springer: New York, USA.
89. P. Lind, “Organic and Organometallic Compounds for Nonlinear Absorption of Light”, **2007**, PhD Thesis, Umeå University, Sweden.
90. J. Harris, “BODIPY Dyes for Singlet Oxygen and Optical Limiting Applications”, **2017**, MSc Thesis, Rhodes University.
91. X. Wang, Y. Wang, D. Mao & L. Li, “Passively Q-Switched Nd:YVO_4 Laser Based on Fe_3O_4 Nanoparticles Saturable Absorber”, *Optical Materials Express* **2017**, 7, 29913.
92. M. Sheik-Bahae & E.W. Van Stryland, “Nonlinear Optics in Semiconductors I”, *Semiconductors and Semimetals* **1998**, 58, 257-318.
93. M.V. Vijisha, S. Parambath, R. Jagadeesan, C. Arunkumar & K. Chandrasekharan, “Nonlinear Optical Absorption and Optical Limiting Studies Studies of Fluorinated Pyridyl Porphyrins in Chlorobenzene: And Insight into the Photo-Induced Protonation Effects”, *Dyes and Pigments* **2019**, 169, 29-35.
94. D.A. Zainuri, S.K. Alsaee, M.F. Zaini, S.N.F.A. Rahman, M.A.A. Bakar, M. Abdullah, M.A. Razak & S. Arshad, “Role of Electron-Withdrawing Groups on Nonlinear Optical Response of Conjugated Anthracenyl Fused Rings Chalcone: Experimental and DFT Study”, *Physica B: Condensed Matter.* **2023**, 655, 414744.
95. G. de la Torre, P. Vásquez,, F. Aguelló-Lópes & T. Torres, “Role of Structural Factors in the Nonlinear Optical Properties of Phthalocyanines and Related Compounds”, *Chemical Reviews* **2004**, 104, 3723-3750.
96. M. Sheik-Bahae, A.A. Said, T.H. Wei, Y.Y. Wu, D.J. Hagan, M.J. Soileau & E.W. Van Stryland, “Z-Scan: A Simple and Sensitive technique for Non-Linear Refraction Measurements”, *Proocedings SPIE* **1990**, 1148, 41-51.

97. A.K. May, “Singlet Oxygen and Optical Limiting Applications of BODIPYs and Other Molecular Dyes”, **2021**, PhD Thesis, Rhodes University, South Africa.
98. J. Harris, L. Gai, G. Kubheka, J. Mack, T. Nyokong & Z. Shen, “Optical Limiting Properties of 3,5-Dithienylenevinylene BODIPY Dyes at 532 nm”, *Chemistry − A European Journal* **2017**, 23, 14507-14514.
99. M. Sheik-Bahae, A.A. Said, T-H. Wei, D.J. Hagan, E.W. Van Stryland, “Sensitive Measurement of Optical Nonlinearities Using a Single Beam”, *IEEE Journal of Quantum Electronics* **1990**, 26, 760-769.
100. G. Tsigaridas & I. Polyzos, “A Novel Approach for Analyzing Open Z-scan Experiments”, *Optics Communications* **2006**, 266, 284-289.
101. Y. Chen, L. Gao, M. Feng, L. Gu, N. He, J. Wang, Y. Araki, W.J. Blau & A. Ito, “Photophysical and Optical Limiting Properties of Axially Modified Phthalocyanines”, *Mini-Reviews in Organic Chemistry* **2009**, 6, 55-65.
102. International Commission on Non-Ionizing Radiation Protection (ICNIRP), “Revision of Guidelines on Limits of Exposure to Laser Radiation of Wavelengths Between 400 nm and 1.4 μm. International Commission on Non-Ionizing Radiation Protection”, *Health Physics* **2000**, 79, 4.
103. R.C. Hollins, “Materials for Optical Limiters”, *Current Opinion in Solid State and Materials Science* **1999**, 4, 189-196.
104. J.J. Doyle, J. Wang, S.M. O’Flaherty, Y. Chen, A. Slodek, T. Hegarty, L.A. Carpenter II, D. Wöhrle, M. Hanack & W.J. Blau, “Nonlinear Optical Performance of Chemically Tailored Phthalocyanine-Polymer Films as Solid-State Optical Limiting Devices”, *Journal of Optics A Pure and Applied Optics* **2008**, 10, 075101.
105. Veo Vision Centre, “Polycarbonate lenses”, **2023**. https://www.veovisioncenter.com/eyeglasses-contacts/prescription-eyeglasses/polycarbonate-lenses/#:~:text=In%20fact%2C%20most%20protective%20eye,material%20for%20time%20spent%20outdoors, accessed 11th May 2023.
106. T.H. Tran Thi, C. Desforge, C. Thiec & S. Gaspard, “Singlet-Singlet and Triplet-Triplet Intramolecular Transfer Processed in a Covalently Linked-Porphyrin-Phthalocyanine Heterodimer”, *Journal of Physical Chemistry* **1989**, 93, 1226-1233.
107. M. Taniguchi, J.S. Lindsey, D.F. Bocian & D. Holten, “Comprehensive Review of Photophysical Parameters (ε, Φ_f, τ_s) of Tetraphenylporphyrin (H_2TPP) and Zinc Tetraphenylporphyrin (ZnTPP) – Critical Benchmark Molecules in Photochemistry and Photosynthesis”, *Journal of Photochemistry and Photobiology C: Photochemistry Reviews* **2021**, 46, 100401.
108. Gaussian 09, Revision E.01, M. J. Frisch, G. W. Trucks, H. B. Schlegel, G. E. Scuseria, M. A. Robb, J. R. Cheeseman, G. Scalmani, V. Barone, G. A. Petersson, H. Nakatsuji, X. Li, M. Caricato, A. Marenich, J. Bloino, B. G. Janesko, R. Gomperts, B. Mennucci,

H. P. Hratchian, J. V. Ortiz, A. F. Izmaylov, J. L. Sonnenberg, D. Williams-Young, F. Ding, F. Lipparini, F. Egidi, J. Goings, B. Peng, A. Petrone, T. Henderson, D. Ranasinghe, V. G. Zakrzewski, J. Gao, N. Rega, G. Zheng, W. Liang, M. Hada, M. Ehara, K. Toyota, R. Fukuda, J. Hasegawa, M. Ishida, T. Nakajima, Y. Honda, O. Kitao, H. Nakai, T. Vreven, K. Throssell, J. A. Montgomery, Jr., J. E. Peralta, F. Ogliaro, M. Bearpark, J. J. Heyd, E. Brothers, K. N. Kudin, V. N. Staroverov, T. Keith, R. Kobayashi, J. Normand, K. Raghavachari, A. Rendell, J. C. Burant, S. S. Iyengar, J. Tomasi, M. Cossi, J. M. Millam, M. Klene, C. Adamo, R. Cammi, J. W. Ochterski, R. L. Martin, K. Morokuma, O. Farkas, J. B. Foresman & D. J. Fox, Gaussian, Inc., Wallingford CT, 2013.

109. S. Mondal, T. Pain, K. Sahu & S. Kar, “Large-Scale Green Synthesis of Porphyrins”, *ACS Omega* **2021**, 6, 22922-22936.

110. S. Dingiswayo, “The Synthesis and Characterisation of Sn (IV) Porphyrin Derivatives and Their Potential Application in Anti-Cancer and Anti-Microbial Photodynamic Therapy”, **2021**, MSc Thesis, Rhodes University.

111. L.C. Makola, S. Mgidlana & T. Nyokong, “Amphiphilic Axially Modified Cationic Indium-Porphyrins Linked to Hydrophilic Magnetic Nanoparticles for Photodynamic Antimicrobial Chemotherapy Against Gram-Negative Strain; *Escherichia coli*”, *Dyes and Pigments* **2021**, 192, 109262.

112. A.D. Adler, L. Sklar, F.R. Longo, J.D. Finarelli & M.G. Finarelli, “A Mechanistic Study of the Synthesis of *Meso*-Tetraphenylporphin”, *Journal of Heterocyclic Chemistry* **1968**, 5, 669-678.

113. Z.H. Mazumdar, D. Sharma, A. Mukherjee, S. Basu, P.K. Shukla, T. Jha & D. Sengupta, “*Meso*-Thiophenium Porphyrins and their Zn(II) Complexes: a New Category of Cationic Porphyrins”, *ACS Medicinal Chemistry Letters* **2020**, 11, 2041-2047.

114. B. Koszarna & D.T. Gryko, “Efficient Synthesis of *Meso*-Substituted Corroles in a H_2O-MeOH Mixture”, *Journal of Organic Chemistry* **2006**, 71, 3707-3717.

115. J. Ferreira, C. Kurachi, L.T. Moriyama, P.F.C. Menezes, J.R. Purussi, C. Sibata, Z. Zucoloto, O. Castro e Silva Jr. & V.S. Bagnato, “Correlation Between the Photostability and Photodynamic Efficacy for Different Photosensitizers”, *Laser Physics Letters* **2006**, 2, 91-95.

116. E. Scarcello, A. Lambremont, R. Vanbever, P.J. Jacques & D. Lison, “Minding your Assays: Misleading Cytotoxicity in the Presence of Manganese”, *PLoS One* **2020**, 15, e0231634.

117. Merck, “Cell Proliferation Reagent WST-1”, **2023**. https://www.sigmaaldrich.com/ZA/en/product/roche/cellproro?gclid=CjwKCAjwgqejBhBAEiwAuWHioP9yxT58bvKR2P0vBHx2a0LxF2ulP7Ttl7vuv_XLjv3JdeLChaorgxoCdKAQAvD_BwE&gclsrc=aw.ds, accessed 21st May 2023.

118. O. L. Osifeko, I. Uddin, P.N. Mashazi & T. Nyokong, “Physicochemical and Antimicrobial Photodynamic Chemotherapy of Unsymmetrical Indium Phthalocyanines Alone or in the Presence of Magnetic Nanoparticles”, *New Journal of Chemistry* **2016**, 40, 2710-2721.
119. R. Soy, B. Babu, J. Mack & T. Nyokong, “The Photodynamic Activities of the Gold Nanoparticle Conjugates of Phosphorous (V) and Gallium (III) A_3 *meso*-triarylcorroles”, *Dyes and Pigments* **2021**, 194, 109631.
120. I.N. Meshkov, V. Bulach, Y.G. Gorbunova, F.E. Gostev, V.A. Nadtochenko, A.Y. Tsivadze & M.W. Hosseini, “Tuning Photochemical Properties of Phosphorous (V) Porphyrin Photosensitisers”, *Chemical Communications* **2017**, 53, 9918-9921.
121. J.M. Fisher, V.K. Kensy & G.R. Geier III, “Two-Step, One-Flask Synthesis of an N-confused Porphyrin Bearing Pentafluorophenyl Substituents”, *Journal of Organic Chemistry* **2017**, 82, 4429-4434.
122. G.R. Fulmer, A.J.M. Miller, N.H. Sherden, H.E. Gottlieb, A. Nudelman, B.M. Stoltz, J.E. Bercaw & K.I. Goldberg, “NMR Chemical Shifts of Trace Impurities: Common Laboratory Solvents, Organics and Gases in Deuterated Solvents Relevant to the Organometallic Chemist”, *Organometallics* **2010**, 29, 2176-2179.
123. C.N. Chiyumba, “Photodynamic Anticancer and Antimicrobial Activities of π-Extended BODIPY Dyes and Cationic Mitochondria-Targeted Porphyrins”, **2022**, MSc Thesis, Rhodes University.
124. H. Shi, Z. An, P-Z. Li, J. Yin, G. Xing, T. He, H. Chen, J. Wang, H. Sun, W. Huang & Y. Zhao, “Enhancing Organic Phosphorescence By Manipulating Heavy-Atom Interaction”, *Crystal Growth & Design* **2016**, 16, 808-813.
125. Y.I. Openda, B.P. Ngoy & T. Nyokong, “Photodynamic Antimicrobial Action of Asymmetrical Porphyrins Functionalised Silver-Detonation Nanodiamonds Nanoplatofrms for the Suppression of *Staphylococcus aureus* Planktonic Cells and Biofilms”, *Sec. Medicinal and Pharmaceutical Chemistry* **2021**, 9, 628316.
126. M. Thandu, C. Comuzzi, D. Goi. “Phototreatment of Water by Organic Photosensitizers and Comparison with Inorganic Semiconductors”, *International Journal of Photoenergy* **2015**, 2015, 521367.
127. M. Bartolomeu, S. Reis, M. Fontes, M.G.P.M.S. Neves, M.A.F. Faustino & A. Almeida, “Photodynamic Action Against Wastewater Microorganisms and Chemical Pollutants: An Effective Approach with Low Environmental Impacts”, *Water* **2017**, 9, 630.
128. Z. Malá, L. Žárská, R. Bajgar, K. Bogdanová, M. Kolár, A. Panáček, S. Binder & H. Kolárová, “The Application of Antimicrobial Photodynamic Inactivation on Methicillin-Resistant *S. aureus* and ESBL-Producing *K. Pneuminiae* Using Porphyrin Photosensitiser in Combination with Silver Nanoparticles”, *Photodiagnosis and Photodynamic Therapy* **2021**, 33, 102140.

129. S.G. Jenkins & A.N. Schuetz, “Current Concepts in Laboratory Testing to Guide Antimicrobial Therapy”, *Mayo Clinic Proceedings* **2012**, 87, 290-308.
130. B. Babu, A. Sindelo, J. Mack T. Nyokong, “Thien-2-yl Substituted Clhorins as Photosensitizers for Photodynamic Therapy and Photodynamic Antimicrobial Chemotherapy”, *Dyes and Pigments* **2021**, 185, 108886.
131. D.C. Swinney, “Molecular Mechanism of Action (MMoA) in Drug Discovery”, *Annual Reports in Medicinal Chemistry* **2011**, 301-317.
132. S. Dingiswayo, K. Burgess, B. Babu, J. Mack & T. Nyokong, “Photodynamic Antitumour and Antimicrobial Activities of Free-Base Tetra(4-methylthiolphenyl)chlorins and its Tin(IV) Complex”, *ChemPlusChem* **2022**, 87, e202200115.
133. B. Babu, E. Prinsloo, J. Mack & T. Nyokong, “Synthesis, Characterisation and Photodynamic Activity of Sn(IV) Triarylcorroles with Red-Shifted Q bands”, *New Journal of Chemistry **2019**, 43, 18805-18812.*
134. R.C. Soy, B. Babu, J. Mack & T. Nyokong, “The Photodynamic Activities of the Gold Nanoparticle Conjugates of Phosphorous(V) and Gallium(III) A_3 *meso*-triarylcorroles”, *Dyes and Pigments* **2021**, 194, 109631.
135. T. Wada, H. Sasabe, A.F. Garito, H. Higuchi & J. Ojima, “Optical Nonlinearities of Macrocyclic Conjugated Systems”, *Nonlinear Optics* **1992**, 299-204.
136. L. Li, J. Hu, X. Shi, W. Ruan, J. Luo & X. Wei, “Theoretical Studies on Structures, Properties and Dominant Debromination Pathways for Selected Polybrominated Diphenyl Ethers”, *International Journal of Molecular Sciences* **2016**, 17, 927.
137. T. Ding, E.A. Alemán, D.A. Modarelli & C.J. Ziegler, “Photophysical Properties of a Series of Free-Base Corroles”, *Journal of Physical Chemistry* **2005**, 109, 7411-7417.
138. R. Giovanetti. “The Use of Spectrophotometry UV-Vis for the Study of Porphyrins.” *Macro to Nano Spectroscopy.* **2012**.